Karlsruher Institut für Technologie

From Micro to Nano: Shining Light on Complex Macroscopic and Nanoscopic Structures

Zur Erlangung des akademischen Grades eines

DOKTORS DER NATURWISSENSCHAFTEN
(Dr. rer. nat.)

der KIT-Fakultät für Chemie und Biowissenschaften

des Karlsruher Instituts für Technologie (KIT)

genehmigte

DISSERTATION

von

Dipl. Chem. Tanja Kristina Claus

aus
Heilbronn-Neckargartach

KIT-Dekan:	Prof. Dr. W. Klopper
Referent:	Prof. Dr. C. Barner-Kowollik
Korreferent:	Prof. Dr. H.-A. Wagenknecht
Tag der mündlichen Prüfung:	25.04.2017

Die vorliegende Arbeit wurde im Zeitraum zwischen November 2013 und April 2017 im Institut für Technische Chemie und Polymerchemie (KIT) unter der Betreuung von Prof. Dr. Christopher Barner-Kowollik angefertigt.

Meiner liebevollen, leicht verrückten Familie gewidmet.

Lucundi acti labores.

- *M. T. Cicero, de finibus, 2, 105.*

ABSTRACT

Photochemical methods have proven to be a versatile tool in polymer and surface science. With light as energy source, chemical reactions can be performed in a clean, spatially and temporarily resolved way. In the herein presented study, (visible) light triggered ligations were employed for complex functionalizations of micro- to nanometer sized objects.

First, two novel photoreactive methacrylate monomers were designed for the direct incorporation into structures fabricated by direct laser writing (DLW). One monomer posesses a phenacyl sulfide moiety, while the other one is based on an α-methylbenzaldehyde functionality. Both monomers were incorporated in DLW photoresists and specific parts of three dimensional (3D) microscaffolds were subsequently written with these resists. The incorporated photoreactivity allowed for a direct, simultaneous, and dual postmodification by irradiation with UV light. The resulting dual functionalized scaffolds were thoroughly characterized by Time-of-Flight Secondary-Ion Mass Spectrometry (ToF-SIMS) and Confocal Fluorescence Microscopy (CFM). Consequently, the obtained dual photoreactivity of the 3D structures was employed to simultaneously immobilize two proteins at different positions. The so obtained cell adhering scaffolds were ultimately subjected to cell experiments by the collaboration partner whereby their cell guiding abilities were proven. In a short excursion, infrared microscopy (IRM) was investigated as mild surface characterization method for DLW written structures.

In the next project presented in the current thesis, a reversible, visible light triggered surface patterning technique was developed. Thereto, a new, electron rich anthracene derivative, able to anchor to silicon surfaces, was synthesized. The absorption spectrum of the anthracene moiety was red shifted by expanding the π system with a triazolyl substituent attached to the 9-position. This allowed for a visible light triggered cycloaddition and a cycloelimination triggered by near-UV light. Millimeter sized, erasable patterns of small molecules as well as polymer strands were achieved on silicon wafers utilizing a wavelength of 410 nm for the writing step and 360 nm for the erasing step. Again, the obtained pattern and erased surfaces of the writing/erasing cycles were characterized employing ToF-SIMS. The presented method crucially expands the toolbox of visible light cycloaddition reactions and could prove valuable for future coating applications.

In the final part of the presented thesis, dual photoreactivity was implemented in triblock copolymers, enabling sequential single chain nanoparticle (SCNP) folding. The aforementioned light reactive methacrylic monomers were copolymerized with methyl methacrylate (MMA) by reversible addition fragmentation chain transfer (RAFT) polymerization. High conversions of both monomers were achieved while control over the

polymerization process was maintained, which enabled a one pot block copolymerization procedure. Subsequently, the (dual) photoreactive polymers were employed for covalent, crosslinker assisted SCNP formations. The successfully compacted SCNPs were analyzed by size exclusion chromatography (SEC) and dynamic light scattering (DLS). Utilizing a dual photoreactive triblock copolymer, a stepwise compaction of a SCNP, mimicking the folding behavior of proteins, was achieved.

In summary, within the current thesis, the utilization of (visible) light triggered ligations for the facile functionalization of 3D microscaffolds, reversible surface patterning and stepwise SCNP folding is presented.

ZUSAMMENFASSUNG

Photochemische Methoden haben sich als vielseitiges Werkzeug für die unterschiedlichsten Anwendungen sowohl in der Polymer- als auch in der Oberflächenchemie erwiesen. Die Verwendung von Licht als Energiequelle erlaubt eine zeitlich sowie örtlich kontrollierte Ausführung von chemischen Reaktionen. Dies wurde in der vorliegenden Dissertation ausgenutzt um komplexe Micro- bzw Nanostrukturen mittels (sichtbaren) lichtinduzierten Prozessen zu derivatisieren.

Im ersten Teil der Arbeit wurden zwei neuartige, photoreaktive Monomere auf Methacrylatbasis entwickelt, die in Lacken für Direktes Laserschreiben (DLW) eingesetzt wurden. Als lichtsensitive Gruppen wurden Phenacylsulfid- bzw. α-Methylbenzaldehydsubstituenten in die Monomere eingeführt. Durch Zumischen der Monomere in DLW-Lacke konnten so zweifach reaktive 3D Microstrukturen erhalten werden. Diese wurden anschließend in einer dualen, simultanen, lichtinduzierten Oberflächenmodifikation an definierten Punkten funktionalisiert. Die so erhaltenen, zweifach modifizierten Gerüste wurden per Sekundärionen-Flugzeitmassenspektrometrie (ToF-SIMS) und konfokaler Fluoreszenzmikroskopie (CFM) charakterisiert. In einem nächsten Schritt wurde die duale Photoreaktivität der Strukturen genutzt um verschiedene Proteine ortsaufgelöst zu immobilisieren. Die erhaltenen Mikrostrukturen wurden schließlich für gezielte Zellanbindungen in der Gruppe des Kooperationspartners in sog. Zellsortierungsexperimenten eingesetzt. In einem kurzen Exkurs wurde gezeigt, dass die o.g. DLW Strukturen auch mit Hilfe der milden, zerstörungsfreien Infrarotmikroskopie untersucht werden können.

Im zweiten Abschnitt der vorliegenden Dissertation wurde eine neue Methode zur reversiblen, ortsaufgelösten Oberflächenmodifikation mittels (sichtbarem) Licht entwickelt. Dazu wurde ein neuartiges, elektronenreiches Anthracenderivat synthetisiert, dessen Struktur eine Anbindung auf Siliziumoberflächen ermöglicht. Das Absorptionsspektrum des Anthracenderivats wurde durch Vergrößerung des π Systems mittels eines Triazolyl-Substituents an 9-Position rotverschoben. Dies ermöglichte eine Cycloaddition durch Bestrahlung mit sichtbarem Licht und eine Cycloeliminierung unter Anwendung von nahem UV Licht. Eine millimetergroße, reversible Musterung von Siliziumwafern mit kleinen organischen Molekülen und mit Polymersträngen konnte so mit einer Wellenlänge von 410 nm realisiert werden. Das Ablösen der Muster erfolgte anschließend unter Bestrahlung bei 360 nm. Wie im vorhergehenden Abschnitt auch, wurden die Resultate der einzelnen Schreib-/Ablösevorgänge mittels ToF-SIMS analysiert. Die entwickelte Methode erweitert entscheidend den Werkzeugkasten der sichtbaren lichtinduzierten Cycloadditionen und

könnte sich in Zukunft als nützlich erweisen, insbesondere in Anwendungen auf dem Gebiet der reversiblen Beschichtungen.

Im letzten Teil der vorliegenden Arbeit wurden die zuvor erwähnten photoreaktiven Methacrylatmonomere zur Synthese doppelt photoresponsiver Triblockcopolymere für Einzelkettenanopartikelfaltungen eingesetzt. Zu diesem Zweck wurde die reversible Additions-Fragmentierungs-Kettenübertragungspolymerisation (RAFT Polymerisation) zur (Block)Copolymerisation der einzelnen Photomonomeren mit Methylmethacrylat angewendet. Es konnten – trotz hoher Monomerumsätze – definierte, engverteilte Polymere erhalten werden. Die Polymerisation zu hohen Umsätzen erlaubte eine direkte Kettenverlängerung in einer Eintopfreaktion. Anschließend wurden die erhaltenen Polymere in einer lichtinduzierten Faltung von Einzelkettennanopartikeln mittels eines kovalenten Vernetzers eingesetzt. Die erhaltenen Nanopartikel wurden mittels Größenausschlusschromatografie (SEC) und dynamischer Lichtstreuung (DLS) analysiert. Unter Verwendung des doppelt photoreaktiven Triblockcopolymers konnte eine schrittweise Kompaktierung der einzelnen Kette erhalten werden. Dieses Verhalten zielt auf ein besseres Verständnis und Nachahmung des natürlichen Faltungsprozesses von Proteinen.

Zusammengefasst werden in der vorliegenden Dissertation neue, vielseitige, durch (sichtbares) Licht induzierte Methoden für die schnelle Funktionalisierung von 3D Mikrostrukturen, zur reversiblen Oberflächenmusterung und zur schrittweisen Einzelkettenfaltung von Polymeren vorgestellt.

ERKLÄRUNG

Ich erkläre hiermit, dass die vorliegende Arbeit im Rahmen der Betreuung durch Prof. Dr. Christopher Barner-Kowollik selbstständig von mir verfasst und keine anderen als die angegebenen Quellen und Hilfsmittel verwendet wurden. Wörtlich oder inhaltlich übernommene Stellen sind als solche durch Zitate kenntlich gemacht. Die Satzung des Karlsruher Instituts für Technologie (KIT) zur Sicherung guter wissenschaftlicher Praxis wurde beachtet und die Abgabe und Archivierung der Primärdaten gemäß Abs. A (6) der Regeln zur Sicherung guter wissenschaftlicher Praxis des KIT beim Institut ist gesichert. Ich versichere, dass die elektronische Version mit der gedruckten Ausgabe übereinstimmt. Des Weiteren erkläre ich, dass ich keine vorausgegangenen Promotionsversuche unternommen habe und mich derzeit auch nicht in einem weiteren, laufenden Promotionsverfahren befinde.

Karlsruhe, 15.03.2017

_____

Tanja Claus

PUBLICATIONS ARISING FROM THE PRESENT THESIS

[3] **T. K. Claus**, J. Zhang, L. Martin, M. Hartlieb, H. Mutlu, G. Delaittre, S. Perrier, C. Barner-Kowollik, Macromol. Rapid Commun. **2017**, *1700264*. https://doi.org/10.1002/marc.201700264.

[2] **T. K. Claus**, S. Telitel, A. Welle, M. Bastmeyer, A. P. Vogt, G. Delaittre, C. Barner-Kowollik, *Chem. Commun.*, **2017**, *53*, 1599.

[1b] **T. K. Claus**, B. Richter, V. Hahn, A. Welle, S. Kayser, M. Wegener, M. Bastmeyer, G. Delaittre, C. Barner-Kowollik, *Angew. Chem.*, **2016**, *128*, 3882.

[1a] **T. K. Claus**, B. Richter, V. Hahn, A. Welle, S. Kayser, M. Wegener, M. Bastmeyer, G. Delaittre, C. Barner-Kowollik, *Angew. Chem. Int. Ed. Engl.*, **2016**, *55*, 3817.

TABLE OF CONTENTS

1

INTRODUCTION

Besides the presence of water, light is the most critical factor enabling life on earth. Green plants utilize sunlight as energy source for the production of livestock by the process of photosynthesis. Plant-based biomass is then digested by other living species at the start of the food chain, meaning that practically any energy accessible on earth is derived from sunlight. However, the nature of light and its importance for nature remained undisclosed up until the late 18th century, when researchers first reported the observation of photosynthetic processes.[1-2] Nowadays, light plays an important role in many scientific fields, such as chemistry, physics, biology, engineering or medicine. As contactless, spatially and temporally controllable energy transmitter, light enables a vast variety of techniques and precise process control. Organic chemists realized the importance of light after Hermann Trommsdorf reported the first organic photochemical reaction in 1834.[3] In the sequel, further photochemical reactions such as the light induced *cis-trans*-isomerizations of olefins, halogenations of aromatic compounds and the first photodimerizations of anthracene and cinnamic acid were discovered, however not synthetically exploited.[4] With physicists providing an improved understanding of the nature of light in the early 20th century[5-6] and the development of advanced irradiation sources (i.e., lasers) in the middle of the same century,[7] light triggered reactions gained popularity. Especially with the growing discussion on global warming accompanied by a rising awareness about the damage done to nature by fossil or nuclear power supplies, focus is shifting towards (sun)light as environmental friendly, clean source of energy. This enhanced interest in exploiting light and its energy for forming or breaking covalent bonds in organic and polymer chemistry.[8-10] Additional features such as spatial and temporal control as well as

the tunability of the energy supplied by adjusting the wavelength regime or light intensity, allow for a wide range of applications for light induced reactions.[11-13] Furthermore, photoreactions, except photoredox catalysis,[14] do not require the utilization of sensitive/aggressive reagents or/and metal catalysts and can usually be performed under ambient conditions. Thanks to the potentially mild conditions, photoreactions can in specific cases even be applied in biological contexts.[15-16]

In the present thesis, light as trigger is employed to functionalize micro- and nanometer sized objects and surfaces. Novel photoreactive monomers are utilized to functionalize three dimensional (3D) microscaffolds in a biological context to achieve cell guiding scaffolds (Chapter 3). The same monomers are further exploited to achieve a stepwise compaction of single polymer chains, mimicking protein folding behavior (Chapter 5). Moreover, reversible surface patterns were achieved by designing a visible light reactive anthracene derivative (Chapter 4). An overview of the projects investigated in the present thesis is illustrated in **Scheme 1**.

Although photochemical ligation represents a standard procedure in contemporary polymer and surface science, some areas of applications critically lack adequate techniques. For example, so far, fabrication of precisely modifiable 3D structures is either coupled to extensive efforts[17] or lacks spatial control.[18] Particularly, there is still a need for better defined 3D microenvironments to study cell matrix interactions, the latter playing a key role for cellular functions (e.g., proliferation, adhesion or differentiation behavior).[19] To fully

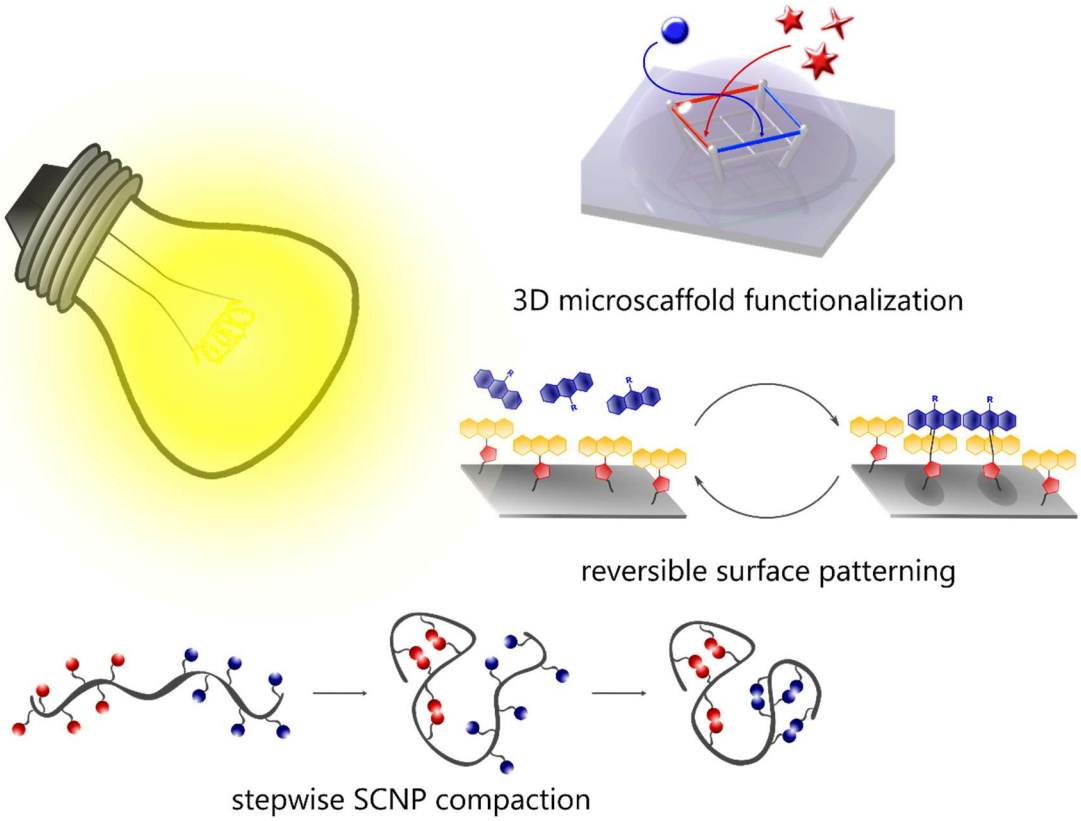

Scheme 1: Schematic representation of the projects described in the current thesis. (Visible) light was employed for dual, simultaneous 3D microscaffold postmodification, reversible surface patterning and stepwise SCNP formation.

understand how cells interact with their environment and which factors influence the aforementioned behaviors, their direct surroundings needs to be perfectly suited. Among other aspects, the chemical nature of the environment is an important one. Therefore, one aim of the current thesis is to fabricate well-defined 3D microscaffolds with controllable surface chemistry employing direct laser writing (DLW). DLW allows for rapid construction of micrometer sized scaffolds, building up perfectly suited niches for cell attachment studies.[20] As photochemical methods provide a mild and precise approach to modify substrates, photoligations were selected to realize such structures. As multifunctional environments are found in nature, it was important to also develop methods to achieve controlled multiple, independent surface modification. In this respect, orthogonally addressable photoreactive groups were were of particular interest.

A wide field of research in organic photochemistry focuses on the red shifting of the absorption range of molecules in order to achieve milder reaction conditions.[21] Visible light photocatalysis is well-established.[22] However, the requirement for a soluble catalyst may be undesirable. Recently, the first catalyst-free visible light induced cycloaddition reactions were introduced by Barner-Kowollik and coworkers.[23-24] and utilized to functionalize small molecules and polymer strands. However, one drawback of both techniques is the lack of reversibility. Reversibility allows for a vast variety of applications, such as self-healing materials or coatings for high performance materials as well as the reversible coding of cell scaffolds.[25] Therefore, an additional aim of the present thesis was the development of a red-shifted, reversible photoligation method. Anthracene was selected as starting point, since the photoreversibility of its dimerization is a long known fact.[26]

In the last part of the current thesis, it was the aim to harness light for the synthesis of another biology related type of material. The concept of single chain nanoparticle (SCNP) formation is highly inspired by the natural process of protein folding. Although a vast variety of ligation tools, among them light induced ones, have already been reported to achieve SCNP folding,[27-29] only one step compactions are commonly employed. However, the actual folding process of proteins occurs in a stepwise fashion.[30] Two examples of stepwise compartmentalization of polymer chains have been reported already,[31-32] yet both require protection group strategies and employ toxic chemicals such as diisocyanates. Light based protocols can help to circumvent both drawbacks. Hence, the aim to investigate a dual compaction strategy based upon photochemical ligations was set.

Over the course of the current study, all aforementioned aims were investigated to provide a valuable contribution to photochemistry in the realm of polymer and surface science. Thus, known ligation tools were exploited to achieve new applications, and a known ligation method was modified to obtain new reactivity in longer wavelength regimes.

2

THEORY AND BACKGROUND

The purpose of the following section is to provide key insight into the theoretical background of the various subjects covered in the present thesis. To achieve this, it offers a literature review of topics relevant for the thesis, while not attempting to be entirely comprehensive. It commences with an introduction to basic radical polymerization protocols (Section 2.1) and, proceeds with a short introduction to the fundamental laws of photochemistry (Section 2.2.1-2.2.2) and its applications to polymer and surface science (Sections 2.2.3 and 2.2.4). The fabrication of microstructures via DLW is introduced in Section 2.3. Furthermore, an explanation of important surface characterization techniques employed in the current thesis is given in Section 2.4. Finally, the chemistry and characterization of single chain nanoparticles (SCNPs) is introduced in Section 2.5.

2.1 Radical Polymerization

2.1.1 Free Radical Polymerization (FRP)

Of the 230 Mt of polymeric material produced worldwide (2009), 40-45 % were formed by free radical polymerization protocols, demonstrating the importance of this polymerization technique.[33] The reasons for the wide use of free radical polymerizations[34-35] are their versatile application to a vast variety of functional monomers, different production processes (bulk polymerization, solution polymerization or emulsion polymerization), high tolerance towards functional groups and mild reaction conditions. These allow the synthesis

of very different polymer materials ranging from low density polyethylene (LDPE), polystyrene (PSt) to polyvinylchloride (PVC).

The FRP process can be divided in four parallel occurring main steps:[34]

1 Initiation
2 Propagation
3 Termination
4 Chain transfer

The initiation itself consists of two sub steps, first the homolytic decomposition of the initiator, second the actual initiation by addition of an initiator radical to the vinylic moiety of the employed monomer M (see **Scheme 2**).

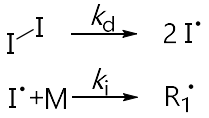

Scheme 2: Initiation process in FRP: First, a homolytic dissociation of the initiator molecule resulting in two initiator radicals; Second an addition of an initiator radical to the employed monomer.

In this two-step process, the dissociation rate of the initiator is the rate determining step.[36] The decay of the initiator can be triggered by various stimuli, such as heat, light or redox processes. After the first addition, the polymerization continues via propagation of the newly formed radical R_1 by successive addition of more and more monomer units to the propagating chain (see **Scheme 3**). The rate of the propagation step is determined by the reactivity of the monomer unit, ranging from very high propagation rate coefficients (i.e. fast propagation reaction) (k_p) for e.g., acrylate based monomers (10^4 L mol^{-1} s^{-1} at 60 °C) to slow propagating radicals (e.g. methacrylates) with a k_p of ~10^2 L mol^{-1} s^{-1} at 60 °C.[34]

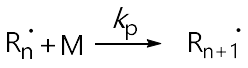

Scheme 3: Propagation process in FRP: A monomer unit is added to a propagating radical species with the rate coefficient k_p.

Such a propagating chain can, in general, be terminated by two potential reaction pathways (depicted in **Scheme 4**).

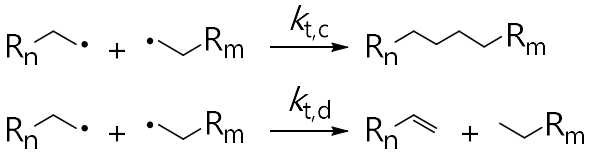

Scheme 4: Potential termination events in FRP: Recombination of two radical centers leading to one dead chain (top) and disproportionation (bottom), where two radical centers are inactivated by a hydrogen abstraction.

The first possible termination reaction is a simple recombination of two active radical centers (rate coefficient $k_{t,c}$), e.g. two propagating chains, creating a dead chain of higher molecular weight. The second possibility is a disproportionation reaction (rate coefficient $k_{t,d}$), where after a β hydrogen abstraction, one dead chain and one chain with a vinylic chain end is

obtained. This newly formed macro monomer can participate again in the polymerization process, leading to chain branching. The ratio in which these reactions occur is highly dependent on the type of monomer employed in the polymerization. If the monomer is e.g. sterically hindered at the radical center (methacrylates), the recombination pathway is suppressed and is therefore not taking place to a large extent. In such a case, the termination occurs to a high degree via the disproportionation pathway. For less sterically hindered monomers (e.g. styrene) more recombination is observed.[37]

In a last main elemental reaction step, a propagating chain can undergo different side reactions, with the most important one being, the so-called chain transfer reaction. (see **Scheme 5**).

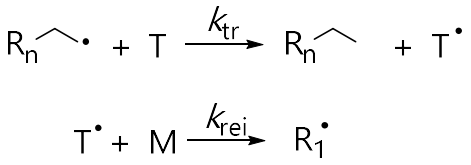

Scheme 5: Chain transfer reaction in FRP: A propagating chain is terminated by a transfer agent (T) that subsequently reinitiates the polymerization by attacking a monomer unit (M).

An active radical center is captured by a so-called transfer agent (T) present in the reaction mixture, terminating the propagating chain. The transfer agent can now reinitiate the polymerization by attacking a monomer unit or a macro monomer formed by disproportionation and therefore creating a new propagating chain. Depending on the type of monomer employed, the transfer process can be of high importance and can also occur as a chain transfer to the backbone via an abstraction of a backbone hydrogen atom (e.g. for acrylates).[38] The transfer reaction also limits the maximal reachable molecular weight in a FRP that can be calculated via the Mayo equation (**Equation 1**):[36]

$$\frac{1}{DP_n} = (1+\lambda)\frac{k_t[R]}{k_p[M]} + C_M + C_T\frac{[T]}{[M]}$$

Equation 1: Mayo equation to calculate the maximum achievable molecular weight with DP_n as degree of polymerization, λ as ratio of the rate coefficient for recombination $k_{t,c}$ and disproportionation $k_{t,d}$ and k_t as the sum of both termination rate coefficients. Furthermore [R], [M] and [T] stand for the concentrations of radicals, monomer and transfer agent, respectively. The constants C_M and C_T are the ratios of the transfer-to-monomer or the transfer-to-transfer agent rate coefficients to the propagation rate coefficient (k_p).

The degree of polymerization (DP_n) is given via the variables λ (ratio of the rate coefficient for recombination $k_{t,c}$ and disproportionation $k_{t,d}$), C_M and C_T (ratios of the transfer-to-monomer or the transfer-to-transfer agent rate coefficients with the propagation rate coefficient (k_p)) and the concentrations of radicals [R], monomer [M] and transfer agent [T]. However, since the Mayo equation is still a differential equation, it provides only the instantaneous DP_n. The main drawback of FRP is the existence of termination and chain transfer reactions. These processes both lead to a broadening of the polymer distribution. Chains are terminated early via termination reactions and transfer agents and new chains

are randomly started via transfer to monomer. If a transfer to the backbone of an already existing chain occurs, a branched polymer is obtained. The generated polymer sample after a FRP is therefore often very disperse in molecular weight, end group functionality and architecture. To improve these features more advances polymerization techniques were developed.

2.1.2 Reversible Deactivation Radical Polymerization (RDRP)

To overcome the drawbacks of FRP processes (as mentioned above) the effects of an early termination need to be eliminated. To achieve this, the reversible deactivation radical polymerization (RDRP) techniques, formerly known as controlled/living radical polymerizations, were introduced over the last decades. Today, three methods became apparent: nitroxide mediated polymerization (NMP),[39] atom transfer radical polymerization (ATRP)[40] and reversible addition fragmentation chain transfer (RAFT) polymerization.[41] The underpinning principle is the same for those three techniques and lies in the reversible deactivation of the propagating chain, therefore suppressing the actual termination via recombination or disproportionation that would lead to dead chains.[42] In a true living polymerization (e.g. anionic polymerization) termination and chain transfer events are not present in the reaction mechanism, leading to a narrow molar mass distribution and uniform functionalities at the end of the polymers (chain end fidelity).[43] Although the termination of radical centers cannot be eliminated completely, the suppression via an equilibrium between a dormant species and the active, propagating radical chain has proven to be a powerful tool to obtain a better control over the disparity and chain end fidelity of the polymer sample. Additionally, typical RDRP processes feature the following criteria: narrow dispersity of polymer samples ($Đ \leq 1.2$), a linear growth of the molecular weight with monomer conversion, a complete and fast initiation step that exceeds the rate of propagation to ensure a steady number of radical centers and a high end group fidelity (i.e. chemically uniform end groups) allowing for subsequent synthetic end chain functionalizations.[44] In the context of this work, the RAFT polymerization was employed and its features will therefore be discussed in more detail in the next chapter.

2.1.2.1 Reversible Addition Fragmentation Chain Transfer (RAFT) Polymerization

In Section 5 of the present thesis, the synthesis of blockcopolymers containing photoreactive monomers employing the RAFT polymerization is described. The RAFT process is one of the most important RDRP techniques, employing a degenerative chain transfer equilibrium to suppress irreversible chain terminations. In comparison to other techniques (such as NMP or ATRP), the overall radical concentration is not reduced (in

comparison to FRP) to lower the probability of chain termination (persistent radical effect), but a transfer agent is added to deliberately induce a frequent transfer of propagating chains to the transfer agent. Therefore, chains are protected from termination ("dormant chains"), but new propagating radicals are formed as well. Typical transfer agents are dithiobenzoates or trithiocarbonates.[45] The overall mechanism of a RAFT process entails six steps:

1 Initiation
2 Preequilibrium
3 Reinitiation
4 Propagation
5 Main equilibrium
6 Termination

The initiation, propagation and termination resemble their FRP analogs (see **Scheme 6**), whereby the propagation step occurs during both equilibria.[46] In the preequilibrium, a propagating chain ($Pn^{\cdot}$) is trapped by a chain transfer agent (CTA). The radical adds to the thiocarbonyl group of the RAFT agent, forming an intermediate radical (kadd). This intermediate radical can now either fragment back to the propagating chain ($Pn^{\cdot}$) and the CTA (k-add), or decay into a protected chain

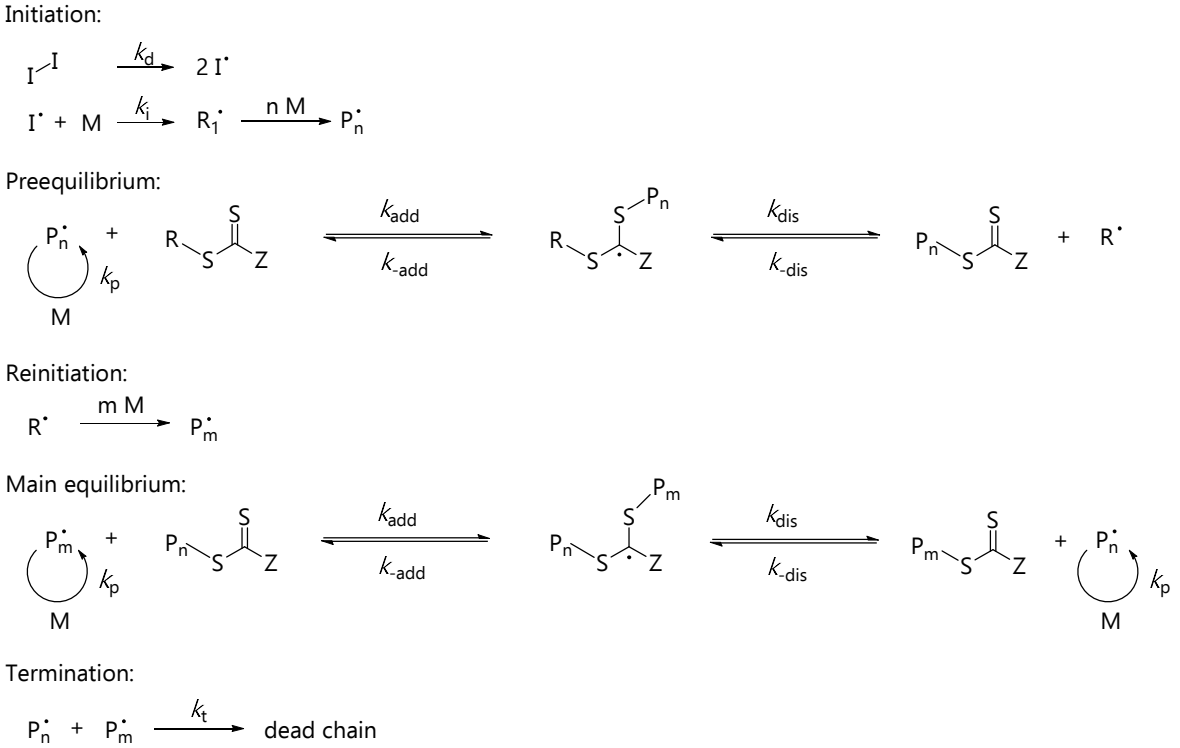

Scheme 6: General overview of the RAFT mechanism. The six reaction steps are depicted (initiation, preequilibrium (with propagation), reinitiation, main equilibrium (again with propagation) and termination.[46]

Scheme 7.[47] If, for example, a relatively stable radical like a methyacrylic radical is to be captured by a RAFT agent, the formed intermediate radical has to be well stabilized. However, if too well stabilized, a fragmentation into the macro-RAFT and the R-group is inhibited. The formed R-group radical also needs to be in the stability range of the monomer

derived radical to allow for a fragmentation in this direction and a fast reinitiation. Therefore, a CTA allowing a good control over a methacrylic polymerization, requires a Z-group highly stabilizing the intermediate radical (e.g. a phenyl ring) and an R-group forming a very stable, Scheme 7. Given that the RAFT agent is judiciously selected, a vast variety of – functional – monomers can be polymerized due to the robustness and tolerance of the RAFT process towards functional groups.[46] An additional avenue to incorporate functionality into the formed polymer structure is to employ functional RAFT agents exhibiting tailor made Z- or-R- or both groups allowing for a facile post-modification of the polymer. Typical post modification procedures are hetero Diels–Alder (HDA) reactions of dithioesters with

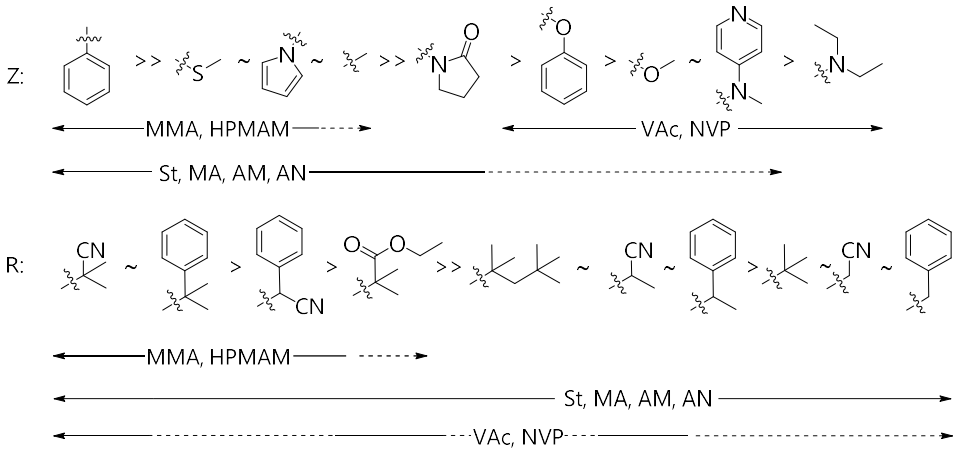

Scheme 7: Schematic overview of R- and Z-group substitutions and their ability to obtain good (—) or limited (---) control when employed in RAFT polymerizations of various monomer groups: methyl methacrylate (MMA), N-(2-hydroxypropyl)methacrylamide (HPMAM), vinyl acetate (VAc), N-vinylpyrrolidone (NVP), styrene (St), methyl acrylate (MA), acrylamide (Am) and acrylonitrile (An). The Scheme was redrawn from Ref. [47], Copyright (2012) ACS publishing.[47]

dienes,[48] photo ligations via a 1,3 dipolar cycloaddition,[49] or even supramolecular post-modifications.[50]

A key additional feature of a living polymerization that is also fulfilled by RDRP procedures, is the possibility of a direct chain extension in a subsequent polymerization step yielding blockcopolymers.[51] This can either be achieved by polymerizing the first monomer, precipitating the resultant polymer to isolate a macro-RAFT initiator that can then be employed in a further polymerization step as transfer agent, or by sequentially adding the monomers to the polymerization in a one pot reaction.[52] The latter method bears less synthetic effort, as the macro-RAFT agent has not to be isolated and purified in between the polymerization steps. However, when adding the monomers in a one pot approach, a quantitative monomer conversion (≥ 99 %) has to be reached for each block to obtain a defined block sequence.[53] Usually, when a RAFT experiment is conducted, the polymerization is quenched after low conversions to maintain a high proportion of living end groups.[54] An alternative common method to retain controlled characteristics while applying a one pot procedure is to add a sequel monomer after the initial RAFT polymerization. As a result, a monomer mixture is polymerized by this process and the

composition of the quasi blockcopolymer is mainly determined by the monomers' copolymerization reactivity ratios.[55] However, it requires certain features to be fulfilled to achieve a true blockcopolymer instead of a quasi blockcopolymer. In a RAFT process, the amount of dead chains that have undergone bimolecular termination directly correlates with the amount of radicals generated by the initiator.[56] Therefore, a reduction of the added radical initiator' proportion should reduce the generation of dead chains. However, in a conventional RAFT procedure, the rate of polymerization is reduced when lowering the radical concentration, as can be seen in **Equation 2**:

$$R_p(t) = k_p + [M] + \sqrt{\frac{f * k_d * [I]_0 * e^{-k_d t}}{k_t}}$$

Equation 2: Rate of polymerization (R_p(t)) in a conventional RAFT process. With k_p, k_d, and k_t as rate coefficients for the propagation, dissociation and termination, respectively, the monomer [M] and initial initiator $[I]_0$ concentration, f as initiator efficiency and t as time.

Besides the initiator concentration, the rate of polymerization can be influenced by varying the monomer concentration, or the temperature (polymerizing at higher temperatures to increase k_p), while keeping the initiator concentration at a low level.[56] Concerning the equation for the theoretical livingness (L) of the RAFT process (**Equation 3**), it is apparent, that L is increased by a decreased initial initiator concentration:

$$L = \frac{[CTA]_0}{[CTA]_0 + 2 * f * [I]_0 * (1 - e^{-k_d t}) * (1 - \frac{f_c}{2})}$$

Equation 3: Degree of livingness in a conventional RAFT process. With $[CTA]_0$ and $[I]_0$ as the initial concentration of RAFT agent and the initial initiator concentration, respectively, f as the decay efficiency for the employed initiator, k_d as rate coefficient for the decomposition, t as time and f_c as coupling factor of bimolecular termination reactions.

The initial concentration of RAFT agent is $[CTA]_0$ and the initial initiator concentration is $[I]_0$, respectively. f represents the efficiency for the employed initiator (probability that a formed radical will actually start chain growth), while the factor 2 takes into account that for a typical azo initiator, 2 initiating radicals are produced. The last term ($1-f_c/2$) correlates with the number of bimolecular termination events.[57] It can be derived that in order to get a high theoretical livingness, a high [CTA] over [I] ratio as well as a fast polymerization process is crucial (i.e., short polymerization time t). Recently, Perrier and co-workers introduced conditions based on these theoretical considerations to synthesize well defined RAFT multiblock copolymers (up to 20 blocks) employing acrylate based monomers in one pot approaches achieving quantitative monomer conversions.[52, 56, 58] Similar conditions were utilized in the present thesis to synthesize photoreactive (triblock)copolymers with methacrylate based monomers in a one pot approach, pushing the conversion of the monomers to over 90 % (see Chapter 5).

2.2 Photochemistry

In Nature, light plays a key role to maintain life, growth and (re)production processes. Scientists started to realize the importance of light when the first description of the photosynthetic process was published by Joseph Priestley in 1772.[1] However, he was not able to identify the role of light in the process of plants 'refreshing' – what he called – 'injured air'. Picking up these experiments on plants and pneumatic processes, John Ingenhousz discovered the importance of sunlight for the 'purification of air' in 1779.[2] In the following decades, researches focused on light induced biological processes,[59] until Hermann Trommsdorf observed the first directly light triggered chemical reaction in 1834.[3] He reported the color change of α-santonin from white to yellow when exposed to sunlight. Following this report, more discoveries were made, including the first synthetically employed photoreactions by Giacomo Ciamician and Paolo Silber in the early 1900s.[60-61] At the same time, physicists turned their attention towards the theoretical background of photochemistry, leading to the groundbreaking theory of the quantum nature of light by Max Planck in 1901[5] and its experimental proof by Albert Einstein in 1905.[6] Since then, both the theory of the interaction between light and matter as well as the synthetically applied photochemistry were widely investigated, leaving scientists today with a vast variety of chemistries and theories to exploit.

2.2.1 Physical background of molecular photochemical processes

The absorption of photons by matter is quantitatively described by Beer-Lambert's law of absorption (**Equation 4**):

$$\log\left(\frac{I}{I_0}\right) = -\varepsilon * c * l$$

Equation 4: Beer-Lambert's law of absorption with I and I_0 as transmitted and incident intensity of the light, respectively, ε as the extinction coefficient, c as concentration of the absorber and l as length of the absorbing system.[62]

The fact that the number of collisions between a photon and an absorbing molecule is proportional to the loss of photons serves as basis for the law. The extinction coefficient ε, determined via the ratio I/I_0, quantifies the ability of a chromophore to absorb light of a certain wavelength. After the absorption of energy and the resulting excitation of electrons to higher energy levels, several processes can occur inside the molecule, visualized in the so-called Jablonski-diagram (see **Scheme 8**):

- **Vibrational relaxation** from higher vibrational states to the lowest vibrational state of each electronic state.
- **Internal conversion (IC)** as radiationless transition from a higher electronic state to an exited vibrational state of a lower electronic state. IC occurs between states of

the same electronic multiplicity (triplet-triplet or singlet-singlet) and between isoenergetic vibrational levels. IC processes occur on very short time scale (picoseconds) allowing for following vibrational relaxations afterwards.

- **Inter system crossing (ISC)** as radiationless spin conversion from two isoenercetic vibronic levels of an excited singlet state to an excited triplet state. Again, ISC occurs on a picosecond timescale, and usually, vibrational relaxations occur afterwards, allowing for the system to reach the lowest vibrational state of the excited triplet state.
- **Fluorescence** results in the emission of light, while the system reaches an energetically lower state. The transition occurs from the lowest exited singlet state (S_1) to the ground singlet state (S_0) (Kasha's rule). As no change in multiplicity is necessary, fluorescence takes place fast, on a timescale of nanoseconds.
- **Phosphorescence** also occurs as a luminescent transition from an excited triplet state (T_1) to the ground singlet state (S_0). As the multiplicity change is a spin forbidden process, phosphorescence as a slow transition occurs on the timescale of seconds, and is less likely to happen.

Apart from releasing the energy thermally or photochemically, chemical reactions induced by light can occur either from an excited singlet or triplet state ($S_{1/2}$ or $T_{1/2}$). Possible reaction pathways for excited molecules are depicted in **Scheme 9**.

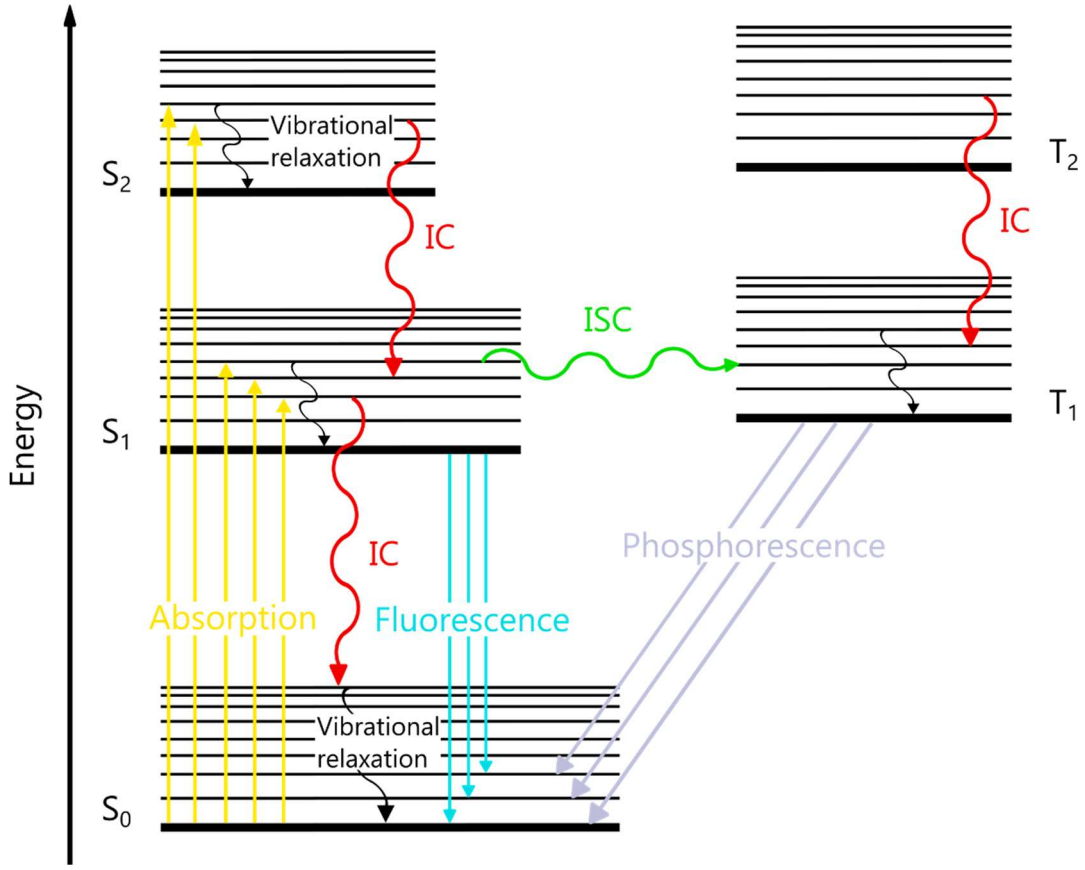

Scheme 8: Jablonski-diagram illustrating the possible photochemical processes in a molecule upon irradiation. Radiationless transitions such as vibrational relaxations, internal conversions (IC) and inter system crossing (ISC) are represented by wavy arrows, Absorption, fluorescence and phosphorescence, aka processes where light is involved, are depicted with straight arrows.[63]

Isomerization:	A*	⟶	A'
Dissociation:	A–B*	⟶	A + B
Addition/Insertion:	A* + B	⟶	A–B
Abstraction/Fragmentation:	A* + B	⟶	C + D
Dissociative excitation:	A* + C–D	⟶	A + C* + D

Scheme 9: Summary of processes that can occur from an excited molecule, with A, B, C and D illustrating arbitrary molecules.[62]

In the present thesis, dissociation and isomerization processes are the most important light induced trajectories and are therefore further discussed in Sections 2.2.3 and 2.2.4.

2.2.2 Molecular absorption and reactivity in the visible light range

The wavelength regime in which a molecule absorbs light greatly depends on the actual electronic transitions occurring in the molecule, which is closely related to the specific origin

of the electron. In organic molecules, electrons typically originate from 2s and 2p orbitals of carbon, oxygen or nitrogen atoms that are interacting to form chemical bonds. This interaction results in several types of molecular orbitals, highly depending on the nature of the atoms present. Generally, bonding and antibonding σ- and σ*-, bonding and antibonding π- and π*- orbitals as well as non-bonding orbitals n are formed. Non-bonding orbitals n occur when heteroatoms (e.g., oxygen, nitrogen, sulfur, halogens) are involved, and are occupied by electrons not involved in bond formation (aka lone pairs). The lowest possible electronic transition of an electron generally occurs between the highest occupied molecular orbital (HOMO) and the lowest unoccupied molecular orbital (LUMO). Depending on the electronic configuration of a molecule and occupancy of the molecular orbitals, several electronic transitions are observable:[64]

- transitions between the highest energetic bonding electron pair (σ) and the lowest energetic antibonding electron pair (σ*) are referred to as **σ→σ*** transitions and occur usually in saturated hydrocarbons.
- when π electrons are involved in bond formation, e.g., in aromatic systems, transitions between an occupied, bonding π molecular orbital and an unoccupied, antibonding π* molecular orbital (**π→π*** transition).
- when non-bonding orbitals are present, they most likely form the HOMO (e.g., carbonyl groups). However, due to a poor overlap between the localized n and delocalized π molecular orbitals, transitions to an unoccupied, antibonding π* orbital are forbidden and therefore **n→π*** transitions only exhibit a weak intensity.
- when molecules are strongly polarized, and exhibit non-bonding electron pairs (molecular orbitals), a so called **charge transfer (CT)** transition can occur (e.g., metal complexes). Due to the strong polarization, the excited electrons are delocalized over the entire system upon irradiation, leading to a pronounced red-shift and a strong absorption.

An overview of typical absorption regions of the above described transitions is depicted in **Scheme 10**. Apparently, only π→π* and n→π* transitions of conjugated

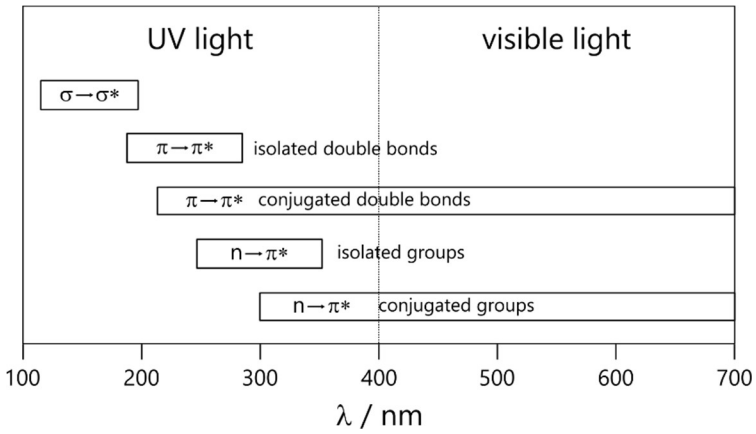

Scheme 10: Overview of the absorption wavelength ranges of the electronic transitions described above. (The scheme was adapted from Ref.[64])

systems occur in the visible light regime (above 400 nm), enabling for mild photochemical transformations. A first indication, whether a molecule is able to react under visible light irradiation, is its ability to absorb light around or above 400 nm. Absorption characteristics of a molecule are measured by UV-vis spectroscopy. In an UV-vis absorption spectrum, absorption bands derived from all electronic transitions present in the molecule are illustrated. It is therefore usually not possible to assign specific absorption bands to specific functional groups within the molecule. However, some structural motifs and substituents can influence to absorption spectrum of a molecule. Hereby, four general effects are possible:[64]

- A shift of the absorption maxima to longer wavelengths (bathochromic effect)
- A shift of the absorption maxima to shorter wavelengths (hypsochromic effect)
- An increase of the overall absorption intensity (hyperchromic effect)
- A decrease of the overall absorption intensity (hypochromic effect)

To achieve a red shift of the absorption spectrum for a given molecule, substituents inducing a bathochromic effect and, ideally, inducing a hyperchromic effect as well need to be attached to the structure. Well known structure-absorption correlations red shifting $n\rightarrow\pi^*$ and $\pi\rightarrow\pi^*$ transitions are for instance the enlargement of conjugated systems (lifting the energy level of the HOMO, while lowering the energy level of the LUMO), the introduction of electron accepting groups with an inductive effect (and therefore lowering the energy levels of HOMO, LUMO and n-orbitals) or the incorporation of conjugative substituents with an electron donating effect (lifting the energy levels of HOMO and LUMO, without having an effect on the n-orbitals).[65] These basic concepts have proven to be useful tools in the synthesis of organic dyes.[65] However, the bare existence of absorption in a specific light range, does not necessarily lead to the desired reactivity.[66]

Today, the most widely employed class of organic reactions where visible light is exploited, is the well-established field of photoredox catalysis.[14, 22] However, these type of reaction always require the addition of a catalyst and are therefore not discussed in the present thesis, as the subject was not covered in any of the conducted experiments. Nevertheless, a few examples of successfully red shifted organic photocycloadditions were reported in the recent literature.[23-24] For both 1,3-dipolar cycloadditions, the introduction of an enlarged π system tethered to the photoreactive moiety shifted the wavelength necessary for a photoreaction towards the visible light range (above 400 nm). The structures of the reported visible light reactive azirine and tetrazole species are depicted in **Scheme 11** in comparison to their UV light reactive counterparts. Pyrene acted as augmenter of the π system in both examples, shifting the necessary wavelength regime for a successful photoreaction from about 280 nm[67] to around 400 nm for the pyrene azirine,[23] and from 300-320 nm [68] to 410-420 nm for the pyrene aryl tetrazole species.[24]

A further example of a visible light induced cycloaddition is demonstrated in the present thesis, where an electron rich triazolyl anthracene derivative exhibiting an enlarged π system was employed to reversibly functionalize surfaces in a spatially resolved manner.[69]

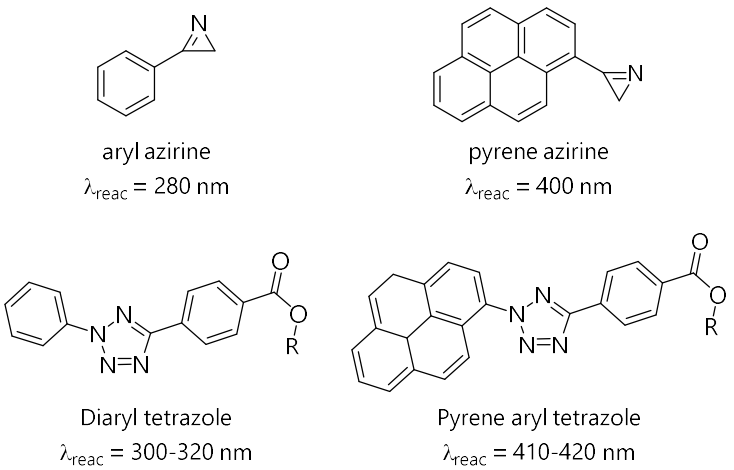

Scheme 11: Comparison between the structures of UV light vs visible light reactive azirine and tetrazole species. The enlargement of the π system from a single benzene ring to a pyrene substituent shifts the wavelength necessary for a photocycloaddition from the UV to the visible range of the light spectrum.

2.2.3 Light induced Diels–Alder (DA) reactions

In Chapter 3 and 5 of the current thesis, photo induced ligation reactions, where either an ene or a diene species is generated photochemically, and subsequently undergoes a [4+2] cycloaddition reaction with the corresponding diene or ene counterpart, are presented. Due to the Woodward-Hoffmann rules of orbital symmetry, a directly photo induced DA reaction is forbidden.[70] However, a light induced generation of one of the reaction partners, followed by a rapid thermal [4+2] cycloaddition, results in a pseudo-photo induced DA reaction. One obvious advantage of light as a trigger for the reaction instead of temperature, is its temporal and spatial control. The start and dimensions of the reactions can therefore be easily controlled and often orthogonality towards thermally induced reaction protocols is achieved (e.g. copper catalyzed azide alkyne cycloaddition (CuAAC), conventional DA reactions). In this chapter, the employed light induced DA reactions from Chapter 3 and 5 are introduced and described in detail.

2.2.3.1 Photoreactivity of Phenacyl sulfides

Upon irradiation, phenacyl sulfides undergo photofragmentation, according to a Norrish type II reaction.[71] However, two competing reaction pathways either a β-cleavage[72] or a γ-hydrogen abstraction (Norrish type II mechanism),[73] are possible after excitation. Both reaction pathways are illustrated in **Scheme 12**. Depending on the substitution of the phenacyl sulfide in α-position to the ketone (γ-position regarding the sulfur) and the employed solvent, the β-cleavage leading to various side products can be suppressed.[74] A methylene substitution providing γ-hydrogen atoms for a radical abstraction combined with an aprotic solvent have proven as the conditions of choice to achieve a clean Norrish type II mechanism. Once the highly reactive thioaldehyde moiety is generated photochemically, it can undergo several transformations, e.g., reaction with various nucleophiles or in a HDA

reactions with dienes. An overview of possible reaction trajectories for the thioaldehyde is illustrated in **Scheme 13**.[75] In the course of the present thesis, amines, thiols and dienes were all successfully employed as reaction partners trapping the thioaldehyde formed by a photo induced phenacyl sulfide decay. All conducted reactions, especially the HDA reaction with an open chain diene derivative, proceeded faster than reactions with aldehydes. The increased reactivity of the thioaldehyde in comparison to carbonyl groups in DA reactions can be rationalized by considering the relative energy levels of the HOMO and LUMO. Vedejs et al. performed molecular orbital calculations on a model system comparing formaldehyde and thioformaldehyde.[76] These calculations revealed that the n_S HOMO in thioaldehyde, represented by the sulfur's lone pair, is 2.1 eV higher in energy than the n_O HOMO of formaldehyde (i.e., the oxygen's lone pair). Moreover, and for pericyclic reactions more importantly, the π^*_{CS} LUMO of the thiocarbonyl moiety is calculated to be 2.8 eV lower than the corresponding π^*_{CO} LUMO of the carbonyl group. As a consequence, the HOMO-LUMO gap between the LUMO of the dienophile (here the thiocarbonyl group) and the HOMO of the diene is smaller as if a carbonyl moiety is employed, resulting in an accelerated reaction towards the DA product. Additionally, due to the overall decreased energy gap between the n_S HOMO and the π^*_{CS} LUMO, thiocarbonyl compounds usually absorb light

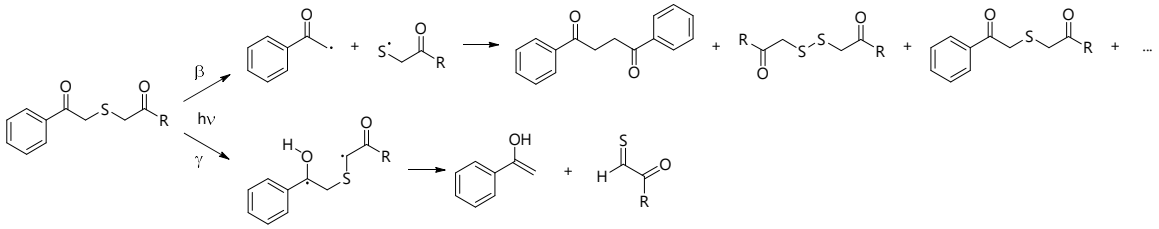

Scheme 12: Possible reaction pathways after a photoexcitation of a phenacyl sulfide derivative.[74]

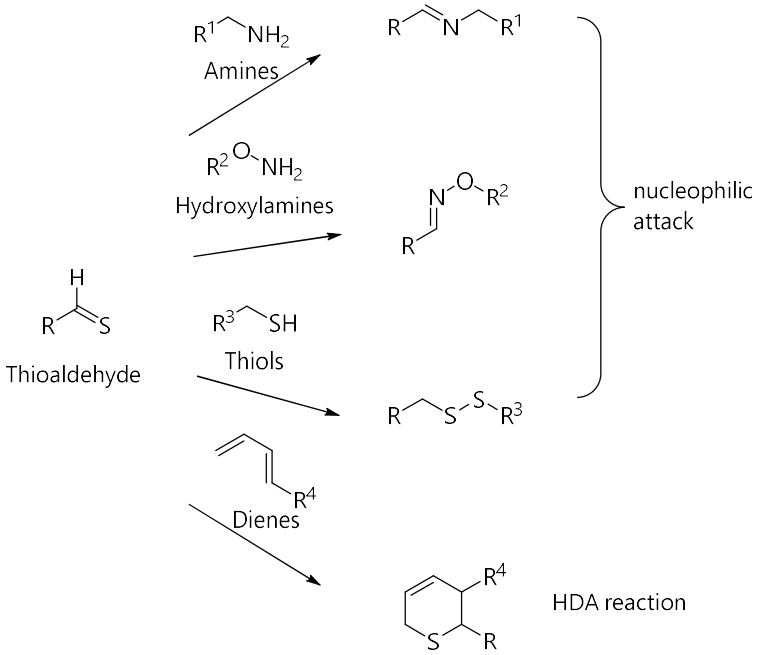

Scheme 13: Possible reaction pathways for a photochemically generated thioaldehyde moiety and the obtained products. Various nucleophilic attacks from amines, hydroxylamines or thiols are leading to imines, oximes and disulfides respectively. HDA reactions with dienes are illustrated on the lowest row.[75]

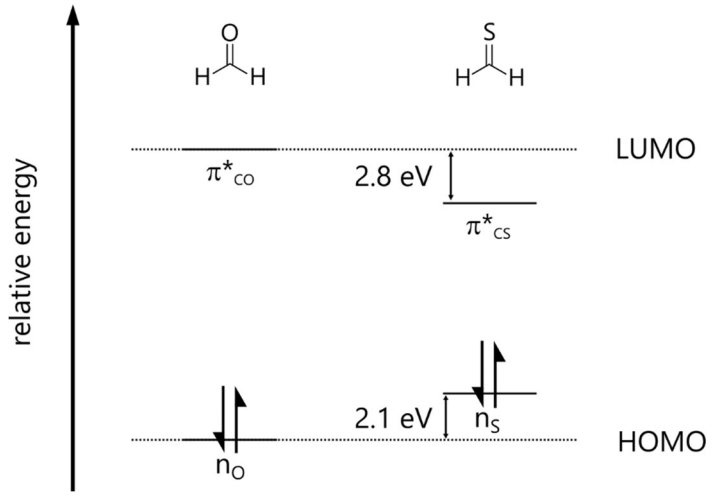

Scheme 14: Relative calculated HOMO/LUMO energies for formaldehyde compared to thioformaldehyde.[76]

in the visible wavelength regime, resulting in colored compounds. The described calculations are graphically summarized in **Scheme 14**. One drawback arising from the high reactivity of thioaldehydes, however, is the loss of regioselectivity. Due to the similar electronegativity of carbon and sulfur, the thiocarbonyl group is only weakly polarized. As a consequence, the molecular orbital coefficients for both reactive centers are equal and regioselectivity for interaction with the dienes may not be provided. One must therefore bear in mind that – when employing the phenacyl sulfide – a mixture of several regioisomers may be obtained.

Nevertheless, its high reactivity and affinity towards a vast variety of substrates enables for numerous applications in the fields of polymer and surface science, mainly exploited in the author's research group. Cyclopentadiene end functionalized poly(ethylene glycol) chains,[77] amine and thiol terminal small molecules,[75] and even metal complexes[78] were tethered to silicon substrates in a spatially resolved manner. Moreover, the photochemically generated thioaldehyde was utilized to functionalize cellulose substrates[79] and microspheres[80] with polymer strands or peptides. In the present thesis, the application of the phenacyl sulfide photochemistry for the surface functionalization of 3D microscaffolds[81-82] and the stepwise compaction of dual photoreactive RAFT blockcopolymers is demonstrated.[83]

2.2.3.2 Photoreactivity of α-methylbenzaldehyde derivatives

The second light induced DA reaction utilized in the present thesis, is the phototriggered generation of ortho-quinodimethane, an enol species, acting as diene in subsequent cycloadditions. This reaction, later called photoenolization,[84] was first discovered by Nien-Chu Yang and Carlos Rivas in 1961.[85] The photochemical rearrangement leading to the reactive diene derivative was thoroughly investigated by flash photolysis experiments on 2-methyl benzophenone and the resulting mechanism is illustrated in **Scheme 15**.[86-87] These experiments were conducted in cyclohexane and the reported lifetimes of the generated intermediates are only valid for the respective solvent.

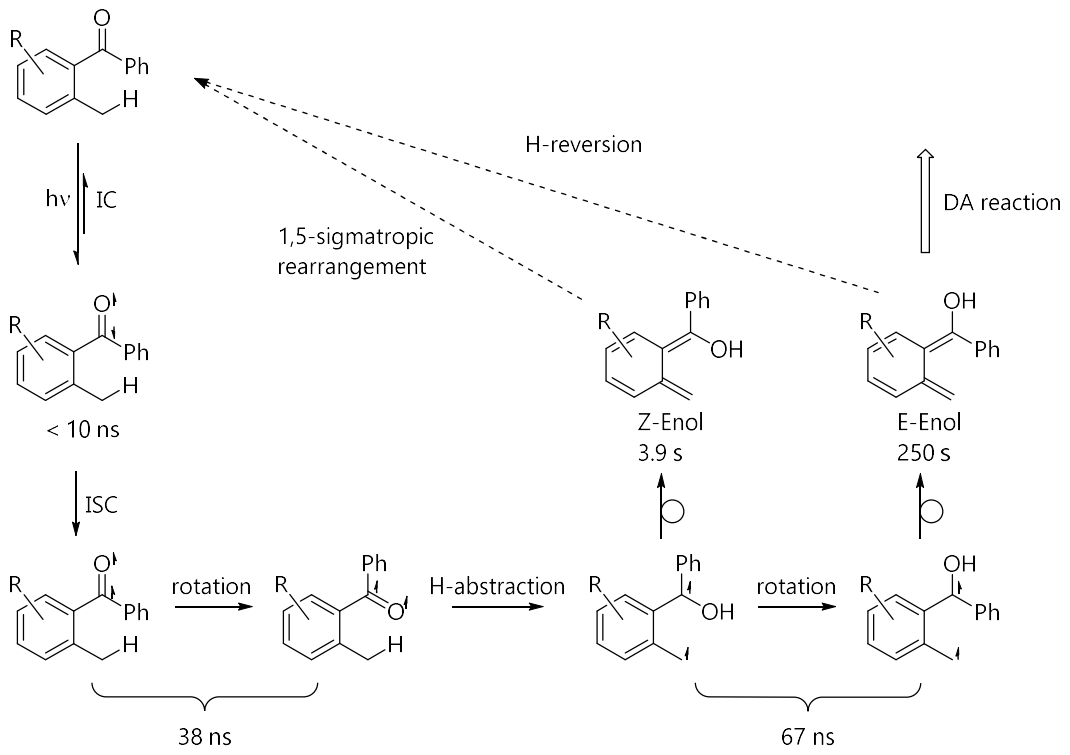

Scheme 15: Tautomerization mechanism of a 2-methyl benzophenone as investigated by flash photolysis experiments.[86-87] Experiments were conducted in cyclohexane and the lifetimes of the intermediates are reported accordingly.

Upon irradiation, a vibronic n→π* transition occurs to a transient singlet state. Via an ISC process, a triplet state is reached. A rotation of the carbonyl group around the aromatic-radical bearing bond can result in a hydrogen abstraction, forming a triplet alcohol species. After a second possible rotation and a π electron rearrangement, two enol species, a Z-enol and an E-enol, are obtained. Due to steric reasons, only the E-Enol undergoes a subsequent DA-reaction, whereas the Z-Enol isomer relaxes back to the ground state via a 1,5-sigmatropic rearrangement. If no reaction partner for a cycloaddition is present, the E-Enol also relaxes back to the electronic ground state via a hydrogen reversion. The prolonged lifetime of the E-Enol isomer in aprotic solvents is promoted by a possible hydrogen bonding as depicted in **Scheme 16**. If a hydrogen acceptor is present in the ortho position to the aldehyde moiety, a stabilization of the E-Enol isomer is obtained in aprotic solvents, resulting in a prolonged lifetime and therefore an overall increase in reaction rate.[88]

Although the cycloaddition behavior of such α-methylbenzaldehyde derivatives was discovered more than 40 years ago, only in the last years the scope of the reaction was exploited by Barner-Kowollik and co-workers. The photoenolization has proven useful in light induced modular blockcopolymer formation,[89-90] surface patterning of silicon wafers[88] and cellulose substrates.[91] Additionally, 3D microscaffolds coated with a photoenol silane were modified in spatially resolved manner[17] (for more details, refer to Chapter 3).

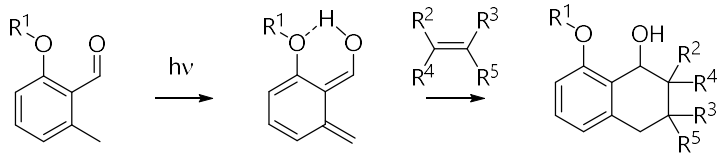

Scheme 16: Exemplary photoreaction of an α-methylbenzaldehyde via a photoenol intermediate. The E-Enol can be stabilized by a hydrogen bonding if a hydrogen acceptor is present in ortho position (here an oxygen atom). The stabilized photoenol is trapped in a DA product by a dienophile.

In the current thesis, a photoenol moiety was tethered to a methacrylate monomer and successfully employed to achieve dual light reactive 3D microscaffolds (Chapter 3) and block copolymers (Chapter 5).

2.2.4 Light induced [4+4] dimerization of anthracene

All photo induced cycloaddition reactions described so far lack one important feature: photoreversibility. One prominent example of light reversible cycloadditions is the [4+4] dimerization of anthracene derivatives. First discovered in 1867 when a solution of anthracene in benzene was irradiated with sunlight,[93] the photochemistry of anthracene derivatives was widely investigated by physical and organic chemists thereafter.[26, 92, 94-95] According to the Woodward-Hoffmann rules of orbital symmetry and interaction in concerted reactions, a [4+4] cycloaddition proceeds as photochemically 'allowed' [$4\pi_S+4\pi_S$] process, compared to the thermally 'allowed' [$4\pi_S+2\pi_S$] Diels–Alder cycloaddition.[96] The mechanism of the anthracene photodimerization proceeds via an excimer, either formed as short lived complex, or as longer living intermediate species. The kinetic scheme of the anthracene dimer formation is illustrated in **Scheme 17**.[92] Upon irradiation, an anthracene molecule is excited into a first singlet state ($^1A^*$) and forms an excimer with a second, non-activated anthracene molecule (k_{ef}). Consequently, the excimer can either convert to the desired photodimer (A_2 with k_R) or be deactivated by non radiative transitions (k_{NRD}), fluorescence (k_{FD}) or can split to form the starting materials (k_{-ef}). Non radiative transmissions include IC or ISC, either leading back to the ground electronic state S_0, or the first excited triplet state T_1. As the dimer formation occurs from the first excited singlet state S_1, ISC to T_1 prevents the reaction. The efficiency of the $S_1 \rightarrow T_1$ as well as the $T_1 \rightarrow S_0$ spin transition can be altered by exploiting the heavy atom effect (HAE).[97] When heavy atoms (i.e., with higher

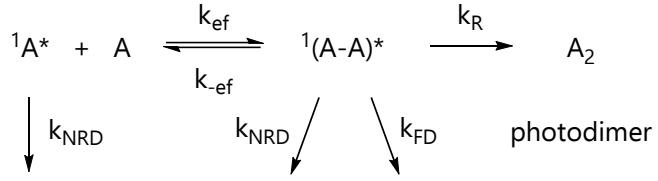

Scheme 17: Kinetic Scheme of the photodimer formation of anthracene upon irradiation. The mechanism proceeds via an excimer formation if a one photon process is given (aka irradiation with a classic lamp). k_{NRD}, k_{ef}, k_{FD}, and k_R as kinetic rate coefficients of the non radiative deactivation, excimer formation, fluorescence deactivation and dimer reaction, respectively.[92]

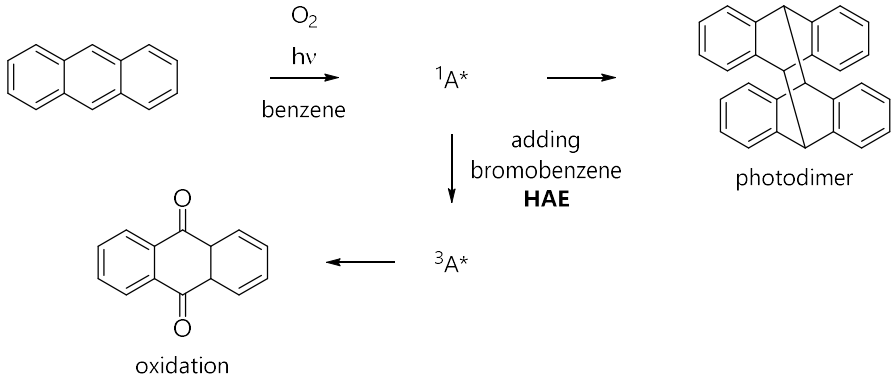

Scheme 18: HAE on the photodimerization and photooxidation of pure anthracene. If no heavy atoms are present, a population of the first excited singlet state (^{1}A*) takes place and due to low ISC the dimer is the only product observed. If bromobenzene is added, ISC is enhanced and the triplet state (^{3}A*)is populated, opening up the photooxidation pathway.[97]

atomic number) are present in the surrounding (either in the solvent (external HAE) or as substituent (internal HAE)), the enhanced spin-orbit coupling increases the rate of spin forden processes (such as ISC). An example is depicted in **Scheme 18**. If the photodimerization of unsubstituted anthracene is conducted in benzene with exposure to air, the first singlet excited state is populated (^{1}A*) and the dimer is obtained as only product (according the mechanism depicted above). When bromobenzene is added, the external HAE is induced and a population of the first excited triplet state (^{3}A*) is observed. However, a photooxidation that proceeds via an interaction of molecular oxygen with the excited triplet state can now occur. Therefore, a product mixture of the anthracene dimer and anthraquinone is obtained. If working in oxygen free conditions, the reaction rate is significantly reduced when heavy atoms are present.[97-98]

An important consideration especially when conducting a cross reaction between two different anthracene derivatives, is the electron density and electronegativity of the substituents tethered to the anthracene systems. Electronically diverging anthracene derivatives generally provide a decreased energetic separation of the significant HOMO and LUMO compared to electronically equal ones.[70] This results is an increased dimerization rate and an altered stability of the product.[99] These effects were also experienced in the course of the present thesis, when a test reaction of an electron rich surface tethered anthracene was subjected to a reaction with an equally electron rich polymeric anthracene compound (see Chapter 4.2.2, Figure 39). A poor dimer formation was observed via a weak dotted pattern on the silicon substrate.

As the photoreversible dimerization of anthracene is known for a long time and its properties have extensively been studied,[26, 95, 100-102] it comes at no surprise that the reaction has found a vast variety of applications in a high number of fields such as surface chemistry,[103-104] polymer chemistry[105-107] or material science.[108-110] The reversible nature of the linking was exploited e.g. when forming blockcopolymers,[111] single chain nanoparticles,[107] supramolecular assemblies[104] or surface patterns.[104] However, usually

reversal of the dimerization is achieved by applying rather harsh conditions such as UVA irradiation (≤ 300 nm) or elevated temperatures.[112] In the present thesis, a visible light reactive triazolyl anthracene derivative is introduced, allowing for a reversible surface patterning employing mild conditions (dimerization in the visible light range and reversibility by irradiation at 360 nm).

2.3 Direct laser writing (DLW)

The process of direct laser writing (DLW) is based on a multiphoton photon absorption. In her first theoretical report, Maria Göppert-Mayer described the two photon absorption (2PA) of molecules as early as in 1931.[114] However, the effect that one molecule absorbs two photons simultaneously was not proven experimentally until 1961, immediately after the invention of the laser.[115] The 2PA is crucial to obtain a lateral resolution in three dimensions, as with a one photon absorption (1PA) lithographic process (e.g. employing a shadow mask), only two dimensional layer of structures or pattern can be achieved. The reason for this becomes apparent, when realizing that as a consequence of the interaction of the molecule with two photons, the absorption correlates with the square of the light intensity and not in a linear dependency (as in a 1PA process).[116] The electronic excitation occurs via a virtual intermediate state as depicted in **Scheme 19**a). As a result, the excitation can be triggered with half the necessary energy (i.e., double the wavelength) in comparison to the 1PA process. Therefore, a very short laser pulse comprising a high photon density in a confined area, is necessary to favor a 2PA process over a 1PA one (see Scheme 19b) and 19c).[113] In common setups, a femtosecond pulsed laser with pulse lengths of around 100 fs

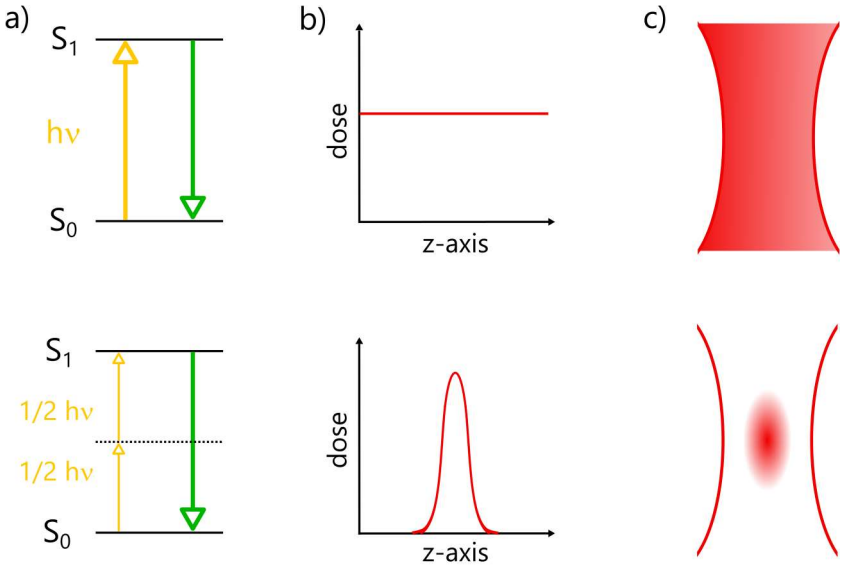

Scheme 19: One photon absorption (1PA) process (upper row) compared to a two photon absorption (2PA) (lower row). a) In 1PA a direct excitation from S_0 to S_1 occurs, while the electronic excitation in a 2PA proceeds via a virtual intermediate state; b) the energy profile in z direction is constant in a 1PA process, but proportional to z^{-2} for a 2PA one; c) resulting laser beam foci in a 1PA compared to a 2PA process. A constant, linear focus is obtained in a 1PA process, whereas a confined voxel laser focus is obtained for two photon laser beam.[113]

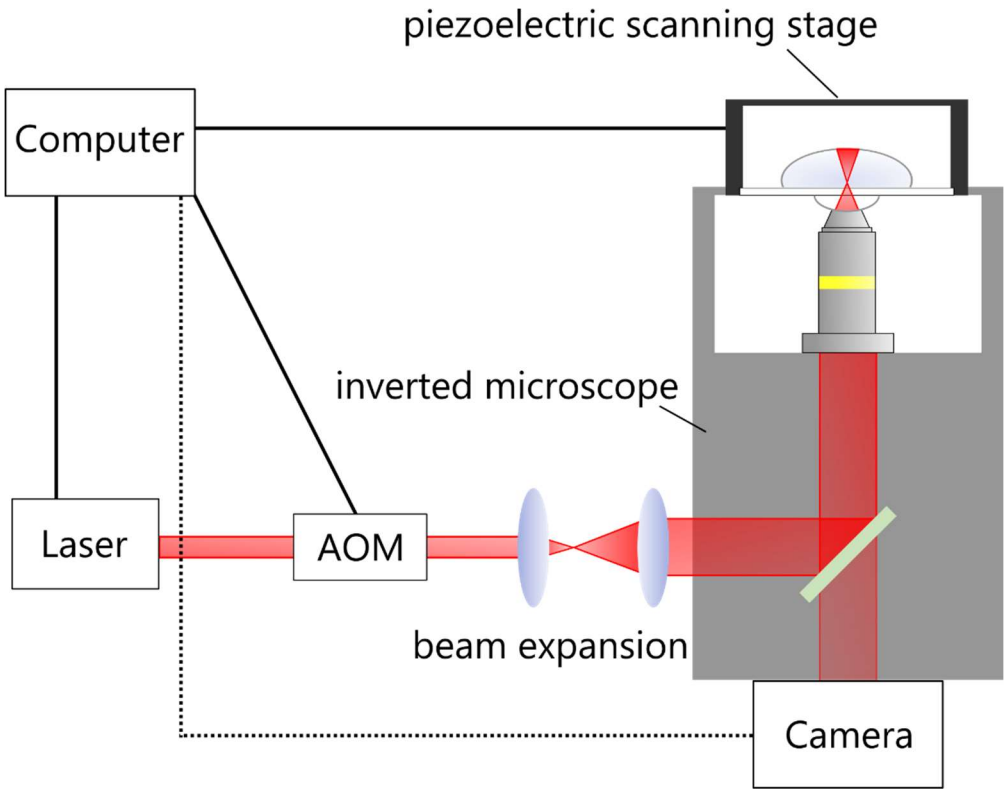

Scheme 20: Schematic general representation of a common, commercially available DLW setup. A piezoelectric scanning stage, femtosecond pulsed laser and acoustooptic modulator are coupled to a computer. The photopolymerizable substrate is placed onto a glass slide on top of an immersion oi lens and is moved relatively to the laser focus controlled by the computer to achieve the desired design.[118]

at 80 MHz is utilized to achieve a very high photon flux in the center of the focus allowing for a 2PA. This creates a sharp 3D region in which 2PA processes (in DLW a photopolymerization) exclusively occur, the so called voxel.[117] Therefore, a resolution along the z axis is gained, opening up the possibility to laser print 3D structures. The focus is moved according to a Computer Aided Manufacturing / Computer Aided Design (CAM/CAD) model inside a transparent photoreactive material initiating a 2PA photopolymerization inside the voxel.[119] The basic idea of a DLW setup is illustrated in **Scheme 20**.[118, 120] A computer is connected to the laser, an acoustooptic modulator (AOM, for intensity tuning of the laser beam) and a piezoelectric scanning stage. The relative movement of the laser focus in the substrate is achieved by moving the stage containing the polymerization mixture. The movement is controlled by the computer and precisely conducted by a piezoelectric element allowing for a nanometer precise movement. However, the writing speed is limited to 100-200 µm s^{-1}. As light source, conventionally a frequency doubled erbium fiber laser operating at a wavelength of 780 nm is employed.[121] Furthermore, a beam expansion ensures good illumination of the substrate and a camera allows an online control over the process. Besides the experimental setup, the features of the photochemical reaction performed in the voxel volume greatly influence the writing process. A large number of different photoreactions can be conducted in a 2PA process. However, as a stable 3D structure has to be generated, the solubility of the produced material needs to be significantly decreased, usually realized by network formation. Popular

photoresists also employed in the current thesis are based on the FRP procedure of multifunctional (meth)acrylate moieties. A typical printing procedure consists of 3 steps: sample preparation, the actual writing step and a development step. To ensure the covalent attachment of the written structures to the solid support, the substrates are coated, then the transparent polymerization resist is added and the structure is written to the surface. Next, the leftover resist is washed away and the resulting structures are rinsed (development). Typically employed solid substrates are glass slides since they are transparent, as coating agents, silanes are utilized. In **Scheme 21**, common triacrylate based network formers and commercially available 2PA photoinitiators are depicted.[118] In Chapter 3 of the present thesis, TPE-TA was utilized as base for all employed photoresists and Irgacure® 369 as radical photoinitiator. In addition to acrylate based resists, commercially available inorganic-organic hybrid resists, such as Ormocomp® or Ormocer® are frequently employed.[119] Possible applications for written microstructures featuring a resolution of less than 100 nm are found in a vast variety of fields.[122-123] Optical waveguides,[124] microsupercapacitors,[125] photonic crystals,[126] lab-on-a-chip systems[127] or cell attachment scaffolds[20, 128] were successfully fabricated employing DLW processes utilizing the aforementioned resists. In recent years however, researchers turned their attention towards the chemical diversity and postmodifictaion of the employed resists. Thiol ene[129] and thiol yne[18] based resists for stepgrowth radical induced photopolymerizations have therefore been developed to obtain scaffolds exhibiting thiol functionalities on the surface. Such an approach enables the facile postmodification of the written structures, but lacks spatial resolution. In an alternative approach, spatially resolved surface functionalizations were achieved by employing the aforementioned α-methylbenzaldehyde as a tetralinking network former in a stepgrowth polymerization together with a maleimide linker. However, this light triggered cycloaddition stepgrowth polymerization process requires a custom

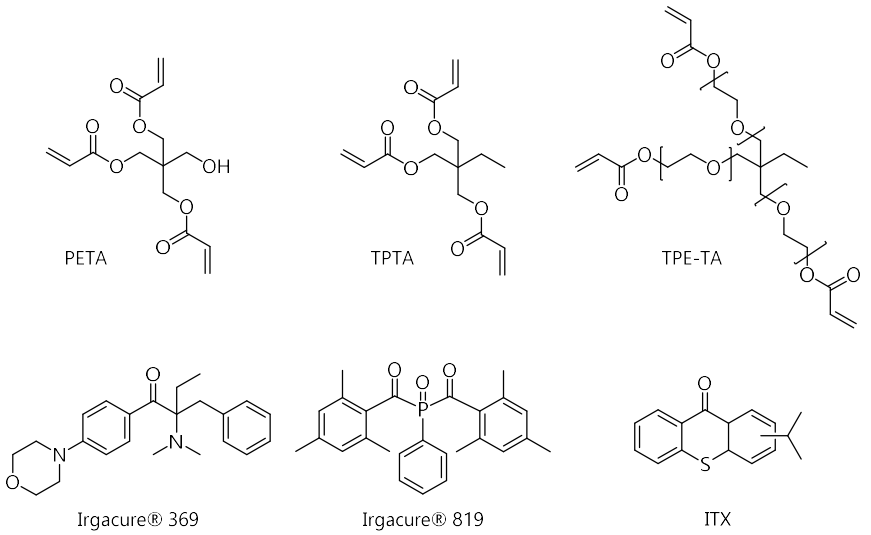

Scheme 21: Top row: commonly utilized triacrylate based network formers in DLW polymerizations; bottom row: commercially available 2PA radical photoinitiators. TPE-TA and Irgacure® 369 were employed in Chapter 3 of the present thesis.

made DLW setup employing a wavelength tunable laser.[130] In the present thesis (Chapter 3), photoreactive methacrylate based monomers are reported allowing for a spatially resolved light induced postmodification utilizing only commercially available setups. The so obtained dual functionalized microscaffolds were successfully employed as cell guiding / cell sorting substrates.[81-82]

2.4 Surface functionalization and characterization

In the first half of the 20th century, inorganic materials were commonly defined by their bulk properties and the features of surfaces were often neglected.[131] However, the need for defined interfaces gradually became apparent for biology,[132] medical technologies,[133] and computer science, among others.[134]

2.4.1 Surface preparation and anchoring methods

In the current thesis, either silicon wafers or glass slides were utilized as surface substrates. To anchor functional molecules, silanization protocols were employed. However, a vast variety of other surface substrates and anchoring methods for organic molecules are known in the contemporary literature. As surface substrates, synthetic organic polymers (e.g., polycarbonates, polystyrene),[135] natural polymers (e.g., hyaluronic acid or cellulose),[79, 91] or inorganic materials (e.g., gold or titanium dioxide)[136-137] have been employed besides silicon and glass. The anchoring methods of choice usually depend on the utilized substrates. For gold, a self-assembly of thiol monolayers is commonly utilized to achieve surface functionalization and patterning.[138] Biological substrates exhibit hydroxyl or amine functionalities on the surface that can be directly addressed with etherification, esterification, or amidation protocols.[91, 139] For synthetic polymeric substrates, end or side chain can be modified depending on their reactivity.[140-141] Silicon or glass can be functionalized by hydrosilylation protocols besides silanization.[142] One universal surface anchoring method is the formation of polydopamine (PDA) films by polymerization of dopamine derivatives that strongly adhere to all inorganic or organic substrates.[143] To achieve a successful surface anchoring with the aforementioned methods, surface cleaning/activation is necessary. Most substrates, are either activated by piranha acid/base or by non-thermal plasma prior to an anchoring process.[144] On glass slides or silicon wafer both methods are applicable. In the current thesis, glass slides were cleaned and activated using air plasma (Chapter 3) and silicon wafer were treated with piranha acid (Chapter 4) prior to a silane attachment. As silane moieties, enabling a covalent surface coating, trichloro-, trimethoxy-, or triethoxysilane derivatives are commonly employed.[145] Chemical

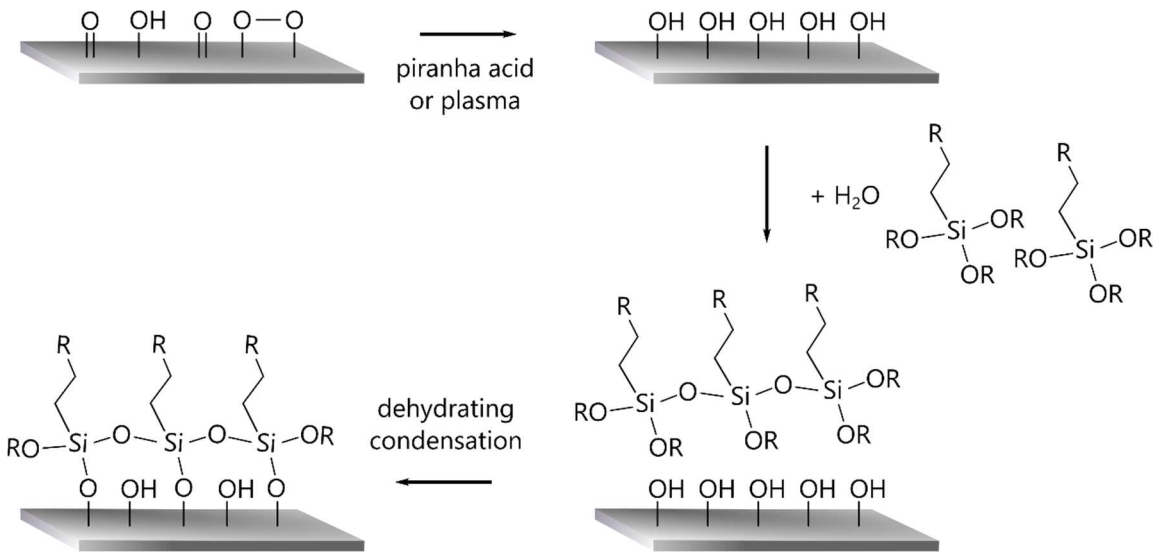

Scheme 22: Chemical details of the surface coating process of glass or silicon substrates employing trioxoalkylsilanes. First, the oxidized surface is activated either by piranha acid or non thermal plasma treatment. Second, a partial hydrolysis results in a prepolymerized silane network. In a last step employing elevated temperature, a dehydrating condensation leads to a covalently bond silane network on the surface.[146]

details of the cleaning/activation and the surface attachment process utilizing silane anchoring groups are depicted in **Scheme 22**.[146] The oxidized, non-reactive surface is treated either with piranha acid or non-thermal plasma leading to an activated substrate expressing hydroxy functionalities. Subsequently, trichloro-, trimethoxy-, or triethoxysilane derivatives are prepolymerized in solution, forming a silane network. Employing elevated temperatures, the network is covalently attached to the surface via a dehydrative condensation. As both processes are taking place in one vessel, they occur rather simultaneously than stepwise. A vast variety of functional trichloro-, trimethoxy-, or triethoxysilanes are available for the generation of organic moieties on the surface that can afterwards be modified by various synthetic protocols.[147]

In the context of the present thesis, especially spatially resolved functionalization methods such as photolithography or photopatterning were investigated. Generally, a photomask covering parts of a light responsive surface can be utilized to achieve spatial resolution. Other methods for obtaining a surface pattern are microcontact printing, where a structured elastomeric stamp (e.g., made of poly(dimethyl siloxane) (PDMS)) is loaded with the desired molecule and shortly pressed onto the substrate,[148] or inkjet printing, applying a so called ink (i.e., a solution of reactive small molecules or polymers) precisely onto the substrate, leaving a pattern behind after the evaporation of the solvent.[149]

2.4.2 Surface characterization methods

In the current thesis, two surface characterization methods were particularly important: Time-of-Flight Secondary-Ion Mass Spectrometry (ToF-SIMS) employed in Chapters 3 and 4, and attenuated total reflectance Fourier transform infrared microscopy (ATR-FT-IRM)

utilized in Section 3.4. Therefore, a short introduction to both analytical methods is provided in the following.

2.4.2.1 Time-of-Flight Secondary-Ion Mass Spectrometry (ToF-SIMS)

Via ToF-SIMS measurements, a spatially resolved analysis of the chemical composition of a surface is accessible. The first spatially resolved SIMS measurement of surfaces beyond the monolayer dimension was reported in 1969.[150] The method combines a time-of-flight (ToF) mass analyzer with a secondary ion source. The secondary ions (and fragments) are generated by sputtering a surface with a primary ion beam. As primary ions, Ag^+, Ar^+, or Bi^+ ions or clusters thereof are employed.[151] **Scheme 23** illustrates the secondary ion sputtering process.[152] The penetration depth of the primary ions and therefore the degree of surface damage mainly depends on the kind of primary ions utilized, their kinetic energy, and the impact angle (e.g., if Ag^+ ions with a kinetic energy in the order of keV are striking the surface in a vertical angle, a medium penetration depth is approx. 10 nm).[153] The amount of secondary ions detected, originating from a species A present on the surface (SI_A), depends on the local sample composition. However, apart from the concentration [A] of the respective species on the surface, its actually detected secondary ion signal depends on the ionization probability β_A, the primary ion current PI of the source, the sputtering yield Y, and the detection efficiency of the mass spectrometer τ and can be described by **Equation 5**:[154]

$$SI_A = P \ * Y * [A] * \beta_A * \tau$$

Equation 5: Detected secondary ion signal for species A (SIA), with PI as primary ion current, Y as sputtering yield, [A] as concentration of species A on the surface, β_A as ionization probability of species A and τ as detection efficiency.

However, especially when it comes to organic molecules or biological substrates, the ionization process is not fully understood yet.[154] The obtained secondary ions are desorbed

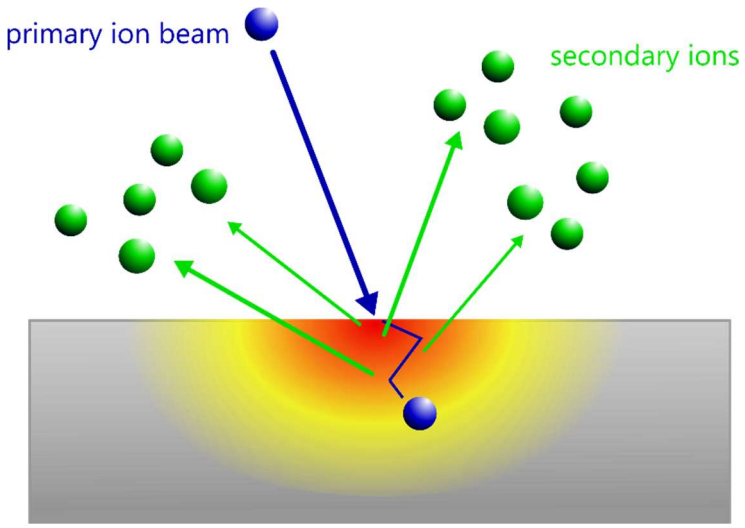

Scheme 23: Schematic illustration of the secondary ion emission process. A primary ion beam (blue) hits the surface and kicks out secondary ions (green). Primary ions enter the surface and cause damage to variable degrees (red to yellow).[152]

from the surface and accelerated by electronic lenses, before entering the ToF analyzer.[62] The working principle of a ToF analyzer can be summarized by **Equation 6**:

$$\frac{m}{z} = \frac{2 * U_{ac} * t^2}{l^2}$$

Equation 6: Separation occurring in a ToF analyzer according to the mass to charge ratio (m/z) with U_{ac} as acceleration voltage, l as length of the analyzer and t as measured time.

The secondary ions are separated according to their mass to charge ratio (m/z). The ions are accelerated into the analyzer by applying the acceleration voltage U_{ac}. The flight time t of the ions, necessary to cover the length l of the analyzer is measured. In principle, several operation modes for the ToF-SIMS instrument are possible:[155]

- **Surface spectrometry:** A classic, static SIMS investigation of the surface composition. A very low primary ion dose is applied to minimize surface damage and achieve a quasi-non-destructive surface analysis of the upper monolayer of a substrate. Elemental and molecular information is obtained combining high sensitivity (ppm / ppb region), high mass resolution, and a high mass range.
- **Depth profiling:** An analysis of the vertical distribution of components in a substrate. Two primary ion beams are utilized, where the first beam sputters a crater into the surface and the second one is subsequently used to analyze the cleared surface composition. Depth ranges of a few nm to several μm with a resolution of approx. 1 nm can be investigated.
- **Surface imaging:** A fine focused primary ion beam scans the surface and a mass spectrum obtained for each spot is analyzed simultaneously resulting in a 2D image of the surface functionality (chemical image / ion map). A field of view ranging from a few μm^2 to cm^2 can be characterized with a high resolution of ≤ 60 nm.
- **3D Analysis:** 3D sample structures can be analyzed when combining depth, imaging, and mass spectral information. The shape, surface composition, and position of 3D scaffolds can be analyzed with high depth and mass resolution by a parallel mass detection.

In the current thesis, especially the latter two modes were utilized. For a successful ToF-SIMS analysis, sufficient mass resolution combined with a sufficient spatial resolution is needed. A high mass resolution is obtained by short primary ion pulses, a long mass analyzer, and a fast detection process.[156] A ToF analyzer is preferred in contemporary SIMS analysis, as it allows for the simultaneous detection of multiple ion fragments, high mass resolution, and high ion sensitivity.[157] The spatial resolution mostly depends on the operation mode of the primary ion pulse:[158]

- **Bunched mode:** The primary ion beam is 'bunched' (combining a short pulse time and high primary ion number, i.e., ~2000) to achieve a very high mass resolution and a high secondary ion count. Since at shorter pulse length, a higher mass resolution (Δm/m ~ 8000) is obtained, a typical pulse length of ~ 600 ps is utilized. However, spatial resolution is lost and cannot be higher than 2-5 μm in this mode.

- **Burst alignment mode:** A smaller amount of primary ions (≤ 600) and a longer pulse length (20-100 ns) results in a spatial resolution of ~ 200 nm and a nominal mass resolution.
- **Collimated mode:** The amount of primary ions is lowered further (≤ 35) compared to the 'burst alignment mode', resulting in an even higher spatial resolution (~ 100 nm).

In addition, in the course of the present thesis, a new imaging mode, the so called **delayed extraction**, was introduced by A. Welle (KIT) and S. Kayser (ION-TOF GmbH).[81] A high lateral (~ 150 nm) and good mass resolution (Δm/m ~ 5000) is achieved by delaying the extraction pulse in relation to the primary ion pulse. A more detailed description of the mode is given in Section 7.2.2.

However, one disadvantage of ToF-SIMS analysis is the partial destruction of the surface and molecules due to the harsh ionization conditions. The high degree of fragmentation additionally complicates the interpretation of the obtained mass spectra.

2.4.2.2 Attenuated total reflectance Fourier transform infrared microscopy (ATR-FT-IRM)

ATR-FT-IRM allows for a destruction free, spatially resolved surface investigation at ambient conditions, either in wet or dry environments.[159] The combination of IR spectroscopy and microscopy is already known since the early 1950s.[160-161] In comparison to a conventional IR spectroscopic analysis, in IR microscopy a spatially resolved measurement is achieved by a point-by-point mapping of a sample with an IR beam on a moving sample table.[162] A focal plane array (FPA) detector is utilized to obtain a spatially resolved analysis. However, as in all optical microscopy methods, the resolution is physically limited by the diffraction limit.[163] Therefore, the maximum achievable optical resolution is approx. λ/2, i.e., 1-2 µm for an infrared irradiation based microscopy.[164] In principle, IR imaging can be conducted in reflection, transmission, or attenuated total reflection (ATR) mode. In the present thesis, an ATR based instrument equipped with a germanium single crystal was employed. The tip of the crystal is flattened, resulting in a circular surface with a diameter of 100 µm. The principle of an ATR based microscope objective and the measurement fundamentals are depicted in **Scheme 24**.[165]

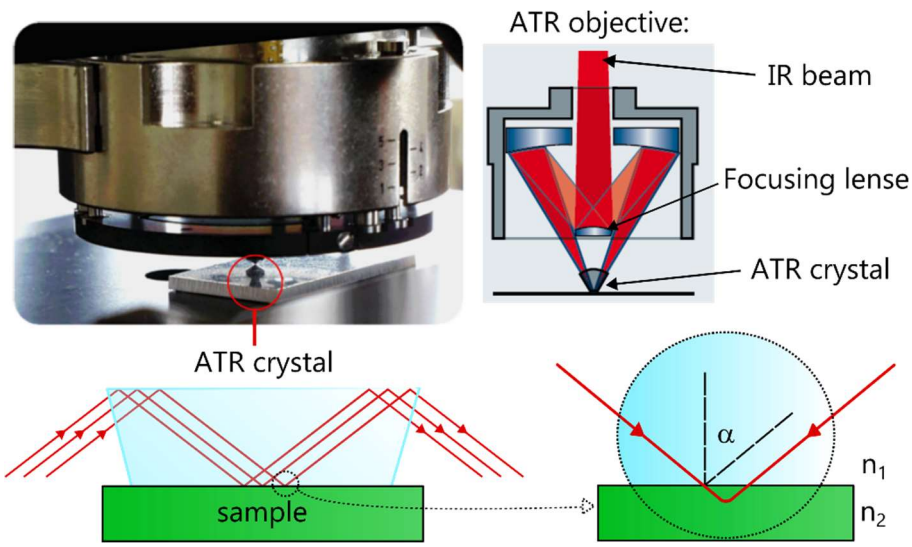

Scheme 24: Principle of an ATR based microscope objective and the fundamentals of an ATR-IR measurement. A germanium single crystal is utilized as ATR crystal in the current thesis. The illustration was adapted from Ref [165].

The measured surface area is restricted by the dimensions of the FPA detector. In case of the utilized device, 4096 single channel IR spectra are measured on an area of 32 x 32 µm, resulting in 4096 pixel of the measured image. The penetration depth of the IR beam into the sample (i.e., the generated evanescent wave) depends on the wavelength and the incidence angle. For a germanium single crystal based ATR objective with an incidence angle of 45°, a penetration depth of approx. 1 µm is observed.[165] In such a spatially resolved IR microscopy measurement, four dimensional data sets are obtained. For an evaluation, the spectra are integrated over a selected wavelength area, resulting in an intensity heat map of the signal, illustrating a spatially resolved image of the distribution of the corresponding chemical functionality on the surface.

2.5 Single chain nanoparticles (SCNP)

For a single chain nanoparticle (SCNP), as the name implies, a linear polymer chain is compacted/folded intramolecularly to form a nanoparticle. The first SCNP has already been reported as early as 1956.[166] However, most of the research field remained dormant thereafter, due to the lack of precise polymer synthetic procedures and adequate characterization methods. With the emergence of RDRP procedures and the development of advanced characterization techniques, the field started to flourish.[29, 167-168] The particular interest in SCNP folding is the mimicking and understanding of a protein folding mechanism. In the following sections, a brief overview of the common principles in synthesis and characterization reported in literature is given.

2.5.1 SCNP synthetic principles and considerations

For achieving a tertiary structure in a single polymer chain, two main concepts are known: the selective point folding and the repetition unit folding, both illustrated in **Scheme 25**.[169] The repetition unit folding approach relies on a statistical distribution of nonspecific reactive points along the polymer chain either by a statistical copolymerization of functional monomers or post polymerization modification. A non-directed collapse of the single chain is obtained as the connections of the reactive points occurs randomly. On the other hand, in the selective point folding, orthogonal recognition units are placed at precise positions alongside the polymer backbone. Therefore, a well-controlled folding of the single chains and even distinct architectures such as 8- or a P-shape are achievable.[167] Thereby, the folding process can be better controlled and is better understood. However, the latter approach is synthetically more demanding, especially if more than one recognition pair is implemented. As the repeating unit approach bears less synthetic effort, it comes as no surprise that a large amount of studies is based on it. The repeating unit approach was also exploited in the current thesis (Chapter 5).

A vast variety of crosslinking procedures is established[27, 29, 169-171] and can be categorized in three main groups:[168, 172] Homofunctional crosslinking of pendant reactive groups, heterobifunctional crosslinking of two complementary moieties, and crosslinker assisted collapse utilizing an added molecule connecting two functional groups along the polymer chain. For all categories, covalent as well as supramolecular strategies are reported. Examples for homofunctional reactions exploited in SNCP formation are the photodimerization of anthracene[107], the thermal dimerization of benzocyclobutene derivatives[173] or self-complementary hydrogen bonding units.[174-175] As heterobifunctional crosslinking reactions, 'click' reactions such as the copper catalyzed azide-alkyne cycloaddition (CuAAC)[176] or the nitrile-imine mediated tetrazole-ene cycloaddition

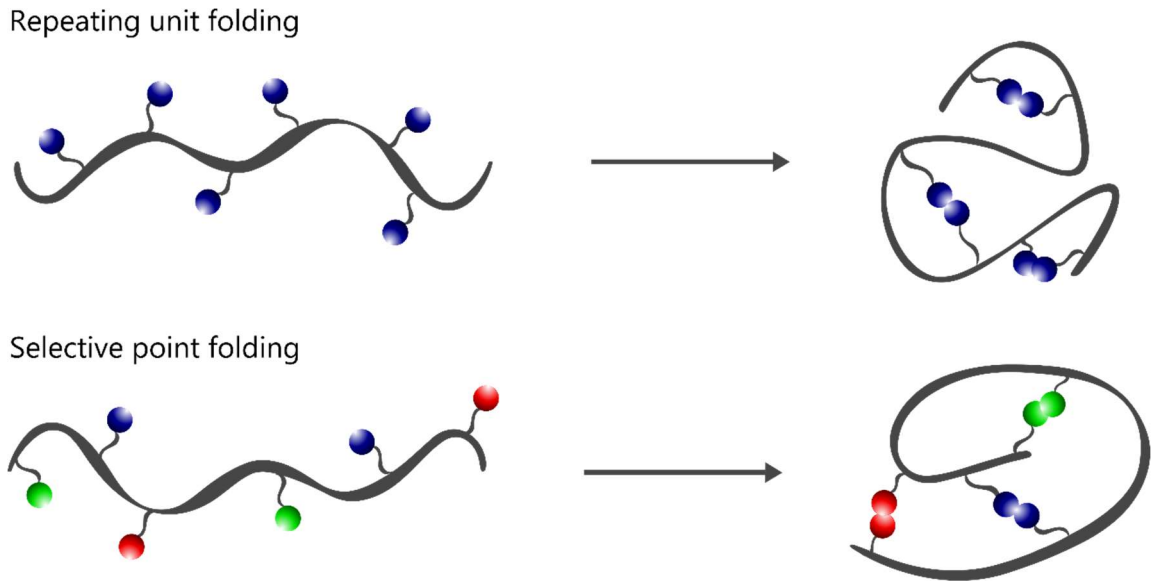

Scheme 25: Random repeating unit folding compared to a defined selective point folding SCNP approach.

(NITEC)[28] as photoinduced procedure were successfully employed for SCNP collapses. Supramolecular heterobifunctional conversions utilized for SCNP foldings are typically host-guest complex forming reactions or asymmetric hydrogen bonding.[177-178] A commonly utilized and synthetically little demanding method for crosslinker assisted SCNP formation is the combination of (di)isocyanates with diamines or diols.[32, 179] As supramolecular alternative for a crosslinker assisted SCNP formation, metal complexations are frequently employed.[180-181] In the present thesis, a crosslinker assisted, covalent, phototriggered SCNP folding approach was adopted.

Since SCNP formations are usually conducted to mimic protein behavior, research has not only been focused on the folding process itself, yet also on the properties of the generated products. By implementing metal complexes, catalytically active centers are introduced, approaching the function of enzymes. Zimmerman and coworkers, for example, demonstrated the incorporation of Cu-complexes in reactive SCNPs to catalyze a CuAAC in cells.[182] Other obvious fields of application for SCNPs are drug delivery or bioimaging. Fluorescent, water soluble SCNPs for imaging and cell labeling applications were synthesized by Barner-Kowollik and coworkers employing a photo induced NITEC conjugation in water.[183] Liu et al. demonstrated extracellular labeling by employing polyelectrolyte SCNPs.[184] For drug delivery, SCNPs capable to respond to an external stimulus such as irradiation, pH, or temperature changes or redox conditions are necessary. The group of Huang introduced poly(oligo(ethylene glycol)methacrylate) SCNPs crosslinked with uracil-diamidopyridine (U-DPy) hydrogen bonding units that respond to temperature changes.[185] Zwitterionic core shell SCNP, reacting to a redox stimulus as well as a pH change were introduced for drug delivery applications by Dong and coworkers.[186] For an improved understanding of the folding process itself, a dual compartmentalizing triblock copolymer was reported by Lutz and coworkers,[31] whereas Barner-Kowollik and coworker introduced a reverse approach by synthesizing a dual, orthogonally unfolding SCNP system based on supramolecular chemistry.[187] One approach of a dual compaction of a triblock copolymer employing covalent photochemical linkings is demonstrated in the present thesis (Chapter 5).

2.5.2 Common techniques for SCNP characterization

Due to the small size and often intricate architecture, an in depth analysis of SCNPs has proven to be a challenging task. In theory, no existing analytical method today allows for a fully comprehensive standalone measurement. Therefore, complementary characterization methods are commonly employed to support each other. By a careful selection of measurement parameters and direct comparison measurements with the precursor polymers, conclusive analyses can be obtained. In the literature, a large variety of analytical techniques are utilized for SCNP characterization, such as size exclusion chromatography (SEC), dynamic light scattering (DLS), 2D NMR based techniques such as diffusion ordered

spectroscopy (DOSY) or nuclear Overhauser enhancement spectroscopy (NOESY), small angle neutron or X-ray scattering (SANS or SAXS) or microscopy methods such as atomic force microscopy (AFM) or transmission electron microscopy (TEM). In this chapter however, only SEC and DLS are described in detail, as these methods were employed for SCNP characterization in Chapter 5 of the present thesis.

2.5.2.1 Size exclusion chromatography (SEC)

In an SEC experiment, macromolecules in solution are separated according to their hydrodynamic volume, whereof the molar mass can be calculated. Additionally, a size exclusion chromatogram also illustrates the molar mass distribution (MMD) of a polymer sample. As it combines a relatively non complicated setup and a facile sample analysis, SEC has become a well-established, standard polymer characterization techniques today.[188] The setup consists of one or several columns, usually filled with porous gels, coupled to an isocratic pump on one side and detectors on the other side. A dilute solution of the polymer sample is slowly (typical flow rates are ~ 1 mL min^{-1}) pumped through the columns as mobile phase.[189] The porous gel scaffolds commonly consist of crosslinked polymeric materials, such as polystyrene, polyacrylamide, cellulose, dextran, or silica particles and exhibit a wide range of pore sizes.[190] The entire column volume is divided in an inner column volume (V_i) inside the gel pores and an outer volume (V_o) outside the beads. Depending on the different hydrodynamic volumes of the polymers, a specific fraction (γ) of V_i and V_o is accessible for the polymer strands, the so called elution volume V_e (**Equation 7**):[188]

$$V_e = \gamma V_i + V_o$$

Equation 7: Elution volume V_e accessible for a polymer chain as fraction γ of the inner volume plus the outer gel volume.

If the polymer chain is too large in size, it cannot diffuse in any of the pores ($\gamma = 0$), meaning that V_e equals V_o. For such chains, no retention on the column and therefore no separation occurs (upper exclusion limit). If the polymer chain is too small in size, on the other hand, all of the inner gel volume ($\gamma = 1$) is accessible and the molecules are retained on the column for a non-defined time and again, no separation is achieved (lower exclusion limit). Only if the size of the polymer coils (hydrodynamic volume) allows them to access a specific fraction ($0 \leq \gamma \leq 1$) of the gel pores, separation is achieved. The sample specific factor γ depends on various parameters besides the polymer itself and pore size, such as temperature, solvent, the type of gel, and the shape of the polymer analyzed, i.e., its branching density.[188] Therefore, it is not possible to calculate γ as a function of the molar mass. As a consequence, SEC is not an absolute method and setups need to be calibrated employing standard samples exhibiting a narrow mass distribution. An in depth description of the calibration process and determination of the MMD is beyond the scope of the current section. Interested readers are referred to standard textbooks.[188, 191]

As the hydrodynamic volume of the chain decreases significantly upon the transition from a random coil towards a denser, crosslinked SCNP, SEC has proven as useful tool for their

characterization. The compaction of the SCNP leads to longer retention times than obtained for the precursor polymer, whereas the MMD is not altered, and should apparently become even narrower. The first theoretical considerations relating that matter were conducted by Pomposo and coworkers.[192] Assuming a soft nanoparticle possesses a molar mass M and a density ρ, it exhibits a theoretical hydrodynamic radius R_h (see **Equation 8**) according to:

$$R_h = q_F M^{(1+\alpha_F)/3}$$

Equation 8: Theoretical hydrodynamic radius R_h of soft nanoparticle like objects with q_F as constant and $\alpha_F \geq 0$ as 'softness' factor

with q_F as a constant depending on ρ and $\alpha_F \geq 0$ as the 'softness' factor (i.e., the deviation from a perfect hard sphere, one of the Mark-Houwink parameters). When an SEC measurement is performed, the nanoparticle is imaginarily replaced by a linear polymer chain of the same size. The measured R_h for the SCNP is correlated to an 'apparent' molar mass M_{app} for this corresponding linear, flexible chain (**Equation 9**):

$$R_h = q_L M_{app}^{(1+\alpha_L)/3}$$

Equation 9: Hydrodynamic radius R_h derived from an SEC measurement of an imaginal linear chain with the same size as the SCNP with q_L as constant and $\alpha_L \geq 0$ as 'softness' factor.

with the same constant q_L and 'softness' factor α_L as before, related to a linear chain. When combining both equations, a term ('power law') for the calculation of M_{app} for a SCNP with an actual molar mass of M is obtained (**Equation 10**):

$$M_{app} = c\, M^{\beta}$$

Equation 10: 'Apparent' molar mass M_{app} measured for an SCNP in an SEC analysis with an actual molar mass of M. The constant c is derived from the density dependent constants q_F and q_L and the exponent β can be calculated according to **Equation 11**.

with the constant c derived from the density dependent constants q_F and q_L and the 'power law' exponent β calculated as follows (**Equation 11**):

$$\beta = \frac{1 + \alpha_F}{1 + \alpha_L}$$

Equation 11: Expression for the 'power law' exponent β deduced from the Mark-Houwink parameters α_F and α_L.

The 'power law' for the corresponding 'apparent' dispersity $Đ_{app}$ can be derived from the assumption of a log-normal function for the MWD of the linear precursor and can be stated according to **Equation 12**:

$$Đ_{app} = Đ^{\beta^2}$$

Equation 12: 'Apparent' dispersity $Đ_{app}$ derived from SEC measurements, based on the actual dispersity $Đ$ and the 'power law' exponent β.

with the actual dispersity $Đ$ and the 'power law' exponent β (see Equation 11). The above equations allow to quantify the reduction of the (apparent) molar mass and dispersity for a SEC measurement of a SCNP sample.

As SEC is a relative method, sensitive to various environmental parameters (e.g., temperature, pressure of the system) it is prone to variations in the obtained results even if measured on the same device. To ensure comparability of the results collected for the

precursor and the SCNP, both samples therefore have to be always analyzed directly after each other (see Chapter 5).

2.5.2.2 Dynamic light scattering (DLS)

Dynamic light scattering (DLS) (also called photon correlation spectroscopy) is based on two physical phenomena for particles in solutions or suspensions: the Tyndall effect (scattering) and the Brownian motion.[193] It can be employed to determine the mean hydrodynamic diameter and the size distribution of small scattering particles in solution.[194] After the introduction of the laser in the 1960s, DLS was developed for macromolecular characterization.[195] Light scattering originates from the interaction of an oscillating electromagnetic field (of the light wave) with the electrons of the particle, and occurs if the size of the particle is in the same range as the incoming wavelength. A coherent, monochromatic laser beam is focused on a sample, scattering the light. The detector, usually a photonmultiplier, collects the scattered photons at a given scattering angle. The photon signal is digitalized and sent to an autocorrelator and a time dependent auto correlation function of the normalized scattering light intensity is obtained (**Equation 13**):

$$C(t) = \frac{\langle I(t)\, I(0)\rangle}{\langle I(0)\rangle^2} = \left[1 + \gamma \left[g^{(1)}(t)\right]^2\right]$$

Equation 13: Time dependent autocorrelation function of the normalized light intensity with $I(0)$ as initial light intensity, $I(t)$ as light intensity at a certain time. The 'coherence factor' γ combines all experimental setup parameters and $g^{(1)}(t)$ as normalized first order time autocorrelation function (scattered electric field).

with $I(0)$ as initial light intensity, $I(t)$ as light intensity at a certain time, the 'coherence factor' γ (determined by the experimental setup) and $g^{(1)}(t)$ as normalized first order time autocorrelation function (scattered electric field). In an ideal case, γ should equal 1, leading to a value of 2 at $t = 0$. Over time it eventually slowly decays to a value of 1. As the particles are moving in solution (Brownian motion), a Doppler effect is observable and the decay over time of the autocorrelation function for a monodisperse particle in a dilute solution is depending on the self-translation diffusion coefficient D and the scattering vector q (**Equation 14**):

$$g^{(1)}(t) = e^{(-q^2\, D\, t)}$$

Equation 14: Autocorrelation function depending on the self-translation diffusion coefficient D of a monodisperse particle in solution and the scattering vector q.

According to **Equation 15**, q can be derived from the scattering angle θ and the incoming wavelength λ:

$$q = \left(\frac{4\,\pi}{\lambda}\right)\sin\left(\frac{\theta}{2}\right)$$

Equation 15: Term for the scattering vector q as a function of the scattering angle θ and the employed wavelength λ.

To deduce the hydrodynamic radius (R_h) from the diffusion coefficient D for monodisperse, spherical particles in a dilute solution, the Stokes-Einstein relation (**Equation 16**) can be exploited:

$$D = \frac{k_B T}{6\,\pi\,\eta\,R_h}$$

Equation 16: Stokes-Einstein relation for the diffusion coefficient to determine the hydrodynamic radius (R_h) with the Boltzmann constant k_B, the temperature T and the viscosity η of the solution.

with k_B being the Boltzmann constant, T the temperature, and η the viscosity of the solution. The aforementioned relations hold true for perfect monodisperse, spherical particles in dilute conditions. However, polymeric samples usually consist of particles that are disperse in size and shape. Therefore, not all particles exhibit the same translational diffusion coefficient D and the autocorrelation function becomes a sum of exponentials of all coefficients D_i (**Equation 17**):

$$g^{(1)}(t) = \sum_i A_i\, e^{(-q^2\, D_i\, t)}$$

Equation 17: Autocorrelation function for a solution of disperse particles in solution with the scattering vector q, the diffusion coefficients for each particle D_i and a weighing factor A_i proportional to the corresponding scattering fraction of particles.

For a continuous dispersity distribution, the continuous limit of the sum can be integrated. The determination of the full distribution of the diffusion coefficients from measurements of $g^{(1)}(t)$ becomes now a complex mathematical task, with an inverse Laplace transformation being necessary.[194] Several methods have been developed allowing such a transformation to obtain the full size distribution. Today the most common ones are the methods of cumulants,[196] exponential sampling,[197] non-negatively constrained least-squares (NNLS),[198] or the CONTIN method.[199] Herein, data analysis was carried out employing a cumulative method. The initially derived distribution in a DLS measurement is the intensity weighted distribution and all other distributions (number and volume weighted) are intrinsically calculated. In the current thesis, the number weighted distribution is reported as it represents the actual situation within the measured sample best. DLS has become a standard procedure in the SCNP community for comparing hydrodynamic diameters of polymeric precursors with formed SCNPs. However, one must bear in mind that the intensity of the scattering light is related to the sixth power of the radius of the scattering particles. Therefore, the nanometer ranged particles that are analyzed in the context of SCNP folding produce only a small amount of scattering light compared to larger aggregates.[193] This can result in non optimal measurement conditions and thus obtaining reliable values for R_h is often complicated. As a consequence, in the present thesis, only the obtained distributions for precursor and the related SCNP are reported, neglecting the actual values for R_h.

3

LIGHT INDUCED CHEMISTRY FOR 3D SCAFFOLDS

During the last years, extensive efforts have been taken to generate a perfectly controlled 3D environment for cell studies.[200-201] However, it still remains challenging to construct 3D structures suitable for cell attachment that exhibit more than one type of attachment point.[202] Although DLW proved to be a powerful tool for the construction of 3D microscaffolds, featuring a suitable size for cell attachments,[128] there are not many options when it comes to the facile surface functionalization of these microscaffolds. In an earlier approach,[17] microscaffolds were fabricated employing a commercial, non-passivating resist, then coated with a photoreactive silane, and finally functionalized in a spatially resolved manner by employing a custom built 2-photon absorption laser setup. However, due to the non-passivating nature of the resist, immobilization of cells could not be achieved. To allow for such a targeted cell attachment and to simplify the sample preparation process, two new photoresists exhibiting specific features were developed. The first important feature is the passivating nature of the fabricated microscaffolds, preventing non-specific bioadhesion and therefore allowing for a controlled cell attachment. Moreover, the photoresists consist of (meth)acrylic based monomers, to ensure that a commercial laser setup can be employed. As a last feature, photoreactive groups were incorporated, that are unaffected by the writing process and allow a facile post-modification. Additionally, the

employed photoreactive groups allow an orthogonal modification process to achieve a spatially resolved pattern.[81]*

3.1 Design of Photoreactive Monomers

To obtain the new photoresists with the aforementioned features, two new photoreactive monomers, based on a (meth)acrylic monomer moiety to allow a FRP in the DLW process, were designed. As functional groups, two photoreactive moieties that are orthogonal the writing process and are additionally chemically orthogonal to each other once immobilized on the surface were selected. At first, 2-hydroxethyl acrylate (HEA) as vinylic moiety was chosen to ensure a uniform polymerization during the DLW writing process when copolymerized with a commercial triacrylate network former usually employed in the commercial Nanoscribe DLW setup. The initial design of the two new monomers is depicted in **Scheme 26**.

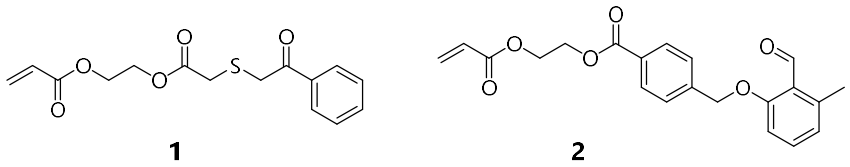

1 **2**

Scheme 26: Initial design of the novel photoreactive monomers based on 2-hydroxyethyl acrylate as vinylic moiety and phenacyl sulfide (**1**) as the first and photoenol (**2**) as the second photoreactive moiety.

As photoreactive moieties the phenacyl sulfide and an α-methylbenzaldehyde, forming a photoenol upon irradiation, were chosen since they should both be invariant to the 800 nm 2PA writing process and allow for a subsequent orthogonal surface modification. The α-methylbenzaldehyde, in the following named photoenol for simplification, was known to not be triggered at 400 nm (800 nm 2PA) from previous studies, since a custom built setup had to be employed.[130] The ability of the phenacyl sulfide to withstand the writing process had to be investigated by a control experiment. Therefore, a literature known phenacyl sulfide silane (**3**) was synthesized[77] and was attached to an activated glass slide via a silanization protocol. Subsequently, the functionalized glass slide was placed in a commercially available DLW setup (Photonic Professional, Nanoscribe GmbH) and a droplet of a solution of an amino-terminated PEG-derivative in DMF was added. In an area of 1 mm^2 a square pattern was tentatively written onto the surface by irradiation with the internal laser

*Parts from chapters 3.1 and 3.2 are reproduced or adapted from T. K. Claus, B. Richter, V. Hahn, A. Welle, S. Kayser, M. Wegener, M. Bastmeyer, G. Delaittre, C. Barner-Kowollik, *Angew. Chem. Int. Ed.* **2016**, *55*, 3817-3822, with permission from John Wiley and Sons. B. Richter and V. Hahn carried out the microstructure fabrication, the fluorescent staining and imaging. A. Welle and S. Kayser developed the new ToF-SIMS imaging mode. A. Welle provided the ToF-SIMS analysis in discussion with T. Claus. M. Wegener, M. Bastmeyer, G. Delaittre and C. Barner-Kowollik contributed to the scientific discussions and supervised the project.

(800 nm, 2-photon absorption). As a control experiment, the same setup was irradiated with a conventional UV lamp through a dotted shadow mask. The results of a subsequent ToF-SIMS analysis of both glass slides are depicted in **Figure 1**. The control sample displays a clear dotted pattern of a PEG-derived fragment, proving the successful outcome of the photoreaction (**Figure 1**b)). On the other hand, the DLW-treated surface does not show the square pattern of PEG fragments (Figure 1a)). Furthermore, the fragments derived from the phenacyl sulfide group are still detectable, evidencing the presence of the phenacyl sulfide moiety after the DLW process.

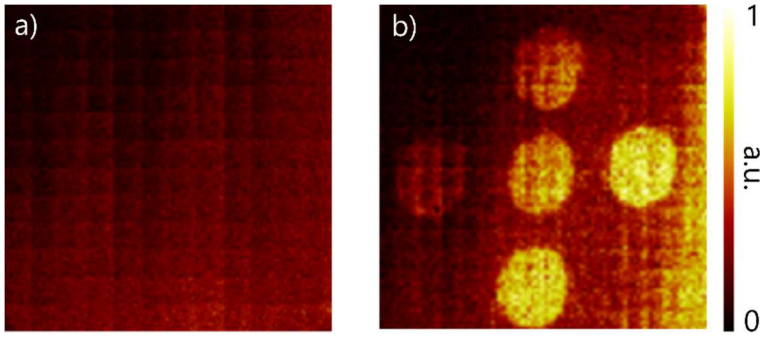

Figure 1: ToF-SIMS ion maps of glass slides silanized with phenacyl sulfide silane and irradiated in the presence of an amino-terminated PEG derivative. The samples were irradiated with a) the DLW laser at 800 nm and b) a conventional UV lamp (for specifications, refer to Section 7.2).

After it was shown that the phenacyl sulfide moiety is stable under the conditions of the writing process, a synthetic route for a phenacyl sulfide acrylate **1** was designed, as shown in **Scheme 27**. Esterification of HEA with phenacyl sulfide acid **3** should lead to the desired product.

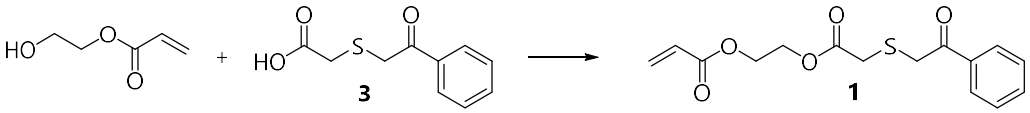

Employed conditions: (a) HEA, DCC, DMAP; DCM, a.t.; (b) HEA, EDC, DMAP, DCM, a.t.; (c) i) oxalyl chloride, DCM/DMF, 0 °C ii) HEA, NEt_3, DCM, a.t.; (d) HEA, ambelyst15, THF, a.t.

Scheme 27: Proposed synthetic route and conditions to obtain a phenacyl sulfide acrylate monomer (**1**).

However, none of the proposed esterification conditions (a-d) in Scheme 27 led to the desired product. The activated-ester route employing EDC as coupling agent led to decomposition of the phenacyl sulfide moiety. When DCC was employed, formation of the desired ester could be established by NMR spectroscopy. However, isolation via silica gel column chromatography was not possible, because the monomer polymerized during the purification process on the column. Therefore, other conditions that do not require a purification via column chromatography were applied. In a first step, acid **3** was converted into an acid chloride employing oxalyl chloride as activating agent. Subsequently, the volatile components were removed under vacuum and the formed acid chloride was directly used in an esterification with HEA and NEt_3. However, the phenacyl sulfide moiety did not prove stable under the applied reaction conditions. In a last attempt, Amberlyst® 15 was

employed as an acidic cation exchanger and catalyst. Using these conditions, the formation of the desired ester could be established. However, isolation was not possible due to polymerization during workup. To minimize the workup steps with the vinylic moiety present, the synthetic route was adjusted as depicted in **Scheme 28**. The route consists of two esterification steps: first the attachment of an ethylene glycol spacer to acid **3** to obtain alcohol **4** as intermediate, second an activated esterification protocol with acryloyl chloride as reactant.

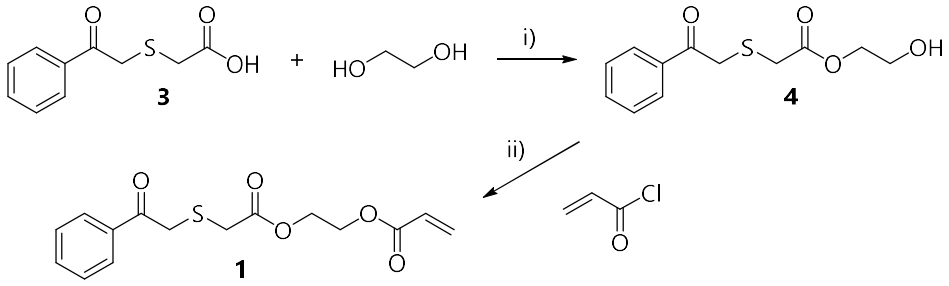

Employed conditions: i) (a) amberlyst® 15, THF, a.t.; (b) p-toluenesulfonic acid, water seperator, toluene, 140 °C; (c) H_2SO_4, water separator, toluene 150 °C; (d) DCC, DMAP, DCM, a.t.; ii) NEt_3, DCM, 0 °C-a.t.

Scheme 28: Adjusted synthetic pathway and reaction conditions to obtain monomer **1** from acid **3**. Two step esterification process; first attachment of an ethylene glycol spacer and in a second step an activated esterification procedure with acryloyl chloride to obtain the final product.

For the first step, several synthetic procedures were applied (see Scheme 28), which – after appropriate workup – all led to the desired product. A ^{1}H NMR spectrum of the purified alcohol **4** is depicted in **Figure 2**.

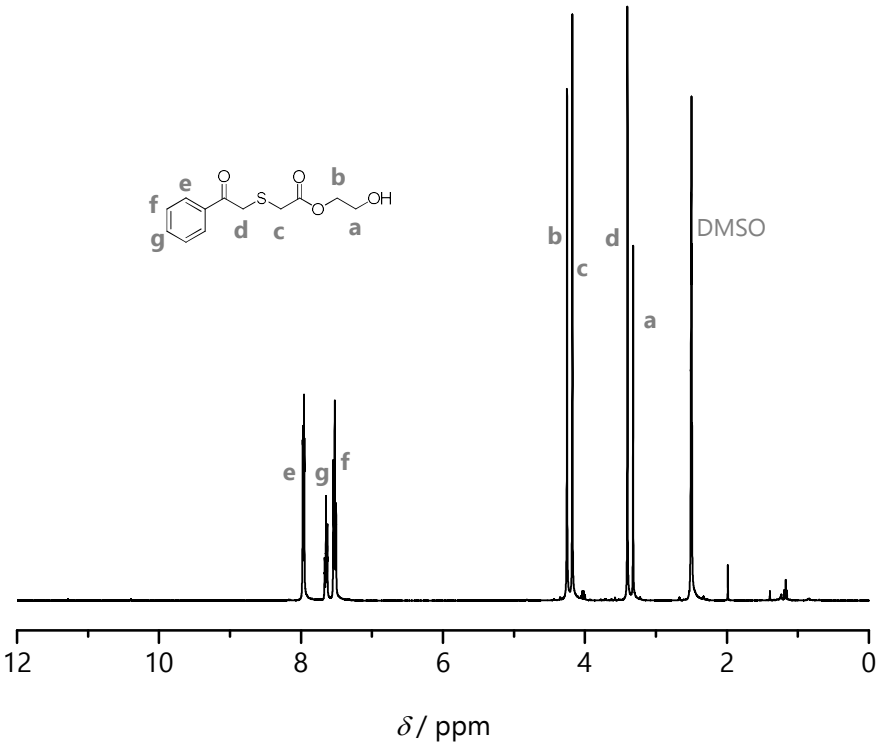

Figure 2: ^{1}H NMR spectrum (400 MHz, DMSO-*d6*, ambient temperature) of phenacyl sulfide alcohol **4**.

The second esterification step was carried out via a well-established procedure with acryloyl chloride and NEt_3 in DCM. However, an unknown substance originating from the

degradation of the phenacyl sulfide was again the only product. A third synthetic strategy based on amidation and subsequent esterification was conducted as depicted in **Scheme 29**. Here, 2-aminoethan-1-ol instead of ethylene glycol is introduced as spacer in the first step.

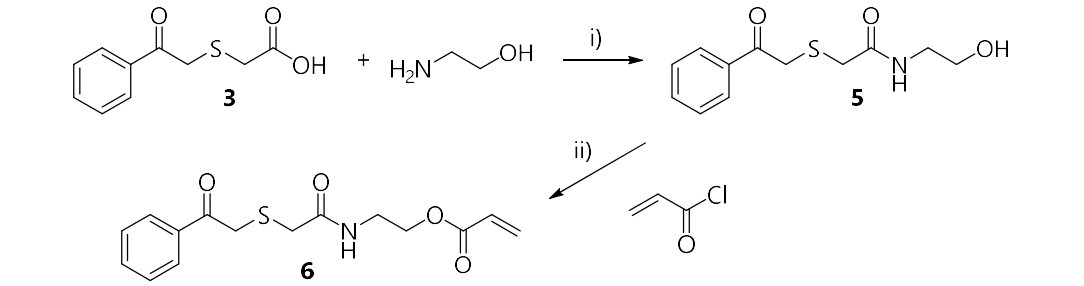

Scheme 29: Third synthetic strategy for the synthesis of an acrylic phenacyl sulfide monomer (**6**). The first step is an amidation reaction with 2-aminoethan-1-ol employing ethylchloroformiate ad coupling agent. The second step was planned the same way as in Scheme 28.

The insertion of an amide instead of an ester moiety was assumed to lead to a more stable product that is less susceptible to transesterification side reactions. Yet again, the phenacyl sulfide moiety did not prove stable under the conditions applied in the first step, where ethylchloroformiate is employed as coupling agent. It seems that the phenacyl sulfide moiety is not stable to acid chloride esterification/amidation conditions. Since the aforementioned conditions did not prove to be successful in the synthesis of an acrylate based phenacyl sulfide monomer, the strategy was changed and the monomers were designed on a methacrylic basis. This should lead to more stable structures that are less susceptible to spontaneous polymerization during work up procedures due to a less reactive vinyl moiety. The new designed structures of the two photo monomers are depicted in **Scheme 30**.

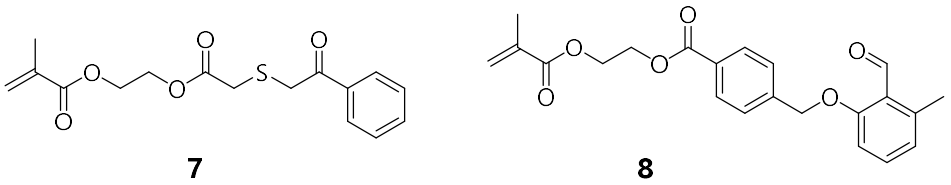

Scheme 30: Revised design of the novel photoreactive monomers as methacrylate type monomers based on phenacyl sulfide (**7**) and photoenol (**8**) moieties.

The new synthetic strategy to obtain the phenacyl sulfide methacrylate (**7**) is shown in **Scheme 31**.

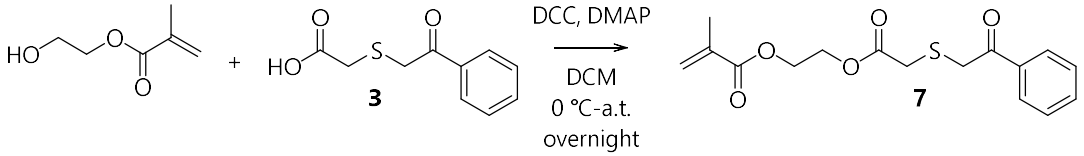

Scheme 31: Synthetic strategy based on a simple esterification reaction of acid **3** with HEMA employing DCC as coupling agent.

DCC/DMAP was selected as coupling agent for the esterification of acid **3** with HEMA, since it provided the best results in the previous trials. Applying these conditions the phenacyl sulfide methacrylate (PS-MA, **7**) could be obtained and the resulting ^{1}H NMR analysis is depicted in **Figure 3**.

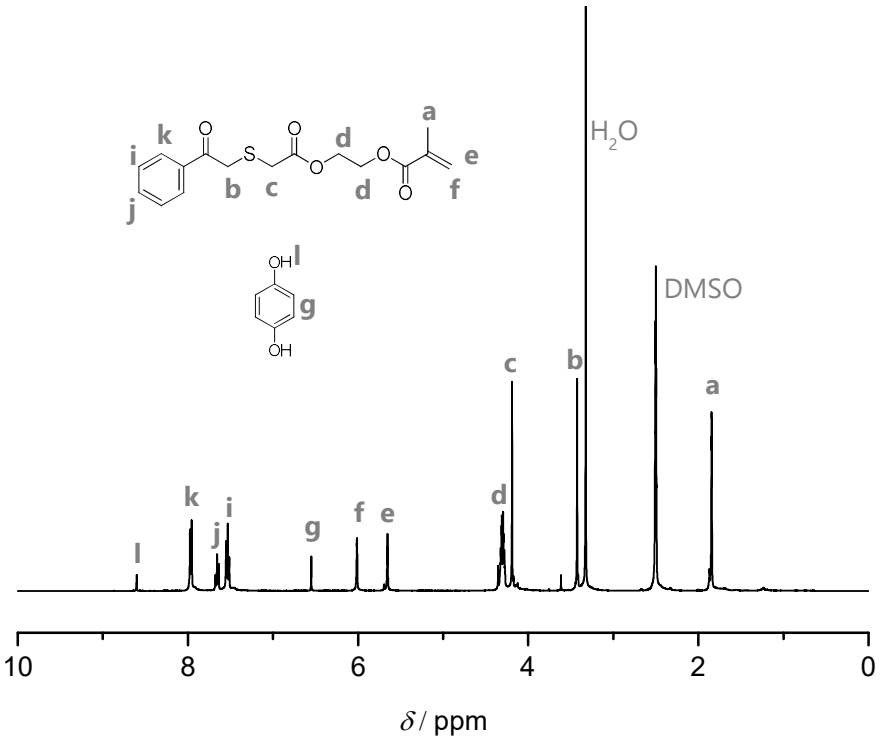

Figure 3: ^{1}H NMR spectrum (400 MHz, DMSO-*d6*, ambient temperature) of PS-MA (**7**), stabilized with 1 wt% hydroquinone to prevent polymerization upon storage.

After the successful synthesis of the first novel photoreactive monomer, the second monomer, photoenol methacrylate (PE-MA, **8**) was synthesized with the same conditions, employing DCC/DMAP as coupling agent. The successful outcome of the reaction was again proven via ^{1}H NMR spectroscopy (see **Figure 4**).

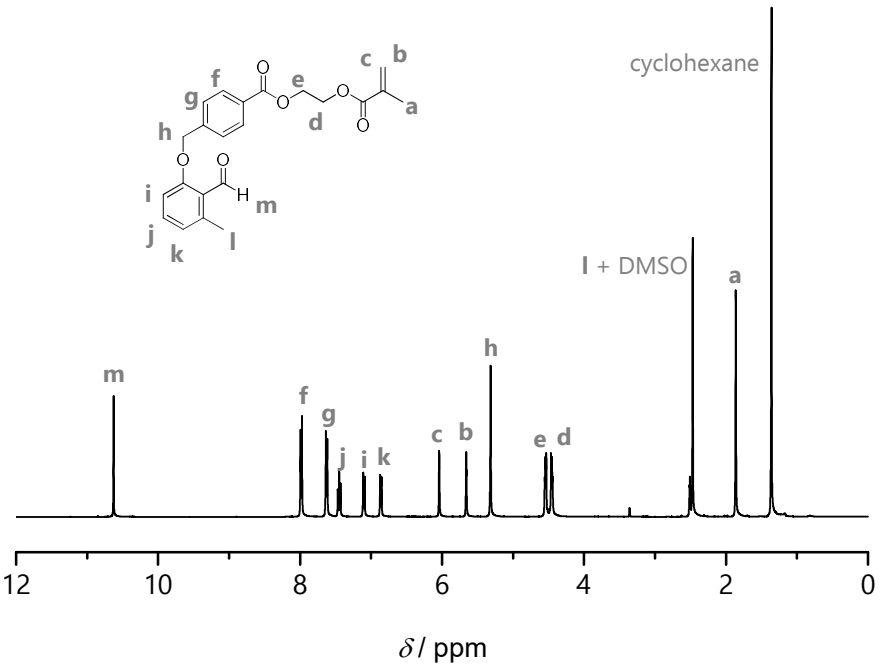

Figure 4: ^{1}H NMR spectrum (400 MHz, DMSO-*d6*, ambient temperature) of PE-MA (**8**).

Additionally, both monomers were characterized via UV-vis spectroscopy, the results are depicted in **Figure 5**.

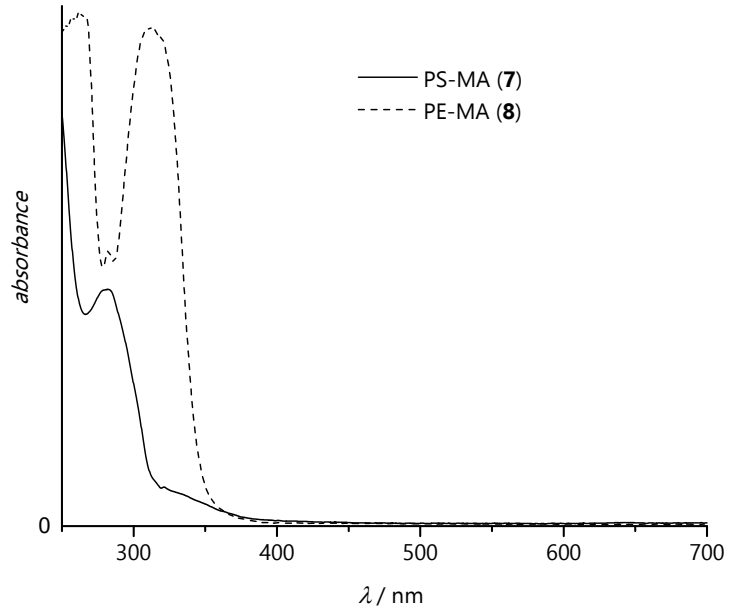

Figure 5: UV-Vis absorption spectra of PS-MA (**7**) and PE-MA (**8**) (0.5 mg mL^{-1} in acetonitrile, l = 0.5 cm, a.t.).

The UV-vis spectra clearly show that both photoreactive monomers do not exhibit significant absorption at 400 nm and should therefore be suited for the DLW writing process.

3.2 Fabrication and Characterization of Dual Photoreactive 3D Scaffolds

3.2.1 Fabrication of dual functional DLW structures and ToF-SIMS characterization of light triggered post-modification

To achieve dual photoreactive microscaffolds that also exhibit passivating features, three DLW resists were formulated. To ensure the passivating nature and a good incorporation of the methacrylate based photoreactive monomers, trimethylolpropane ethoxylate triacrylate (TPE-TA, **9**, see **Scheme 32**) was chosen as network former. The commercially available triacrylate **9** bears an average of 3-4 ethylene glycol units per arm as spacer between the core and the vinylic moieties and should thus enable the formation of cell passivating networks. To obtain dual photoreactive 3D scaffolds, three DLW resists were composed. One

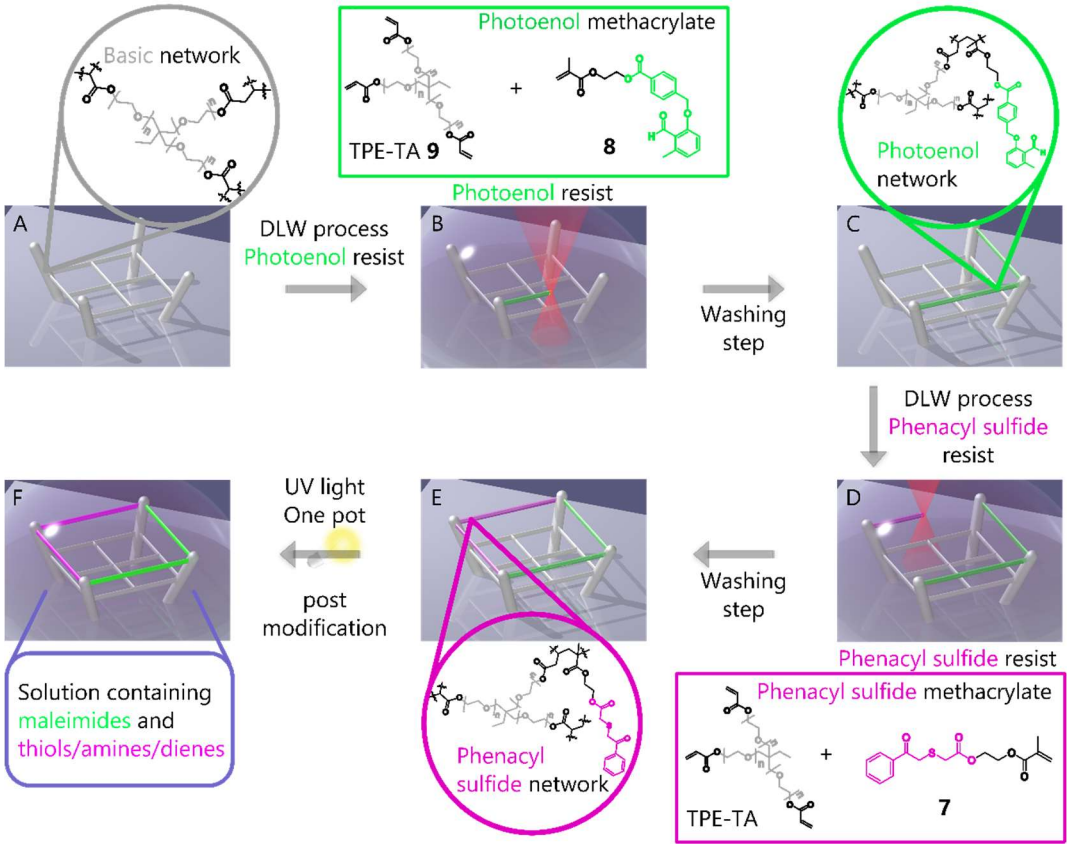

Scheme 32: Schematic drawing of the overall scaffold preparation and post-modification process. A) First writing process (not depicted) with the basic resist consisting of TPE-TA and the photoinitiator to obtain a skeletal structure; B) and C) Second DLW writing step with the photoenol resist constructing two beams of the scaffolds consisting of a photoenol containing network; D) and E) Third DLW writing step with the phenacyl sulfide resist to obtain the missing two beams of the scaffolds consisting of a phenacyl sulfide network; F) Post-modification as a last step to obtain the final dual functionalized scaffolds. The microstructures are globally irradiated in the presence of functional maleimides and functional thiols/amines or dienes with UV light to induce the surface functionalization. For simplification the photoinitiator (Irgacure® 369) was omitted in the resist recipes. The Scheme was adapted from Ref.[81] with permission of John Wiley and Sons © 2016.

basic resist, consisting of TPE-TA and 3 wt% of a commercially available photoinitiator (Irgacure® 369), one phenacyl sulfide resist (PS-resist), consisting of a 9:1 (w/w) mixture of TPE-TA and PS-MA (**7**) plus 3 wt% of the photoinitiator, and one photoenol resist (PE-resist), consisting of a 9:1 (w/w) mixture of TPE-TA and PE-MA (**8**) plus 3 wt% of the photoinitiator. The microscaffolds were intended to be prepared in three consecutive DLW steps using the three resists (see Scheme 32) and subsequently post modified via a one pot dual photo reaction. To first investigate the properties and behavior of the new functional resists in DLW writing and for a simpler characterization of the modified scaffolds 2D checkerboard pattern were written onto glass cover slides and functionalized under UV light irradiation, employing a commercial UV lamp (for details, refer to Section 7.2.2). The extent of the writing process, stability, and smoothness of the written structures was analyzed via scanning electron microscopy (SEM) imaging. The outcome of the post-modification was analyzed employing ToF-SIMS analysis as well as confocal fluorescent microscopy (CFM). Despite the incorporation of close to 10 wt% of mono functional monomer into the network, SEM images (**Figure 6**) evidence well defined 2D surfaces with homogeneous surface topologies. **Figure 6**a) shows an overview of a typical glass slide sample covered with various 2D and 3D structures originating from different photoresist combinations. In Figure 6b), a square pattern written with the basic resist is depicted. Figure 6c) and 6d) show checkerboard structures written with the basic resist and either the functional PS- resist or

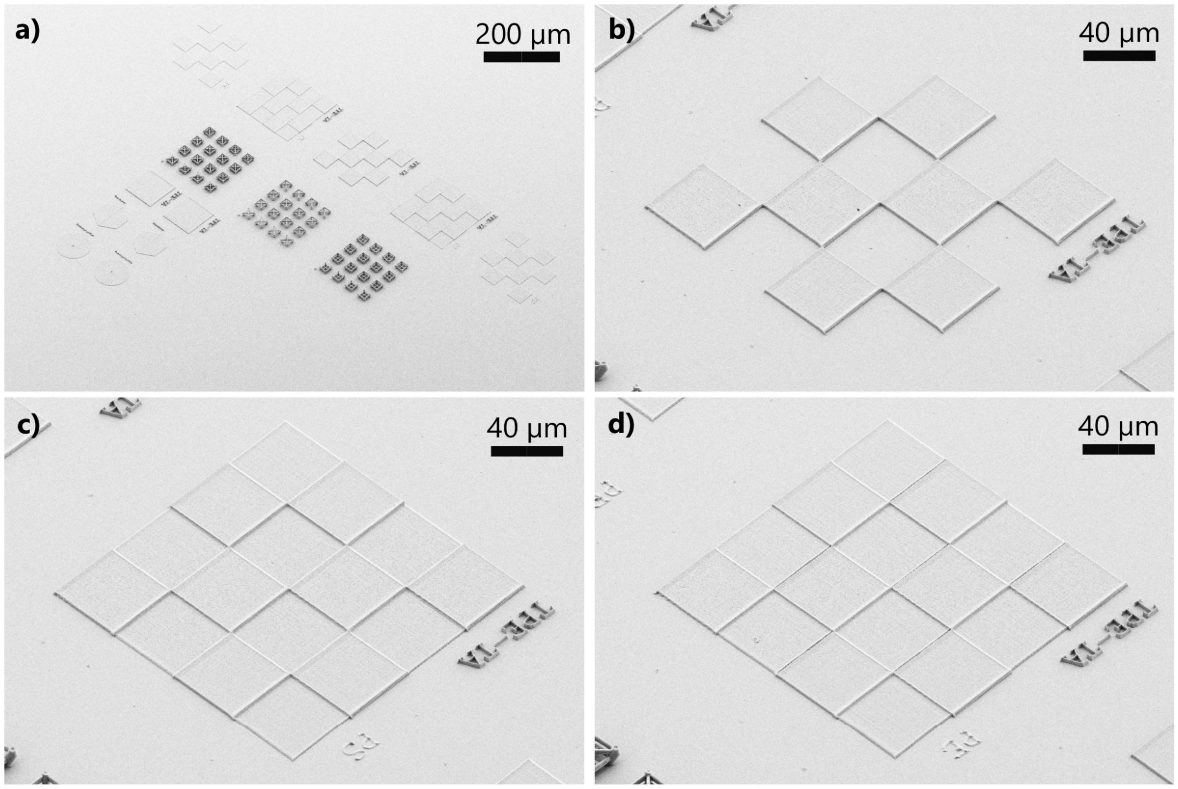

Figure 6: SEM images of the obtained 2D checkerboard structures. a) Overview of a complete glass slide with 2D and 3D structures. b) 2D squares written with the basic resist consisting of TPE-TA and the photoinitiator. c) 2D checkerboard structure consisting of squares written with the basic resist and squares written with the photoenol resist. d) 2D checkerboard structure consisting of squares written with the basic resist and squares written with the phenacyl sulfide resist.

the PE-resist. To analyze the photoreactivity of the obtained 2D scaffolds, ToF-SIMS was chosen. Therefore, halogenated molecules were employed in the phototriggered post-modification reaction as marker in ToF-SIMS measurements. The employed reagents and the products of the reactions with the corresponding photo moieties are depicted in **Scheme 33** and **Scheme 34**.

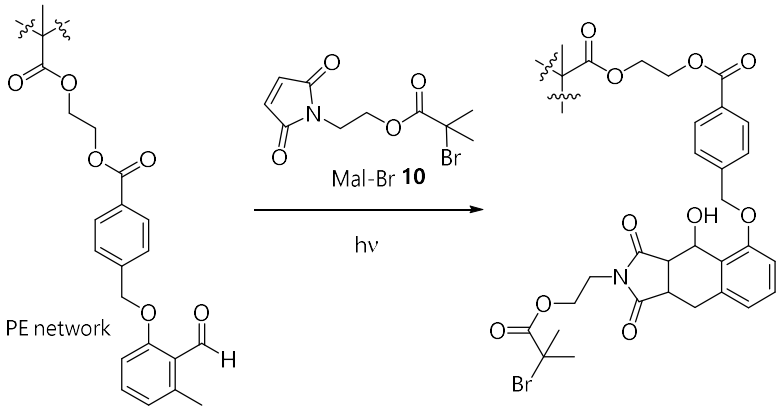

Scheme 33: Phototriggered post-modification reaction of the photoenol bearing network employing a brominated maleimide (Mal-Br, **10**) as marker for ToF-SIMS analysis.

For the photoenol containing network a brominated maleimide derivative (Mal-Br, **10**) was selected as reaction partner in the phototriggered Diels–Alder (DA) reaction. This allows an unambiguous characterization of the photoenol post-modification reaction, since, successful post-modification provided, only on the PE-functionalized squares of the 2D checkerboard structures bromine fragments should be detected via ToF-SIMS.

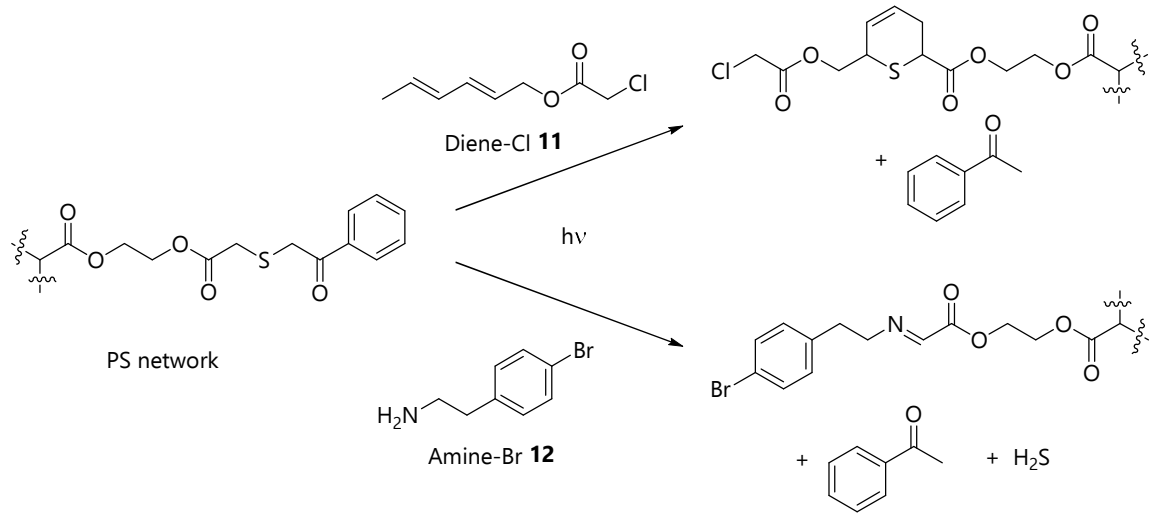

Scheme 34: Phototriggered post-modification reaction of the phenacyl sulfide bearing network employing either a chlorinated sorbic acid derivative (Diene-Cl, **11**) or a brominated amine derivative (Amine-Br, **12**) as marker for ToF-SIMS analysis.

For proofing the reactivity of the phenacyl sulfide containing network, either a chlorinated sorbic acid derivative (Diene-Cl, **11**) or an aromatic, brominated am amine (Amine-Br, **12**) derivative were employed. Diene-Cl **11** can react with the photo generated thio aldehyde in a hetero Diels–Alder reaction, whereas Amine-Br **12** and the thio aldehyde undergo a condensation reaction to form an imine derivative. The post-modification reactions were

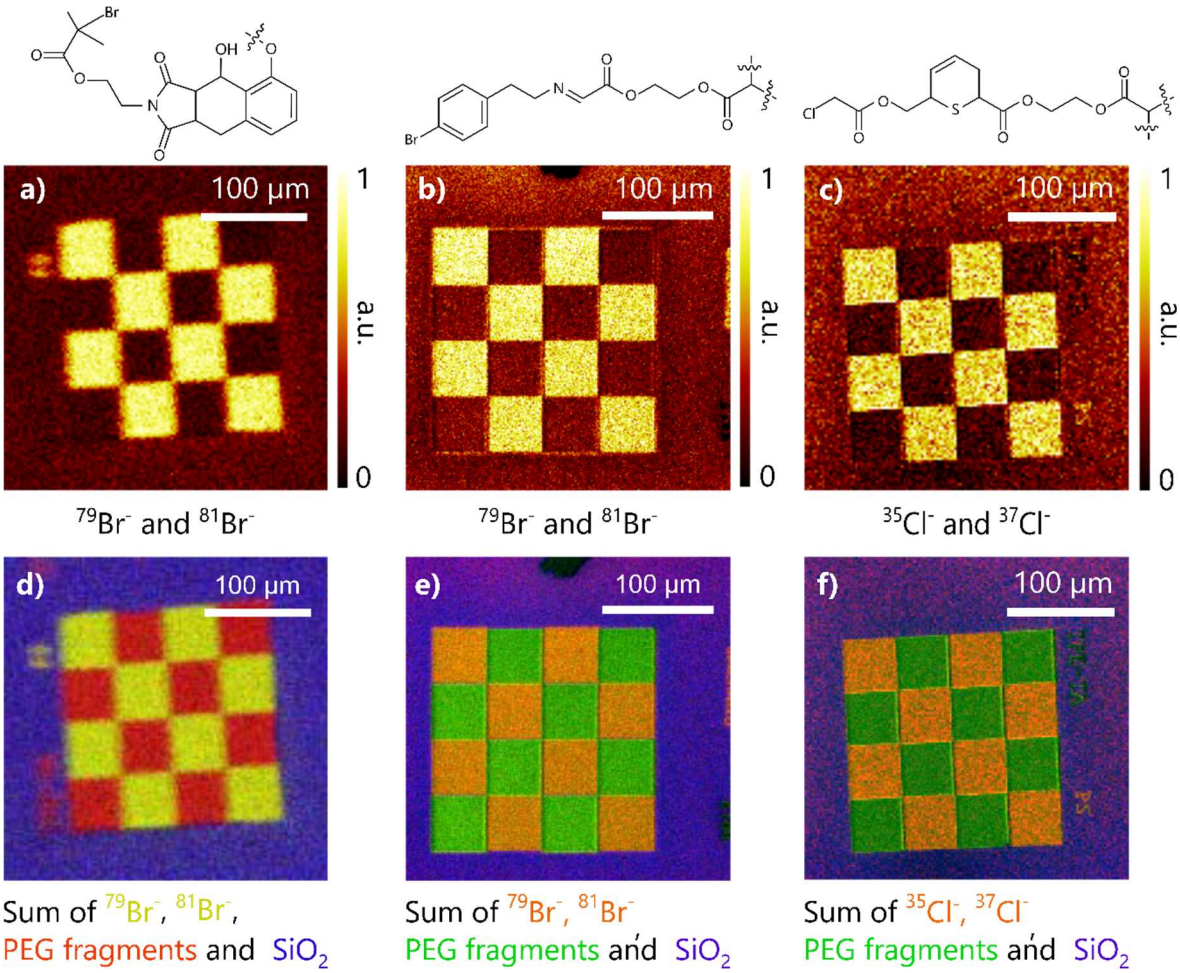

Figure 7: ToF-SIMS ion maps of the phototriggered post-modifications of the functional DLW 2D checkerboard structures with halogenated marker molecules. The checkerboard structures consist of the basic resist versus one of the functional resists (PE or PS resist). Top row: Single fragment ion maps for the respective specific halogen fragments; bottom row: Colored overlay picture of the sums of characteristic fragments of the whole sample. a) and d) results for the photoenol post-modification with Mal-Br **10**; b) and e) results for the phenacyl sulfide post-modification with Amine-Br **12**; c) and f) results for the phenacyl sulfide post-modification with Diene-Cl **11**.

carried out by placing a droplet of a solution of the respective halogenated marker molecule in DMAc (1 mg mL^{-1}) onto the written structures. This droplet was kept in place by a PDMS ring. The as-prepared glass slides were irradiated under a broadband UV lamp for 30 min, subsequently rinsed with acetone, soaked in DMF for 30 min, again rinsed with isopropanol, and finally dried with a gentle stream of nitrogen gas. The results of the ToF-SIMS analysis of the 2D checkerboard structures containing one type of photoreactive resist are depicted in **Figure 7**. In Figure 7a), the ion map of the detected bromine fragments for the surface functionalization of a checkerboard consisting of PE-resist squares and squares written with the basic resist with Mal-Br **10** is shown. The clear detection of bromine fragments only on the PE-resist squares evidences the successful spatial resolved functionalization reaction. In Figure 7b) and 7c) the ion maps for the post-modifications of checkerboards consisting of PS-resist and basic resist are shown. Figure 7b) demonstrates the successful surface functionailzation with Amine-Br **12** and Figure 7c) the surface functionalization with Diene-Cl **11**. The bottom row (Figure 7d)-f)) depicts a colored overlay of the sums of characteristic

fragments from the according samples. For the image with the results of the PE-resists (Figure 7d)), the sum of bromine fragments is depicted in the yellow channel, PEG fragments in the red one. Figure 7e) and 7f) depict the images for the PS-resist (red channel: bromine respectively chlorine fragments, green channel: PEG fragments). The blue channel corresponds to SiO_2 fragments derived from the glass support in all images. The ToF-SIMS images for the PE-resist were imaged in the so-called "bunch mode", whereas the images for the PS-resist were recorded in the so-called "delayed extraction mode", allowing a better lateral resolution at the same mass resolution (for more details please refer to the Methods and Instrumentation Section 7.2.2). After the spatially resolved surface modification employing the combination of one photoreactive resist with the basic resist, had been evidenced in 2D, the feasibility of the combination of both photoreactive resists in one sample was examined. Upon irradiation, the α-methylbenzaldehyde forms a diene – the photoenol, the phenacyl sulfide in contrast forms a highly reactive ene. When applying an ene as reaction partner for the PE-resist and a diene for the PS-resist respectively, the simultaneous dual patterning in one step can be achieved. In a "one pot" reaction, a droplet of a solution containing both reaction partners (mixing the Mal-Br **10** solution and the Diene-Cl **11** solution 1:1) was placed on dual functional checkerboards and irradiated as described above. The ToF-SIMS results of these simultaneous dual light triggered post-modifications on 2D checkerboard structures are shown in **Figure 8**. The first two images (Figure 8a) and 8b)), depict the ion maps of the halogen fragments derived from the corresponding functional resist. It is clearly evidenced that no cross reactivity between the functional resist occurs, since there are no chlorine fragments found on the PE-resist and no

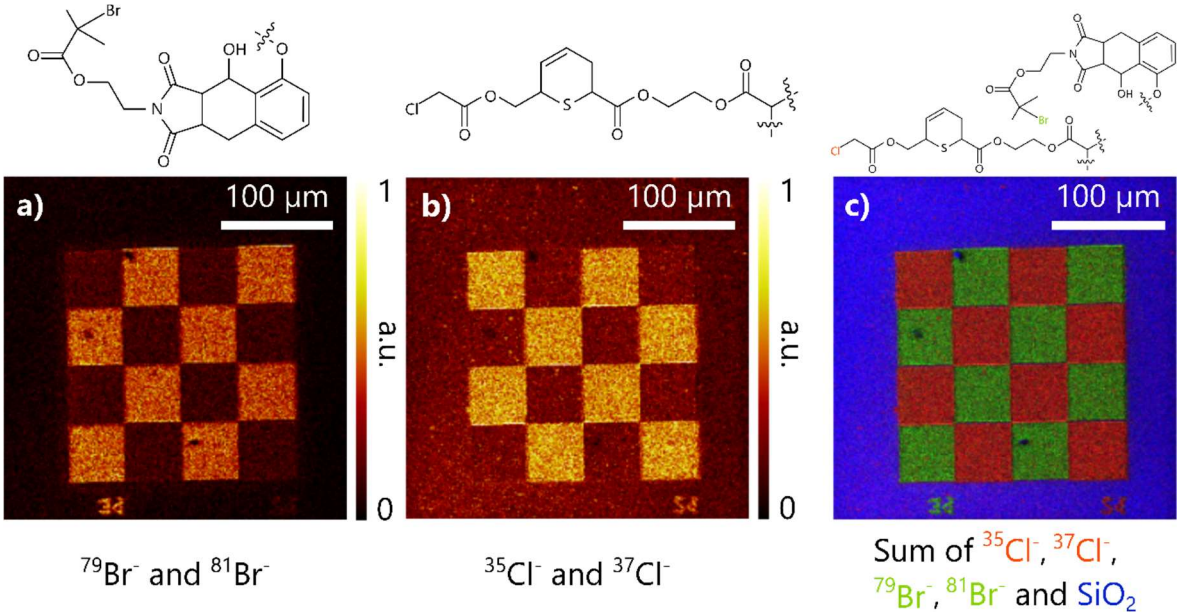

Figure 8: ToF-SIMS ion maps obtained after light triggered post-modification employing Mal-Br **10** and Diene-Cl **12** simultaneously on a dual functional checkerboard structure. a) Ion map depicting the sum of bromine fragments arising from Mal-Br **10** only attached to the PE-resist; b) Ion map depicting the sum of chlorine fragments arising from Diene-Cl **11** only attached to the PS-resist. c) Colorized overlay picture of ion maps shown in a) and b); red channel: sum of chlorine fragments, green channel: sum of bromine fragments, blue channel: SiO_2 fragments arising from the glass support.

bromine fragments on the PS-resist respectively. This underpins the success of the simultaneous dual one pot functionalization. Additionally, in Figure 8c), a colored overlay of the first two pictures is depicted with the chlorine fragments imaged in red, the bromine fragments in green, and the fragments arising from the glass substrate in blue. A clear three colored image is obtained, further underlining the successful spatially resolved surface modification.

After the successful fabrication and post-modification of dual photoreactive 2D structures, 3D scaffolds were designed. With the purpose of attaching cells in a defined fashion, boxing ring like 3D structures were constructed. SEM images of well-defined 3D boxing rings with a homogeneous surface structure for ToF-SIMS analysis are depicted in **Figure 9**. Here, the support of the structures and the cross in the center is written with the basic resist, the two beams facing down are written with the PS-resist (Figure 9c) and 9d)) and the two beams facing upwards are written with the PE-resist (Figure 9b) and 9d)). The cross in the middle was inserted to ensure that all three resist are present on the same level, simplifying ToF-SIMS analysis. For the light triggered post-modifications of the 3D scaffolds, the same chemistries and procedures as for the 2D functionalization were employed (see Scheme 33 and Scheme 34). The ToF-SIMS results of the functionalization of 3D scaffolds with the basic resist and one of the functional resists combined are depicted in **Figure 10**.

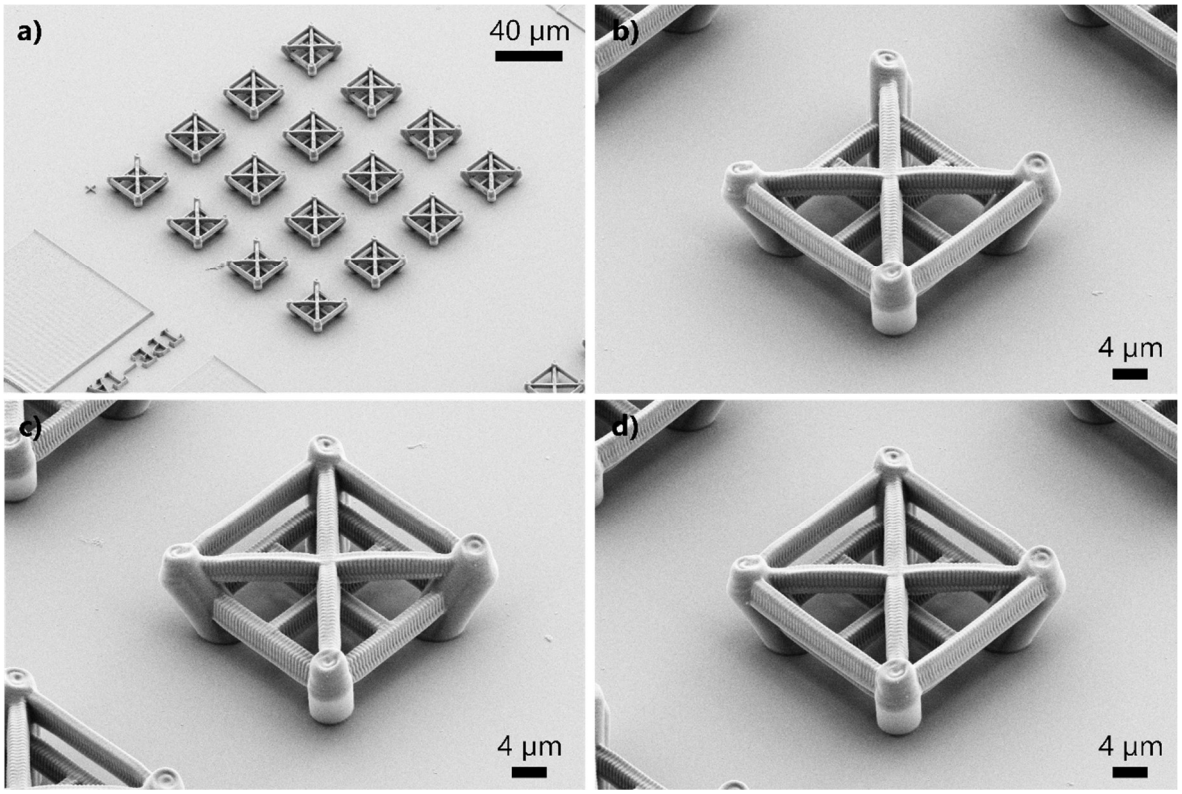

Figure 9: SEM images of the obtained 3D boxing ring structures. a) Overview of a complete grid of 16 boxing ring structures containing one or two functional resists. b) 3D boxing ring written with the basic resist consisting of TPE-TA to obtain the supporting scaffold. The lower two beams are written with the PE-resist. c) 3D boxing ring written with the basic resist consisting of TPE-TA to obtain the basic scaffold. The upper two beams are written with the PS-resist. d) Complete 3D boxing ring structure with the basic scaffold written with the basic resist, the upper two beams written with the PS-resist and the lower two beams with the PE-resist.

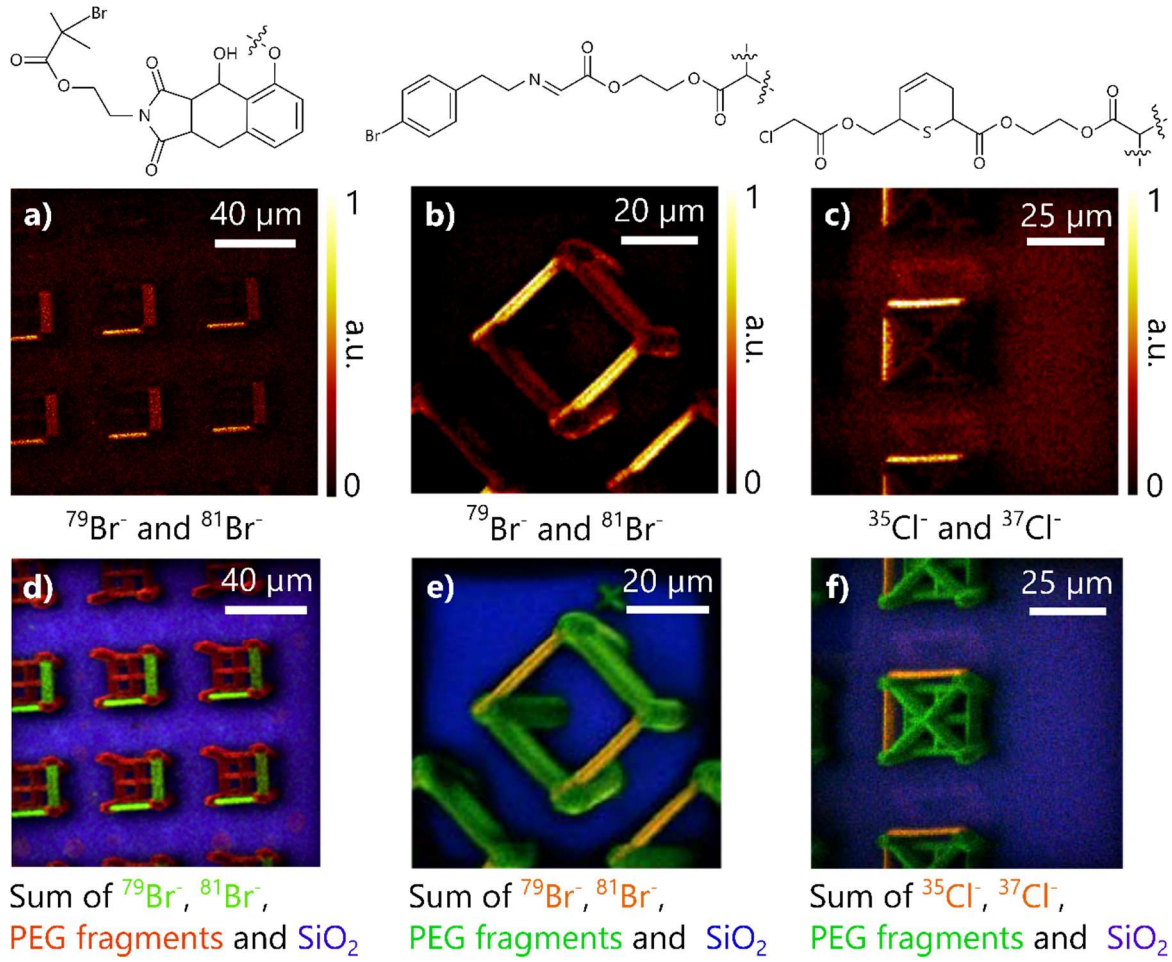

Figure 10: ToF-SIMS ion maps measured after phototriggered post-modifications of the functional DLW 3D boxing ring structures with halogenated marker molecules. The boxing rings consist of the basic resist and one of the functional resists (PE or PS resist). The top row depicts single fragment ion maps for the respective specific halogen fragments, the bottom row shows colored overlay pictures of the sums of characteristic fragments of the whole sample. a) and d) results for the photoenol post-modification with Mal-Br **10**; b) and e) results for the phenacyl sulfide post-modification with Amine-Br **12**; c) and f) results for the phenacyl sulfide post-modification with Diene-Cl **11**.

The top row of images depicts the single ion maps for the respective halogen fragments ($^{79}Br^-$ + $^{81}Br^-$ for PE-resist and $^{35}Cl^-$ + $^{37}Cl^-$ and $^{79}Br^-$ + $^{81}Br^-$ for PS-resist). In the bottom row colored overlay images of the sums of all characteristic fragments for the basic resist, the respective functionalized photoresist and the glass slide are shown. In Figure 10a) and 10d) it is evidenced that bromine fragments only arise from areas written with the PE-resist. The same holds true for the post-modification of the PS-resist with Amine-Br **12**, depicted in Figure 10b) and e). The images in the rightmost column of Figure 10 indicates the realization of the spatially resolved functionalization of the PS-resist with Diene-Cl **11**. With this, as for the post-modification of the 2D checkerboards, the success of the reaction is clearly indicated. Therefore, in a next step, all three resists were combined and a 3D boxing ring was fabricated in three consecutive DLW steps according to Scheme 32. The resulting structure is depicted in Figure 9d) and the results of the corresponding ToF-SIMS analysis are depicted in **Figure 11** and **Figure 12**. Figure 11 shows, equivalently to Figure 8 for the 2D results, the ion maps for the employed halogen marker ($^{79}Br^-$ +$^{81}Br^-$ for PE-resist functionalization and $^{35}Cl^-$ + $^{37}Cl^-$ for PS-resist functionalization; Figure 11a) and 11b)), and

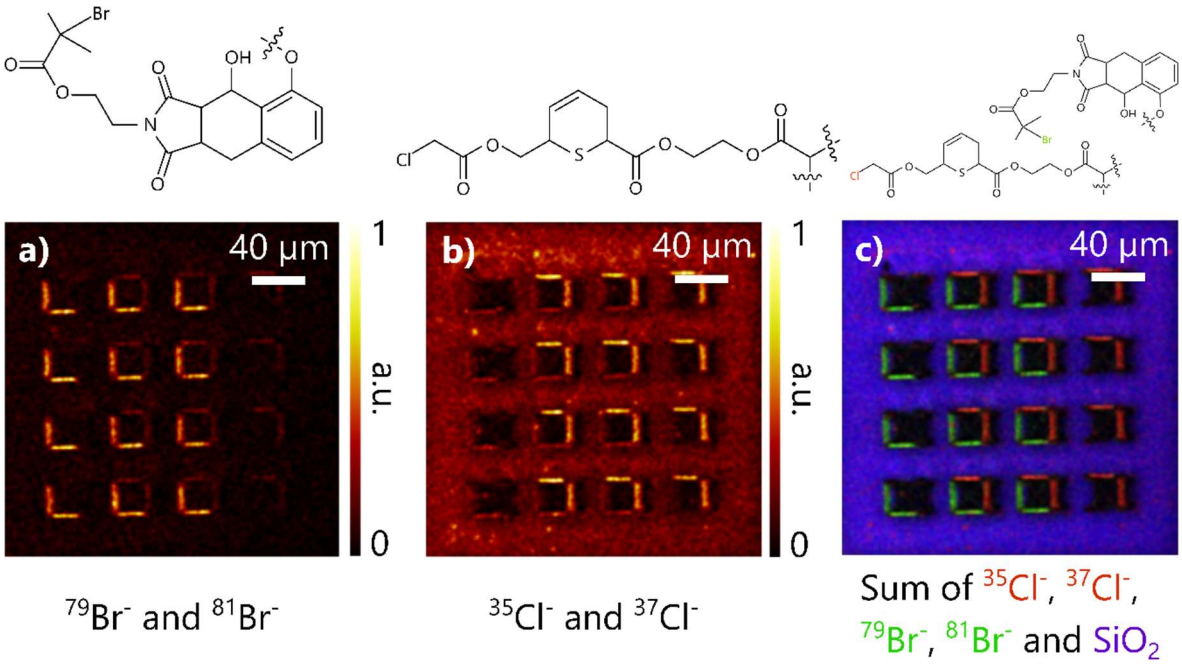

Figure 11: ToF-SIMS ion maps of the light triggered post-modification employing Mal-Br **10** and Diene-Cl **12** simultaneously on a dual functional boxing ring structure. a) Ion map depicting the sum of bromine fragments arising from Mal-Br **10** only attached to the PE-resist; b) Ion map depicting the sum of chlorine fragments arising from Diene-Cl **12** only attached to the PS-resist. c) Colorized overlay picture of ion maps shown in a) and b); red channel: sum of chlorine fragments, green channel: sum of bromine fragments, blue channel: SiO_2 fragments arising from the glass support.

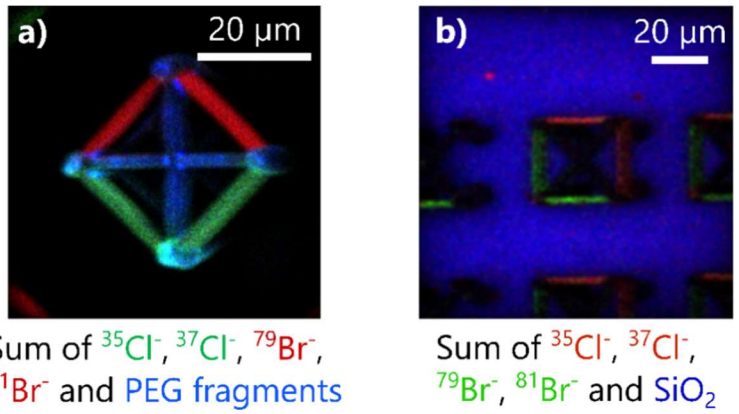

Figure 12: Magnification of dual functionalized 3D boxing rings. a) Colored overlay of chlorine (green) bromine (red) and PEG fragments (blue); b) In this overlay, chlorine fragments are depicted in red, bromine fragments in green and fragments of the glass support are depicted in blue.

a colored overlay of all halogen fragments and fragments arising from the glass support (green channel: bromine fragments; red channel: chlorine fragments and blue channel: SiO_2 fragments) is shown in Figure 11c). As in such an overlay only three color channels can be assigned, fragments from the basic resist (derived from the TPE-TA) appear in black. In Figure 12, two magnified colored overlay images are depicted. In Figure 12a) the fragments derived from the functionalized PS-resist (chlorine fragments) are depicted in the green channel, the fragments derived from the functionalized PE-resist (bromine) are depicted in the red channel and the fragments derived from the basic resist (PEG fragments) are depicted in the blue channel. Therefore, the background appears in black, as no color channel was assigned to the glass support. Figure 12b) illustrates a magnified 3D boxing

ring with the same assignments as in Figure 11c). Both color combinations indicate the high spatial resolution and selectivity of the employed post-modification step. The assigned colors do not overlap in the magnified images, proving that no cross reactivity between the PE- and PS- resists occurs. All obtained ToF-SIMS results underpins the successful application of the two novel photoreactive monomers in DLW written structures and the resulting simultaneous photoreactivity of the scaffolds.

3.2.2 Confocal Fluorescence Microscopy (CFM) characterization of dual functionalized DLW structures

After the feasibility of the one pot light triggered post functionalization of dual functional 3D scaffolds had been unambiguously proven, the next step towards an application of this protocol for targeted cell attachment was to introduce fluorescent marker molecules and proteins by the same protocol. A maleimide labeled rhodamine (Mal-Rhod **13**) was selected as fluorescent marker for the functionalization of the PE-resist (depicted in **Scheme 35**). For the fluorescent staining of the PS-resist, a two-step strategy involving a fluorescent protein

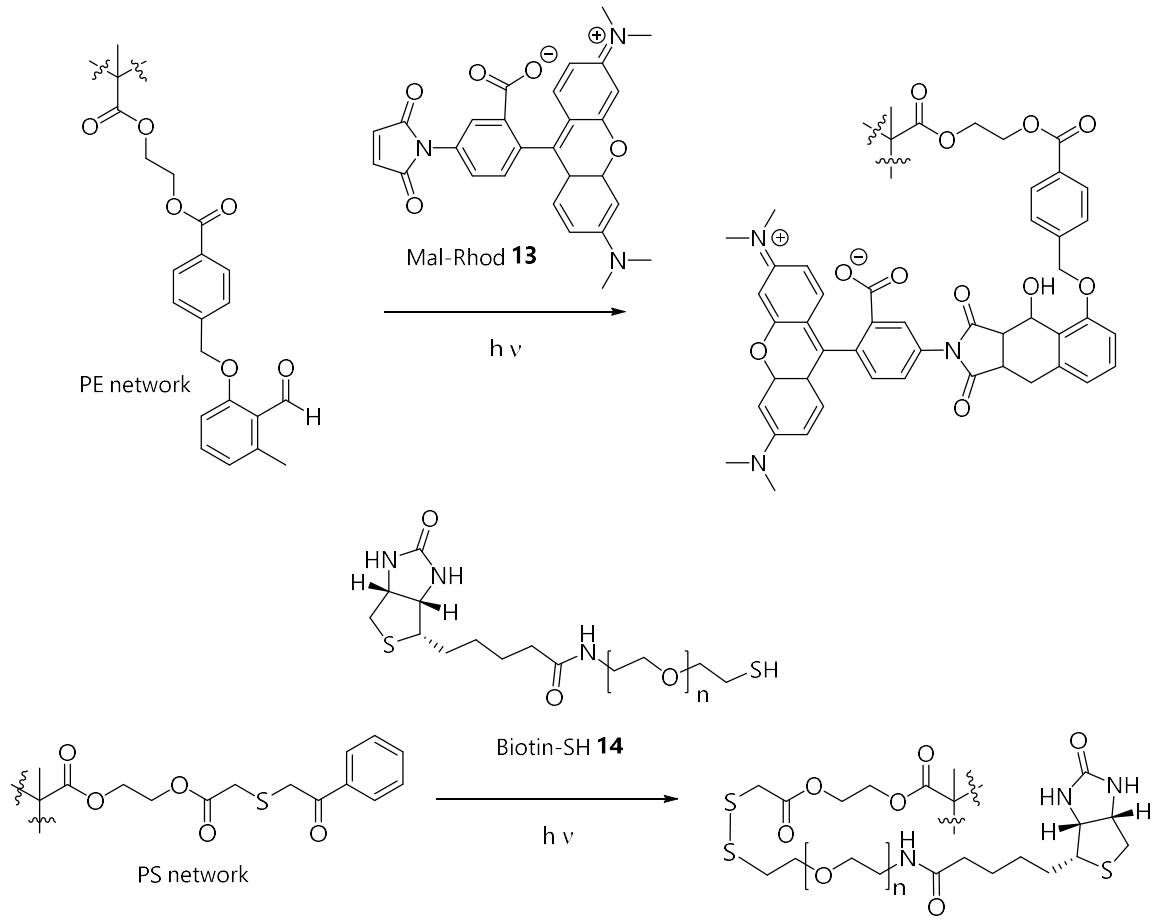

Scheme 35: Chemistry of the light triggered post-modification to achieve dual fluorescent DLW structures. For the surface reaction with the PE-resist a fluorescent maleimide rhodamine derivative (Mal-Rhod **13**) was employed. To achieve fluorescence on the PS-resist containing patches, a biotinylated thiol (biotin-SH **14**) is tethered to the phenacyl sulfide via a disulfide linkage. The biotin was subsequently sutilized for docking of a fluorescent streptavidin conjugate (SAv-647).

binding was chosen. First, a biotinylated thiol compound (biotin-SH **14**) was employed in the phototriggered dual post-modification (Scheme 35). In a subsequent staining step, a fluorescent streptavidin conjugate (SAv-647, see Materials Section 7.1) was added and a dual fluorescent substrate was achieved. The postmodification reactions were carried out in a similar way as with the halogenated marker molecules. A solution of the respective fluorophore (0.1 mg mL^{-1} in DMAc for Mal-Rhod **13**) and the fluorescent protein binder (1 mg mL^{-1} in DMAc for biotin-SH **14**) was added to the fabricated 2D and 3D structures and irradiated under a conventional UV lamp for 30 min. Subsequently the fluorescent staining with SAv-647 was performed in PBS (0.01 mg mL^{-1}) with an incubation time of 30 min. The Confocal Fluorescence Microscopy (CFM) images were recorded in three channels: a white one corresponding to the autofluorescence of the microstructures ($\lambda_{exitation}$ = 405 nm; $\lambda_{detection}$ = 420–480 nm), a green one corresponding to the Mal-Rhod **13** ($\lambda_{excitation}$ = 561 nm; $\lambda_{detection}$ = 575–615 nm) and a purple one corresponding to the SAv-647 ($\lambda_{excitation}$ = 633 nm; $\lambda_{detection}$ > 650 nm). Single channel images of all three imaging channels

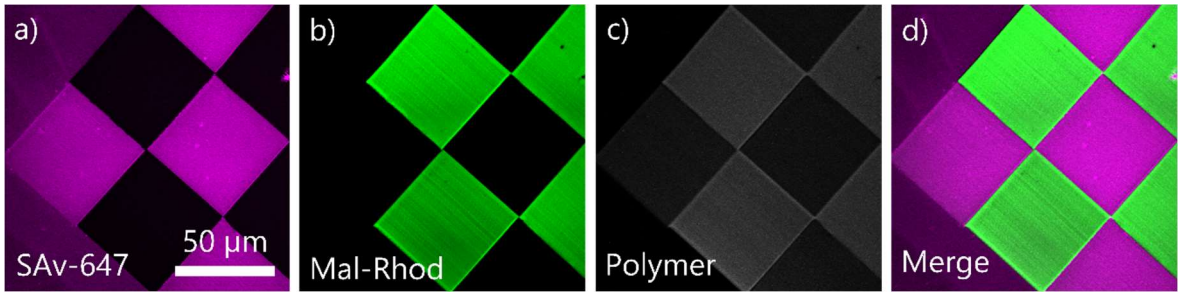

Figure 13: CFM images of a 2D checkerboard written with the PE and PS-resist and irradiated in the presence of Mal-Rhod **13** and Biotin-SH **14**. The sample was subsequently incubated with SAv647 and rinsed to stain the attached Biotin-SH **14**. a) Fluorescence of SAv-647 connected to the PS-resist; b) Fluorescence of Mal-Rhod **13** covalently attached to the PE-resist; c) Autofluorescence of the polymer structures arising from the employed photoinitiator (Irgacure® 369); d) Merge image of the fluorescence channels depicted in a) and b).

and a merge image of the simultaneous dual functionalized 2D checkerboards are depicted in **Figure 13**. In the single channel fluorescence images shown in Figure 13a) and 13b) no cross functionalization between the respective PE and PS-resist areas can be detected as the complementary squares appear completely dark in the respective fluorescence channel. Figure 13c) depicts the autofluorescence arising from Irgacure® 369, the employed photoinitiator. The merge image (Figure 13d)), similarly to the colored overlay pictures from

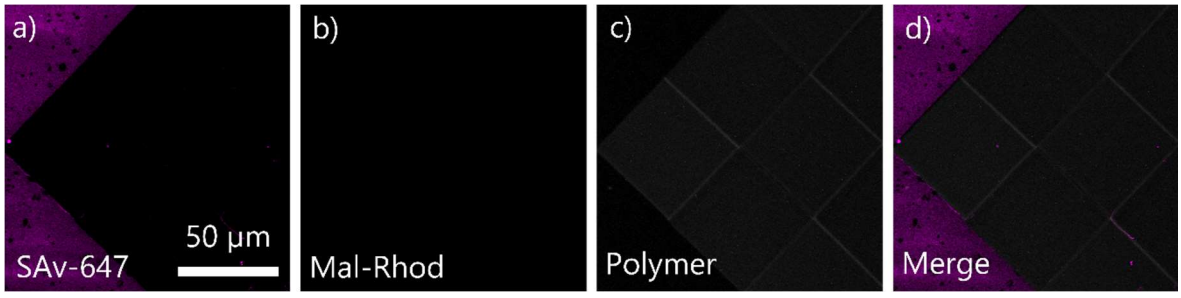

Figure 14: CFM images of a control sample written with both functional photoresists and treated in the same way as the sample shown in Figure 13, without employing the UV light during the post-modification. The same channels as in Figure 13 are depicted.

the ToF-SIMS analysis, indicates clearly the successful simultaneous dual post functionalization of the two photoresists. Comparison with a control sample, where no UV light was employed during the post-modification (see **Figure 14**) evidences the suggested reaction pathway. No unspecific attachment of the fluorescent dye or protein is observed on the written structures, however, in the channels depicting the fluorescence of SAv-647 (Figure 14a) and 14d)), the adsorption of the fluorescent protein to the non-passivated glass carrier is evidenced. No unspecific attachment of the fluorescent dye or protein is observed on the written structures, however, in the channels depicting the fluorescence of SAv-647 (Figure 14a) and 14d)), the adsorption of the fluorescent protein to the non-passivated glass carrier is evidenced. This underlines the passivating nature of the formed microstructures. Consequently, the dual functionalization of 3D structures with the fluorescent markers was carried out. The results are depicted in **Figure 15**; the same three fluorescence channels are shown again. **Figure 15**a) illustrates the purple channel corresponding to the fluorescence of SAv-647, Figure 15b) depicts the green channel, corresponding to the fluorescence of Mal-Rhod **13** and the channel represented in Figure 15c) corresponds to the autofluorescence of the photoresists. On the last image (Figure 15d)), a merge image of the previous described channels is shown. For a clearer impression of the three dimensionality of the obtained dual modified microstructures, a 3D reconstruction of the confocal image stacks was created (**Figure 16**).

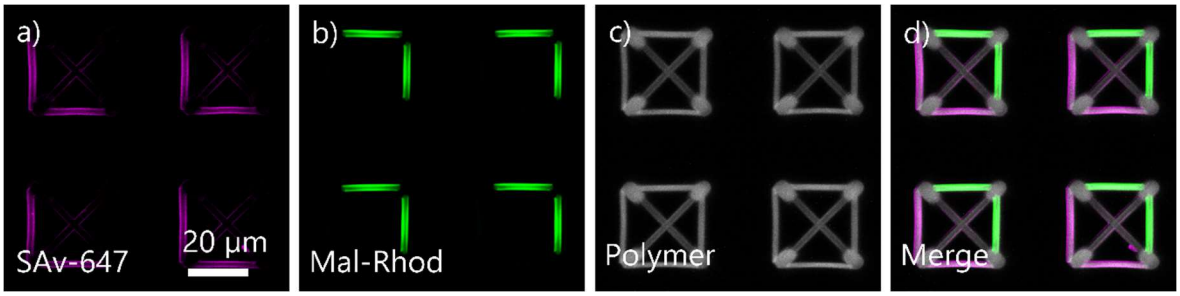

Figure 15: CFM images of 3D boxing rings written with the PE and PS-resist and irradiated in the presence of Mal-Rhod **13** and Biotin-SH **14**. The sample was subsequently incubated with SAv647 and rinsed to stain the attached Biotin-SH **14**. a) Fluorescence of SAv-647 connected to the PS-resist; b) Fluorescence of Mal-Rhod covalently attached to the PE-resist; c) Autofluorescence of the polymer structures arising from the employed photoinitiator (Irgacure® 369); d) Merge image of the fluorescence channels depicted in a) and b).

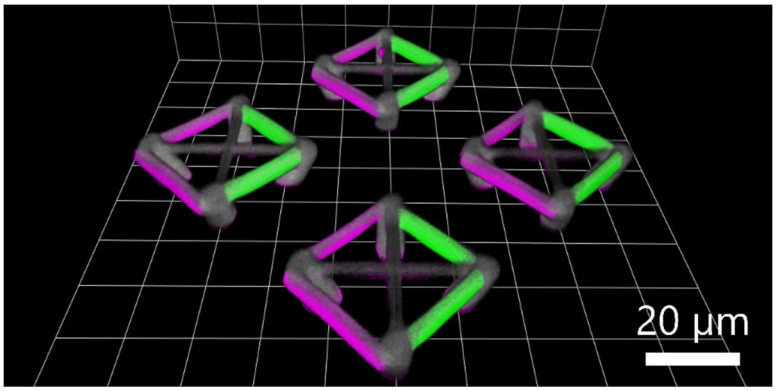

Figure 16: Confocal image stack of the obtained fluorescent dual functional 3D boxing ring structures after a one pot light-triggered post-modification procedure.

These results indicate that an application of the dual modified microscaffolds can be fabricated in a reliable, reproductive and mild fashion. These features seem to be well suited for an utilization in targeted cell attachment due to their protein repellent nature.

3.3 Application of dual functionalized 3D microscaffold for targeted cell attachment

After the successful fabrication and characterization of DLW written 3D microscaffolds employing the newly designed photoreactive monomers described in the previous chapters, the established protocols were employed to attach various proteins to the structures to obtain cell adhesive scaffolds and guide cells onto the structures.[82]†

In a first step, samples were prepared as depicted in **Scheme 36**. A boxing ring scaffold was fabricated, again utilizing three consecutive DLW steps. First, the supporting structure was constructed employing the basic resist (**Scheme 36**A). Secondly, two upper row beams opposite to each other were fabricated using the PE-resist (Scheme 36B). In a last DLW writing step, a commercially available organic-inorganic hybrid resist (Ormocomp®, details see Materials Section 7.1) was employed to fabricate the last two upper row beams (Scheme 36C). Consequently, light triggered postmodification of the respective employed PE- or PS-network was carried out using either a maleimide labeled biotin (**15**) or biotin-SH (**14**). The boxing ring structures were thereto irradiated under a conventional UV lamp in the presence of **15**/**14** dissolved in DMF (1 mM, see Scheme 36D, here depicted for the PE-network). For the attachment of the first protein (Scheme 36E), the simple feature that all resists are protein repellent, except the organic-inorganic hybrid resist, was exploited. The 3D structures were incubated in a solution of either fibronectin (FN) or laminin (LN) (20 µg mL^{-1} or 50 µg mL^{-1} in phosphate-buffered saline (PBS), respectively) for 30 min at room temperature and subsequently rinsed with PBS. To immobilize the second protein, the microscaffolds (coated with either FN or LN in some areas and with both in others) were incubated in a solution of avidin (10 µg mL^{-1} in PBS for 30 min), then subsequently in a solution of biotinylated vitronectin (VN) (20 µg mL^{-1} in PBS for 30 min). Each incubating step was followed by a washing step with PBS (see Scheme 36F).

† Parts from chapter 3.3 are reproduced or adapted from Richter, B., Hahn, V., Bertels, S., Claus, T. K., Wegener, M., Delaittre, G., Barner-Kowollik, C. and Bastmeyer, M. **2016**, *Adv. Mater.* doi: 10.1002/adma.201604342. with permission from John Wiley and Sons. B. Richter and V. Hahn carried out the microstructure fabrication, B. Richter provided the fluorescent staining and imaging, S. Bartels the cell experiments. T. Claus provided the photoreactive resists and contributed to the scientific discussions. M. Wegener, G. Delaittre, C. Barner-Kowollik and M. Bastmeyer contributed to the scientific discussions and supervised the project.

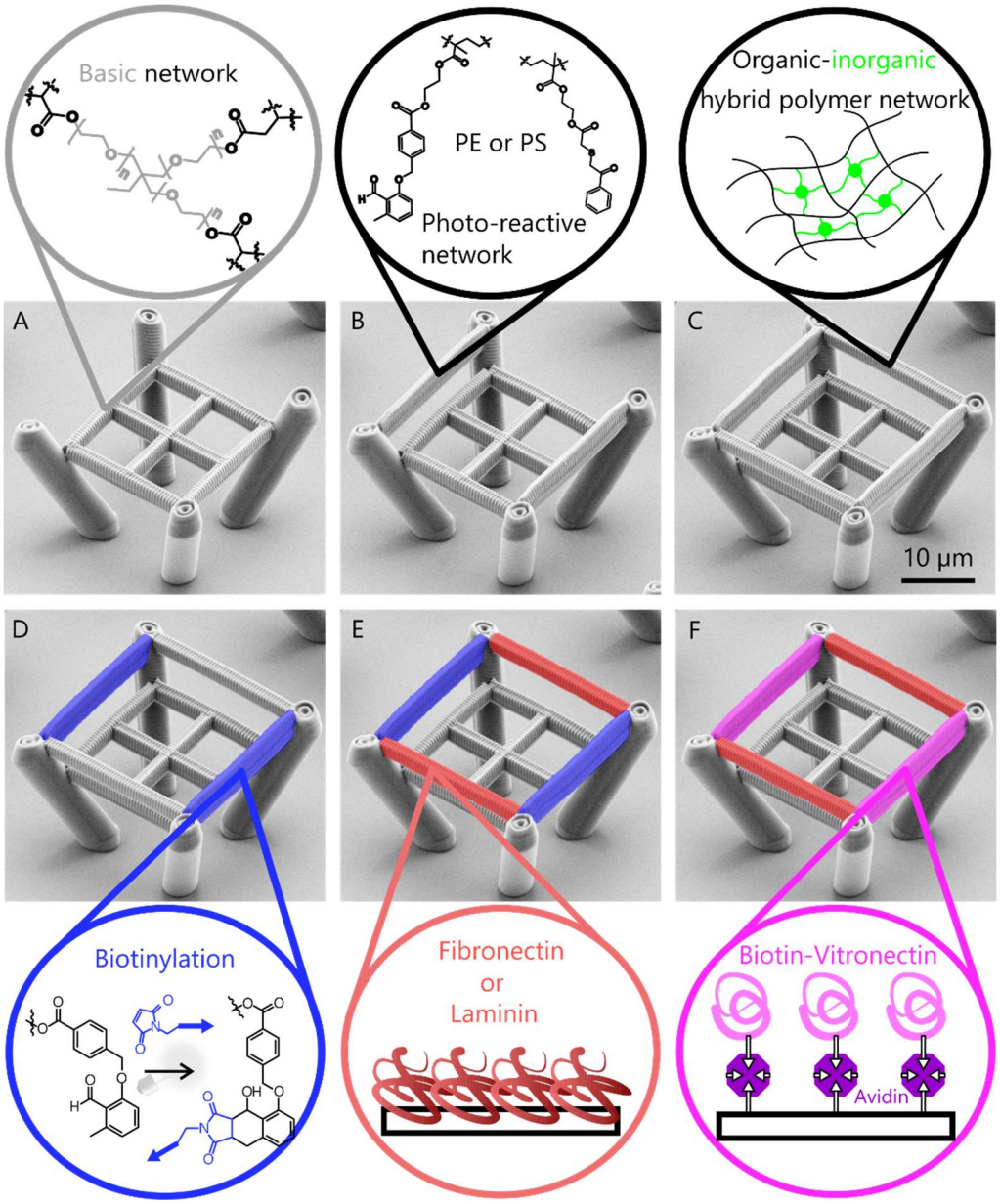

Scheme 36: Sample preparation and applied modification strategy shown on pseudo-colorized SEM images. A) Basis of the scaffold was written with the basic resist; B) Fabrication of two of the upper row beams with PE or PS-resist to obtain photoreactive structures; C) Third DLW step with the commercial Ormocomp® resist to obtain a non-passivating network; D) Light-triggered post-modification step of the PE or PS network with a maleimide functionalized biotin derivative.; E) Coating of the non-passivating areas of the structures by incubating the microscaffolds with either fibronectin or laminin; F) Coating of the afore biotinylated areas of the microstructures by incubating them first with avidin and subsequently with vitronectin. The Scheme was adopted from Ref.[82] with permission of John Wiley and Sons © 2016.

Please note that in this chapter only always one of the functional photoresists was employed in the fabricated structures, in contrast to the previous chapter. Before the 3D structures were fabricated, a similar strategy was applied to obtain 2D checkerboard structures and challenge the passivation potential of the basic and different functionalized resists. The CFM results of these cell studies are depicted in **Figure 17**. As a stand-in for the organic-inorganic hybrid network, the glass surface itself was coated with FN and epithelial cells A549 were employed. First, a 2D checkerboard structure was written via DLW onto a glass substrate, incubated with FN (20 µg mL^{-1} in PBS, 30 min) and finally A549 cells were grown onto the

samples in serum-free medium. After 3 h, the cells were fixed and a fluorescent staining was performed: antibody staining against FN (red), actin (green) and cell nuclei (white). As shown in **Figure 17**a), no fluorescence arising from the ECM protein could be detected on the basic resist. Furthermore, the majority of the cells (98.4 ± 0.8 %) are found on the FN functionalized glass surface (the allocation of the nuclei was employed to determine and quantify the cell binding position). In Figure 17b) and 17c) biotin functionalized PE or PS-resists are shown. Their passivating properties were conserved even if biotinylated. Only 3.7 ± 1.1 % of the cells bound to the functionalized PE-resist and only 2.2 ± 1.7 % were located on the modified PS-resist. However, when the biotinylated resists were further functionalized with biotinylated VN (Bt-VN, via an avidin binding bridge), they acquire cell attractive features. In Figure 17d) and 17e) about half of the cells are located on the glass and half of the cells are bound to the functionalized PE or PS-resist. The cells therefore do not exhibit preferences for any of the domains anymore. This clearly evidences that the amount of surface bound biotin with coupled protein is sufficient to overcome the passivating properties of the functional resists. Consequently, 3D structures were fabricated with DLW according to Scheme 36 employing either the PE or the PS resist. In comparison to the boxing ring structures fabricated for ToF-SIMS analysis, the cross beams in the upper row were omitted to create a niche for the cell to fit in. After fabrication, the boxing ring scaffolds were functionalized in the depicted sequence. When the combination of FN and VN is utilized, the order of attachment is crucial: FN should be attached first, followed by VN to the biotinylated photoreactive resists. A reversed order led to only FN

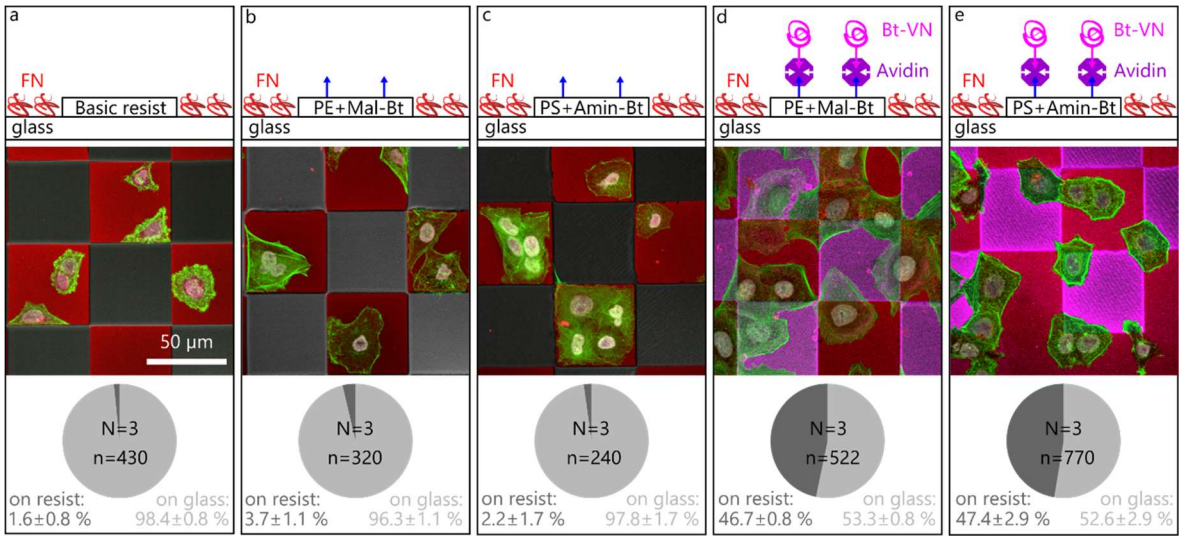

Figure 17: CFM results (merge images) for the epithelial cell (A549) and protein binding study of the variuos employed resist. A549 cells: green (actin) and white (nuclei), FN: red, VN: magenta; a) 2D checkerboard pattern of the basic resist on a glass substrate, b) and c) 2D checkerboard pattern of PE-resist and PS-resist, respectively, on a glass substrate and post-modified with biotin (employing a Mal-Bt for PE functionalization and Amine-Bt for PS functionalization). Both resists preserve their passivating properties; d) and e) after incubating with avidin and biotinylated VN (Bt-VN) a distinct pattern of the two attached proteins (FN on glass, VN on the respective functional resist) can be seen. By functionalizing the PE or PS-resist with a VN protein, it acquires cell attractive features. The cell binding was quantified by the position of the cell nuclei; N=number of independent experiments; n=number of counted cells per experiment. The Figure was reprinted from Ref.[82] with permission from John Wiley and Sons © 2016.

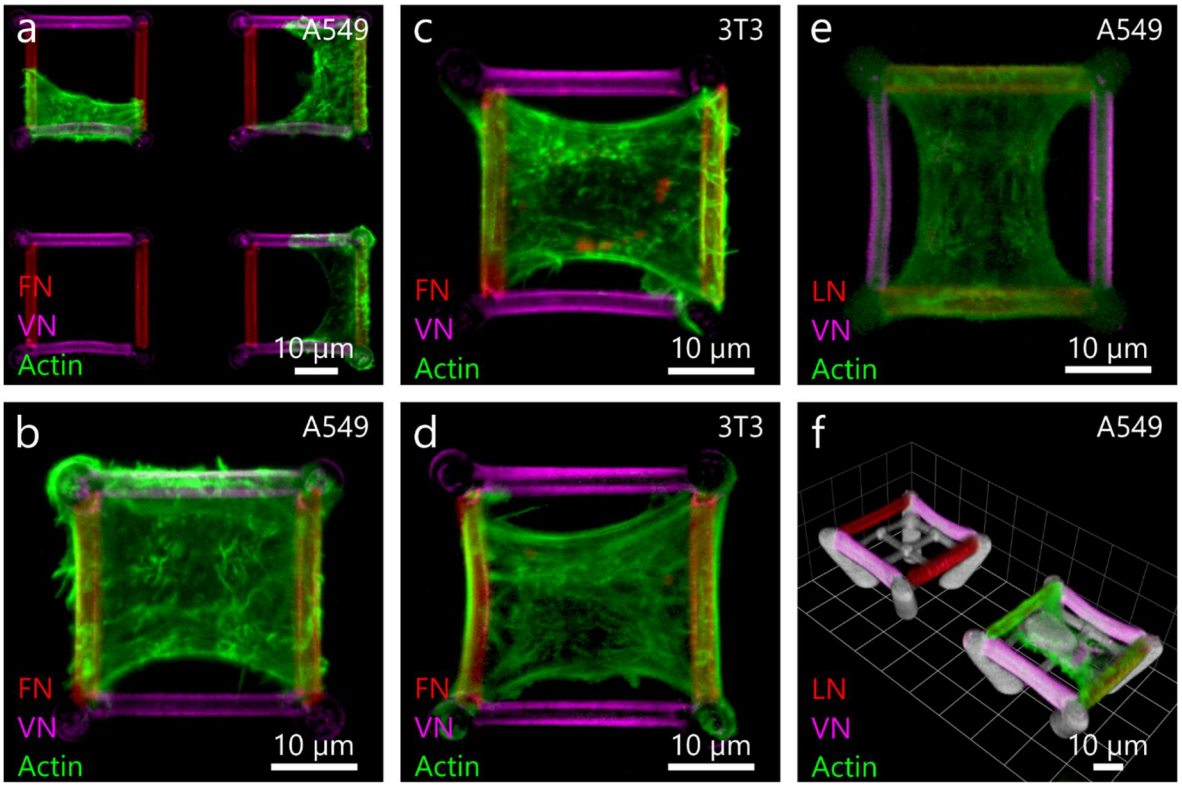

Figure 18: CFM results for cell studies employing 3D boxing ring structures for targeted cell attachment. Fluorescent merge images of the following channels are depicted: red (FN/LN), magenta (VN) and green (actin). a) and b) Overview and zoom in of A549 cells grown on FN and VN functionalized scaffolds employing either the PS-resist (a) or the PE-resist (b) as functional resist. The cells adhere equally to both surface-expressed proteins (compare to Figure 17 e). c) and d) When culturing 3T3 cells instead of A549 cells on the FN/VN modified scaffolds (PS-resist or PE-resist, respectively), they clearly prefer adhesion to the FN over the VN coated beams. e) Boxing ring structure coated with LN/VN instead of FN/VN. Cultured A549 cells prefer now the LN coated beams versus VN functionalized ones. f) 3D stack of confocal images depicting the full height of LN/VN coated scaffolds (basic network and cell nuclei in white) prove again that A549 cells only adhere to the LN coated beams. The Figure was reprinted from Ref.[82] with permission from John Wiley and Sons © 2016.

functionalization, most likely due to a weak binding of VN to the hydrophobic organic-inorganic hybrid network. Probably for the same reason, in the case of LN, a relatively high concentration in comparison to the other used proteins (50 µg mL^{-1} instead of 20 µg mL^{-1}) was required to obtain a distinct functionalization, most likely for the same reason.

The results of cell attachment experiments culturing either epithelial A549 or fibroblast NHT 3T3 cells on scaffolds functionalized with different protein combinations, are depicted in **Figure 18**. Again, Confocal Fluorescence Microscopy was utilized to analyze the obtained samples with AlexaFluor647 labeled FN/LN ($\lambda_{excitation}$ = 633 nm; $\lambda_{detection}$ > 650 nm, red), Cy3 labeled VN ($\lambda_{excitation}$ = 561 nm; $\lambda_{detection}$ = 575–615 nm, magenta), AlexaFluor488 labeled actin ($\lambda_{excitation}$ = 488 nm; $\lambda_{detection}$ = 505–550 nm, green), a white channel corresponding to a DAPI staining of the cell nuclei ($\lambda_{excitation}$ = 405 nm; $\lambda_{detection}$ = 420–480 nm) and the autofluorescence of the polymer structures. Firstly, the experiments conducted in 2D (Figure 17d) and 17e)) were reproduced on 3D scaffolds. A549 cells were cultured on structures written either with the PE- or PS-resist, employing FN and VN as surface expressed proteins. As on the 2D checkerboards, the cells adhered equally to the FN and VN coated upper row

beams of the 3D microstructures (Figure 18a) and 18b)). Consequently, fibroblast cells (3T3) were applied to the same kind of functionalized microscaffolds (Figure 18c) and 18d)). These 3T3 cells express another set of integrin receptors compared to A549 cells:[203] they prefer to adhere to FN presented at the surface. Therefore, here they attach to the two opposite upper row beams of the structures. As in the images shown above, no apparent difference is observable when applying either the PS- (Figure 18c)) or the PE-resist (Figure 18d)) as secondary functional resist for the biotin modification. Finally, the ability of the 3D scaffolds to direct cell attachment was further explored. The protein functionalization of the scaffolds was changed to LN/VN and epithelial A549 cells were used. The latter prefer LN over VN as it is the main component of their natural environment. As shown in Figure 18e) the cultured cells specifically adhered only to the beams functionalized with LN, as expected. In Figure 18f), a 3D reconstruction of CFM stack images underlines how the cell exclusively adhered to the LN coated areas and also only spanned across the upper level of the structures, not interfering with the underlying basic resist, possessing passivating features.

To conclude this chapter, the synthesis of two novel photoreactive monomers were introduced and successfully employed in DLW writing processes. The photoreactivity on the surface of the networks was investigated employing ToF-SIMS and CFM characterizations. A simultaneous, one pot dual functionalization protocol was successfully established. Proceeding, various proteins were immobilized on DLW written structures in a spatially resolved fashion. The so coated structures were successfully utilized in cell culturing experiments, analyzed by CFM. It can be unambiguously derived that with the presented method of DLW writing, employing new photoreactive resists in combination with a commercially available cell repellent one and light-triggered post-modification, cell directing 3D scaffolds can easily be fabricated. By selectively coating parts of the microstructures with different proteins, cell type specific binding behavior and targeted cell attachment was achieved in a very sophisticated manner. The herein presented method could prove to be a useful tool for further cell culturing and cell guiding studies employing e.g. stem cells. Their ability to differentiate under well controlled three dimensional conditions could be studied in detail for a better understanding of the overall process.

3.4 Excursion: Investigation of DLW structures via ATR-FT-IR Microscopy

After the successful fabrication of dual photoreactive cell guiding microscaffolds was demonstrated in the aforementioned sections, the application of a new surface characterization method for DLW written scaffolds was investigated.[‡]

ATR-FT-IR microscopy proves to be a versatile surface characterization tool, as it allows a destruction free and spatially resolved analysis of chemical moieties on surfaces at ambient conditions.[204] With an IR microscope coupled to a focal plane array (FPA) detector chemical images of a surface area of 32 μm^2 with a theoretical pixel resolution of 0.25 μm^2 can be recorded. However, due to diffraction limitations, the lateral resolution is limited to about 1 μm^2 at 1000 cm^{-1}. The evanescent IR wave generated from the ATR crystal penetrates the substrate depending on the incident angle and the wavelength. For the instrument and wavelength range employed in the present thesis, a penetration depth of ~10 µm is expected. Hence, the investigated structures need to exhibit a sufficient height.

In the presented approach for surface analysis of DLW structures via IR microscopy, 10 µm thick checkerboard structures, analog to the structures depicted in Figure 6c and 7d were employed. Initially, structures with half of the squares consisting of the basic resist and the other half consisting of a photoreactive resist (PS-resist or PE-resist respectively) were investigated. Ultimately, a checkerboard structure consisting of both functional resists should be investigated.

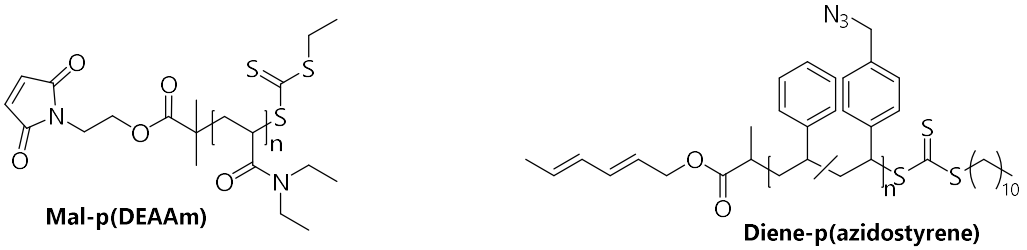

Scheme 37: Functional polymers selected for an IR sensitive surface functionalization of the PE-resist (**Mal-p(DEAAM)**) or the PS-resist (**Diene-p(azidostyrene)**).

For an IR detectable surface coating, two functional polymer strands were selected (see **Scheme 37**). As the resists themselves already contain moieties exhibiting characteristic IR signals (e.g., carbonyl bonds), the polymers employed for surface attachment needed to bear functionalities possessing different characteristic IR signals. For the light induced functionalization of the PE-resist, a maleimide end capped poly (*N,N*-diethyl acrylamide) **Mal-p(DEAAm)**, M_n = 10600 g mol^{-1}, $Đ$ = 1.17), synthesized via a RAFT process, was utilized.

[‡] The results obtained in the current section were achieved in cooperation with Christian Schmitt (KIT) in the context of his Bachelor thesis.

The amide moieties exhibit a distinct IR band at around 1650 cm^{-1} compared to ester or aldehyde bonds with bands at 1700-1750 cm^{-1}. For the functionalization of the PS-resist, an open chain diene modified poly(styrene-*co*-azidomethylstyrene) (**Diene-p(azidostyrene)**, M_n = 4800 g mol^{-1}, $Đ$ = 1.11) with a monomer ratio of styrene/azidomethylstyrene of 5 was synthesized (for more details regarding the synthesis of both polymers, refer to Section 7.3.1). The azide moiety shows a characteristic IR signal between 2100 – 2200 cm^{-1} that can be clearly distinct from other signals. The light triggered postmodifications of the DLW written checkerboard structures were conducted as described in the previous sections. A droplet of a solution of the respective polymer (**Mal-p(DEAAm)** or **Diene-p(azidostyrene)**, 10 mg mL^{-1} in DMAc) was placed onto the structures and the samples were irradiated with UV light for 30 min. After rinsing with several solvents and drying in a stream of nitrogen, the structures were subjected to IR microscopy measurements. To visualize the dimensions and surface functionalizations of the DLW written structure, different integration methods were employed. By integrating over the carbonyl signal (1700-1750 cm^{-1}) all resists are visualized on the corresponding heat map, as the network former TPE-TA, utilized for all resists, contains ester moieties. **Mal-p(DEAAm)**, grafted onto the PE-resist, was visualized by an integration over the amide signal (1630-1670 cm^{-1}). For the detection of a postmodification of the PS-resist, an integration over the azide signal (2100-2200 cm^{-1}) was carried out, deriving heat maps illustrating the azide distribution on the surface. Initially, "half filled", 10 µm thick checkerboard structures, consisting of basic resist squares and unfilled squares were investigated to gain a first impression of the sample and to probe for the suitability of the penetration depth. An integration over the carbonyl signal as described above, generating the heat map, is illustrated in **Figure 19**. A checkerboard pattern of the carbonyl signal intensity is clearly evidenced, with blue 'holes' in between, where no resist exists. However, the squares themselves are not detected with sharp contours as they are pressed down and deformed upon the contact with the ATR crystal. Consequently, a checkerboard structure consisting of basic resist squares and **Mal-p(DEAAm)** functionalized PE-resist squares adjacent to each other was investigated with the IRM. The

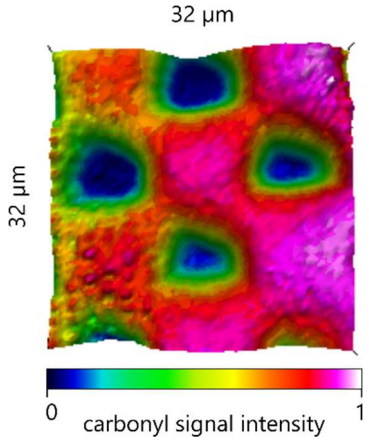

Figure 19: IRM heat map obtained for an integration of the carbonyl signal of a 'half filled' checkerboard structure consisting of the basic resist.

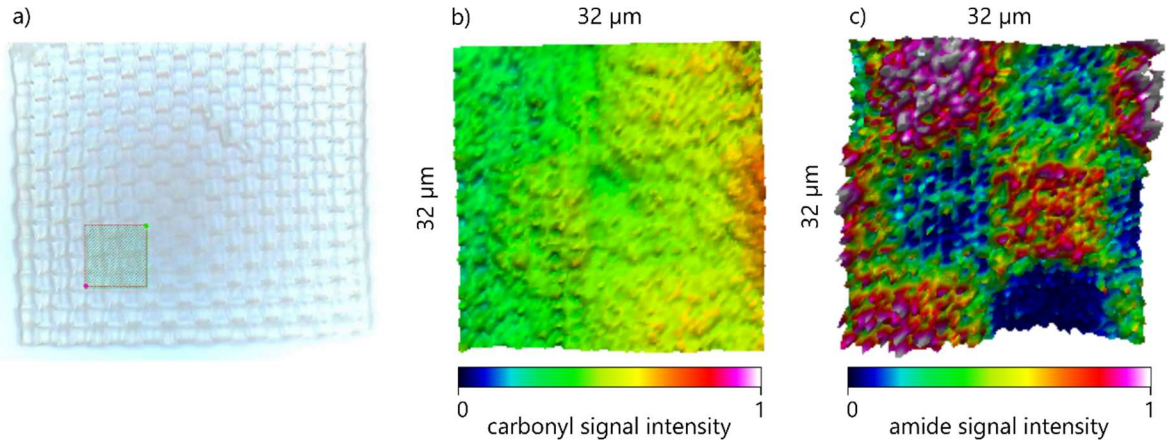

Figure 20: a) Light microscopy image of the analyzed DLW checkerboard consisting of the basic and the PE resists. The measured area is marked with a frame; b) IRM heat map obtained via integration of the carbonyl signal of the respective analysis; c) IRM heat map obtained via integration of the amide signal of the sample.

derived IR spectra were integrated over the carbonyl signal and the amide signal. The resulting IRM heat maps and a light microscopy image of the sample are shown in **Figure 20**. For the carbonyl derived heat map, a homogeneous distribution is illustrated in Figure 20b), as both resists exhibit carbonyl groups. However, the basic resist squares exhibit a slightly enhanced signal intensity, which was attributed to slight topographical variations. The identity of the squares was assigned by examining the distribution of the amide signal on the sample (Figure 20c). Only the squares consisting of PE-resist are functionalized with **Mal-p(DEAAm)**, therefore the amide derived signal can only be detected on these squares. When comparing the obtained pattern with the one depicted in Figure 19, sharper contours are achieved. This may be attributed to squares supporting each other against the pressure exerted by the ATR crystal.

For the checkerboard sample consisting of the basic resist and the PS-resist, postmodified with the **Diene-p(azidostyrene)**, no azide signal could be detected. This could either be caused by a degradation of the azide moiety upon irradiation with UV light during the postmodification, or an insufficient concentration of azide moieties on the surface. Compared to the **Mal-p(DEEAm)**, in the **Diene-p(azidostyrene)** only a fifth of the monomer units bear the IR marker. Additionally, the polymer itself only has a DP_n of approx. 50, compared to an DP_n of approx. 100 for the amide bearing polymer. However, due to time considerations, no further attempts were undertaken to resolve the issue.

To investigate a more 3D like structure, well plate structures with a diameter of 30 µm and a depth of 10 µm were formed from the basic resist and a wall consisting of the PE-resist was added across the wells. The sample was subsequently functionalized with **Mal-p(DEAAm)** under UV light as described above and analyzed under the IR microscope. The resulting heat maps of integrations over the carbonyl signal and the amide signal as well as a light microscopy image of the sample are illustrated in **Figure 21**. Two spots on the sample (i.e., two separate wells) were investigated. The results are depicted in the upper part and the lower part of Figure 21, respectively. The integration over the carbonyl signal for both samples is illustrated in the middle column (Figure 21b). The right column shows the

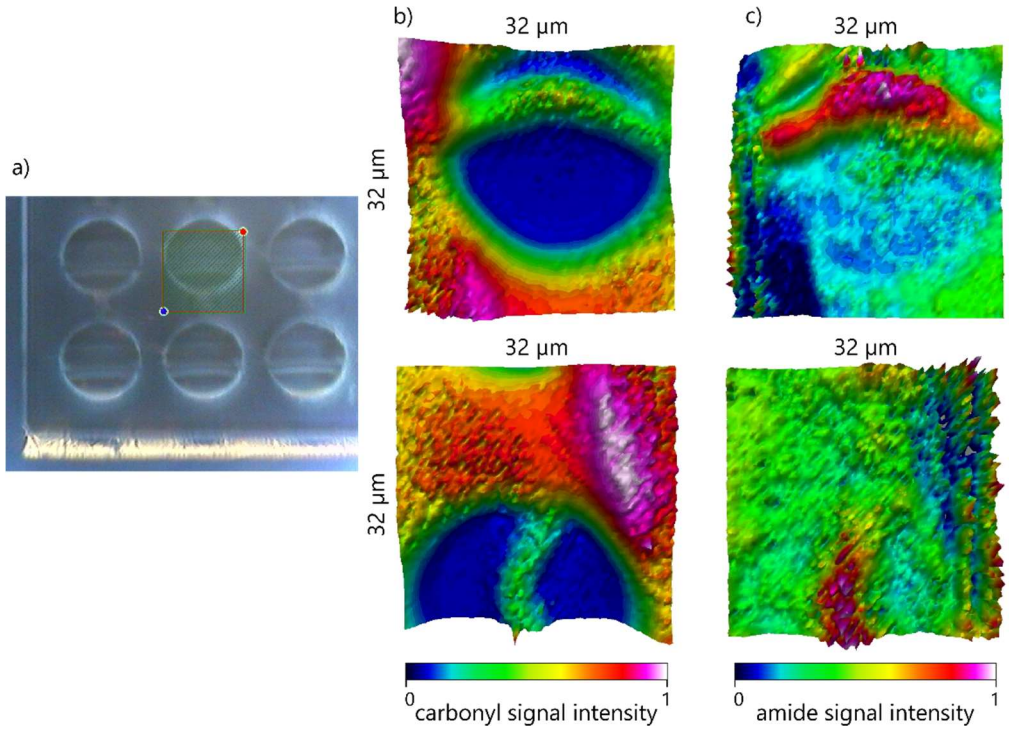

Figure 21: a) Light microscopy image of the analyzed well plate structure consisting of the basic resist and the walls consisting of the PE resist. The measured area of the heat maps in the upper part is marked with a frame; b) IRM heat maps obtained for two independent measurements on one well plate with an integration of the carbonyl signal; c) IRM heat maps obtained for two independent measurements on one well plate with integration over the amide signal. The heat maps depicted on top and the heat maps on the bottom, respectively, belong together.

integration over the amide signal (Figure 21c)). In the images derived from the integration of the carbonyl signal, the well consisting of the basic resist as well as the wall, made of the functional PE-resist, are clearly visible. Due to the pressure from the ATR crystal and its rubbery consistency, the wall is slightly deformed in both measurements. The heat maps for the amide signal both indicate a successful functionalization of the PE-resist wall with the **Mal-p(DEAAm)**, as the corresponding signal is detected only there.

This short excursion demonstrates how ATR-FT-IR microscopy can be utilized to characterize DLW written scaffolds. The surface constitution of 2D checkerboards as well as 3D like well structures was successfully imaged employing the described method.

4

VISIBLE LIGHT TRIGGERED ANTHRACENE CHEMISTRY

A critical consideration to take into account when applying photochemistry in biological systems is the wavelength regime. It has long been known that UV light can cause severe damage to cells,[205] proteins,[206] and small molecules.[207] The development of mild photochemical methods employing functional groups, which can be activated by irradiation in the visible light range (≥ 400 nm) is therefore required. Most of the nowadays widely employed reactions triggered in this wavelength regime rely on the utilization of a photo(redox)catalyst.[14, 22] In recent years however, red shifted photochemistries, conducted above 400 nm without the use of catalysts have been introduced.[23-24] In all cases the photoinduced formation of a 1,3-dipole ultimately reacting in a cycloaddition was red shifted by taking advantage of an extended π-system (pyrene). In this chapter, an alternative approach expanding the π-system of anthracene is introduced. Hereto, an electron rich, conjugated triazole ring tethered to the 9-position of anthracene is employed. The photoinduced anthracene [4+4] cycloaddition brings along one crucial advantage compared to a 1,3-dipolar cycloaddition: reversibility.[101] The reversibility of the [4+4] anthracene dimerization is widely exploited in polymer and surface chemistry (e.g., block copolymer formation and fission,[111] supramolecular assembly and disassembly,[104] or surface writing and erasing[104]). However, when conducting a typical anthracene dimerization, relatively harsh UVA irradiation or elevated temperatures are needed.[112] Via the implementation of a red shift to the cycloaddition reaction, the reverse cycloelimination

reaction is shifted to longer wavelengths (above 350 nm) too, allowing for a possible application of the reaction to write and erase within biological systems. Therefore, the synthesis and surface reactivity of a visible light activatable triazyloylanthracene silane derivative was investigated in the following chapter.[§]

4.1 Synthesis of a red shifted anthracene for surface tethering

To achieve a red shifted anthracene derivative that can be anchored to surfaces the red shifting moiety and a surface anchor have to be introduced. As surface anchor, a triethoxysilane group and as red shifting moiety a triazole ring were chosen. Starting from 9-bromoanthracene (**9-BA**), the triazole ring was introduced in a three-step synthetic process via a Sonogashira cross coupling, deprotection, and subsequent copper catalyzed azide-alkyne cycloaddition (CuAAC) (**Scheme 38**).

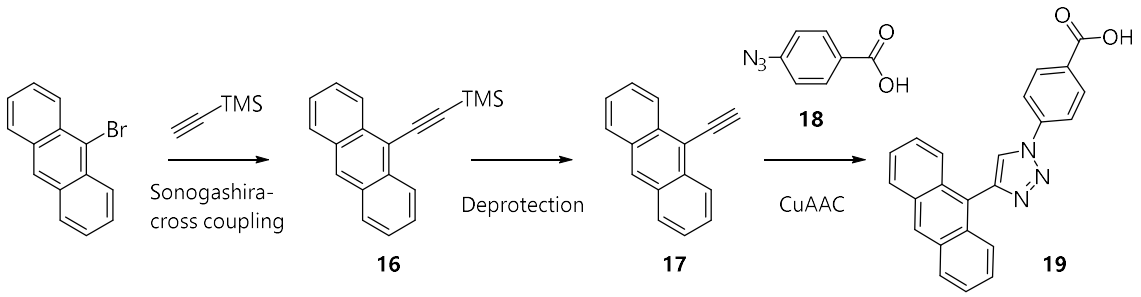

Scheme 38: Synthetic steps to obtain a triazyloyl functionalized anthracene (**19**). First step is a SONOGASHIRA cross coupling reaction employing 9-BA and ethynyltrimethylsilane to obtain a TMS-protected alkynyl anthracene (**16**). The latter is deprotected to obtain the free alkynyl anthracene derivative (**17**), which is subsequently converted to the triazolyl anthracene acid (**19**) via CuAAC with 4-azido benzoic acid (**18**).

4-Azido benzoic acid (**18**) was selected as azide derivative for the triazole formation allowing for further esterification or amidation functionalizations, ultimately leading to the introduction of the silane moiety. The incorporation of the additional benzene ring further expands the π-system. For the SONOGASHIRA cross coupling a standard procedure was utilized employing $Pd(PPh_3)_2Cl_2$ as catalyst, CuI, piperidine, and TEA at 110 °C overnight. For the deprotection of the alkyne bond a well established protocol using K_2CO_3 in THF/MeOH at ambient temperature was employed. The standard CuAAC protocol had to be modified increasing the amount of Cu catalyst due to the carboxyl group, which causes catalyst deactivation by coordinating the copper. As a consequence, 1.5 eq of CuBr had to be

[§] Parts from the current chapter are reproduced or adapted from T. K. Claus, S. Telitel, A. Welle, M. Bastmeyer, A. P. Vogt, G. Delaittre, C. Barner-Kowollik, Chem. Commun., **2017**, *53*, 1599-1602 by permission of The Royal Society of Chemistry. S. Telitel provided the anthracene functionalized polymers. A. Welle provided the ToF-SIMS analysis. XPS data was provided by Vanessa Troulliet. A. Vogt, M. Bastmeyer, G. Delaittre and C. Barner-Kowollik contributed to the scientific discussions and supervised the project.

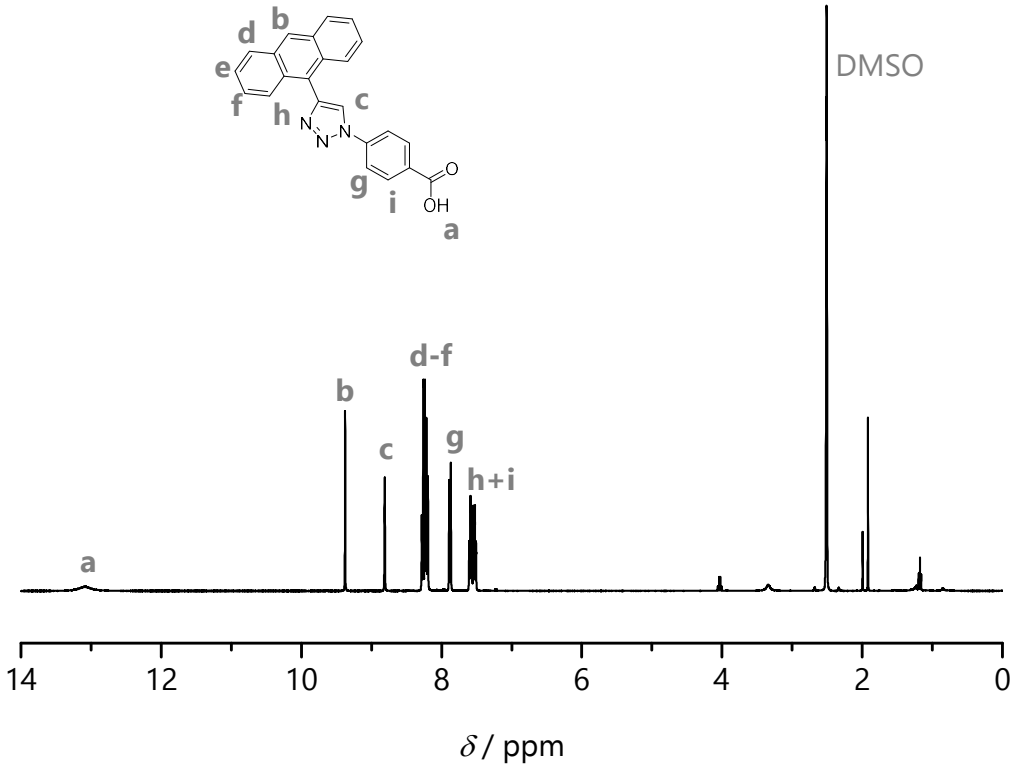

Figure 22: ^{1}H NMR spectrum (400 MHz, DMSO-d_6, ambient temperature) of 4-(4-(anthracen-9-yl)-1*H*-1,2,3-triazol-1-yl)benzoic acid, (triazolyl anthracene acid **19**).

employed. With this adjustment, the triazolyl anthracene acid (**19**) could be successfully synthesized in 67 % overall yield. The ^{1}H NMR spectrum of purified **19** is depicted in **Figure 22**. The red shifting ability of the triazole ring was confirmed by UV-vis spectroscopy. The corresponding spectrum (0.5 mg mL^{-1} in MeCN) is shown in **Figure 23**, clearly indicating

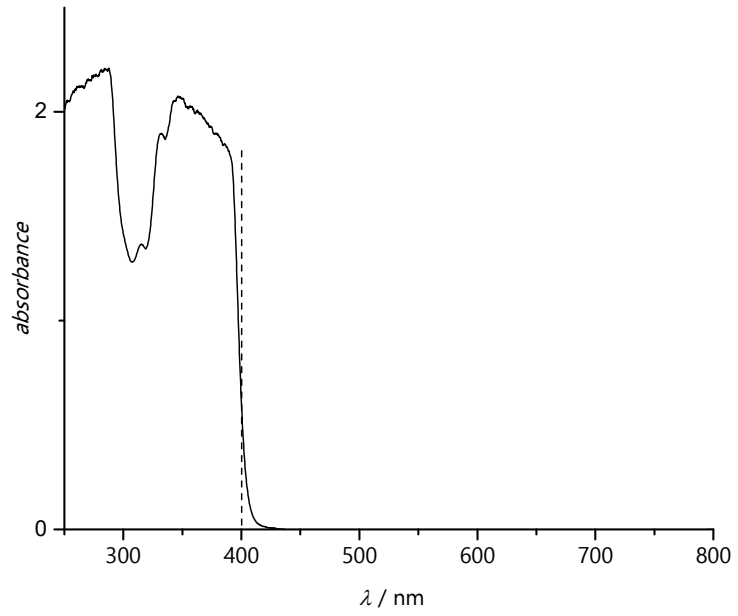

Figure 23: UV-vis absorption spectrum of triazolyl anthracene acid (**19**) (0.5 mg mL^{-1} in acetonitrile, l = 0.5 cm, a.t.). Absorption above 400 nm is clearly indicated by the dotted line.

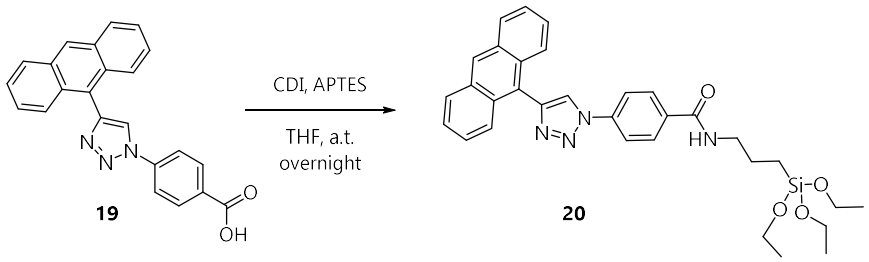

Scheme 39: Synthetic conditions employed to obtain triazolyl anthracene silane **20**.

absorption above 400 nm. Finally, a triethoxysilane moiety, acting as surface anchoring group, was attached by amidation of the carboxyl group with APTES (**Scheme 39**). Employing a standard procedure, 1,1'-carbonyldiimidazole (CDI) was utilized as activating agent. The overall isolated yield of the 4 step procedure was 46 %. The ^{1}H NMR spectrum of the pure visible light reactive anthracene **20** is depicted in **Figure 24**.

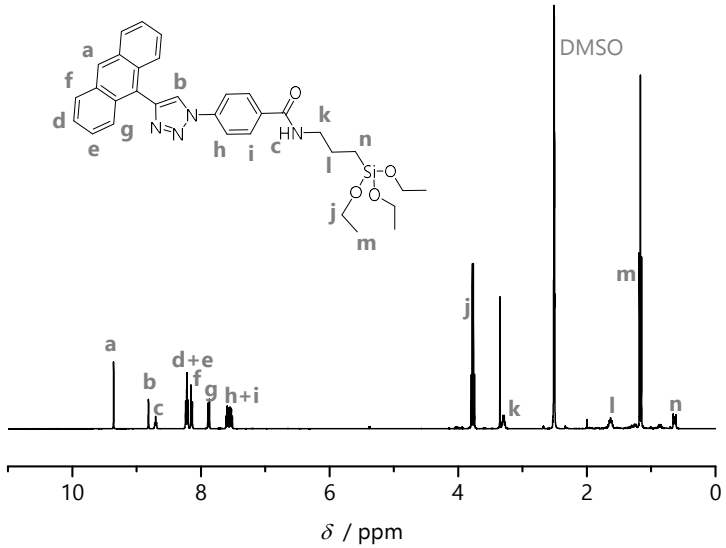

Figure 24: ^{1}H NMR spectrum (400 MHz, DMSO-d_6, ambient temperature) of 4-(4-(anthracen-9-yl)-1*H*-1,2,3-triazol-1-yl)-*N*-(3-(triethoxysilyl)propyl)benzamide (triazolyl anthracene silane **20**).

In the current section, the synthesis of a visible light absorbing anthracene derivative, bearing a triethoxysilane group was established employing an efficient synthetic route. Consequently, the surface anchoring and photoreactivity of the obtained anthracene silane derivative (**20**) was investigated in the following section.

4.2 Photoreactivity of red shifted anthracene on the surface

After the successful synthesis of the red shifted anthracene silane (**20**), its surface anchoring was conducted. Silicon wafers instead of glass slides were chosen as surface substrate as they allow for a faster and more facile characterization via ToF-SIMS and XPS. Silicon wafers were cleaned and activated by treatment with piranha acid (H_2O_2/H_2SO_4 1/2, v/v), rinsed

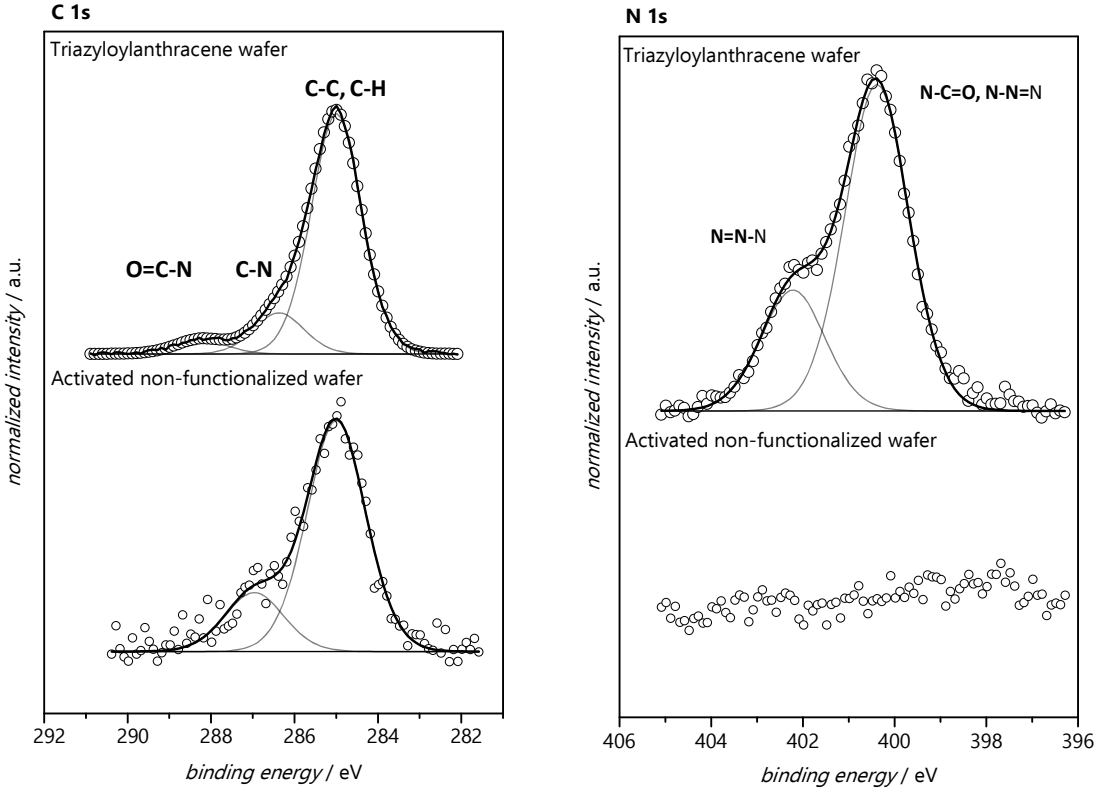

Figure 25: XPS analysis of a silanized wafer treated with anthracene silane (20) versus a cleaned, non-modified wafer. The deconvolutions of C1s and N1s signals are depicted. The C1s signal shows a clear increase of the overall carbonyl content on the wafer (from 2.8 at% to 25.1 at%). Additionally, new peaks arose, corresponding to O=C-N and C-N. Also on the silanized wafer, a N1s signal is detectable that was non-existing on the cleaned non-modified wafer. Moreover, the N1s signal evidences a typical peak pattern for triazole rings.

with MiliQ water and subsequently functionalized by treating with a solution of anthracene silane (**20**) in toluene overnight at 50 °C. Finally, they were rinsed and analyzed by XPS (X-ray photoelectron spectroscopy). As a reference sample, a cleaned, non-modified wafer (treated with piranha acid) was measured. The results of the XPS analysis of a silanized wafer compared with the reference sample are depicted in **Figure 25**.

The most conclusive peaks in this analysis are the C1s and N1s signals and their deconvolution. On the activated, non-modified wafer, only a very low overall carbon content (2.8 at%) and no nitrogen were detectable. After the silanization reaction, the overall detected carbon content increased to 25.1 at% and the N1s signal indicates 3.2 at% of a nitrogen species appearing on the surfaces. The deconvolutions of the respective signals show peaks for *C*-N, O=*C*-N, *N*-C=O/*N*-N=N and N-*N*=N, with the broad N1s signal being characteristic for triazole species.[208] Based on the XPS analysis, it can be clearly stated that the triazolyl anthracene species was tethered to the surface.

4.2.1 Small molecule study

To investigate the photoreactivity, ToF-SIMS was, as in Chapter 3, chosen as method for surface characterization providing very sensitive and spatially resolved analysis of the light-modified surfaces. A schematic representation of the anthracene dimerization reaction on

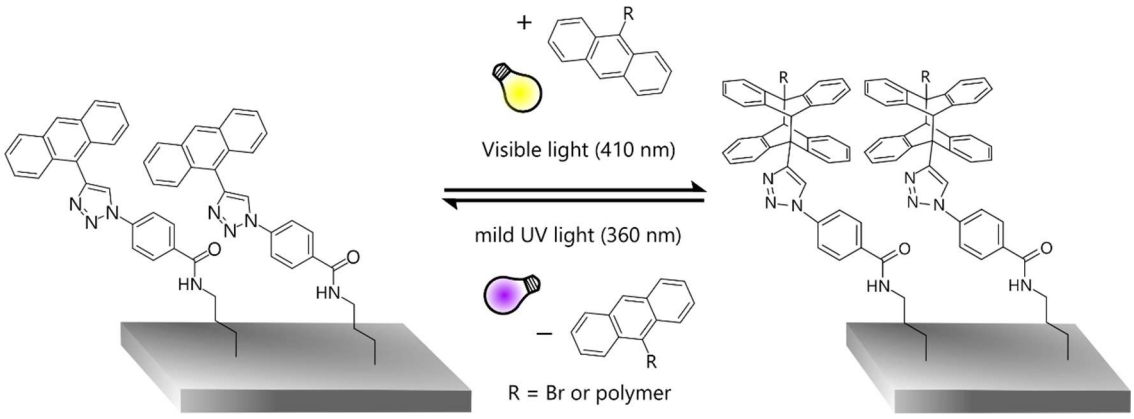

Scheme 40: Schematic representation of the surface tethered visible light reactive anthracene and the conducted dimerization reactions.

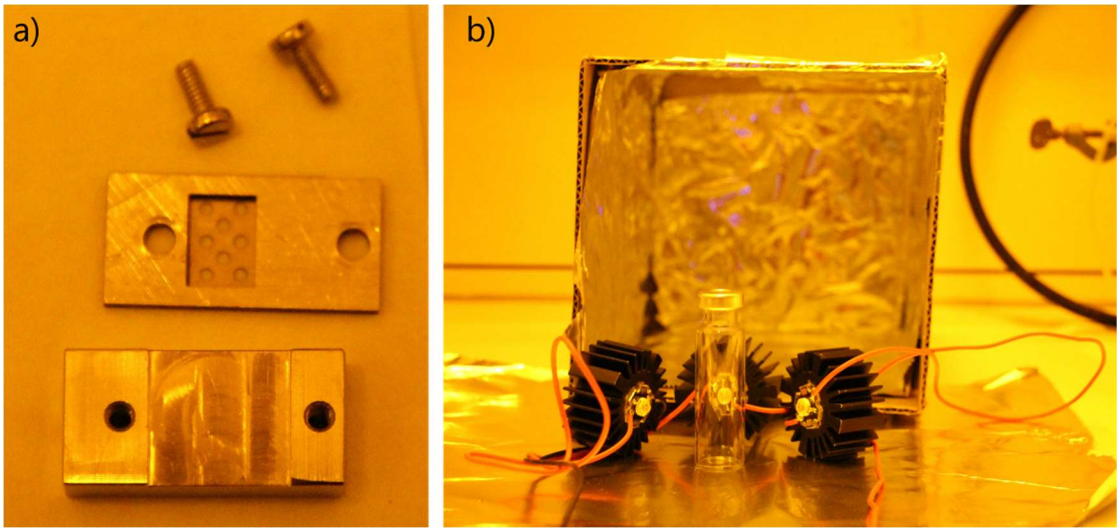

Figure 26: a) Employed sample holder with 1 x 1 cm notch and dotted shadow mask; b) Custom made LED setup consisting of 3 x 3 W LEDs mounted on cooling elements pointing at a headspace vial.

the surface and the employed wavelengths for the cycloaddition/cycloelimination reactions are depicted in **Scheme 40**. First, a small molecule surface reaction, employing a bromine-ated marker molecule – commercially available **9-BA** – was carried out, allowing the facile tracing of the characteristic bromine fragments, as described in Chapter 3.2. For the spatially resolved surface patterning a sample holder suitable for a 1 x 1 cm silicon wafer and a dotted shadow mask were utilized (see **Figure 26**a)) and irradiations were carried out in headspace vials. As light source, emitting solely at 400 nm, three 3 W LEDs, depicted in Figure 26b) were employed. To ensure a defined irradiation at 400 nm and to quantify the spectral irradiation intensity, an emission spectrum of the LED setup was recorded, which is depicted in **Figure 27**. An activated silicon wafer was mounted in a sample holder equipped with the dotted shadow mask and placed in a headspace vial. The vial was sealed and a solution of **9-BA** in DCM (1 mg mL^{-1}) was added. The sample was percolated with a stream of argon gas for5 min and subsequently irradiated at 410 nm for 4 h. The results of a subsequent ToF-SIMS analysis are depicted in **Figure 28**. An unambiguous dotted pattern consisting of bromine isotopic fragments is evident. Both bromine isotopes show an even distribution over the dotted pattern, suggesting a consistent functionalization of the irradiated surface

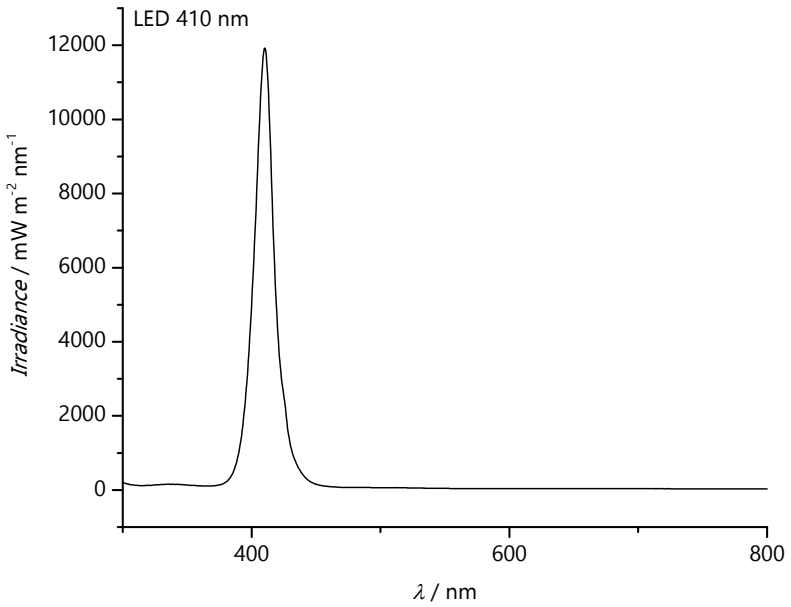

Figure 27: Emission spectrum and intensity of custom built LED setup employed to trigger the visible light anthracene cycloaddition.

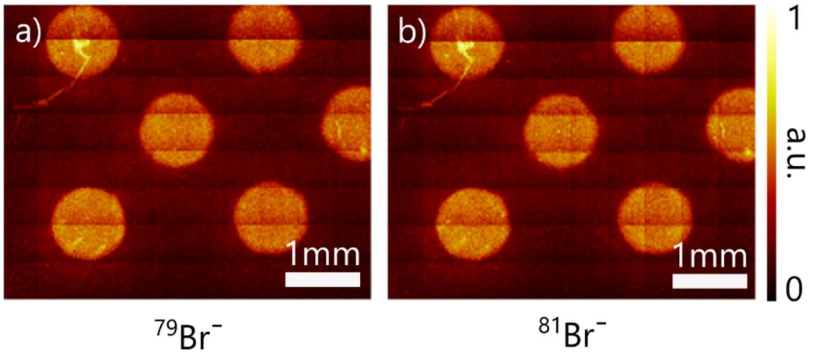

Figure 28: Single fragment ion maps depicting the bromine fragments detected after the first visible light functionalization step; a) Dotted pattern of $^{79}Br^-$ fragments; b) Dotted pattern of $^{81}Br^-$ fragments.

area. To trigger the cycloelimination reaction, a less intense, commercially available UV lamp (Philips PL-L) incorporated in a custom built photoreactor was employed. The corresponding emission spectrum and a photograph of the custom built photoreactor are depicted in **Figure 29**. Due to the significant different irradiation intensity of the UV lamp compared to the LED setup (close to 12000 mW m^{-2} nm^{-1} for the LED setup, and close to 2000 mW m^{-2} nm^{-1} for the UV lamp), the irradiation time for the cycloelimination reaction had to be adjusted. For erasing the dotted pattern obtained in the first irradiation step, the coated silicon wafer was placed in a headspace vial, which was sealed and 5 mL of pure DCM were added. After percolating the solution with an argon stream for 5 min the sample was irradiated with the UV lamp for 24 h. Subsequently, the solvent was replaced and the sample was irradiated for a further 24 h. After rinsing with pure solvent (DCM) and drying under a stream of argon, the sample was subjected to ToF-SIMS analysis. The resulting ion maps are depicted in **Figure 30**. Please note that markings on the sample surface ensured the measurement of the same area on the sample as before.

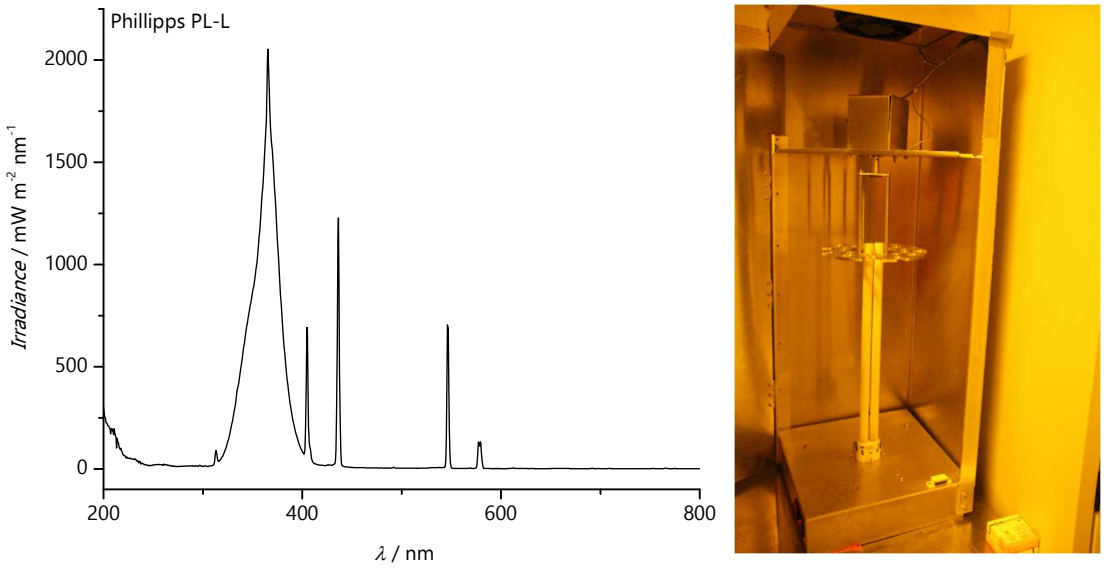

Figure 29: Emission spectrum and intensity of the commercially available UV lamp employed for the cycloelimination reactions and a photograph of the custom-made photoreactor setup.

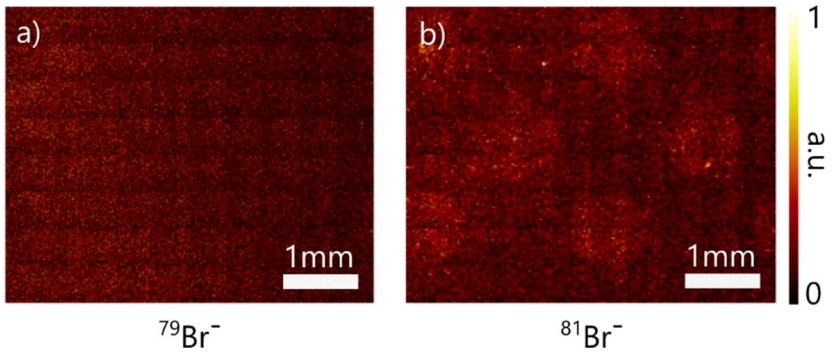

Figure 30: Single fragment ion maps depicting the bromine fragments detected after the first UV light erasing step; a) No dotted pattern of $^{79}Br^-$ fragments is visible; b) Barely visible dotted pattern of $^{81}Br^-$ fragments.

The absence of the dotted pattern derived from both Br- fragments in both depicted ion maps in Figure 30 evidences the successful removal of the attached **9-BA**.

Consequently, it was investigated whether the photoreactivity of the surface bound anthracenes having undergone the write/erase cycle could be preserved and no UV light induced damage was caused to the molecules. Therefore, the same wafer employed in the previous two irradiation steps was again irradiated in the sample holder using the dotted shadow mask in the presence of **9-BA** at 410 nm for 4 h. By scratching one edge of the silicon wafer it was again ensured that the same area of the wafer was irradiated as in the first step. The results of the subsequent ToF-SIMS analysis are depicted in **Figure 31**. A clear dotted pattern is again visible for both isotopic fragments of bromine, proving a successful spatially resolved functionalization with **9-BA**, simultaneously evidencing the preserved visible light reactivity of the surface tethered triazolyl anthracenes. Finally, the surface functionalization was reversed again. Thus, the sample was treated as described for the first erasing step, immersing it in pure solvent and irradiating with mild UV light for 48 h. As before, the sample was analyzed by ToF-SIMS and the resulting images of the single fragment ion maps are depicted in **Figure 32**.

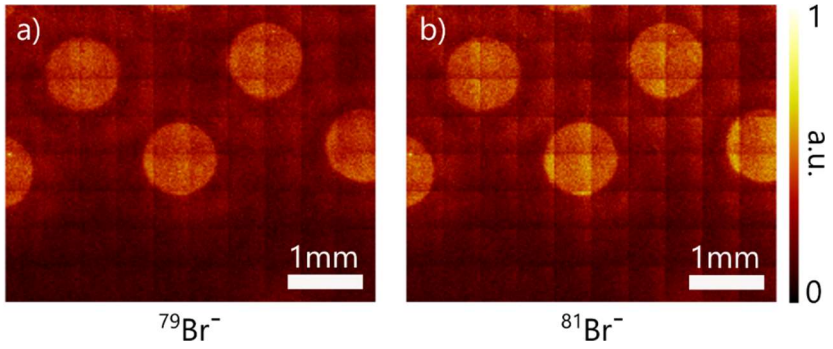

Figure 31: Single fragment ion maps depicting the bromine fragments detected after the second visible light functionalization step; a) Dotted pattern of $^{79}Br^-$ fragments; b) Dotted pattern of $^{81}Br^-$ fragments.

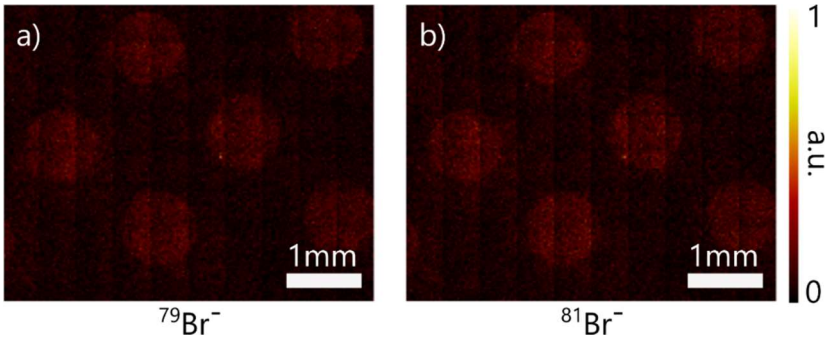

Figure 32: Single fragment ion maps depicting the bromine fragments detected after the second UV light erasing step; only barely visible dotted patterns of both isotopic fragments of bromine.

The repeated erasure of the written structure is clearly evidenced, since the dotted pattern had faded again and is barely detectable for both isotopic bromine fragments. However, the real scope of the established writing/erasing mechanism becomes apparent when referencing all obtained ToF-SIMS ion maps to the same heat scale. For this purpose, the ion maps of both bromine isotopes are summed up for every functionalization step. **Figure 33** depicts a comparison of four ToF-SIMS ion maps of the sums of characteristic bromine fragments obtained after all writing/erasing steps, referenced to the same heat scale. An overview of the surface chemistry for each step is depicted on the left-hand side of Figure 33. A clear dotted pattern is visible for the first writing steps depicted in Figure 33a) and it is regained in the second writing step depicted in Figure 33c). The complete absence of bromine fragments after the first erasing step is displayed in Figure 33b). The dotted pattern of bromine fragments could be deleted for a second time after the second writing step (Figure 33d)). This small molecule study, unambiguously proves that a visible light induced writing/erasing mechanism was successfully established employing surface tethered triazolyl anthracene silane (**20**).

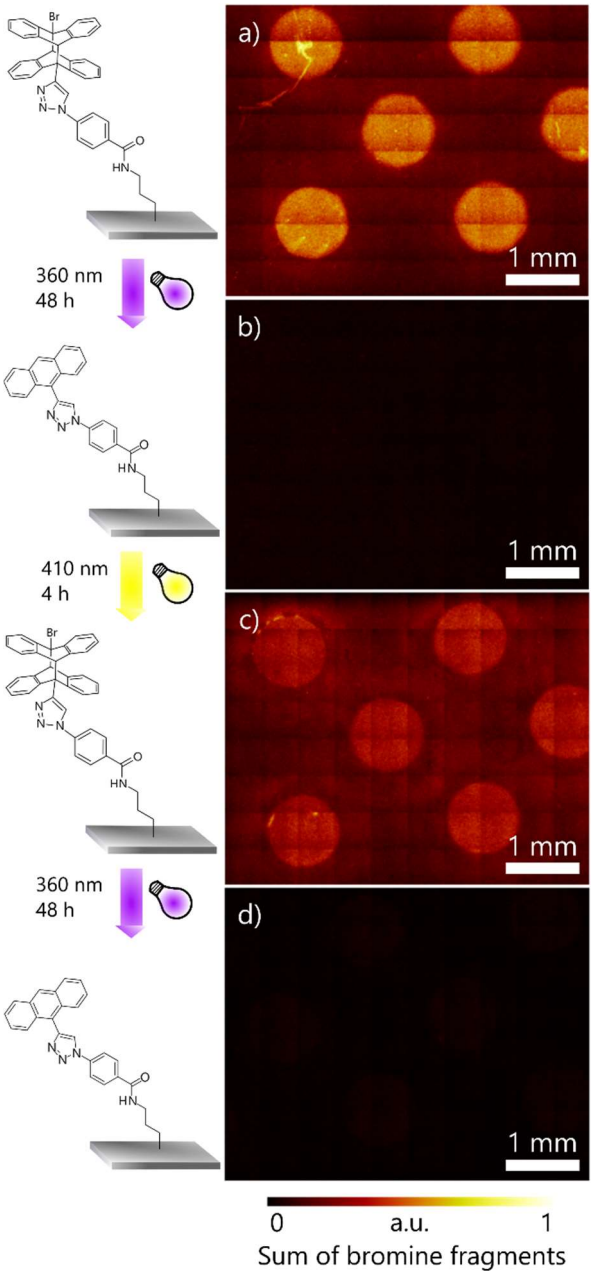

Figure 33: ToF-SIMS ion maps of the sums of bromine fragments obtained after four consecutive writing/erasing steps employing **9-BA** to functionalize a triazolyl anthracene silanized wafer; a) Dotted pattern obtained after the first writing step with visible light irradiation (410 nm); b) Erased dotted pattern after irradiation with long wave UV light (360 nm); c) The reactivity of the surface is preserved and in a second visible light irradiation step, the dotted pattern is recovered; d) Irradiating the surface with mild UV light again leads to an anew deletion of the pattern. The figure was adapted from Ref[69] with permission of The Royal Society of Chemistry.

4.2.2 Reversible polymer immobilization

To exploit the surface reactivity even more, in a next step, not only small molecules but also anthracene endcapped polymer strands were immobilized on the surface. To obtain anthracene functionalized polymers, an anthracene functionalized RAFT agent for the polymerization of styrene and an anthracene functionalized ATRP initiator for the polymerization of *n*-butyl acrylate were utilized. For details concerning the synthesis of the

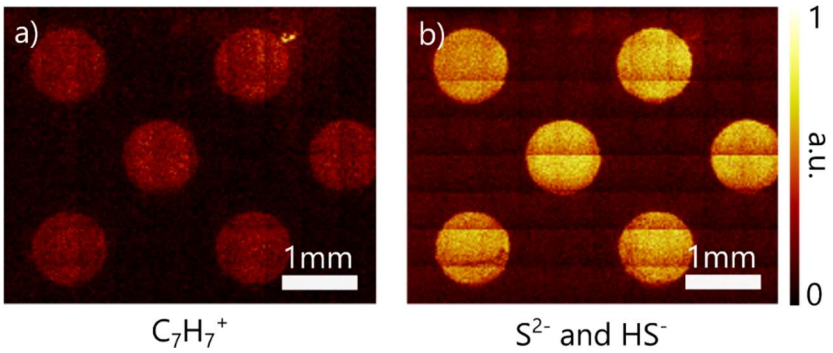

Figure 34: Single fragment ion maps depicting the characteristic fragments derived from **P1**, detected after the first visible light functionalization step; a) Dotted pattern of $C_7H_7^+$ fragments; b) Dotted pattern of S^{2-} and HS^- fragments.

mediating agents, the polymer synthesis and characterization, please refer to the corresponding part in the Experimental Section (7.3.2).

The first polymer was written onto the surface, by irradiating a triazolyl anthracene silane functionalized wafer in the presence of a solution of anthracene endcapped polystyrene (**P1**) (2 mg mL^{-1} in MeCN) employing the conditions developed for the small molecule writing step. Again, the sample was subjected to ToF-SIMS analysis and the obtained results are depicted in **Figure 34**. Associated with the backbone of **P1**, $C_7H_7^+$ fragments were detected, clearly evidencing a dotted pattern. Additionally, S^{2-} and HS^- fragments arising from the RAFT end group of **P1** form a dotted pattern as well, proving the successful visible light surface patterning with **P1**. Consecutively, according to the small molecule study, the wafer was placed in pure MeCN and irradiated with mild UV light for 48 h to erase the obtained pattern. The ToF-SIMS results for the removal of **P1** are depicted in **Figure 35**. As for the small molecule erasure, a clear fading of the intensity of the dotted pattern for the backbone fragments (Figure 35a)) and RAFT end group fragments (Figure 35b)) is evidencing the success of the cycloelimination reaction. Consequently, a second visible light induced writing step was conducted, employing an anthracene endcapped poly(*n*-butyl acrylate) (**P2**) dissolved in MeCN (2 mg mL^{-1}). The wafer was irradiated for 4 h at 410 nm. Following the small molecule study, irradiation of exactly the same spot on the wafer was ensured via marking the silicon surface with scratches. The results obtained from the subsequent ToF-SIMS analysis are depicted in **Figure 36**. In Figure 36a) ion maps of the sum

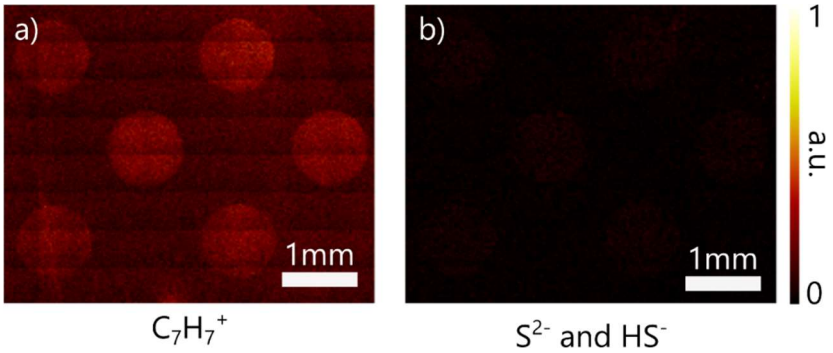

Figure 35: Single fragment ion maps depicting characteristic fragments derived from **P1**, detected after the first UV light induced erasing step; a) and b) only barely visible dotted pattern of $C_7H_7^+$ or S^{2-} and HS^- respectively.

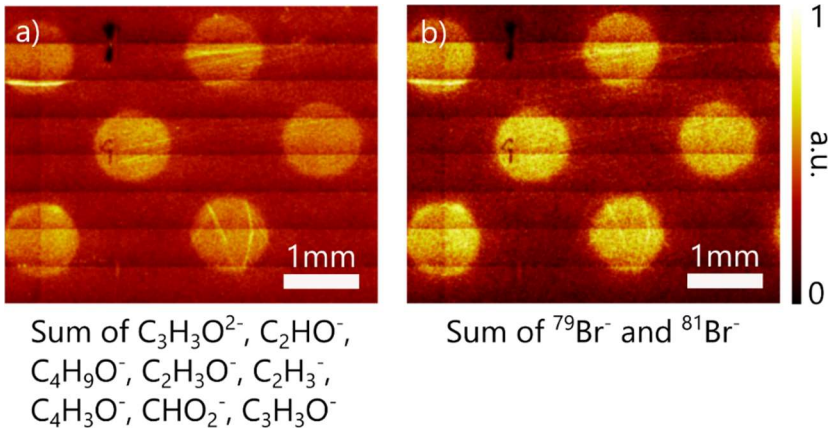

Figure 36: Ion maps depicting the characteristic fragments derived from **P2**, detected after the second visible light functionalization step; a) Dotted pattern of the sum of characteristic backbone fragments derived from **P2**; b) Dotted pattern of both isotopic bromine fragments associated with the ATRP initiator.

of fragments derived from the butyl acrylate sidechains of **P2** in shown, whereas Figure 36b) depicts the sum of both bromine isotopic fragments derived from the bromine end group of the ATRP made polymer. Both figures faithfully replicate the mask pattern, hence indicating a successful second functionalization step. In a last irradiation step conducted on this wafer, the dotted pattern of **P2** was removed employing the typical erasing conditions described above. The wafer was subjected to ToF-SIMS analysis once more, whose results are depicted in **Figure 37**. The clear fading of both dotted patterns, derived from the sidechain fragments of **P2** (Figure 37a)) and from the endgroup derived bromine fragments (Figure 37b)) evidences a successful removal of **P2** from the silanized wafer. As for the small molecule study, an overview depicting all four steps conducted on the wafer is shown in **Figure 38**. In this over-view, the sums of the characteristic fragments of **P1** and **P2**, respectively, are depicted in the ToF-SIMS ion maps. The respective ion maps for the polymers are referenced to the same heat scale to ensure comparability. A surface reaction sequence is depicted on the left-hand side next to the ToF-SIMS ion maps in Figure 38. The results clearly indicate that the scope of the established visible light writing and mild UV erasing procedure can be directly expanded from small molecules to polymer strand surface attachment.

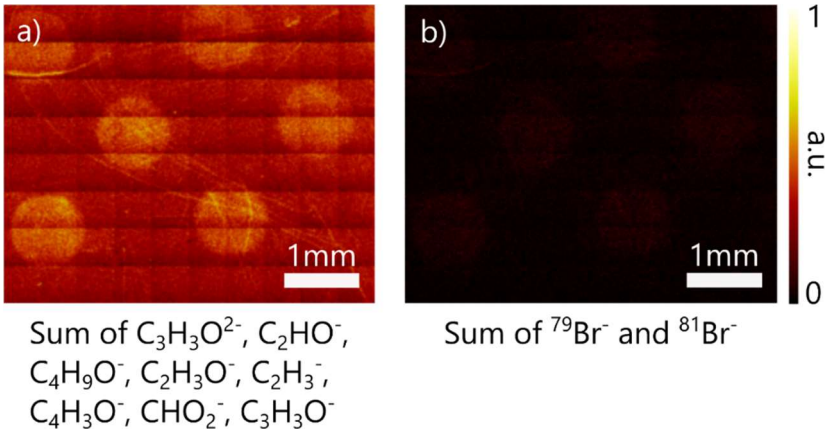

Figure 37: Ion maps depicting the characteristic fragments derived from **P2**, detected after the second UV light erasing step; a) Barely visible, faded dotted pattern of the sum of characteristic backbone fragments derived from **P2**; b) Barely visible, faded dotted pattern of both isotopic bromine fragments.

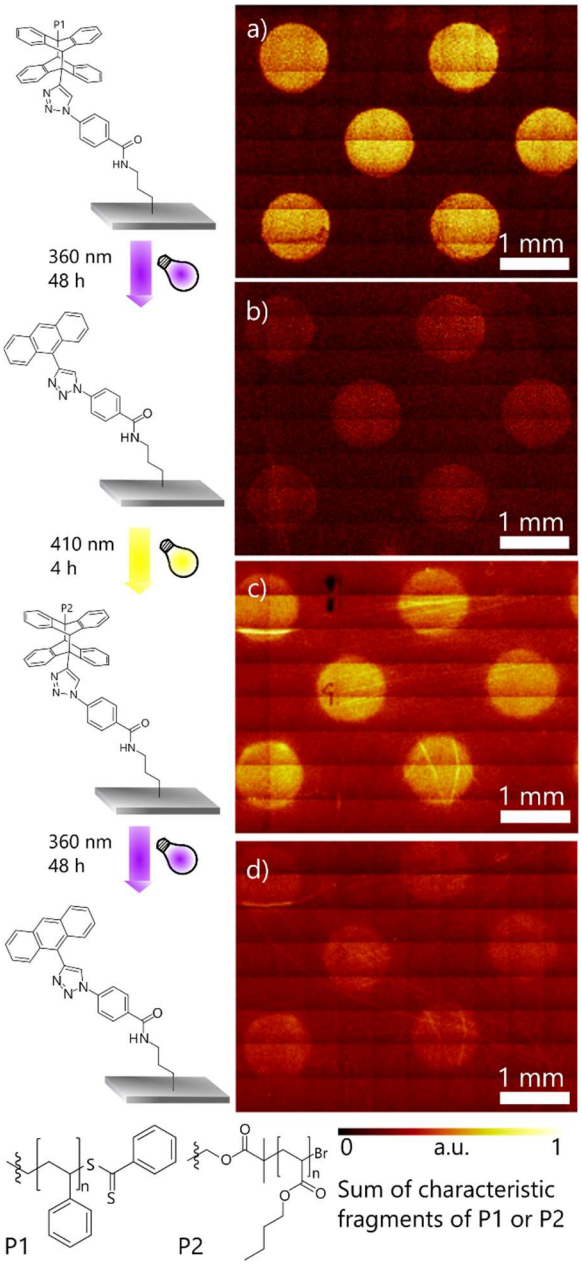

Figure 38: ToF-SIMS ion maps of the sums of characteristic fragments of **P1** and **P2** after four consecutive writing/erasing steps employing the respective polymers to functionalize a triazolyl anthracene silanized wafer; a) Dotted pattern of **P1** obtained after the first writing step with visible light irradiation (410 nm); b) Erased dotted of **P1** after irradiation with long wave UV light (360 nm); c) The reactivity of the surface is preserved and in a second visible light irradiation step employing **P2**, the dotted pattern is recovered; d) Irradiating the surface with mild UV light again leads to a new erasing of the pattern of **P2**. The figure was adapted from Ref[69] with permission of The Royal Society of Chemistry.

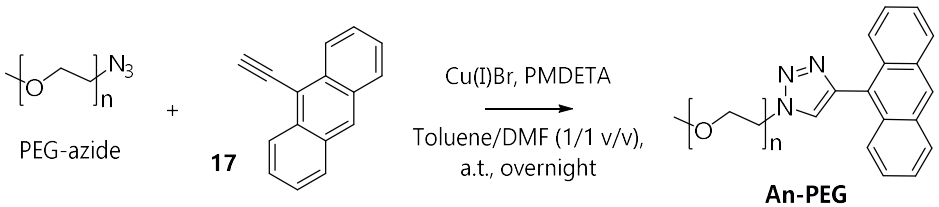

Scheme 41: Synthetic procedure to obtain triazolyl anthracene end capped poly(ethylene glycol) (**An-PEG**).

During the course of this project, the question arose whether the surface tethered anthracene derivatives were able to react with each other and therefore reduce the overall surface reactivity. To assess these considerations, a triazolyl anthracene endcapped poly(ethylene glycol) (**An-PEG**) was synthesized employing a PEG azide derivative and alkyne **17**, as depicted in **Scheme 41**. The so obtained **An-PEG** was employed for the visible light functionalization of a triazolyl anthracene silanized silicon wafer. The wafer was mounted in a sample holder equipped with a dotted shadow mask, immersed in a solution of **An-PEG** (2 mg mL^{-1} in DCM), percolated with argon and irradiated at 410 nm for 4 h. The result of a subsequent ToF-SIMS analysis is depicted in **Figure 39**.

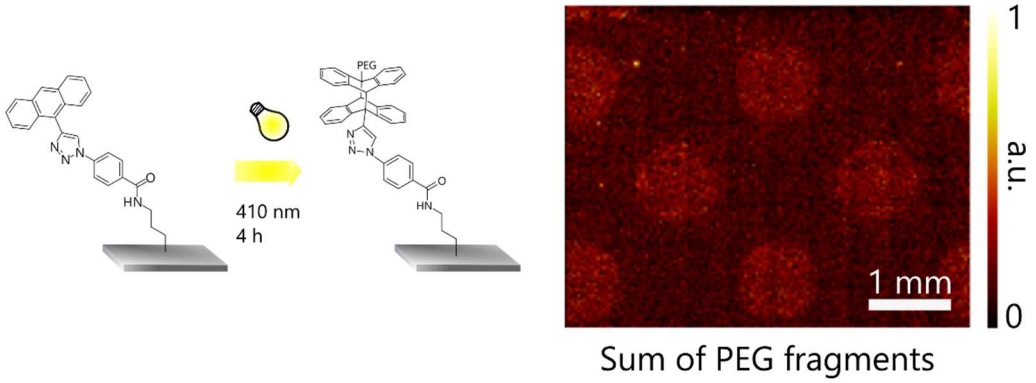

Figure 39: Schematic representation of the visible light mediated surface functionalization with **An-PEG** and obtained ToF-SIMS results. The ion map depicts a sum of all PEG derived fragments arising from the surface. Only a faint dotted pattern can be detected.

On the lefthand side, a schematic representation of the performed visible light functionalization is depicted, whilst on the righthand side the ToF-SIMS ion map for the sum of all PEG derived fragments is shown. Only a barely discernable dotted motif can be observed, prompting the conclusion that a self-dimerization occurs during the photoreaction only to a minimum extent. This result is not against expectation, as both reaction partners of the [4+4] cycloaddition possess a high electron density. A reaction is therefore not favored due to electronic considerations.[70]

4.2.3 Dual functionalization with a small molecule and polymer strand

In a final experiment, the scope of the developed process was further examined by aiming at dual patterns with functional anthracenes. For this purpose, a wafer silanized with visible light anthracene (**20**) was irradiated at 410 nm without a shadow mask in the presence of **9-BA**, yielding a surface entirely coated with **9-BA**. The coated wafer was placed into the sample holder equipped with the dotted shadow mask and irradiated at 360 nm to partially remove **9-BA**, thereby realizing an inversely dotted pattern. Consecutively, without demounting the wafer from the holder, the sample was immersed in a solution of **P1** (2 mg mL^{-1} in MeCN) and again irradiated at 410 nm to obtain a polymer functionalization inside the dots. After the irradiation, the sample was removed from the holder, rinsed with

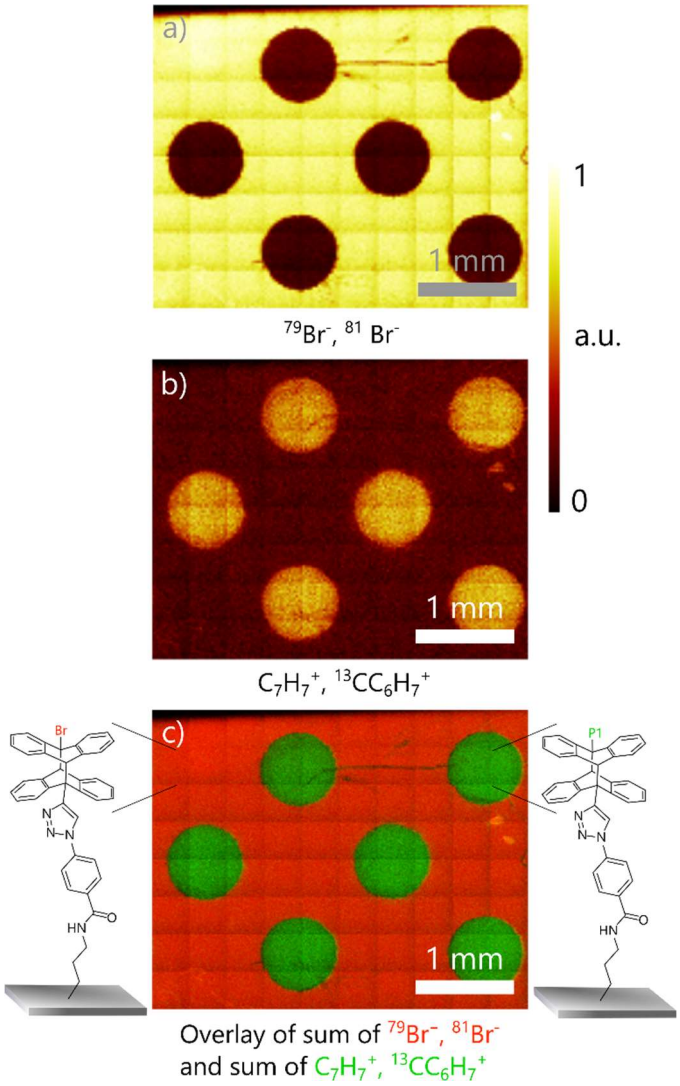

Figure 40: ToF-SIMS ion maps measured after the dual functionalization process; a) Sum of both isotopic bromine fragments originating from **9-BA** depict an inversely dotted pattern; b) Sum of backbone fragments derived from **P1** shows the corresponding dotted pattern; c) Colored overlay image of the ion maps illustrated in a) and b). Bromine fragments are depicted in red, **P1** backbone fragments in green. The figure was adapted from Ref [69] with permission of The Royal Society of Chemistry.

MeCN and subjected to ToF-SIMS analysis. The resulting ion maps are depicted in **Figure 40**. Figure 40a) and 40b) illustrate ion maps of the sums of characteristic fragments derived from the respective surface. In Figure 40a), an inversely dotted pattern is evidenced by the sum of both isotopic bromine fragments, indicating the success of the first two functionalization steps (full surface coverage with **9-BA** and partial removal of the dotted pattern). A distinctly dotted pattern of characteristic fragments characteristic for **P1** evidences the success of the third functionalization step, i.e., the rewriting on the erased dots. To better visualize the dual functionality present on the wafer, a colored overlay image is depicted in Figure 40c). Bromine fragments are visualized in red, whereas backbone fragments of **P1** are visualized in green. The overlay image unambiguously proves the successful fabrication of a dually functionalized wafer obtained via visible light writing, mild UV light erasing, and subsequently rewriting with visible light.

To briefly recapitulate the current chapter, a new visible light induced method to achieve recordable surfaces based on the [4+4] dimerization of anthracenes was introduced. For this purpose, a new, red shifted triazolyl anthracene silane (**20**) was synthesized via an efficient synthetic route. Subsequently, silicon wafers were functionalized with the new silane (**20**). The successful surface anchoring was proven by XPS analysis. To investigate the novel photoreactivity of the surfaces, a small molecule study was conducted employing a brominated anthracene derivative (**9-BA**), which facilitates ToF-SIMS analysis. A successful write-erase-write-erase sequence was performed on a silanized wafer utilizing visible light irradiation at 410 nm and mild UV light at 360 nm for the writing and erasing steps, respectively, recovering the surface reactivity after each erasing step. After this proof of principle, the writing/erasing capability was further exploited to immobilize polymer strands on the surface. Thereto, an anthracene end-capped polystyrene (**P1**) and an anthracene end-capped poly(*n*-butyl acrylate) (**P2**) were utilized. A first writing/erasing cycle was conducted employing **P1**, a second writing/erasing cycle was achieved with **P2**. Again, in depth ToF-SIMS analysis revealed the successful outcome of the experiments. Furthermore, a dually modified wafer was fabricated by complete functionalization of a silanized wafer with **9-BA** under visible light irradiation and subsequent erasing of a dotted pattern by mild UV light irradiation. The reactive dots were then functionalized employing the visible light writing again with **P1** to yield a dually functionalized sample.

The newly introduced method proved its applicability to exploit visible light triggered reactivity on the surface with mild UV light reversibility. As a prospect, reversible protein or cell attachments to surfaces might be achievable utilizing this methodology, taking advantage of the mild reaction conditions.

5

EXPLOITING THE REACTIVITY OF NOVEL PHOTO-MONOMERS FOR SCNP FOLDING

In Chapter 3, a new methodology for the construction of 3D cell guiding scaffolds was introduced. Dual functionalized microstructures with various proteins, immobilized on the surface, were achieved by implementing two novel photoreactive monomers in the structures. These methacrylate based monomers were incorporated in photoresists for DLW by copolymerization with a triacrylate based network former, constituting the functional parts of the scaffolds. However, a polymerization to form linear photoreactive polymers with the novel photomonomers was not investigated. Therefore, to gain a deeper insight into the monomers polymerization behavior, polymerizations incorporating these monomers were studied in detail. As both monomers are not commercially available and synthetically demanding to prepare, copolymerizations with methyl methacrylate (MMA) were conducted to lower the photomonomer consumption. The polymers formed thereby are privileged precursors for the formation of SCNPs, exploiting the photoreactivity of the incorporated monomers. In the literature, SCNPs are often referred to as biomolecule mimics, e.g., for proteins.[170] However, the folding mechanism of proteins is considered a multistep procedure in contrast to one defined folding step.[30, 209-210] Polymer derived SCNPs often lack this feature and are compacted in one step employing various techniques

(photochemical folding, folding via metal complexes, hydrogen-bond folding, etc.).[27, 171] The dual functional nature of the monomers should allow to form polymers that can be stepwise compacted in order to approach more closely a protein folding mechanism. Thereto, the synthesis of well defined (block) copolymers is necessary. The RAFT process was chosen, as it allows for a controlled polymerization process in combination with high monomer conversions as well as a direct block extensions.[53] The initial part of the project was conducted at the University of Warwick in collaboration with Prof. Perrier.**

5.1 RAFT (block) copolymerization employing novel photomonomers

To establish suitable conditions for the copolymerization of the two photoreactive monomers with MMA and to introduce a protocol to obtain block copolymers containing both functional groups, a few initial considerations and investigations were carried out. First, the thermal stability was investigated by dissolving the respective monomer in $CDCl_3$ or DMSO-d_6 and heating the solution for 16 h at 60 °C.

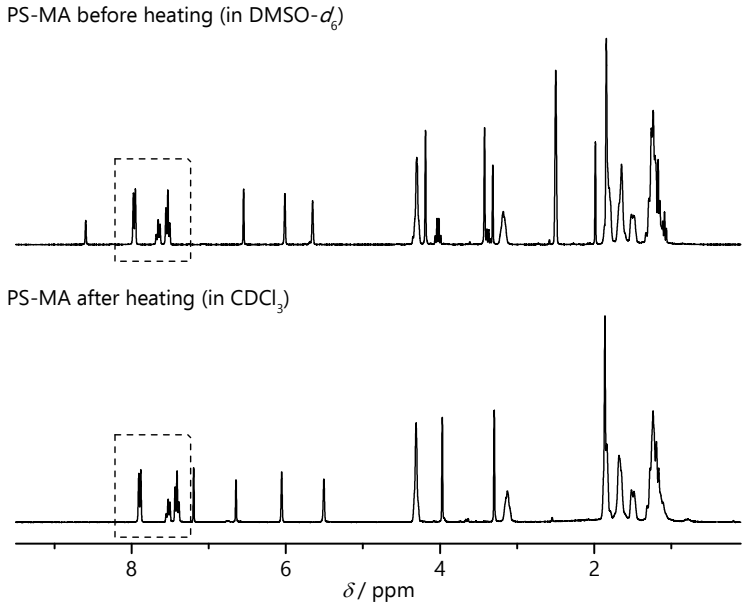

Figure 41: Comparison of ^{1}H NMR spectra (400 MHz, DMSO-d_6 or $CDCl_3$, ambient temperature) before and after the heating of PS-MA (**7**) in $CDCl_3$. The signals derived from the photoreactive moiety are highlighted in the dashed frames.

** Parts of the current chapter are reproduced or adapted from T. K. Claus, J. Zhang, L. Martin, M. Hartlieb, H. Mutlu, S. Perrier, G. Delaittre, C. Barner-Kowollik, Macromol. Rapid Commun. 2017, 1700264. https://doi.org/10.1002/marc.201700264, with permission from John Wiley and Sons. J. Zhang and L. Martin provided support in establishing the RAFT block copolymerization protocols and H. Mutlu conducted the DLS measurements. M. Hartlieb, S. Perrier, G. Delaittre and C. Barner-Kowollik contributed to the scientific discussions and supervised the project.

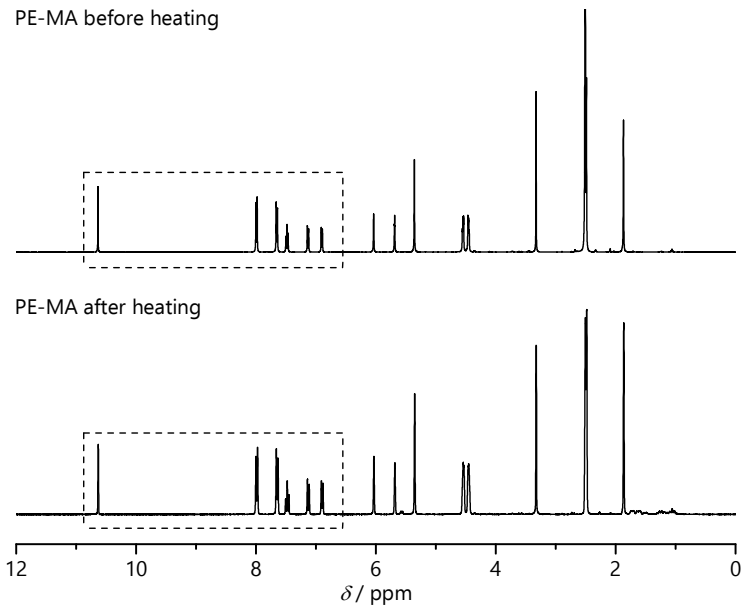

Figure 42: Comparison of ^{1}H NMR spectra (400 MHz, DMSO-d_6, ambient temperature) before and after the heating of PE-MA (**8**) in DMSO-d_6. The signals derived from the photoreactive moiety are highlighted in the dashed frames.

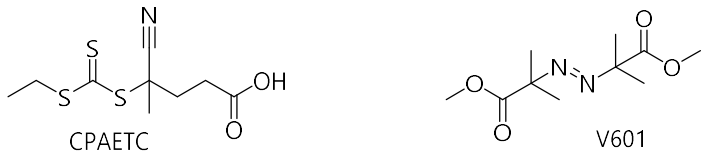

Scheme 42: Selected RAFT agent (CPAETC) and initiator (V601) for the RAFT polymerization of MMA at 60 °C in dioxane.

^{1}H NMR spectra before and after heating are depicted in **Figure 41** (PS-MA (**7**)) and **Figure 42** (PE-MA (**8**)). The characteristic signals of the photoreactive moieties are highlighted in the dashed frames. The spectra evidence no difference in the highlighted regions, proving the stability of both functional groups for at least 16 h at 60 °C. As a next step, a RAFT polymerization of pure MMA at 60 °C was performed to establish conditions for reaching high monomer conversions. The selected RAFT agent and initiator for MMA polymerization at 60 °C in 1,4-dioxane are depicted in **Scheme 42**.[††] A monomer concentration of 3 mol L^{-1}, a CTA-to-initiator ratio of 5 and a targeted degree of polymerization DP_n of 100 after 16 h yielded satisfactory results. SEC and ^{1}H NMR data of the obtained polymer are depicted in **Figure 43**. A conversion of 81 % was calculated based on the depicted ^{1}H NMR spectrum. A well-defined polymer was obtained with a molar mass $M_{n,SEC}$ of 11600 g mol^{-1} and a dispersity $Đ$ of 1.12. Both M_n and $Đ$ indicate a controlled polymerization mechanism as the targeted degree of polymerization DP_n could be reached with a relatively low dispersity. Additionally, a high conversion could be obtained while maintaining control over the polymerization process. This is a crucial feature for the copolymerization procedures employing the photoreactive monomers, as less material will be required. In a next step, the

[††] The RAFT agent was kindly provided by M. Hartlieb (University of Warwick).

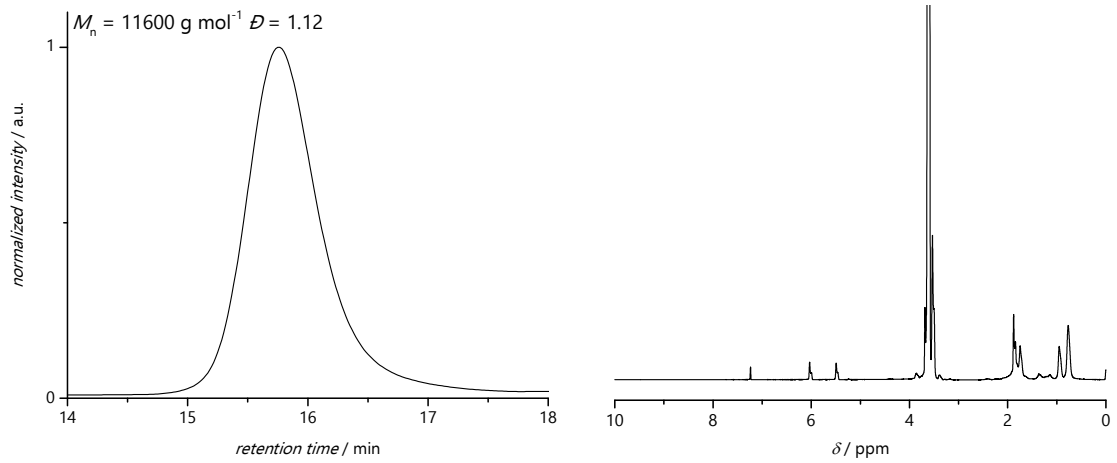

Figure 43: Size exclusion chromatogram (THF, 30 °C) and ^{1}H NMR spectrum (400 MHz, $CDCl_3$, ambient temperature) of a RAFT polymerization of MMA.

established conditions were employed to copolymerize PS-MA (**7**) or PE-MA (**8**) with MMA respectively.

5.1.1 Copolymerization of PS-MA (7) with MMA

The aforementioned conditions (CTA and initiator depicted in Scheme 42, monomer concentration of 3 mol L^{-1}, [CTA]/[I] = 5 and $DP_{n,target}$ of 100) were employed in a kinetic study with a monomer feed of 100 mol% MMA and 10 mol% PS-MA (**7**). Samples were withdrawn from the polymerization mixture at regular intervals (30 min, 1 h, 2 h, 3h, 4 h, 6 h, 8 h, 10 h, 13 h and 16 h). The samples were analyzed via SEC and ^{1}H NMR and the results are depicted in **Figure 44** and **Figure 45** respectively. A steady growth of the polymer over time can be deduced from Figure **44**. However, after 8 h, a subtle high molar mass shoulder arises, accompanied by a slight increase in dispersity. After 16 h, the high molar mass shoulder has grown, leading to the conclusion that the addition of PS-MA (**7**) somehow alters the outcome of the polymerization. Taking the structure, the oily consistency of the monomer, and the synthetic route into account, one possible side reaction happening upon storage is a transesterification resulting in the formation of a proportion of dimethacrylic crosslinker, causing crosslinking at high conversions (see **Scheme 43**). In **Figure 45** a stack of the recorded ^{1}H NMR spectra is illustrated. An increase of the proton signal intensities in the backbone area (between 1.0-0.5 ppm) accompanied by a decrease of the vinylic proton signal intensities indicate a successful polymerization. The conversion of the monomer was calculated by analyzing the ratio of the integrals of the signals derived from the phenylic protons of PS-MA (**7**) to vinylic proton resonances. The derived Number weighted molar mass M_n and dispersity $Đ$ vs conversion plot and a time vs ln(1/(1-conv)) plot is depicted in **Figure 46**.

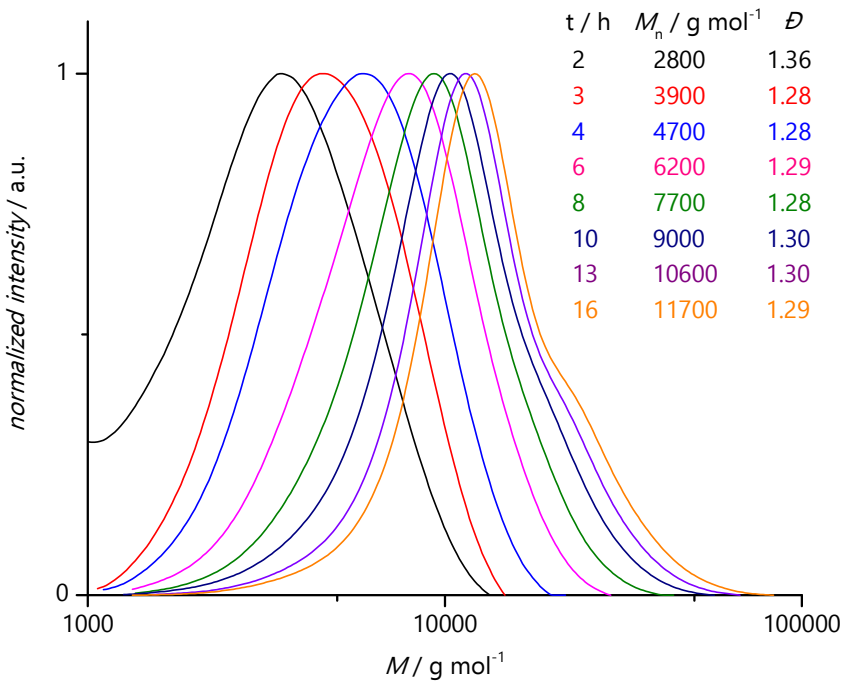

Figure 44: Size exclusion chromatograms (THF, 30 °C) obtained for the RAFT kinetic study of the copolymerization of MMA with PS-MA (**7**), samples were prepared with a concentration of 2 mg mL^{-1}.

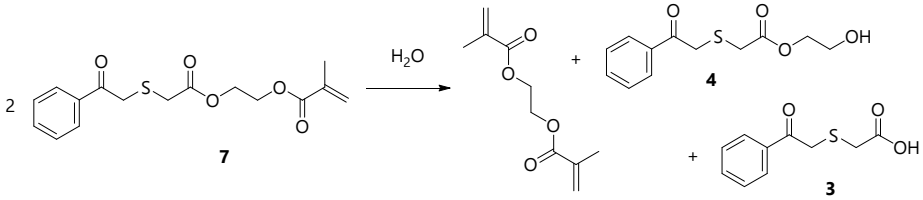

Scheme 43: Possible transesterification side reaction occurring upon storage of PS-MA (**7**).

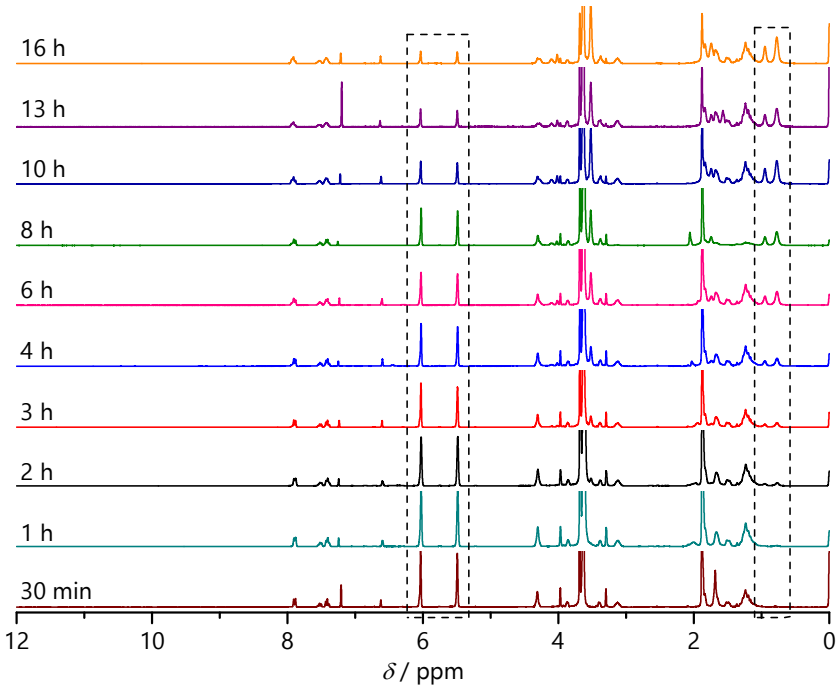

Figure 45: ^{1}H NMR spectra (400 MHz, $CDCl_3$, ambient temperature) of all measured kinetic samples withdrawn directly from the polymerization mixture. A decrease of the vinylic signals (between 6.5-5.5 ppm) and an increase of the backbone signals (between 1.0-0.5 ppm) is evidenced (dashed frames). For experimental details refer to Section 7.3.3.

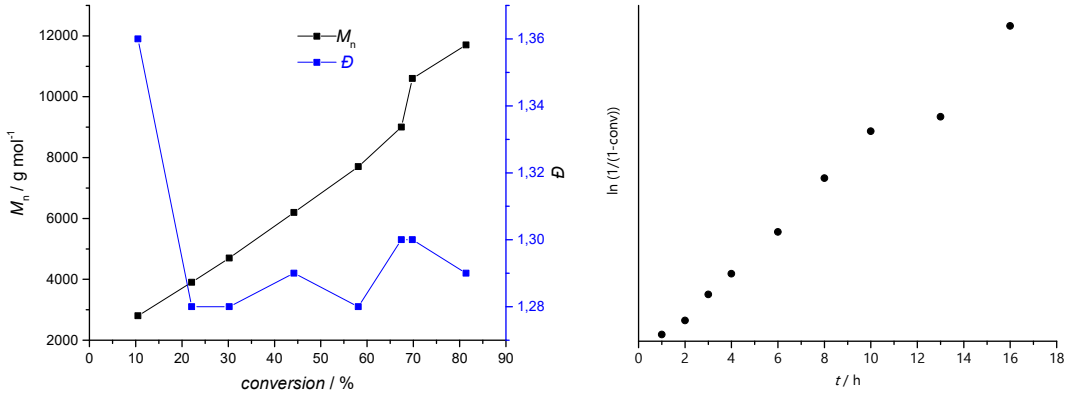

Figure 46: Number weighted molar mass M_n and dispersity $Đ$ vs conversion and ln(1/(1-conv)) vs time plots calculated from ^{1}H NMR spectra shown in Figure 42.

A linear correlation in the M_n and ln(1/(1-conv)) is evidenced in both plots until approx. 75 % conversion (close to 10 h). Next, the graph flattens and seems to reach a plateau, indicating a reduction of the rate of polymerization. This could be explained with the cross-linking side reactions and effects derived thereof. Due to these impurities, a full conversion could not be reached employing the PS-MA (**7**). Therefore, to obtain a polymer with a DP_n of 100, a modified protocol was applied, utilizing the same conditions (CPAETC as CTA, V601 as initiator, [M] = 3 mol L^{-1}, T = 60 °C, [CTA]/[I] = 5, monomer feed 100 mol% MMA + 10 mol% PS-MA (**7**)), but setting the $DP_{n,target}$ to 200 and quenching the polymerization after 50 % conversion, 7 h polymerization time respectively. A size exclusion chromatogram and ^{1}H NMR spectrum of the precipitated polymer ((PS-MA-*co*-MMA)$_{100}$) is depicted in **Figure 47**. It is evidenced from the SEC chromatogram that a controlled polymerization was conducted as a well-defined polymer with a low dispersity of 1.19 and a molar mass within the expected range was obtained. The ^{1}H NMR spectrum clearly indicates that the phenacyl sulfide moiety withstands the polymerization procedure. From the spectrum, the average content of 11 PS-MA (**7**) units per chain was deduced, being in good agreement with the 10 mol% of PS-MA (**7**) in the monomer feed. In a further polymerization, the $DP_{n,target}$ was doubled again

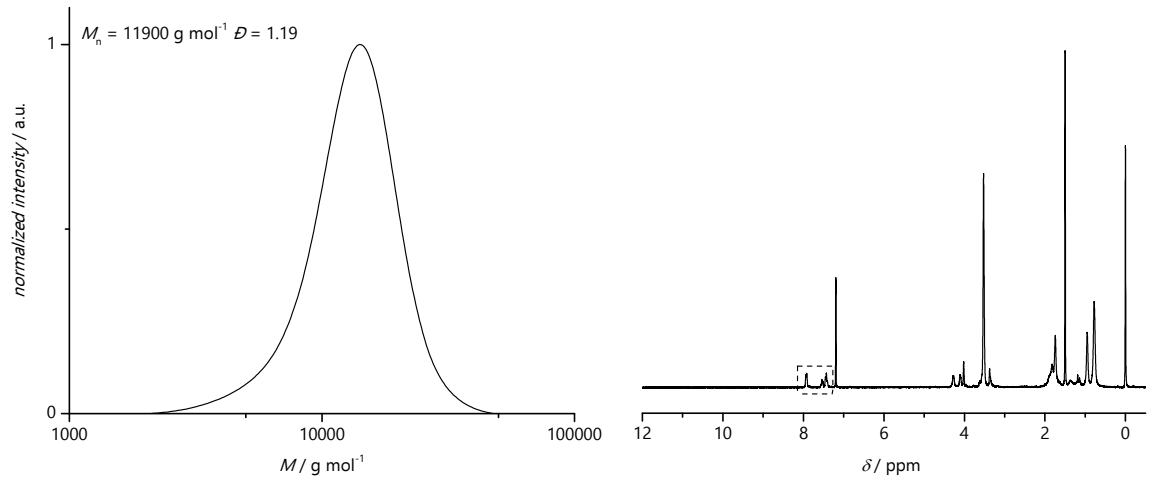

Figure 47: Size exclusion chromatogram (THF, 30 °C) and ^{1}H NMR spectrum (400 MHz, $CDCl_3$, ambient temperature) of precipitated (PS-MA-*co*-MMA)$_{100}$. The proton signals derived from the photoreactive group are highlighted in the dashed square.

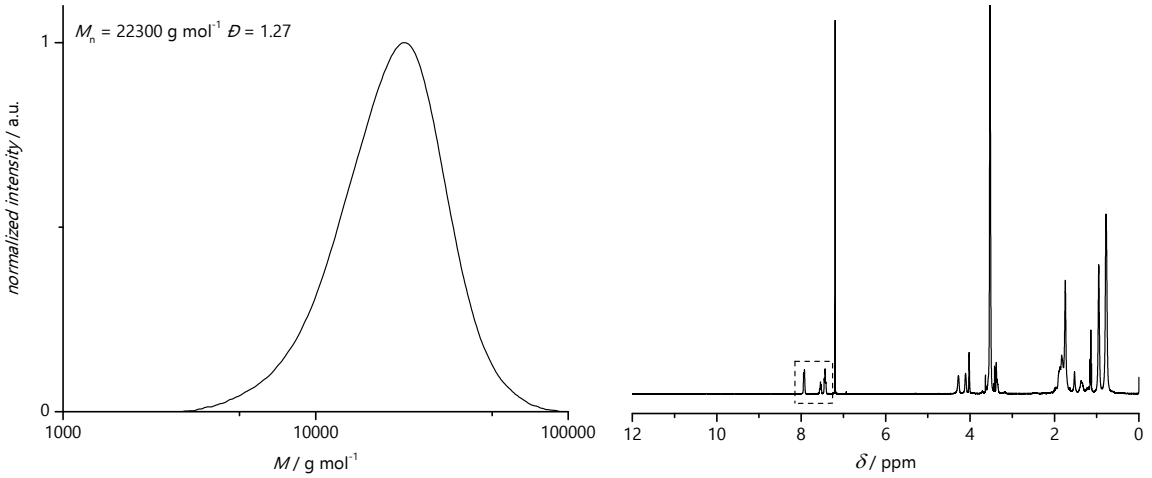

Figure 48: Size exclusion chromatogram (THF, 35 °C) and ^{1}H NMR spectrum (400 MHz, $CDCl_3$, ambient temperature) of precipitated (PS-MA-*co*-MMA)$_{200}$. The proton signals derived from the photoreactive group are highlighted in the dashed square.

and set to 400, to achieve a polymer with a DP_n of 200. The obtained SEC and ^{1}H NMR results are depicted in **Figure 48**.

As for the smaller copolymer (PS-MA-*co*-MMA)$_{100}$, the size exclusion chromatogram indicates a controlled polymerization and the ^{1}H NMR evidences the photoreactive group being unchanged. The average PS-MA (**7**) content of the polymer was calculated as 18 units per chain. It is apparent that the aforementioned RAFT polymerization conditions were successfully employed to achieve well-defined PS-MA-*co*-MMA polymers. In the next step, the established conditions were applied to copolymerizations with PE-MA (**8**).

5.1.2 Copolymerization of PE-MA (8) with MMA

Since the synthesis of the PE-MA (**8**) is more demanding than the synthesis of PS-MA (**7**), a polymerization procedure allowing for 100 % monomer conversion was desired. In contrast to PS-MA (**7**), which has an oily consistency, PE-MA (**8**) is a crystalline solid. Therefore, a transesterification side reaction should be kinetically hindered allowing for the aforementioned RAFT protocol to be applied, reaching 100 % conversion. Its feasibility was investigated by performing a kinetic study. The resulting size exclusion chromatograms are depicted in **Figure 49**. Samples were withdrawn directly from the polymerization mixture as described above at regular intervalls (30 min, 1 h, 2 h, 3 h, 4 h, 6 h, 8 h, 10 h, 13 h and 16 h). After 30 min, 1 h and 2 h no polymer was detectable by SEC, indicating an inhibition period at the beginning of the RAFT polymerization. Afterwards, a steady growth over time can be deduced from the SEC elugram evolution, accompanied by a decrease of the dispersity, evidencing a controlled polymerization. A stack of the corresponding ^{1}H NMR spectra is depicted in **Figure 50**. A decrease in the intensities of proton resonances of the vinylic moieties (between 6.2-5.5 ppm) followed by an increase of the intensity of the backbone proton signals (between 1.2-0.8 ppm) indicates a successful polymerization. The conversion

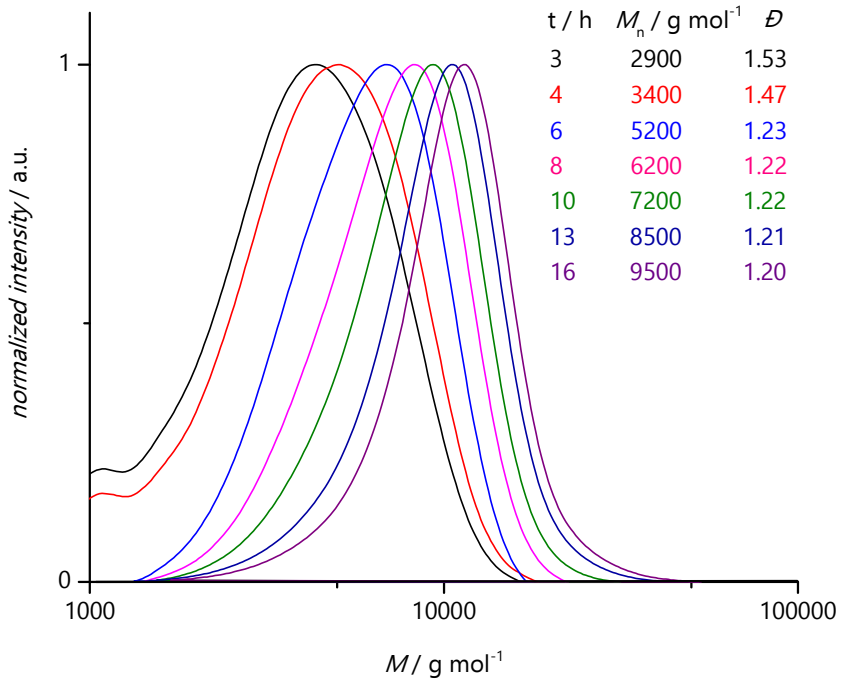

Figure 49: Size exclusion chromatograms (THF, 30 °C) obtained for the RAFT kinetic study of the copolymerization of MMA with PE-MA (**8**), samples were prepared with a concentration of 2 mg mL^{-1}.

was calculated from the ratio of the integrals of the vinylic signals and the aromatic signals of the photoenol group. The corresponding number weighted molar mass M_n and dispersity $Đ$ vs conversion and ln(1/(1-conv)) vs time plots are depicted in **Figure 51**. After 30 min, no conversion is observed, indicating again an inhibition period. After 1 h, the polymerization has started and approx. 6.9 % of monomer was consumed.

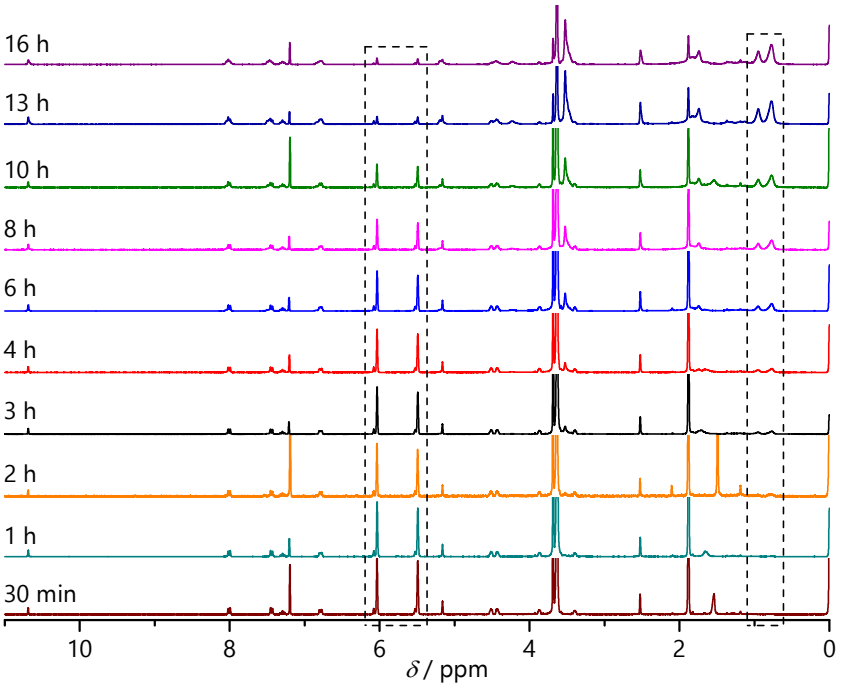

Figure 50: ^{1}H NMR spectra (400 MHz, $CDCl_3$, ambient temperature) of all relevant kinetic samples drawn directly from the polymerization mixture. A clear decrease of the vinylic signals (between 6.2-5.5 ppm) and a clear increase of the backbone signals (between 1.2-0.8 ppm) is evidenced (highlighted by the dashed frames).

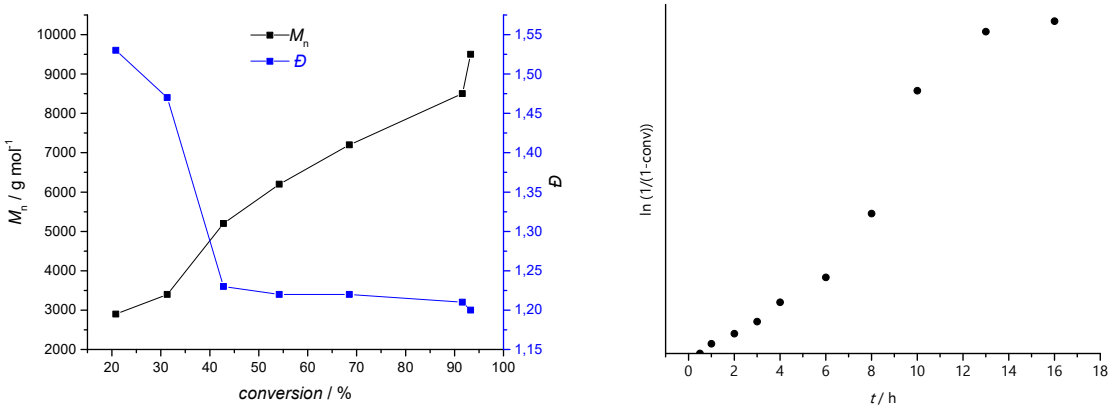

Figure 51: Number weighted molar mass M_n and dispersity $Đ$ vs conversion and ln(1/(1-conv)) vs time plots calculated from ^{1}H NMR spectra shown in Figure 50.

The monomer consumption follows a linear correlation over the course of the next 12 h before leading to a plateau after about 13 h (~91.6 % conversion). Both SEC and ^{1}H NMR results of the kinetic study indicate a controlled RAFT procedure reaching high conversions (≥ 90 %) leading to well-defined polymer chains. Next, the polymerization was performed on a preparative scale employing the same conditions as in the kinetic study. The SEC and ^{1}H NMR results of a precipitated (PE-MA-*co*-MMA)$_{100}$ are depicted in **Figure 52**. A narrow dispersity of 1.17 and a molar mass of 11400 g mol^{-1} were achieved while the ^{1}H NMR indicates that the photoenol groups sustain the polymerization procedure (see aldehyde resonance at close to 11 ppm). The average PE-MA (**8**) content per chain was calculated to 12 units, still being in a good agreement with the monomer feed. The herein demonstrated RAFT copolymerization conditions have proven to yield well-defined copolymers for both photoreactive monomers. Consecutively, the established conditions were employed in the synthesis of a dual functional block copolymer.

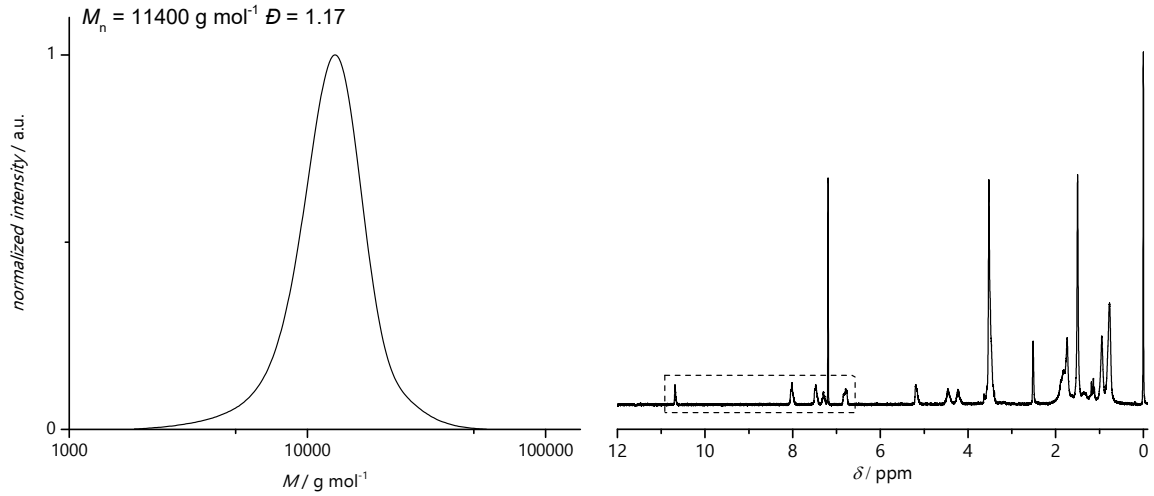

Figure 52: SEC chromatogram (THF, 30 °C) and ^{1}H NMR spectrum (400 MHz, $CDCl_3$, ambient temperature) of precipitated (PE-MA-*co*-MMA)$_{100}$. The proton signals derived from the photoreactive group are highlighted in the dashed frame.

5.1.3 RAFT block copolymerizations with both photoreactive monomers

In order to combine both photoreactive moieties in one polymer chain, the established copolymerization protocols for the polymerizations of the respective monomers with MMA were combined to form a block copolymer. The conducted reaction sequence is depicted in **Scheme 44**.

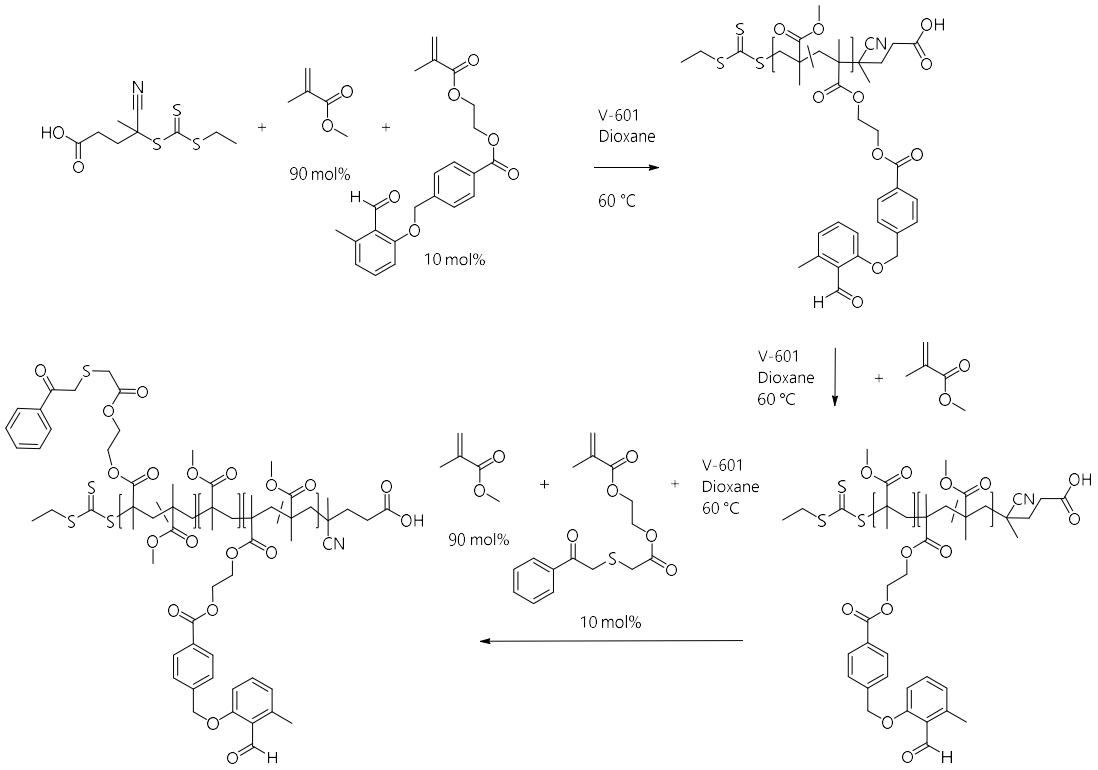

Scheme 44: RAFT block copolymerization procedure conducted to obtain a triblock copolymer. In a one pot approach, the first block was formed by copolymerizing PE-MA (**8**) with MMA to 100 % conversion with the aforementioned conditions. To form a second, short spacer block, pure MMA was added to the mixture and also polymerized to 100 % conversion. For the polymerization of the third block, 100 mol% MMA and 10 mol% were added to the mixture and polymerized until 50 % conversion was reached.

The individual blocks of the copolymer containing the functional monomers are designed in analogy to the monofunctional copolymers described in the previous sections. For a distinct separation between the functional blocks, a small spacer block of pure PMMA was introduced between them, leading to a targeted overall polymer sequence of (PE-MA-*co*-MMA)$_{100}$-*b*-MMA$_{20}$-*b*-(PS-MA-*co*-MMA)$_{100}$. The PE-MA (**8**) containing block was polymerized first, allowing for an overall one pot procedure as the polymerization could be carried out to 100 % conversion in contrast to the polymerization employing PS-MA (**7**). The aforementioned conditions were employed, (CPAETC as CTA, V601 as initiator and a monomer feed of 100 mol% MMA + 10 mol% PE-MA (**8**), in 1,4-dioxane, 3 mol L^{-1}). The mixture was percolated with nitrogen and the polymerization was carried out at 60 °C for 16 h. After cooling to ambient temperature, an SEC sample was withdrawn from the polymerization mixture and fresh MMA was added together with 25 % of the initial amount

of initiator. The mixture was percolated with nitrogen again and the polymerization was continued by heating in an oil bath to 60 °C. In order to consume all added MMA to construct a spacer block, the polymerization was carried out for 4 h. Subsequently, the mixture was cooled to ambient temperature, an SEC sample was taken and the monomer feed for the third block (100 mol% MMA, 10 mol% PS-MA (**7**)) with another 25 % of the initial initiator amount was added. The mixture was percolated with nitrogen for a third time and the polymerization was continued at 60 °C and stopped after 7 h to not exceed a monomer conversion of 50 %. A final SEC sample was recorded from the extremely viscous mixture and the polymer was precipitated in ice cold Et_2O. The SEC traces, obtained after each of the polymerization steps are depicted in **Figure 53**. For the first two blocks, the targeted molar mass and a narrow dispersity was achieved as evidenced by the obtained SEC traces. However, for the third block a lower molar mass as expected is obtained (around 6500 g mol^{-1} instead of 10000 g mol^{-1}) and a high molar mass shoulder indicates small amounts of crosslinking, probably due to the high viscosity of the polymerization mixture at the end of the process. Consequently, the procedure was changed slightly by adding a small amount of solvent in every step to ensure a lower viscosity at the end of the process. Furthermore, the polymerization time for the third block was increased from 7 h to 8 h to access a higher molar mass. The results of the SEC analysis are depicted in **Figure 54**. The SEC traces for the first two blocks resemble those previously obtained, while the size exclusion chromatogram after the third block copolymerization evidenced a longer block size reaching the targeted molar mass (11800 g mol^{-1} compared to 6500 g mol^{-1} before). However, the shoulder was only slightly reduced. Nevertheless, the polymerization was stopped and the polymer was precipitated in ice cold Et_2O.

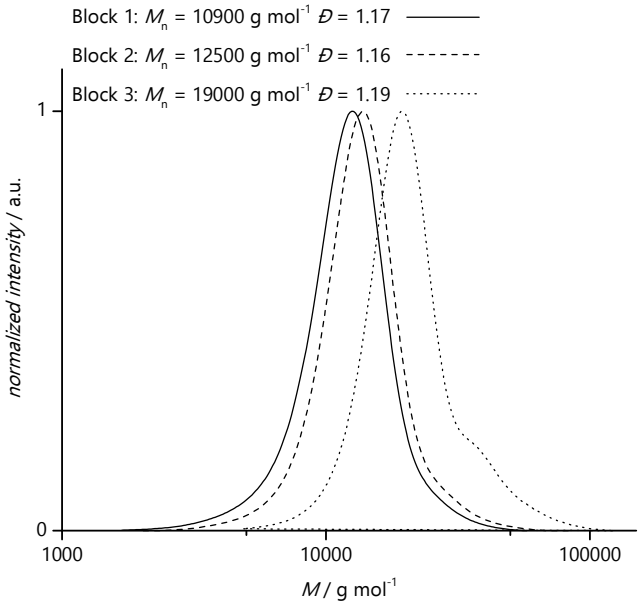

Figure 53: Size exclusion chromatograms derived from the first attempt of the one pot triblock formation. Targeted sequence: (PE-MA-*co*-MMA)$_{100}$-*b*-MMA$_{20}$-*b*-(PS-MA-*co*-MMA)$_{100}$. A well-controlled polymerization is evidenced for the first two blocks, resulting in the targeted molar mass and narrow dispersity. For the last block, the targeted molar mass was not reached and a high molar mass shoulder indicates a small amount of crosslinking due to the high viscosity of the polymerization mixture at the end of the RAFT process.

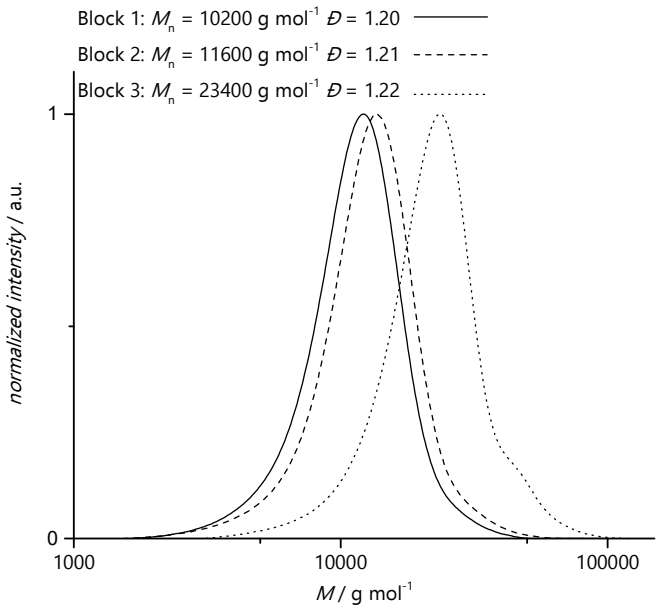

Figure 54: Size exclusion chromatograms derived from the second attempt of the one pot triblock formation. Targeted sequence: (PE-MA-*co*-MMA)$_{100}$-*b*-MMA$_{20}$-*b*-(PS-MA-*co*-MMA)$_{100}$. A well-controlled polymerization is again evidenced for the first two blocks, resulting in the targeted molar mass and narrow dispersity. For the last block, the targeted molar mass was reached this time and the high molar mass shoulder decreased slightly.

A ^{1}H NMR analysis of the resulting polymer compared to the monofunctional copolymers is illustrated in **Figure 55**. The depicted ^{1}H NMR spectra of the triblock copolymer evidences signals from both photoreactive groups, especially visible in the aromatic region between 8.1-6.5 ppm. The average content of both photomonomers in the respective block was deducted from the ^{1}H NMR spectrum to be 14 PE-MA (**8**) units in the first block and 15 PS-MA (**7**) units in the third block. After the synthesis of both monoblock functional copolymers as well as the dual functional triblock copolymer were successfully prepared by employing

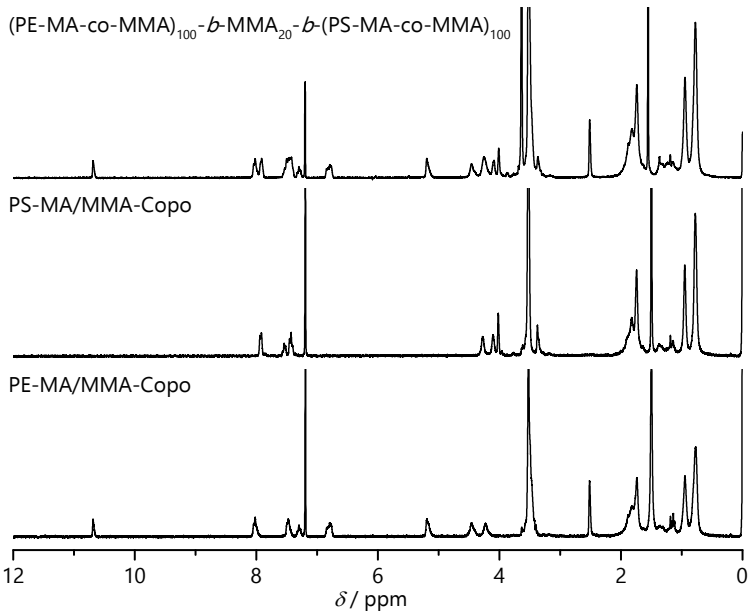

Figure 55: Comparison of ^{1}H NMR spectra (400 MHz, $CDCl_3$, ambient temperature) of the precipitated monofunctional copolymers (bottom and middle) with the obtained (PE-MA-co-MMA)$_{100}$-*b*-MMA$_{20}$-*b*-(PS-MA-co-MMA)$_{100}$ (top). A combination of both monofunctional copolymer spectra is visible in the block copolymer spectrum, especially in the aromatic region between 8.1-6.5 ppm.

a RAFT polymerization protocol, the obtained photoreactive materials were assessed for SCNP folding experiments in the next step of the project.

5.2 SCNP folding experiments with (dual) photoreactive polymers

Both of the obtained monoblock copolymers and the triblock copolymer were consecutively folded by a crosslinker assisted SCNP folding mechanism. The initially selected linkers and their reactivity with the photoreactive side groups are depicted in **Scheme 45**. For the

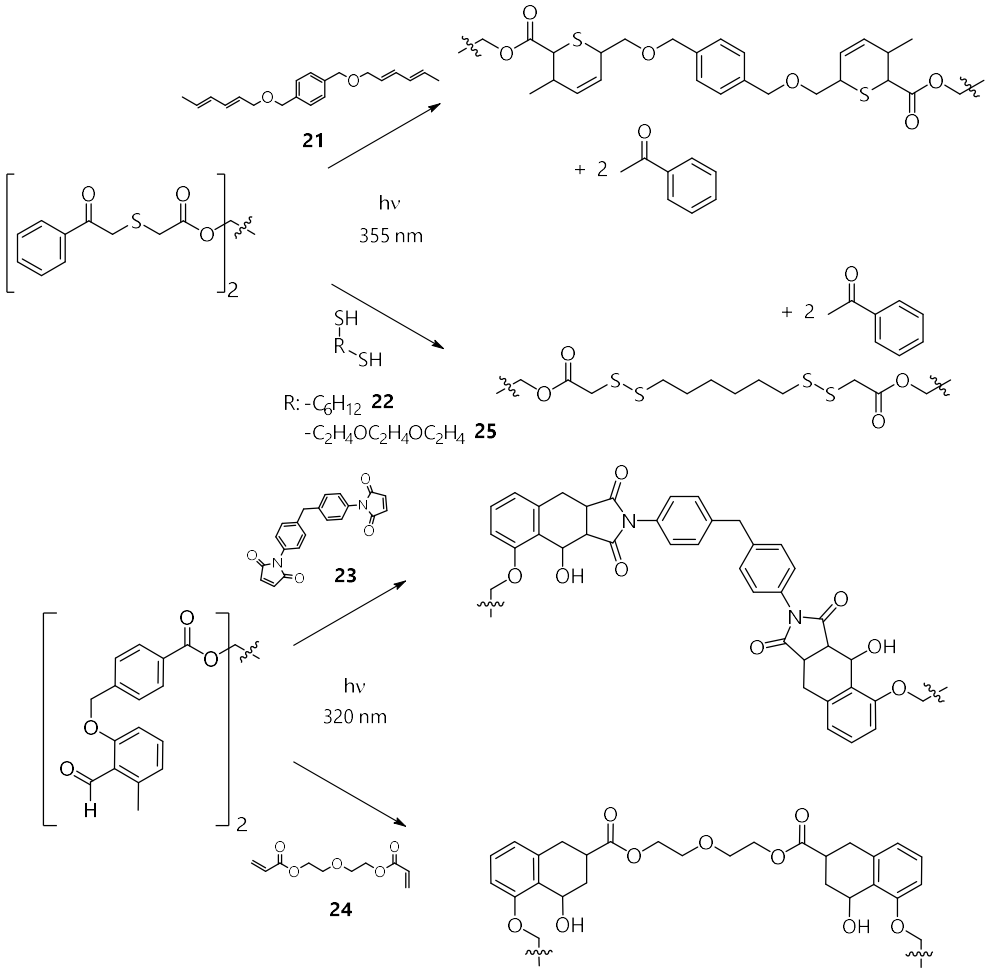

Scheme 45: Selected crosslinkers and photochemical reactions leading to the SCNP folding. Upper part: phenacyl sulfide chemistry, lower part: photoenol folding.

phenacyl sulfide based folding, a diene (1,4-bis((sorbinyloxy)methyl)benzene (**21**)) and a thiol based dilinker (1,6-hexanedithiol (**22**)) were selected as illustrated in **Scheme 45** (top row). In the lower part of Scheme **45**, the selected linkers for the photoenol folding are depicted. As reaction partners for the light induced Diels-Alder reaction, a dimaleimide (1,1′-(methylenedi-4,1-phenylene)bismaleimide (**23**)) and a diacrylate (di(ethylene glycol)diacrylate (**24**)) crosslinker were selected. The investigations of the folding processes

were conducted with the PS-MA-*co*-MMA polymers first, due to high yields and simple synthesis of the corresponding precursors.[#]

5.2.1 SCNP folding of PS-MA-*co*-MMA polymers

The first folding experiments were conducted employing (PS-MA-*co*-MMA)$_{100}$ (**P3**) obtained from the kinetic study described in Section 5.1.1 in combination with the diene crosslinker **21**. A solution of **P3** in DCM containing 1 mg polymer per mL, which is a typical concentration for crosslinker assisted SCNP folding, was prepared.[211-212] Per photoreactive unit, 0.5 eq of the crosslinker **21** were added to the polymer solution. The mixture was irradiated for 1 h employing an OmniCure S2000 UV Curing System with a suitable wavelength filter (320-390 nm) (for a detailed description see Section 7.2). The solvent was removed under reduced pressure and the resulting product was subjected to SEC analysis (**PS-SCNP(1)**). The precursor polymer and the folded polymer samples in this entire section were always measured directly after each other to avoid any variations caused by the SEC measurements and to ensure comparability of the individual samples. The result for the first folding experiment is depicted in **Figure 56**. The size exclusion chromatograms are plotted versus the retention time as it is common in SCNP related literature.[27] The solid line represents the polymeric precursor, the dashed line the result obtained after the irradiation.

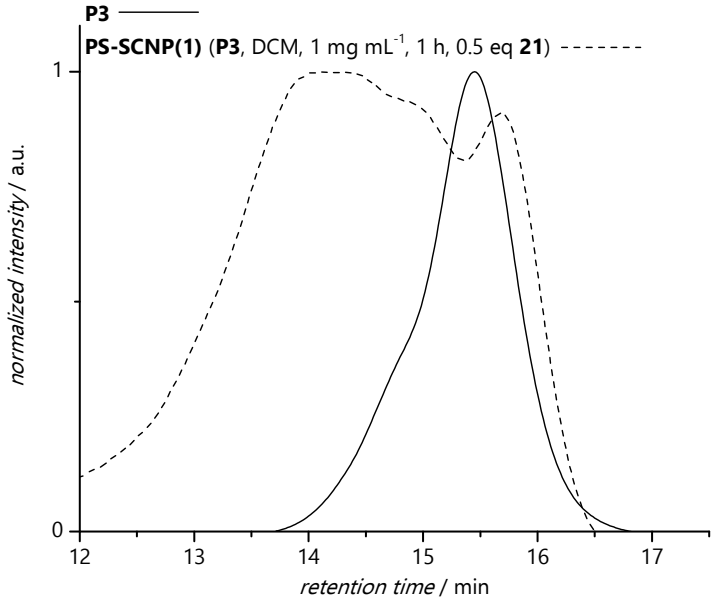

Figure 56: Size exclusion chromatograms obtained after the first SCNP folding experiments employing the (PS-MA-*co*-MMA)$_{100}$ precipitated from the initial PS-MA (**7**) kinetic study (**P3**, solid line) and crosslinker **21**. The dashed line represents the sample after the photoreaction. A shift to longer retention times is observed for the main polymer peak. However, an considerable amount of crosslinked material is detected at shorter retention times.

[#] Crosslinker **21** was kindly provided by M. Kaupp (KIT).

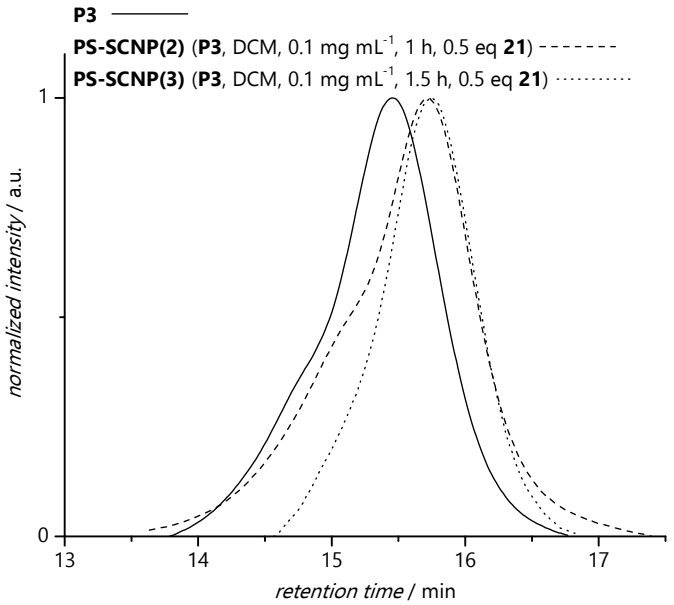

Figure 57: Size exclusion chromatograms obtained after the second and third SCNP folding experiments employing **P3**. The dashed line represents **PS-SCNP(2)** after the photoreaction. A shift to longer retention times is observed for the main polymer peak. However, still a pronounced shoulder hints crosslinked material. For **PS-SCNP(3)** a clean shift to higher retention times is detected.

A small shift to higher retention times indicates a partial SCNP formation. However, intense signals at shorter retention times indicate the presence of significant amounts of crosslinked material, hinting at a too high concentration of the reaction mixture. Therefore, the folding experiment was repeated twice with the same precursor and dilinker content, but with a concentration of 0.1 mg mL^{-1} in DCM. The solutions were irradiated for 1 h (**PS-SCNP(2)**) or 1.5 h (**PS-SCNP(3)**) respectively. The obtained SEC results are depicted in **Figure 57**. The trace obtained from **PS-SCNP(2)** indicates a shift to higher retention times while a pronounced shoulder at lower retention times is still apparent, evidencing crosslinked

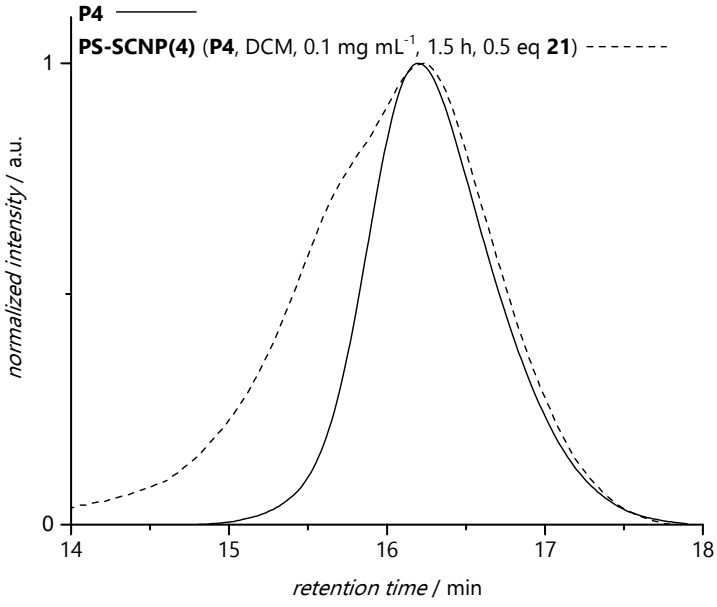

Figure 58: Size exclusion chromatograms obtained after the first SCNP folding experiment employing the new (PS-MA-*co*-MMA)$_{70}$ precursor without a shoulder (**P4**, solid line). The dashed line represents **PS-SCNP(4)** after the photoreaction. A high amount of crosslinked material is detected at shorter retention times.

material. In contrast, the graph for **PS-SCNP(3)** shows a clean shift to longer retention times. To ensure the reproducibility of the results, a further folding experiment was conducted after a new precursor (PS-MA-co-MMA)$_{70}$ (**P4**) was synthesized. The conditions for **PS-SCNP(3)** were repeated employing **P4** as precursor without a shoulder to achieve **PS-SCNP(4)**. The acquired SEC traces are illustrated in **Figure 58**. The measured chromatogram

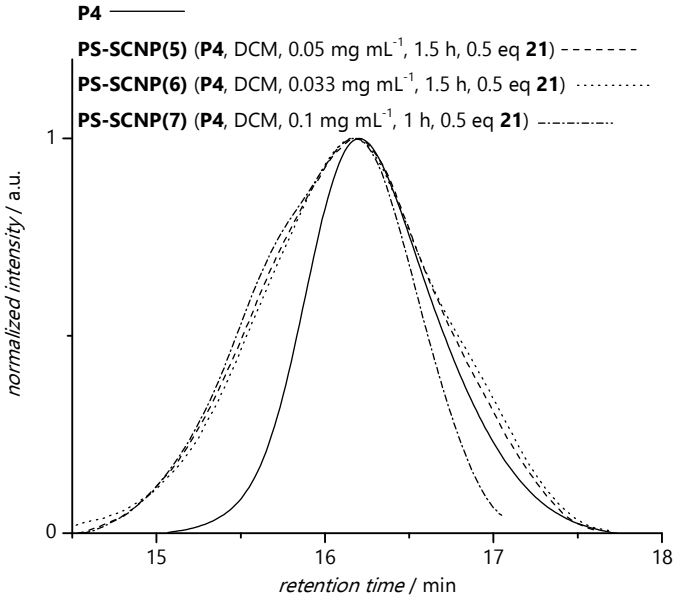

Figure 59: Size exclusion chromatograms obtained for SCNP folding experiments employing precursor **P4** solid line) and crosslinker **21**. The dashed line represents **PS-SCNP(5)**, the dotted line **PS-SCNP(6)** and the dash-dotted line **PS-SCNP(7)**. In all SEC traces, crosslinking is evidenced by a broadening of the SEC traces in comparison to the precursor.

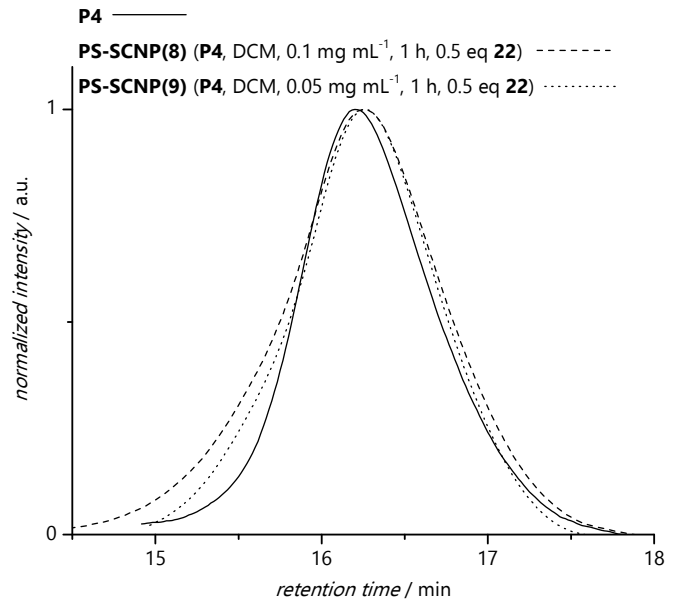

Figure 60: Size exclusion chromatograms obtained for SCNP folding experiments employing precursor **P4** solid line) and crosslinker **22**. The dashed line represents **PS-SCNP(8)**, the dotted line **PS-SCNP(9)**. The chromatograms evidence a reduced amount of crosslinking in comparison to the previous experiments.

indicates that the new precursor exhibits a lower molar mass than the one employed before (DP_n 70 instead of DP_n 100). For the irradiated sample, a high amount of crosslinked material is evidenced again.

Consecutively, further experiments with **P4** as precursor were conducted with an increased dilution of the reaction mixture from 0.1 g mL^{-1} to 0.05 g mL^{-1} (**PS-SCNP(5)**) or 0.033 g mL^{-1} (**PS-SCNP(6)**) respectively, while maintaining the other parameters constant. Additionally, another experiment with 0.1 mg mL^{-1} and a shortened irradiation time (**PS-SCNP(7)**) was performed (conditions as for **PS-SCNP(2)**). The obtained SEC results are summarized in **Figure 59**. For all curves, a broadening in comparison to the precursor chromatogram indicates the presence of crosslinked material. No shift of the main peak to shorter retention times is observable for any of the experiments. After none of the employed conditions utilizing crosslinker **21** lead to the desired results, in a next set of experiments, 1,6-hexanedithiol **22** was used as crosslinker. For the first experiment, **PS-SCNP(8)**, the conditions were adopted from **PS-SCNP(7)** (0.1 mg mL^{-1}, 0.5 eq crosslinker, DCM, 1 h irradiation) whilst the concentration was reduced to 0.05 mg mL^{-1} for **PS-SCNP(9)**. The resulting SEC traces are illustrated in **Figure 60**. The amount of crosslinking (i.e., material detected at lower retention times) is reduced for both samples in comparison to the former approaches employing crosslinker **21**, however still prominent. A slight shift to higher retention times indicates a partial SCNP folding. It seems apparent that with the short (PS-MA-*co*-MMA)$_{70}$ no clean shift can be achieved without partial crosslinking. Therefore, a new (PS-MA-*co*-MMA)$_{100}$ (**P5**) was synthesized as described in Chapter 5.1.1. A new set of experiments was conducted employing 0.5 eq of crosslinker **21**, a concentration of 0.05 mg mL^{-1} and an irradiation time of 1 h. For **PS-SCNP(10)** DCM was used as solvent, whereas MeCN was utilized for **PS-SCNP(11)**. For **PS-SCNP(12)** DCM was employed as well, but the concentration was decreased to 0.01 mg mL^{-1}. **Figure 61** depicts the resulting size exclusion chromatograms for these experiments. The chromatogram for the new precursor indicates a higher molar mass as for **P4**, a DP_n of 100 is reached (see Chapter 5.1.1). The curves for

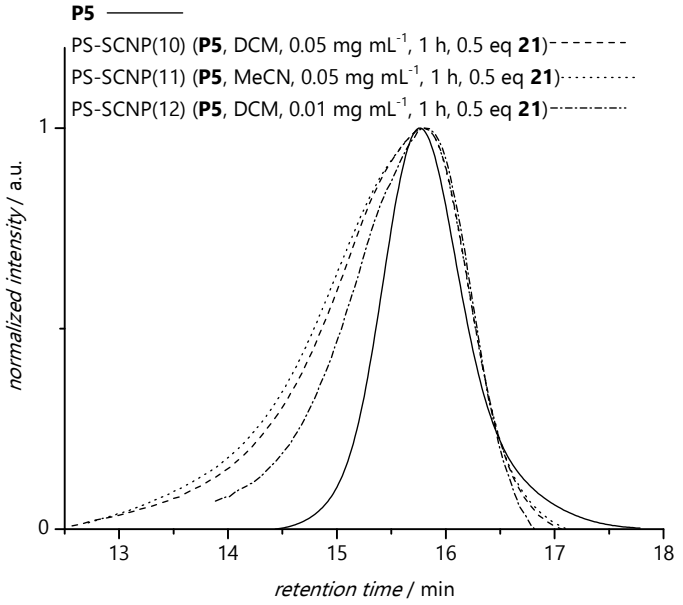

Figure 61: Size exclusion chromatograms obtained for SCNP folding experiments employing the freshly synthesized (PS-MA-*co*-MMA)$_{100}$ precursor (**P5**, solid line) and crosslinker **21**. The dashed line represents **PS-SCNP(10)**, the dotted line **PS-SCNP(11)** and the dash-dotted line **PS-SCNP(12)**.

PS-SCNP(10) and **PS-SCNP(11)** resemble each other evidencing a pronounced shoulder at shorter retention times. The chromatogram obtained for **PS-SCNP(12)** indicates a decreased amount of crosslinked material as the shoulder at lower retention times decreases. However, the measurement was again affected by a low concentration of the SEC sample. These results clearly indicate that a lower precursor concentration can reduce crosslinking significantly. In comparison to the results achieved for crosslinker **21** (Figure 59), it is apparent that crosslinker **22** leads to a lower amount of crosslinking. Therefore, in a consecutive set of folding experiments, crosslinker **22** was employed together with the longer (PS-MA-*co*-MMA)$_{100}$ precursor **P5**. For **PS-SCNP(13)** a concentration of 0.1 mg mL^{-1} in DCM and 0.3 eq of the crosslinker were irradiated for 1 h. The same conditions were utilized for **PS-SCNP(14)**, yet the concentration was decreased to 0.02 mg mL^{-1}. The obtained SEC results are depicted in **Figure 62**. For both folding experiments a small shift to higher retention times, i.e., smaller hydrodynamic volume, is observed. Again, in comparison to the experiments employing the diene crosslinker **21**, the amount of cross-linked material was reduced significantly as evidenced by a decreased intensity of the shoulder at shorter retention times. When comparing the structural features of both crosslinkers, it is apparent that the alkyl chain derived dithiol crosslinker is more flexible then the rather rigid diene crosslinker. The more flexible nature seems to help forming the SCNPs. However, any leftover, non-reacted thiol groups from crosslinker **22** might form disulfide bridges during workup (concentration under reduced pressure) leading to a crosslinking of the material after the actual photoreaction. Therefore, in a next set of folding reactions, 5 eq of a thiol capping agent, 2,2′-dipyridyl disulfide (DPS) were added to the reaction mixture after the irradiation and stirred for 15 min prior to a concentration under vacuum. For **PS-SCNP(15)** the same conditions as for **PS-SCNP(14)** were utilized, but additionally the DPS was added as aforementioned. The folding experiment **PS-SCNP(16)** was performed alike

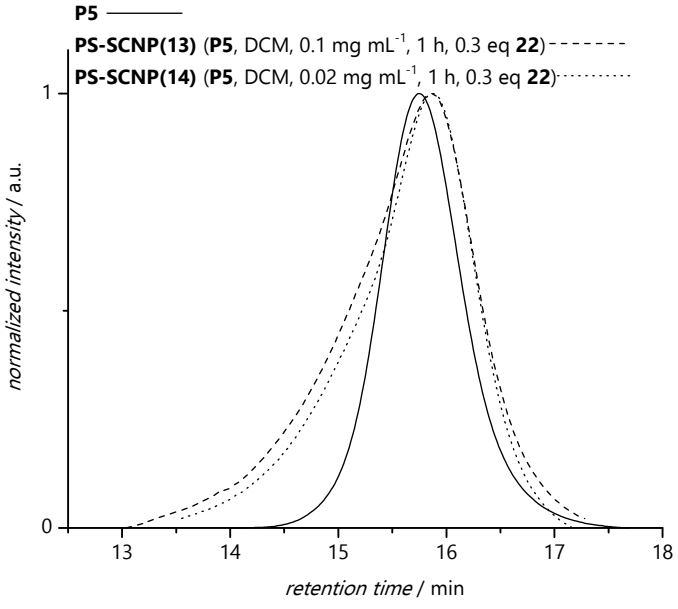

Figure 62: SEC chromatograms obtained for SCNP folding experiments employing **P5** as precursor (solid line) and crosslinker **22**. The dashed line represents **PS-SCNP(13)**, the dotted line **PS-SCNP(14)**.

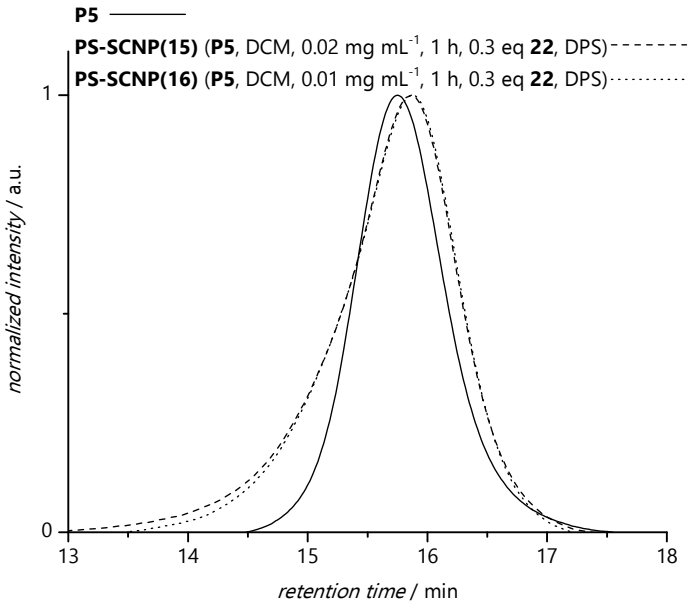

Figure 63: Size exclusion chromatograms obtained for SCNP folding experiments employing **P5** as precursor (solid line) and crosslinker **22**. The dashed line represents **PS-SCNP(15)**, the dotted line **PS-SCNP(16)**. The chromatograms evidence a reduced amount of crosslinking in comparison to **PS-SCNP(14)**.

but the concentration was decreased again to 0.01 mg mL^{-1}. SEC chromatograms for both folding experiments are depicted in **Figure 63**. Again, a small shift to longer retention times is observable, hinting a possible SCNP formation. The crosslinking was reduced as well by employing the thiol capper, however, a small shoulder at shorter retention times remained. All of the aforementioned SEC measurements were performed on an Agilent 390 LC MDS instrument at the University of Warwick, where the first part of the project was conducted. The following data presented in this Section 5.2.1 was measured on a Polymer Laboratories (Varian) PL-SEC 50 Plus Integrated System (for more details, refer to Chapter 7.2) at the KIT. Also, the UV light source was therefore changed from the aforementioned OmniCure® S2000 UV Curing System to the Philips Cleo PL-L lamp also employed in Chapter 4 (detailed descriptions see Section 7.2).

For achieving a larger shift with decreased crosslinking, a longer, but equally flexible dithiol linker 3,6-dioxa-1,8-octane dithiol (**25**) was applied. For **PS-SCNP(17)**, a concentration of 0.01 mg mL^{-1} in DCM with 0.3 eq of **25** as crosslinker, 5 eq DPS as capper and an irradiation time of 1 h was employed. In the folding experiment **PS-SCNP(18)**, the solvent was changed to THF, as it reduces swelling of the polymer chains in comparison to DCM and therefore may lead to a stronger SCNP compaction. To ensure a complete solvation of the polymer strands, the polymer solution was stirred for 30 min prior to the irradiation. The obtained size exclusion chromatograms are depicted in **Figure 64**, accompanied by the SEC trace of the precursor **P5**. The latter exhibits a slight high molar mass shoulder at shorter retention times, suggesting a degradation of the polymeric precursor upon storage. The SEC trace for **PS-SCNP(17)** displays a partial shift to higher retention times, however, a shoulder congruent with the precursor remained, hinting at the fact that the reaction had been stopped before reaching 100 % conversion. Therefore, the irradiation time was increased to

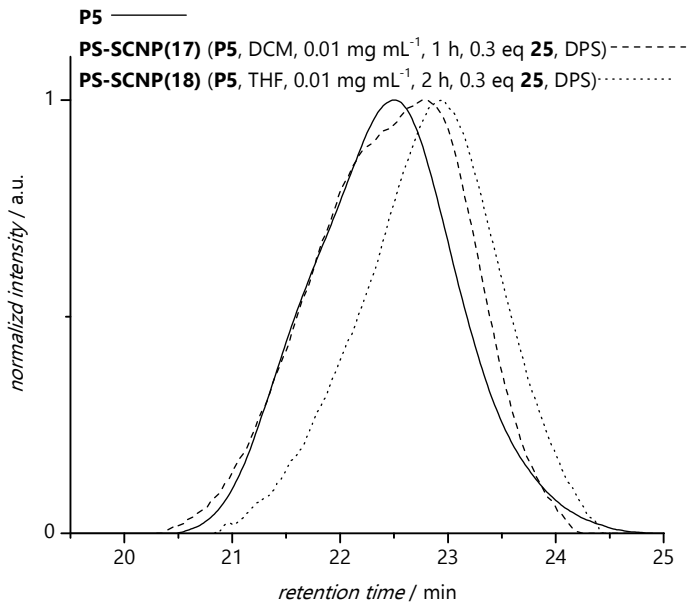

Figure 64: Size exclusion chromatograms obtained for SCNP folding experiments employing **P5** as precursor (solid line) and crosslinker **25**. The dashed line represents **PS-SCNP(17)**, the dotted line **PS-SCNP(18)**.

2 h for **PS-SCNP(18)**. Together with the application of THF as solvent, a strong, clean shift of the SEC trace compared to the precursor was achieved, evidencing a successful SCNP compaction.

As next step, a new precursor with an even higher DP_n was synthesized as described in Chapter 5.1.1. (PS-MA-*co*-MMA)$_{200}$ (**P6**) was obtained and subsequently subjected to a SCNP folding experiment employing exactly the same conditions as for **PS-SCNP(18)**, yielding **PS-SCNP(19)**. The resulting SEC traces are depicted in **Figure 65**. The chromatogram depicted as a dashed line indicates a shift to longer retention times, but also an incomplete compaction. Two more experiments were therefore performed with longer irradiation times of 3 h and 4 h respectively, yielding **PS-SCNP(20)** and **PS-SCNP(21)**. Both

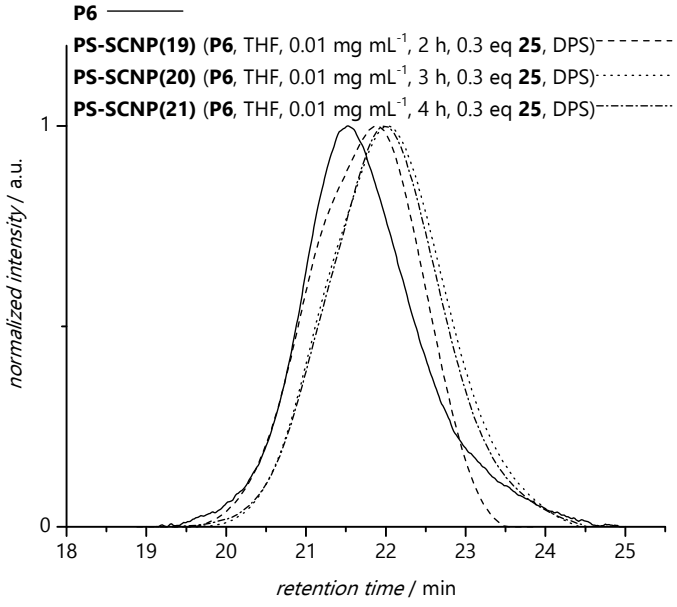

Figure 65: Size exclusion chromatograms obtained for SCNP folding experiments employing a (PS-MA-*co*-MMA)$_{200}$ precursor (**P6**, solid line) and crosslinker **25**. The dashed line represents **PS-SCNP(19)**, the dotted line **PS-SCNP(20)** and the dash-dotted line **PS-SCNP(21)**.

obtained size exclusion chromatograms, depicted as dotted and dash-dotted lines in Figure 65, indicate a strong and clean shift to longer retention times.

These results prove that a successful SCNP formation can also be achieved for the longer precursor polymer (**P6**). To corroborate the obtained compaction results, dynamic light scattering (DLS) measurements were performed for **P6** and **PS-SCNP(20)**. The polymers were dried and dissolved in MeCN (1 mg mL^{-1}). The samples were filtered twice. The obtained DLS number-weighted distributions of the respective hydrodynamic diameters *D* are depicted in **Figure 66**.

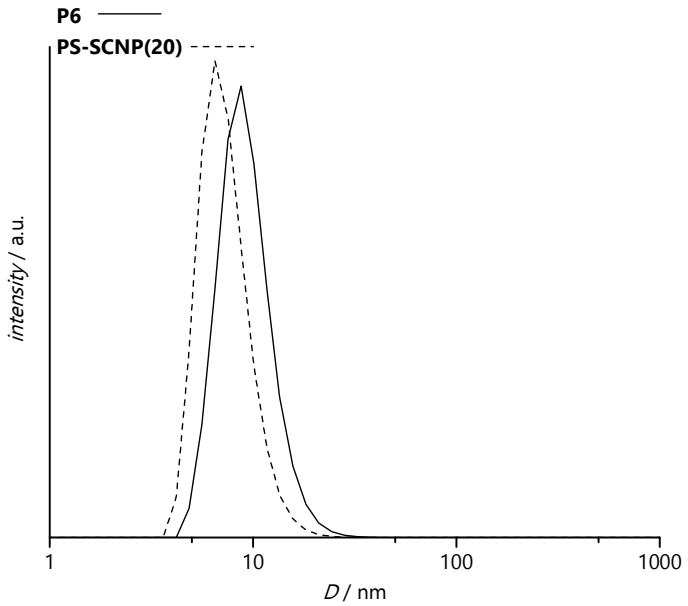

Figure 66: Number-weighted distributions obtained from DLS measurements of **P6** and **PS-SCNP(20)** in MeCN (1 mg mL^{-1}).

For both samples, monomodal distributions were obtained. A clean shift to smaller hydrodynamic diameters is observed for the **PS-SCNP(20)** in comparison to the polymeric precursor **P6**. Both characterization methods prove a successful SCNP formation for the phenacyl sulfide containing copolymers. In parallel to the PS-SCNP experiments, folding reactions for the photoenol containing polymeric precursors were conducted.

5.2.2 SCNP folding of PE-MA-*co*-MMA polymers

As for the PS-MA-*co*-MMA folding, the initial irradiation experiments were performed employing a (PE-MA-*co*-MMA)$_{100}$ (**P7**) resulting from the kinetic study described in Section 5.1.2. The polymer was dissolved in DCM maintaining a concentration of 0.1 mg mL^{-1} and 0.5 eq of bismaleimide **23** (which was utilized as crosslinker) were added. The mixture was irradiated employing the aforementioned OmniCure® S2000 UV Curing System for 1 h. The obtained size exclusion chromatograms are depicted in **Figure 68**. In comparison to the precursor SEC trace (**P7**), a distinct high molar mass shoulder is detected for **PE-SCNP(1)**, evidencing high amounts of crosslinked material.

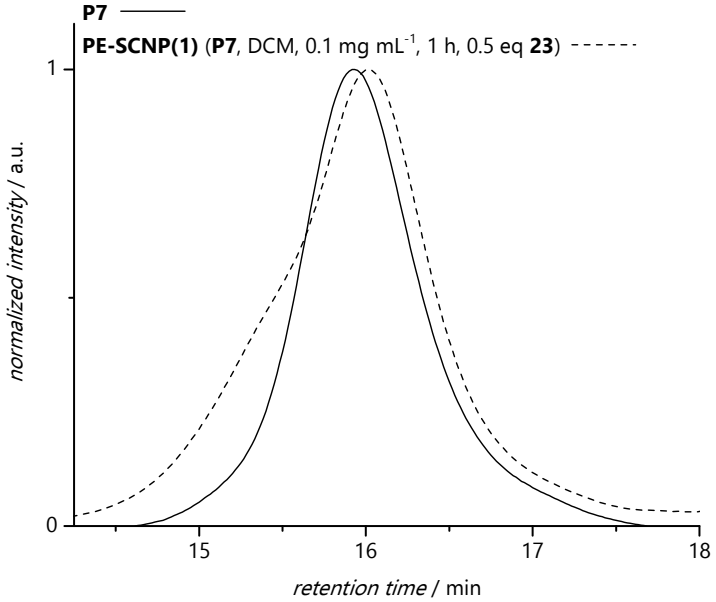

Figure 68: Size exclusion chromatograms obtained for the first PE-SCNP folding experiment employing **P7** as precursor (solid line) and crosslinker **23**. The dashed line represents **PE-SCNP(1)**.

For the subsequent folding experiments, additional (PE-MA-co-MMA)$_{100}$ (**P8**) was synthesized according to the procedure described in Section 5.2.1. In the following set of folding reactions, the dilution of the mixture was increased to 0.025 mg mL^{-1} and the irradiation time was prolonged to 2 h (**PE-SCNP(2)**) and 3 h (**PE-SCNP(3)**) respectively, to ensure a complete photoreaction. For a third irradiation (**PE-SCNP(4)**), the concentration was further decreased to 0.016 mg mL^{-1}. DCM was utilized as solvent and for all samples crosslinker **23** was employed. The resulting SEC traces are depicted in **Figure 67**. The graph for **PE-SCNP(2)** exhibits a distinct shoulder at shorter retention times, although less pronounced as the shoulder of the trace for **PE-SCNP(1)** (compare Figure 68). For **PE-SCNP(3)** and **PE-SCNP(4)** the high molar mass shoulder is significantly decreased.

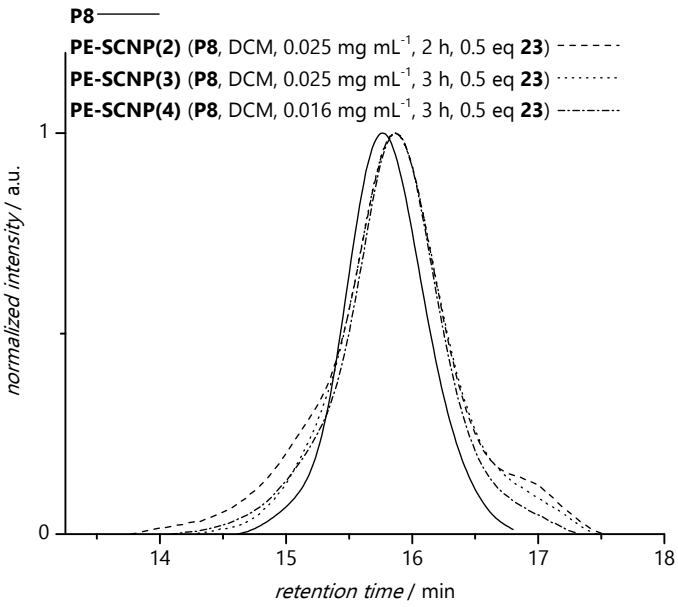

Figure 67: Size exclusion chromatograms obtained for the second set of PE-SCNP folding experiment employing **P8** as precursor (solid line) and crosslinker **23**. The dashed line represents **PE-SCNP(2)**, the dotted line **PE-SCNP(3)** and the dash-dotted line **PE-SCNP(4)**.

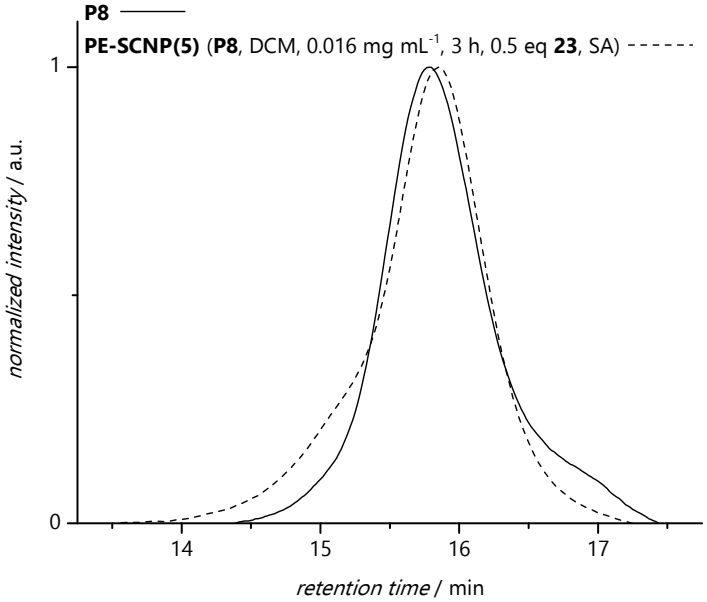

Figure 69: SEC chromatograms obtained for PE-SCNP folding experiment employing a **P8** as precursor (solid line) with dilinker **23** and sorbic acid (SA) endcapper. The dashed line represents **PE-SCNP(5)**.

However, especially for **PE-SCNP(2)** and **PE-SCNP(3)**, a broadening of the distributions is apparent. In a consecutive experiment (**PE-SCNP(5)**), sorbic acid (SA) as capping agent for non-reacted maleimide units was added, to trap the free maleimides in a Diels–Alder fashion. All other conditions were kept the same as for **PE-SCNP(4)**. The results are depicted in **Figure 69**. When comparing the result for **PE-SCNP(5)** with the SEC trace of the polymeric precursor, a shoulder at a shorter retention time indicates the formation of crosslinked material. Compared to **PE-SCNP(4)**, the amount of crosslinking appears to be increased. The precursor itself exhibits a shoulder at longer retention time, hinting at the degradation of the photoreactive polymer. Therefore, a new batch of the (PE-MA-*co*-MMA)$_{100}$ precursor (**P9**) was synthesized employing the RAFT protocol described in Section 5.1.2.

As in the previous Section 5.2.1, all experiments so far were performed on an Agilent 390 LC MDS instrument at the University of Warwick, where the first part of the project was conducted. The data presented from now on, however, was collected on a Polymer Laboratories (Varian) PL-SEC 50 Plus Integrated System (for more details, refer to Section 7.2) at the KIT. Also, the UV light source was therefore changed from the aforementioned OmniCure® S2000 UV Curing System to the Arimed B6 lamp (detailed descriptions see Section 7.2).

In the next folding experiments, conditions similar to those employed for the successful collapse of the PS-MA-*co*-MMA described in Section 5.2.1, were investigated. THF was employed as solvent at a concentration of 0.01 mg mL^{-1} and 0.3 eq of crosslinker **23** were added to the mixture. **PE-SCNP(6)** was irradiated for 1 h, **PE-SCNP(7)** for 2 h. The obtained size exclusion chromatograms accompanied by the SEC trace of the freshly synthesized **P9** precursor are depicted in **Figure 70**. For both compactions, the formation of a high molar mass shoulder evidences a high amount of crosslinked material. However, for the prolonged irradiation time, a decreased shift and an increased amount of crosslinked material is

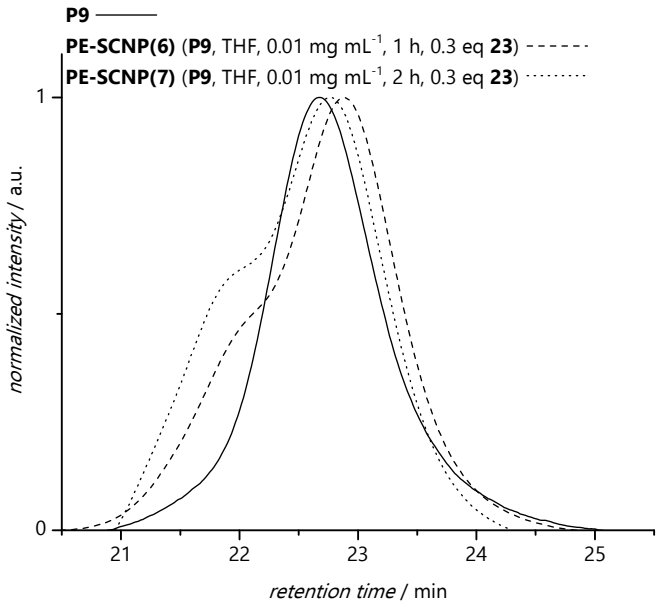

Figure 70: Size exclusion chromatograms obtained for PE-SCNP folding experiment employing **P9** as precursor (solid line) with dilinker **23**. The dashed line represents **PE-SCNP(6)**, the dotted **PE-SCNP(7)**.

observed. When comparing the results to the previous experiments conducted in DCM, it can be concluded that THF is not an appropriate solvent for the PE-SCNP photoreactions. Therefore, MeCN was utilized as solvent in the next set of folding experiments. For **PE-SCNP(8)**, a concentration of 0.025 mg mL^{-1}, 0.3 eq of **23** and an irradiation time of 1 h were employed. The concentration was decreased for **PE-SCNP(9)** to 0.01 mg mL^{-1} and 1 eq of DPS was added as endcapper while the rest of the conditions were retained. The endcapper was added since the irradiated polymer samples had lost their color, indicating the decomposition of the RAFT end group, possibly forming a thiol. The latter could interfere with the maleimide based crosslinker and was therefore trapped by DPS. The resulting SEC chromatograms for both photoinduced folding processes are illustrated in **Figure 71**. Shifts

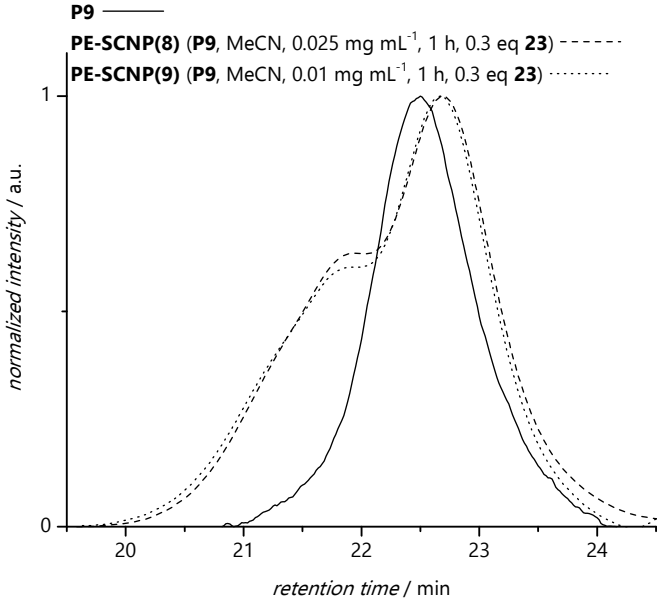

Figure 71: SEC chromatograms obtained for PE-SCNP folding experiment employing precursor **P9** with dilinker **23** in MeCN. The dashed line represents **PE-SCNP(8)**, the dotted **PE-SCNP(9)**.

of the maximum to a higher retention time accompanied by pronounced shoulders at shorter retention time are observed for both folding experiments. For the more diluted samples, a lesser amount of crosslinking is observed. However, in comparison to the results obtained for photoreactions in DCM, the shoulders arising from crosslinked material are still higher when employing MeCN.

Therefore, for the following experiments, the solvent was changed back to DCM. In analogy to the previous chapter, the crosslinker with a dibenzylic core **23**, which was employed up to this point, was replaced with a more flexible di(ethylene glycol) diacrylate linker **24**. For **PE-SCNP(10)**, a dilution of 0.02 g mL^{-1} and 0.3 eq of crosslinker **24** were employed. The mixture was irradiated for 1 h. For **PE-SCNP(11)** those conditions were retained, but 1 eq of DPS was added after the irradiation. In the folding experiment **PE-SCNP(12)**, the conditions for **PE-SCNP(11)** were used, with a decreased concentration to 0.01 mg mL^{-1}. The corresponding SEC traces are depicted in **Figure 72**. For all three foldings, a distinct shift of the peak maximum to smaller hydrodynamic volume, i.e., higher retention time is observed hinting at a successful chain compaction. The SEC trace for **PE-SCNP(10)** additionally evidences a pronounced shoulder at shorter retention time. The addition of the endcapper for a possible UV light induced RAFT agent degradation resulted in a dramatic reduction of the high molar mass shoulder as evidenced in the graphs for **PE-SCNP(11)** and **PE-SCNP(12)**. However, the increased dilution did not change the outcome of the photoreaction. Additionally, it is apparent that the more flexible crosslinker **24** causes less inter chain crosslinking than the more rigid crosslinker **23**.

For a further optimization, in the consecutive folding experiment based on the conditions for **PE-SCNP(12)**, crosslinker **24** was added in two portions. The first half was added prior to the irradiation, the second half after 30 min for a total irradiation time of 1 h. The SEC

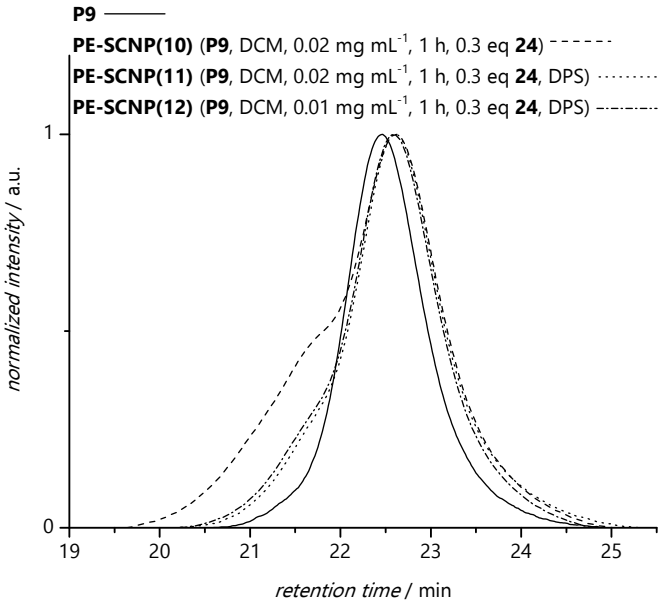

Figure 72: Size exclusion chromatograms obtained for the first set of PE-SCNP folding experiment employing precursor **P9** and crosslinker **24**. The dashed line represents **PE-SCNP(10)**, the dotted **PE-SCNP(11)** and the dash-dotted line represents **PE-SCNP(12)**.

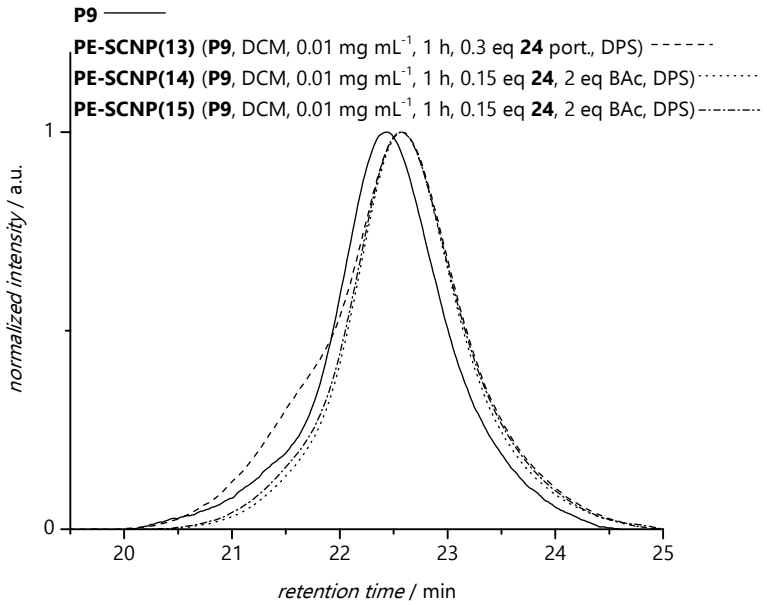

Figure 73: Size exclusion chromatograms obtained for PE-SCNP folding experiments employing precursor **P9** and crosslinker **24**. The dashed line represents **PE-SCNP(13)**, the dotted line represents **PE-SCNP(14)** and the dash-dotted line represents **PE-SCNP(15)**.

results for **PE-SCNP(13)** are depicted in **Figure 73**. A high molar mass shoulder accompanying a shift of the peak maximum is observed again. For the next folding attempt, instead of adding the second half of the crosslinker **24** after 30 min, 2 eq of butyl acrylate as monofunctional capper was employed. The solution was irradiated for another 30 min and the obtained SEC results for **PE-SCNP(14)** are depicted in Figure 73 (dotted line). A clean shift of the entire chromatogram to higher retention times without any shoulder evidences the successful SCNP folding of the **P9** precursor. For **PE-SCNP(15)**, the same conditions as for **PE-SCNP(14)** were employed to assess the reproducibility of the folding. The obtained size exclusion chromatogram is depicted in Figure 73 (dash-dotted line), and proves a successful and identical SCNP compaction. To confirm the folding results obtained by SEC, again DLS measurements were performed as described for the PS-MA system. The obtained number-weighted distributions for the (PE-MA-co-MMA)$_{100}$ precursor (**P9**) and for **PE-SCNP(15)** are illustrated in **Figure 74**. For both samples a monomodal distribution was obtained. A clear shift of the distribution to smaller hydrodynamic diameters is witnessed for **PE-SCNP(15)** in comparison to the distribution of **P9**. As for the phenacyl sulfide photofolding, the photoenol based light induced SCNP formation is thus proven by SEC as well as DLS measurements. After the successful foldings for both single photoreactive copolymers, the sequential compaction of a dual photoreactive triblock copolymer was investigated.

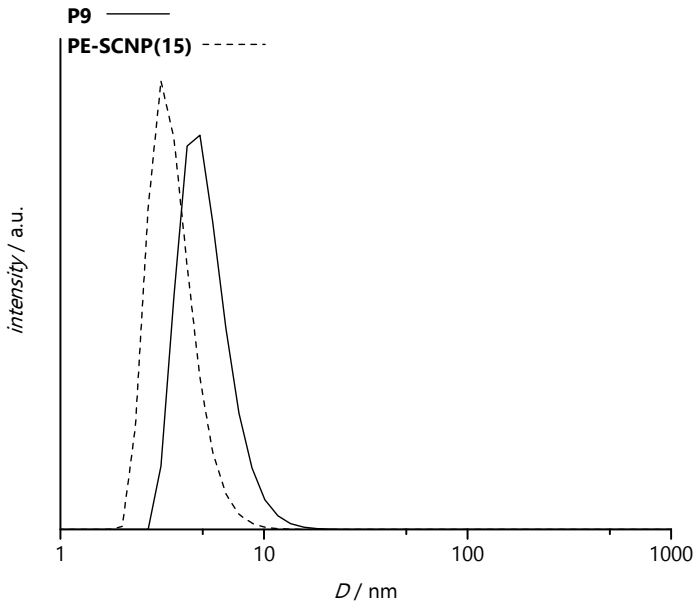

Figure 74: Number-weighted distributions obtained from DLS measurements of **P9** and **PE-SCNP(15)** in MeCN (1 mg mL^{-1}).

5.2.3 Stepwise compaction of a dual photoreactive triblock copolymer

In the two previous sections, conditions for light triggered compactions of the monofunctionalized polymers were established. Subsequently, these conditions were employed to achieve the two-step compaction of the dual photoreactive triblock copolymer introduced in Section 5.1.3. To obtain a stepwise folding based on the photoreactive blocks independently, the photoenol containing block needed to be protected prior to the light induced phenacyl sulfide reaction. Otherwise, both photoreactive moieties would be activated at the same time allowing them to react with each other. The phenacyl sulfide forms an ene upon irradiation, whereas an enol (diene component) is formed upon irradiation of the α-methylbenzaldehyde. When encountering each other in solution, the two activated distinct photomonomer units would therefore react with each other in a Diels–Alder reaction. In an initial approach, the photoenol precursor (a benzaldehyde) was protected by imine formation as depicted in **Scheme 46**. This is a recently established strategy for deactivating the photoreactivity of the photoenol.[213] Hence, to protect the (PE-MA-co-MMA)$_{100}$ (**P9)**, the polymer was dissolved in MeCN (2.5 mg mL^{-1}) and 1 eq of DPS

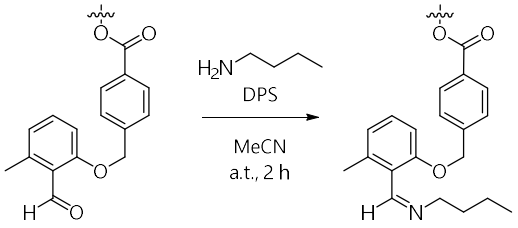

Scheme 46: Photoenol protection by imine formation employing butyl amine. A similar procedure as described in Ref. [213] was utilized.

was added as quenching reagent for the thiol moiety originating from the aminolysis of the RAFT agent. 4 eq of butyl amine were added to the reaction mixture and the solution was stirred for 2 h at ambient temperature. Subsequently, the volatile components were removed under reduced pressure and the obtained solid residue was analyzed via ^{1}H NMR spectroscopy. The resulting spectrum is presented in **Figure 75**. The absence of a signal around 11 ppm and a new resonance at 8.6 ppm (highlighted in the dashed fame) for the forms imine indicates successful conversion of the aldehyde moiety (compare Figure 52,

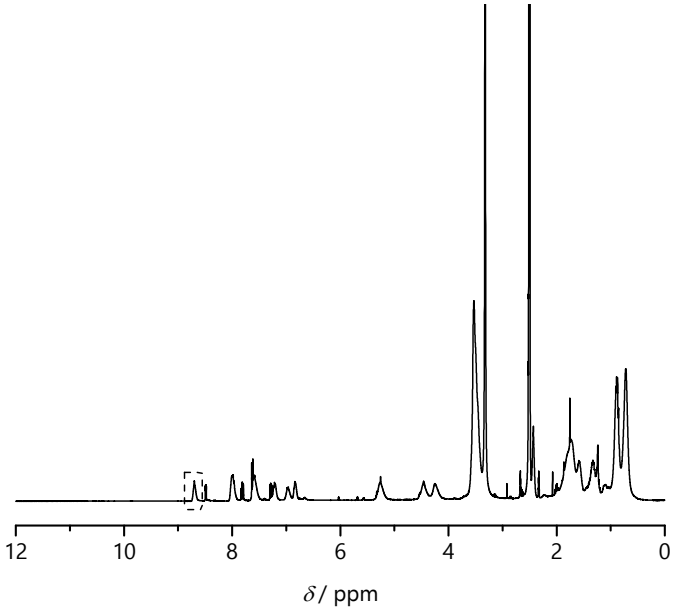

Figure 75: ^{1}H NMR spectrum (400 MHz, $CDCl_3$, ambient temperature) of **P9** after the conversion of the aldehyde moiety in an imine.

Chapter 5.1.2). Consequently, the protection reaction was performed on the triblock copolymer synthesized in Section 5.1.3. The same conditions as for **P9** were employed. A ^{1}H NMR spectrum and a size exclusion chromatogram of the protected (PE-MA-co-MMA)$_{100}$-*b*-MMA$_{20}$-*b*-(PS-MA-co-MMA)$_{100}$ polymer (**P10**) is depicted in **Figure 76**. Again, a strong decrease of the proton resonance associated with the aldehyde and a new resonance at 8.6 ppm (highlighted in the dashed frame) for the imine moiety, indicates a successful protection. The size exclusion chromatogram of **P10** is in good agreement with the SEC trace depicted in Figure 54, however indicating that the protection causes slight crosslinking as evidenced by a slightly increased shoulder at high molar masses. The obtained protected triblock copolymer **P10** was subsequently employed for the light induced folding reaction of the phenacyl sulfide containing block. The established conditions for the folding of a PS-MA-*co*-MMA were utilized (see conditions for **PS-SCNP(20)**, Section 5.2.1). After irradiation, the solvent was removed under reduced pressure and half of the collected solid was analyzed by SEC, while the other half was reserved for the second compaction reaction. The recorded size exclusion chromatogram of **PS-compacted-P10** is depicted in **Figure 77** accompanied by one derived from the non folded precursor **P10** for comparison.

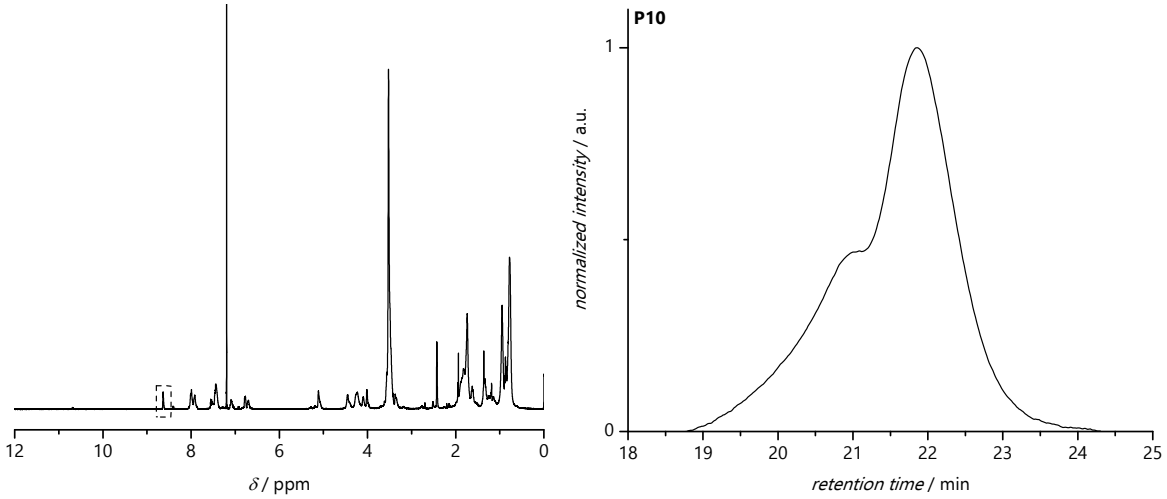

Figure 76: ^{1}H NMR spectrum (400 MHz, $CDCl_3$, ambient temperature) and SEC chromatogram (THF, 35 °C) of protected (PE-MA-co-MMA)$_{100}$-*b*-MMA$_{20}$-*b*-(PS-MA-co-MMA)$_{100}$ (**P10**).

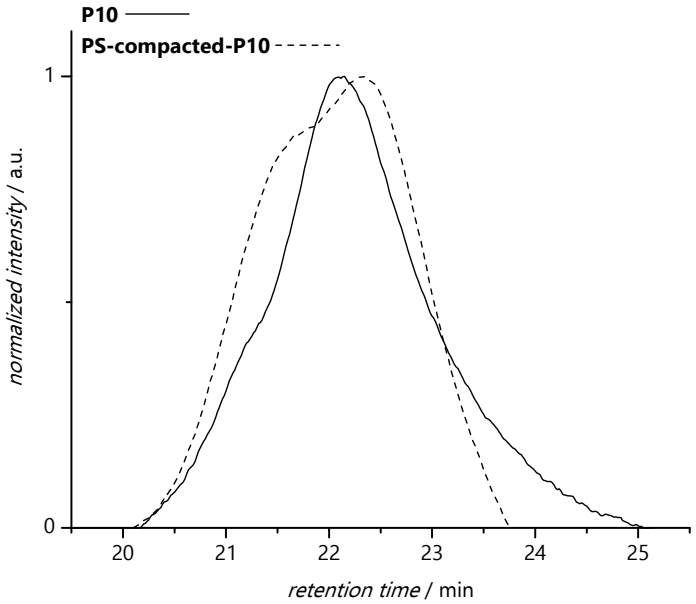

Figure 77: Size exclusion chromatograms (THF, 35 °C) obtained for the first compaction experiments of the triblock copolymer. The solid line represents the protected triblock copolymer (**P10**), the dashed line represents the partially folded **PS-compacted-P10**.

A significant amount of crosslinked material is indicated by a pronounced shoulder at shorter retention times. Possible explanations are that either the imine protection is not sufficiently stable to sustain the conditions during the photoreaction and is hydrolyzed, or that the generated thioaldehyde reacts with it in a nucleophilic substitution reaction. Both cases would produce crosslinking during the folding experiments. Therefore, a second protection strategy for the aldehyde moiety of the α-methylbenzaldehyde was applied utilizing an acetalization protocol (see **Scheme 47**). A previously established protocol for the protection of the employed α-methylbenzaldehyde was applied.[214] The triblock copolymer was dissolved in a mixture of dry MeCN/MeOH (5:1 v/v) with a concentration of 3.3 mg mL^{-1} over dry molecular sieve (4 Å). 20 eq of triethyl orthoformate (TMOF) and 0.16 eq of tosylic acid (TosOH) were added and the reaction mixture was stirred at 40 °C overnight. Subsequently, 5.5 eq of 2,6-lutidine were added and the solvent was removed

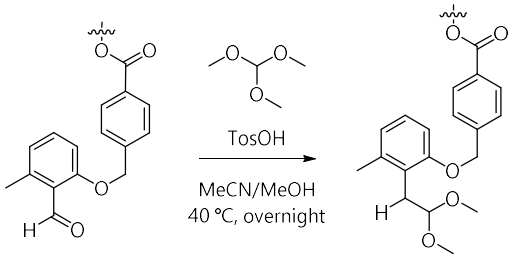

Scheme 47: Photoenol protection as acetal employing trimethyl orthoformate (TMOF) and tosylic acid (TosOH). A similar procedure as described in Ref.[214] was utilized.

under reduced pressure. A crude ^{1}H NMR spectrum and size exclusion chromatogram of the obtained protected triblock **P11** are depicted in **Figure 78**. The polymer distribution of **P11** retained its size and shape as can be appreciated from the SEC trace, while the strong decrease of the peak intensity derived from the aldehyde proton indicates a successful protection. The acetal protected triblock copolymer (**P12**) was resynthesized employing the aforementioned procedure and directly utilized for photocompaction experiments. Again the PS block was compacted first, applying the conditions reported for **PS-SCNP(20)** in Section 5.2.1, with adding 0.3 mL of TEA to the THF, prior to polymer dissolution to ensure the stability of the acetal protection group (resulting in **PS-compacted-P12**).

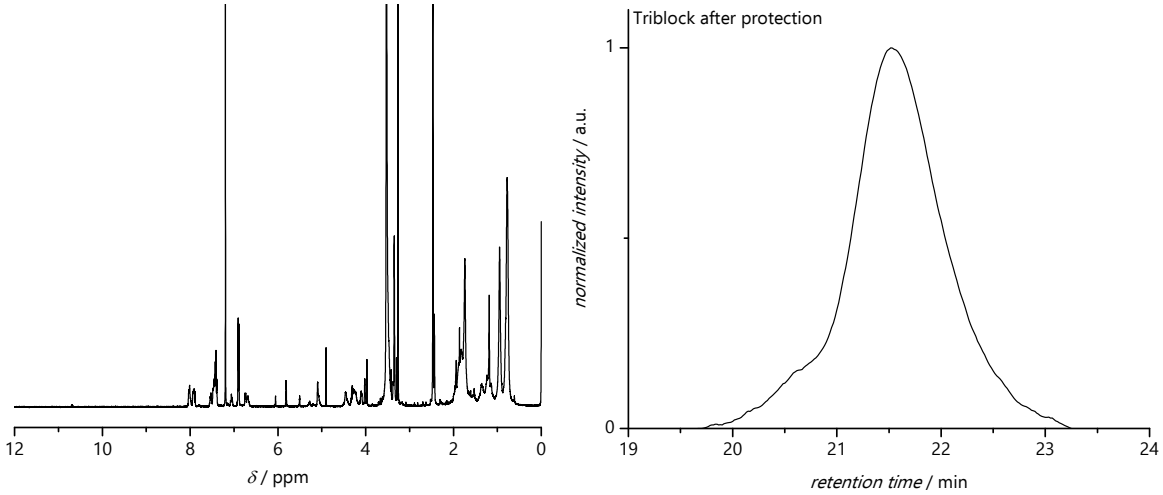

Figure 78: Crude ^{1}H NMR spectrum (400 MHz, $CDCl_3$, ambient temperature) and size exclusion chromatogram (THF, 35 °C) of protected (PE-MA-co-MMA)$_{100}$-*b*-MMA$_{20}$-*b*-(PS-MA-co-MMA)$_{100}$ **P11**.

Afterwards, half of the obtained solid was set aside for SEC and DLS analysis, whereas the other half was directly subjected to the next light induced compaction applying the conditions for **PE-SCNP(15)**, leading to **dual-compacted-P12**. The protective group was removed in situ by the addition of wet molecular sieve (4 Å) to the reaction mixture prior to the irradiation. The size exclusion chromatograms of the protected precursor and of the first and second compaction steps are depicted in **Figure 79**. After the first compaction of the PS block, a complete shift to longer retention times, i.e., smaller hydrodynamic volumes is observed.

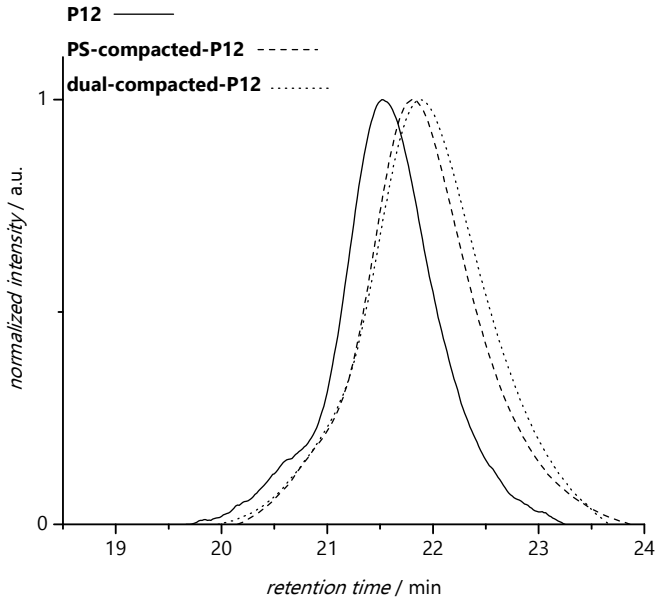

Figure 79: Size exclusion chromatograms (THF, 35 °C) of the protected (PE-MA-co-MMA)$_{100}$-*b*-MMA$_{20}$-*b*-(PS-MA-co-MMA)$_{100}$ **P12** (solid line), **PS-compacted-P12** (dashed line) and **dual-compacted-P12** (dotted line).

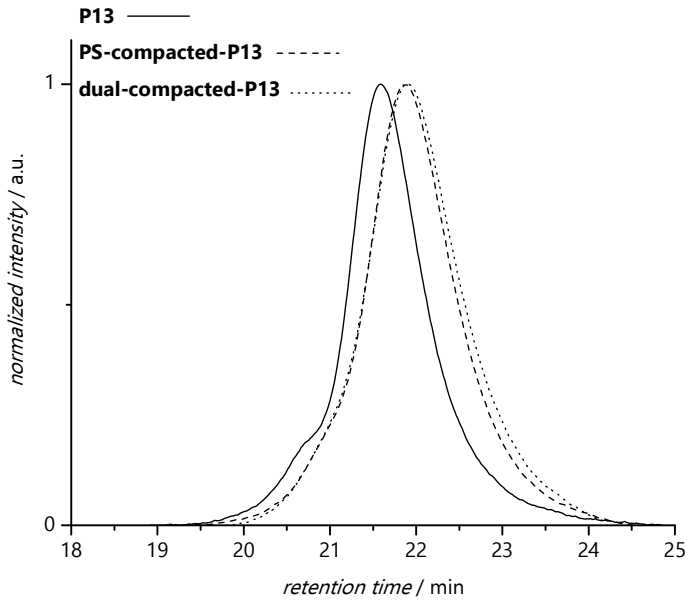

Figure 80: SEC chromatograms (THF, 35 °C) of repeated dual compaction experiment. Again, a clean, very pronounced shift to longer retention time is observable for the PS-block compaction compared to the precursor. The second compaction of the PE-block results in a second, small but clean shift to longer retention time indicating a successful second compaction of the polymer chain.

For the second compaction step, a small shift to longer retention time evidences a successful second light induced compaction. For both experiments, clean shifts without high molar mass shoulders are observed, evidencing the absence of crosslinked material. To prove the reproducibility of the stepwise dual compaction, the reaction sequence was repeated employing the same experimental parameters as for the first photoreaction sequence. The results for the obtained **P13**, **PS-compacted-P13** and **dual-compacted-P13** are illustrated in **Figure 80**. Again, for the PS block photoreaction, a pronounced shift to longer retention times without a shoulder is achieved. For the PE block compaction, a smaller, yet visible shift is again observed as illustrated in Figure 79. The obtained results clearly indicate a successful

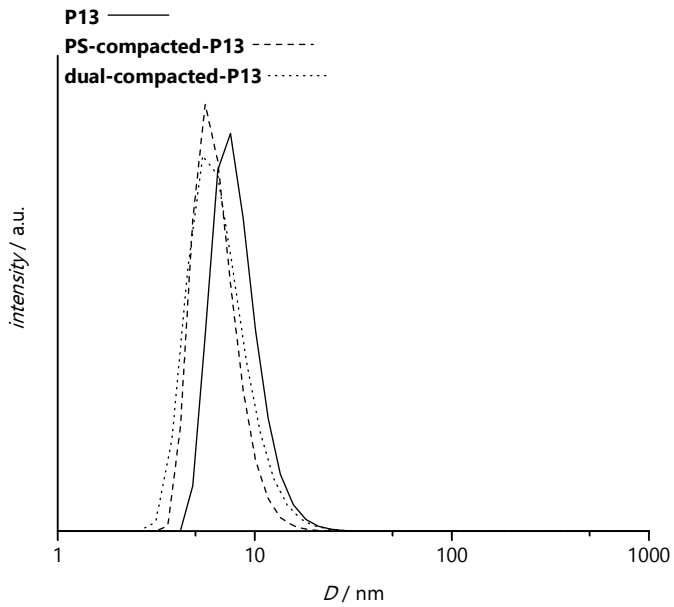

Figure 81: Number-weighted distributions obtained from DLS measurements of **P13** (solid line), **PS-compacted-P13** (dasched line) and **dual-compacted-P13** (dotted line) in MeCN (1 mg mL^{-1})..

dual compaction of the triblock copolymer. In **Figure 81**, DLS number weighted distributions of all thee samples are depicted. The measurements were performed as described in Section 5.2.1. For the first compaction (**PS-compacted-P13**), again a clear shift of the distribution to smaller hydrodynamic diameters is observed compared to the precursor distribution (**P13**). The second shift however (**dual-compacted-P13**), appears to be too small to be detected in DLS measurements.

The first, major and the second, minor shift, is in agreement with the expectations for the photocompaction experiments. In the first folding step, the SCNP is formed by a collapse of the free chain restricting the chain mobility as well as the conformation degrees of freedom greatly, which leads to a pronounced compaction. In the second irradiation step, the chains have already lost a large amount of conformational entropy (less freedom), a further collapse of the chain is therefore less favorable, thus less pronounced. However, the chain is clearly compacted further, but as the SCNP is already formed in the first step, only a small compaction is observable in Figures 79 and 80. Also, the size of the shift detected in SEC measurements is comparable to other results for sequential SCNP folding reported in literature (a relative retention time increase of about 5 %).[32] The obtained SEC and DLS results underpin the hypothesis of a dual photoinduced chain compaction composed of a first, major collapse of the free chain and a second, minor compaction of the previously formed SCNP.

In summary, the photoreactive monomers PS-MA (**7**) and PE-MA (**8**), initially designed for and exploited in DLW experiments, were successfully incorporated into copolymers with MMA. Well defined photoreactive copolymers of both photoreactive monomers were achieved by employing RAFT polymerizations. The polymerization procedures were optimized as described in Sections 5.1.1 and 5.1.2 to produce well-defined copolymers while reaching high monomer conversions. The established procedures were subsequently

employed to form a dual photoreactive triblock copolymer in a one pot RAFT block copolymerization (see Section 5.1.3). After the optimization of the polymerization processes, conditions for light induced foldings of the monoreactive copolymers derived from PS-MA (**7**) and PE-MA (**8**) were established. In Sections 5.2.1 and 5.2.2, successful photofoldings of the copolymers are demonstrated. In the final step of the project, described in Section 5.2.3, the optimized folding conditions were applied to successfully achieve a stepwise light induced dual compaction of the photoreactive triblock copolymer. The stepwise nature of the chain compaction process is a first step towards mimicking the natural stepwise folding processes of proteins.

6

CONCLUDING REMARKS

The nature of light and its effects on matter have appealed to scientists for hundreds of years, as already Galileo Galilei attempted to measure the speed of light in the early 17th century.[215] However, only at the beginning of the 20th century, physicists started to uncover its complex nature.[5-6] Although photochemical reactions have also been known for more than 150 years,[4] organic and polymer chemists only recently started to realize the potential of light as energy source in the context of the ongoing discussion about clean energy.[216] Therefore, the research in the field of photochemical ligations for organic and polymer chemistry is still evolving.[8, 10]

However, light does not only provide the possibility to directly convert clean energy into chemical transformations, it also bears other specific features such as spatial, temporal and energetic control. Additionally, photochemical reactions often proceed in a concerted fashion, thus circumventing the formation of side products or the need for a catalyst. Light induced processes were therefore, within the scope of the current thesis, employed and investigated as tools for complex micro- and nanoscopic applications.

In the first section (Chapter 3), two novel photoreactive methacrylate based monomers bearing either photoenol or phenacyl sulfide moieties were synthesized and successfully integrated in 3D microscaffolds fabricated by directed laser writing (DLW), in order to achieve dual, simultaneous surface functionalization. The monomers were directly incorporated into DLW photoresists utilized to construct specific parts of the structures. Thus, dual photoreactive scaffolds were obtained and subsequently orthogonally functionalized in a one pot fashion with either halogenated markers or fluorophores. The halogenated scaffolds were subjected to Time-of-Flight Secondary-Ion Mass Spectrometry

(ToF-SIMS), allowing for a spatially and chemically resolved characterization, while the fluorophore modified scaffolds were analyzed employing Confocal Fluorescence Microscopy (CFM). Additionally, an attempt at applying Fourier transform infrared microscopy is presented. The thoroughly characterized scaffolds were then successfully functionalized with extracellular matrix proteins and utilized for cell guiding experiments, conducted by collaboration partners. It was successfully demonstrated how the novel photomonomers and the derived light induced ligation protocols could be exploited for the fabrication of cell instructing scaffolds. Nevertheless, only basic cell lines in interaction with common adhesion proteins were studied. In the future, the investigation of the interaction of more advanced cells (e.g., stem cells) and a larger range of proteins should be undertaken by utilizing the newly established microscaffold functionalization protocol. In addition, it may desirable to obtain anchoring points for cells that are dynamic or simply removable at a later stage. The next session partly addresses this aspect.

Indeed, in Chapter 4, a reversible, fully light controlled ligation was investigated: the well known photochemical, reversible anthracene dimerization was modified in order to allow very mild reaction conditions exploiting visible light (above 400 nm). The red shift in absorption for the cycloaddition reaction was achieved by implementing an electron rich substituent, i.e., a triazolyl ring, in the 9-position of the anthracene tricyclic structure, thus expanding the π system. Hereto, an efficient, straightforward synthetic procedure utilizing Sonogashira cross coupling and CuAAC was established. Moreover, by a red-shift of the absorption for the forward reaction, the reverse cycloelimination was also red shifted towards the near UV light region. Employing this newly designed photochemical setup, the light induced reversible surface patterning of small molecules as well as polymer strands was successfully achieved on 2D silicon substrates. These obtained patterns were again thoroughly analyzed by ToF-SIMS measurements. The herein demonstrated modification of a well known photochemical reaction provides a new, very mild, spatially resolved surface writing-erasing methodology for possible biopatterning applications in a biological context. In conjunction with the aforementioned cell guiding scaffolds, removable attachment points for cells are highly desirable to investigate the rearrangement capabilities of a living unit facing a changing environment.

In a final part of the current study (Chapter 5), photochemistry was implemented in another biologically related context, namely single chain nanoparticles (SCNP). Towards mimicking a natural protein folding, a stepwise SCNP compaction under mild reaction conditions was performed. Thereto, the aforementioned novel methacrylate based photoreactive monomers were incorporated in a well-defined block copolymer. This dual photoreactive polymer was synthesized by a one pot reversible addition fragmentation transfer (RAFT) polymerization procedure. For this purpose, the RAFT copolymerization procedures of the photoreactive methacrylates with methyl methacrylate were investigated and conditions were adjusted to enable the highest conversion possible. For one of the monomers, a protocol for achieving full conversion could be established. Subsequently, the synthesized

polymers were subjected to crosslinker assisted SCNP folding reactions, exploiting the photoreactivity of the monomer units. Ultimately, a stepwise SCNP compaction of a dual responsive triblock copolymer was accomplished. However, due to the inherent coil conformation of polymers in solution, independent folding of segments to achieve individually folded domains was not possible with this strategy. Inside of cells, proteins are folded by the help of precisely defined environments, allowing for a controlled interaction of the proteins' folding points. Therefore, a better controlled surrounding for the single chain folding process is highly desirable. Additionally, for a future approach, an implementation of reactive centers via the employed crosslinkers is conceivable to mimic enzyme like behavior.

In summary, over the course of the present study, newly developed photochemical methods were successfully implemented in micro- and nanoscopic applications such as 3D microscaffold functionalizations, reversible surface patterning and SCNP folding. Specifically, novel photoreactive monomers and an unprecedented red-shifted anthracene derivative were introduced. All described methods provide mild reaction conditions and a high level of spatiotemporal control. Such methods allow for the fine design of materials that enable a better understanding of biological processes (e.g., cell adhesion or protein folding). The presented tools are therefore highly valuable for further biochemical research and development.

7

EXPERIMENTAL SECTION

7.1 Materials

3-(Trimethoxysilyl) propyl methacrylate (Sigma-Aldrich, ≥ 98%), trimethylolpropane ethoxylate triacrylate (TPE-TA, M_n ≈ 692 g mol^{-1}, Sigma-Aldrich), Irgacure® 369 (BASF), tetramethylrhodamine-5-maleimide (Mal-Rhod (**13**), Sigma-Aldrich, ≥ 85 %), biotin-PEG-SH (**14**, Nanocs Inc.), streptavidin-Alexa647 (Invitrogen, Thermo Fischer), 2-(4-chlorophenyl)ethylamine (Sigma, 98%), 2-(4-bromophenyl)ethylamine (Sigma, 98%), 2-hydroxyethylmethacrylate (HEMA, Sigma-Aldrich, 97 %, stabilized with 250 ppm hydroquinone), chloro acetic acid (Fluka, 97%), sorbic alcohol (Sigma-Aldrich, 97 %), 9-bromoanthracene (Sigma-Aldrich, 94 %), 9-anthracenemethanol (Sigma-Aldrich, 97%), 1,1'-carbonyldiimidazole (CDI, TCI, ≤ 97 %), (3-aminopropyl)triethoxysilane (APTES, Acros organics, 99%), bis(triphenylphosphine)palladium(II) dichloride ($Pd(PPh_3)_2Cl_2$, Sigma-Aldrich, ≥99 %), copper (I) iodide (CuI, Sigma-Aldrich, ≥ 99.5 %), N,N'-dicyclohexylcarbodiimide (DCC, Acros, 99 %), dimethylaminopyridine (DMAP, Sigma-Aldrich, 99 %), 2,2′-dipyridyl disulfide (DPS, Sigma-Aldrich, 98 %), ethynyltrimethylsilane (Sigma-Aldich, 98 %), N,N,N′,N′′,N′′-pentamethyldiethylenetriamine (PMDETA, Sigmal-Aldrich 99 %), piperidine (Acros Organics, 99 %), di(ethylene glycol) diacrylate (crosslinker **24**, Sigma-Aldrich, technical grade 75 %), dimethyl 2,2'-azobis(2-methylpropionate) (V601, Wako Chemicals), 3,6-dioxa-1,8-octanedithiol (crosslinker **25**, TCI chemicals, ≥97 %), 1,6-

hexanedithiol (crosslinker **22**, Sigma-Aldich, 96 %), 2,6-lutidine (Sigma-Aldrich, 98 %), 1,1′-(methylenedi-4,1-phenylene)bismaleimide (crosslinker **23**, Sigma-Aldrich, 95 %), p-toluenesulfonic acid monohydrate (tosylic acid, TosOH, Sigma-Aldrich, 98 %), trimethyl orthoformate (TMOF, Sigma-Aldrich, 99 %), ammonium chloride (NH_4Cl, Roth, 98 %), potassium bicarbonate (K_2CO_3, Roth, 99 %) sodium sulfate (Na_2SO_4, Roth, 99 %), poly(dimethylsiloxane) (PDMS, Dow Corning), 4-methyl-2-pentanone (Roth), isopropyl alcohol (Roth), chloroform-*d* ($CDCl_3$, Sigma-Aldrich, 99.8 %), dimethylsulfoxide-d_6 (DMSO-d_6, Euriso-Top, 99.8 %), acetonitrile (MeCN, dry, Acros Organics, AcrosSeal®, 99.9 %), N,N-dimethylformamide (DMF, dry, Acros Organics, extra dry, 99,7 %), methanol (MeOH, dry, Acros Organics, AcrosSeal®, 99.9 %), tetrahydrofurane (THF, dry, Acros Organics, AcrosSeal®, 99.95 %), toluene (Acros, dry, Organics, extra dry 99.8 %), 1,4-dioxane (VWR, p.a.), diethylether (Et_2O, VWR, p.a.), DMF (VWR, p.a.), MeOH (VWR, p.a.), triethylamine (TEA, Roth, p.a.), toluene (VWR or Roth, p.a.), dichloromethane (DCM, VWR, p.a.), cyclohexane (VWR, p.a.), ethyl acetate (VWR, p.a.), MeCN (VWR, p.a.), THF (VWR, p.a.), dimethylacetamide (DMAc, Roth, p.a.), sulfuric acid (H_2SO_4, Roth, 96 %) and hydrogen peroxide (H_2O_2, Roth, 35 %) were used as received.

Copper (I) bromide (Alfa Aesar, 98 %) was treated with glacial acetic acid (VWR, 99.7 %) for purification and was stored under inert gas.

Monomers *n*-butyl acrylate (Sigma Aldrich, ≥99 % stabilized with monomethyl ether hydroquinone), styrene (Merck Milipore, stabilized) and methyl methacylate (Merck Milipore, stabilized) were passed over columns of neutal alumina (Merck Milipore) prior to polymerizations.

4-Cyano-4-(((ethylthio)carbonothioyl)thio)pentanoic acid (CPAETC) was synthesized according to a literature procedure.[217]

2-Bromo-2-methyl propionic acid 2-(3,5-dioxo-10-oxa-4-azatricyclo[5.2.1.02,6]dec-8-en-4-yl) ethyl ester (Mal-Br) (**10**) was synthesized according to a literature procedure.[218]

Maleimide endcapped poly(diethyl acrylamide) (**Mal-p(DEAAm)**, M_n = 10600 g mol^{-1}, $Đ$ = 1.17) was synthesized according to a literature procedure.[219]

Hexa-2,4-dien-1-yl-2-((dodecylthio)carbonothioylthio)propanoate (**DoPAT-Sorbin**) was synthesized according to a literature procedure[49] and subsequently employed for a RAFT copolymerization of styrene and *p*-chloromethyl styrene in a ratio of 5:1. The obtained copolymer was subjected to an azide conversion to yield sorbinyl endcapped poly(styrene-*co*-azidomethyl styrene) (**Diene-p(azidostyrene)**, M_n = 4800 g mol^{-1}, $Đ$ = 1.11). The RAFT

polymerization and azide functionalization were conducted employing a literature procedure.[220]

1,4-bis((sorbinyl oxy)methyl)benzene (crosslinker **21**) was synthesized according to a literature procedure.[221]

For the surface reactions, acetone (Fischer, electronis (MOS) grade), MiliQ water, toluene (Acros, extra dry), toluene (Alfa Aesar, HPLC grade), dichloromethane (Fischer, synthesis grade), and ethanol (Fischer, laboratory reagent grade) were used. The argon stream (5.0) was filtered by an activated charcoal filter (Supelco 24518).

Formulation of the functional resists from Chapter 3:

TPE-TA resist (basic resist):

The nonfunctional TPE-TA resist (basic resist) is composed of the monomer trimethylolpropane ethoxylate triacrylate and the photoinitiator Irgacure® 369 (3% w/w).

Phenacyl sulfide resist:

The phenacyl sulfide resist is a 9:1 w/w mixture of the monomer trimethylolpropane ethoxylate triacrylate and the phenacyl sulfide methacrylate (1) containing 3% w/w Irgacure® 369. The phenacyl sulfide monomer includes 25% w/w of the solvent DMAc.

Photoenol resist:

The photoenol resist is a 9:1 w/w mixture of the monomer trimethylolpropane ethoxylate triacrylate and the photoenol methacrylate (2) containing 3% w/w Irgacure® 369. To increase the solubility of the photoenol monomer, small amounts of acetone (less than 10% w/w) were added to the photoresist.

7.2 Methods and Instrumentation

7.2.1 General Methods and Instrumentation

^{1}H and ^{13}C NMR spectroscopy was performed on a Bruker Ascend 400 at 400 MHz for hydrogen nuclei and at 101 MHz for carbon nuclei. All samples were dissolved in $CDCl_3$ or DMSO-d_6. The δ-scale is referenced to the respective residual solvent peak (7.260 ppm for $CDCl_3$ and 2.500 ppm for DMSO-d_6).

Electrospray ionization mass spectrometry (ESI-MS) spectra were recorded on a Q Exactive (Orbitrap) mass spectrometer (ThermoFisher Scientific, San Jose, CA, USA) equipped with an HESI II probe. The instrument was calibrated in the m/z range of 74-1822 using a premixed standard comprising caffeine, Met-Arg-Phe-Ala acetate (MRFA), and a mixture of fluorinated phosphazenes (Ultramark 1621). A constant spray voltage of 4.6 kV and a dimensionless sweep gas flow rate of 5 were applied. The capillary temperature and the S-lens RF level were set to 320 °C and 62.0, respectively. The samples were dissolved with a concentration of 0.05 mg·mL^{-1} in a mixture of THF and MeOH (3:2) containing 100 µmol sodium trifluoracetate (NaTFA). The samples were infused with a flow of 5 µL·min^{-1}. Spectra for molecules **18**, **19** and **20** were recorded in the negative mode.

Size exclusion Chromatography (SEC) measurements were performed on a Polymer Laboratories (Varian) PL-SEC 50 Plus Integrated System, comprising an autosampler, a PLgel 5 mm bead-size guard column (50 x 7.5 mm), one PLgel 5 mm Mixed E column (300 x 7.5 mm), two PLgel 5 mm Mixed C columns (300 x 7.5 mm) and a differential refractive index detector using THF (with 0.01% BHT as additive) as the eluent at 35 °C with a flow rate of 1 mL min^{-1}. The present SEC system was calibrated using narrow linear poly(styrene) standards ranging from 476 to 2.5·10^{6} g mol^{-1}and linear poly(methyl methacrylate) standards ranging from 700 to 2·10^{6} g mol^{-1} (Polymer Standard Service, PSS). The resulting molar mass distributions were determined by using Mark-Houwink parameters for polystyrene (K = 14.1·10^{-5} dL g^{-1}, α = 0.7) or poly(methyl methacrylate) (K = 12.8·10^{-5} dL g^{-1}, α = 0.69) respectively. Experimental molar mass (M_n) and dispersity ($Đ$) values were analyzed using the Varian software.

Dynamic light scattering (DLS) measurements were performed on a Zetasizer NanoZS light scattering apparatus (Malvern Instruments, UK) equipped with a He-Ne laser (operating at a wavelength of 633 nm, 4 mW). The Nano ZS instrument incorporates a non-invasive backscattering (NIBS) optic with a detection angle of 173°. The polymer solutions were prepared in MeCN (1 mg mL^{-1}) and were subsequently filtered (PTFE syringe filter 20 µm, VWR) twice into quartz cuvettes. The prepared samples were stabilized prior to DLS analysis at ambient temperature. All number distributions obtained for the polymer and the SCNPs

were averaged over triplicate measurements (10 runs/measurement), and were automatically provided by the instrument using a cumulative analysis.

Scanning electron microscopy (SEM) images were acquired with a Zeiss SUPRA 55VP.

UV-Vis spectra were recorded on an OceanOptics USB4000 spectrometer coupled to an USB ISS UV Vis detecting unit. All spectra were recorded in acetonitrile with a concentration of 0.5 mg mL^{-1}.

X-ray photoelectron spectroscopy (XPS) measurements were performed using a K-Alpha+ XPS spectrometer (ThermoFisher Scientific, East Grinstead, UK). Data acquisition and processed using the Thermo Avantage software. All samples were analyzed using a microfocused, monochromated Al K α X ray source (400 μm spot size). The K-Alpha+ charge compensation system was employed during analysis, using electrons of 8 eV energy, and low-energy argon ions to prevent any localized charge build-up. The spectra were fitted with one or more Voigt profiles (BE uncertainty: ± 0.2 eV) and Scofield sensitivity factors were applied for quantification. All spectra were referenced to the C 1s peak attributed to C-C, C-H at 285.0 eV binding energy controlled by means of the well-known photoelectron peaks of metallic Cu, Ag, and Au, respectively.

Time-of-flight secondary-ion mass spectrometry (ToF-SIMS) measurements were performed on a TOF.SIMS5 instrument (ION-TOF GmbH, Münster, Germany). This spectrometer is equipped with a bismuth cluster primary ion source and a reflectron type time-of-flight analyzer. UHV base pressure was < 5×10^{-9} mbar. For high mass resolution the Bi source was operated in the "high current bunched" mode providing short Bi^{3+} primary ion pulses at 25 keV energy and a lateral resolution of approx. 4 μm. The short pulse length of < 1.3 ns allowed for high mass resolution. Due to the required large fields of view, the stage scan mode was used and individual patches of 500×500 μm^2 were stitched by moving the sample. Each patch consists of 30 scans, rastered in random mode, with 100 pixels mm^{-2}. Pulsed primary gun target currents were recorded (approx. 0.5 pA @ 10 kHz) and all data were normalized on constant primary ion dose density. Spectra were calibrated on the omnipresent C^-, CH^-, CH^{2-}, C^{2-}, C^{3-}; or on the C^+, CH^+, CH^{2+}, and CH^{3+} peaks. Based on these datasets the chemical assignments for characteristic fragments were determined.

Attenuated total reflectance Fourier transform infrared microscopy (ATR-FT-IRM) measurements were performed employing a Bruker FT-IR microscope HYPERION 3000, coupled to a research spectrometer VERTEX 80. The HYPERION 3000 microscope is HEMA equipped with two types of detectors: a single element MCT-detector (Mercury Cadmium Telluride) for the conventional mapping approach and a multi-element FPA-detector (focal plane array) for imaging. The FPA-detector was used for the laterally resolved

measurements. In the present thesis, only the multi-element FPA-detector consisting of 64 × 64 elements is employed. This setup allows the simultaneous acquisition of 4096 spectra covering a sample area of 32 × 32 µm (for ATR detection). For the FPA-detector in combination with the Germanium ATR-lens, a lateral pixel resolution of 0.25 μm^2 is achieved, with the optical resolution depending on the employed wavelength (λ = 10 µm ~ 1 µm lateral resolution). For further evaluations, baseline corrections and atmospheric compensations were employed.

7.2.2 Special Methods and Instrumentation from Chapter 3

ToF-SIMS measurement mode:

The TOF-SIMS instrument employed in this study utilizes a liquid metal ion gun (LMIG) to analyze the sample. The LMIG provides a pulsed, highly intense and finely focused ion beam (Bi^+, Bi_3^+, Bi_3^{++} or Mn^+) which is scanned across the sample surface. Upon primary ion impact, secondary ions and neutral species are sputtered from the topmost 1-2 nm of the sample surface. Secondary ions are commonly collected in a quasi-static electric field, brought to a constant kinetic energy (2 keV) and mass separated by means of a time-of-flight system. Since every individual primary ion pulse generates an entire mass spectrum, not only integral spectra of the analyzed area are obtained, but also images of the lateral distribution of the secondary ions. The achievable (a) mass resolution (peak width (FWHM, m/Δm), (b) lateral resolution (evaluating a line-scan over a linear border in an SI image (16% to 84 %)), and the (c) data rate (secondary ions per time) depend on the chosen instrument setup (mode of operation).

Current modes:

To obtain highest mass resolution (> 10 000) the mass filtered and pre-chopped primary ion pulse is "bunched" by pulsed axial electric field in the ion column. This bunching strongly reduces the pulse width (< 1 ns), and therefore also the secondary ion peak width. However, this introduces a chromatic aberration of the primary ion beam due to their slightly different kinetic energies. This chromatic aberration limits the effectiveness of the focusing ion optics and results in a lateral resolution on the sample of a few µm. Images can be rapidly obtained (usually the static limit is reached at approx. 1 min analysis time of a 500×500 μm^2 field of view with 128×128 pixel and 100 µs drift time, 1 < m/z < 850) and good image contrast is provided based on high secondary ion count rates.

To obtain the highest lateral resolution the instrument is operated in "collimated" or "burst alignment" mode. In these modes a lateral resolution of below 100 nm can be achieved. However, in these modes no pulse bunching is applied and, as a consequence, the secondary ion pulses at the detector are much longer (100 ns). This results in a much lower mass resolution (> 300) and individual peaks on one nominal mass cannot be separated. Therefore, the "burst alignment" and similar modes with long primary ion pulses are usually not suitable to obtain unequivocal chemical assignments but provide high resolution

images of small features if no cross-talk at the analyzed masses is observed. Generally, measurement times and primary ion fluxes are high in imaging modes; because although the primary ion current is lower as compared to the "bunched" mode, a much higher pixel density is needed. Therefore, the static limit, defined as to which less than 1% of the samples surface area is damaged, is usually exceeded and sample damage is observed in consecutive runs on the same area.

In this study, high mass resolution spectra were recorded first using Bi_3^+ "high current bunched" mode and only in those cases where the surface modifications of the small polymeric structures were characterized by strong signals of heteroatoms without other strong peaks at the same nominal masses (^{35}Cl, ^{37}Cl, ^{79}Br, ^{81}Br) "burst alignment" imaging was performed. However, as shown in **Figure 82** on some samples the bromine signals were accompanied by several other strong signals at 79 m/z and 81 m/z.

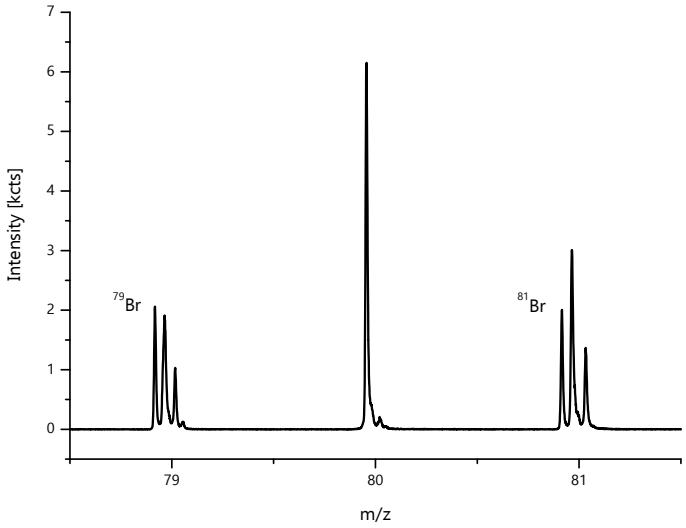

Figure 82: Negative polarity ToF-SIMS spectrum, showing 79Br and 81Br accompanied by several other peaks at identical nominal masses.

Since the three peaks at 79 m/z and the three peaks an 81 m/z differ with respect of the chemical origin, also the lateral distributions of these fragments on the sample surfaces differ from each other, as shown in **Figure 83**.

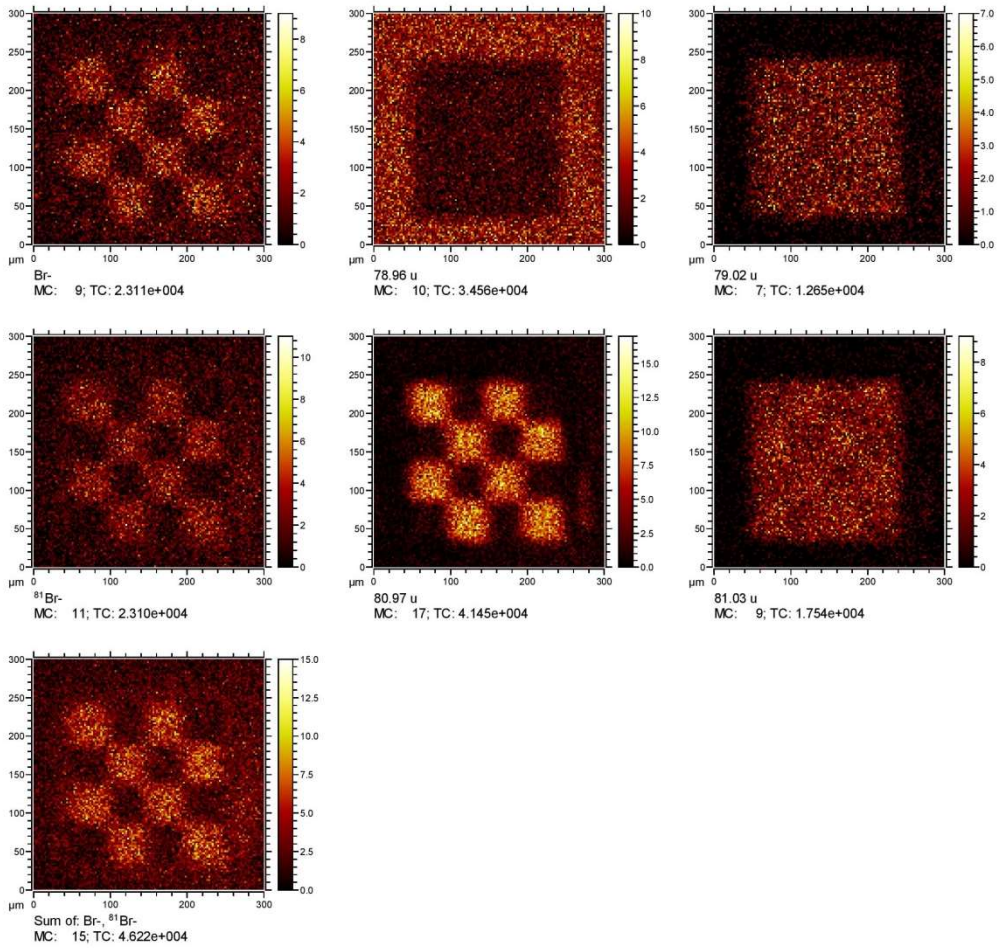

Figure 83: Lateral distributions of all fragments including bromine at 79 m/z (top row), 81 m/z (middle row), and sum of both bromine images (lower row) obtained in low lateral resolution "bunched" mode.

Because of these mass interferences, visible from "high current bunched" data shown in Figure 82 and Figure 83 the images acquired in "burst alignment" mode do not represent the actual distribution of the bromine ions on the sample, as shown in **Figure 84**, bottom row. However, the fragments CN^- at 26 m/z, and SiO_3H^- at 77 m/z, being free of adjacent peaks, result in realistic representations of their lateral distribution (Figure 84, second row).

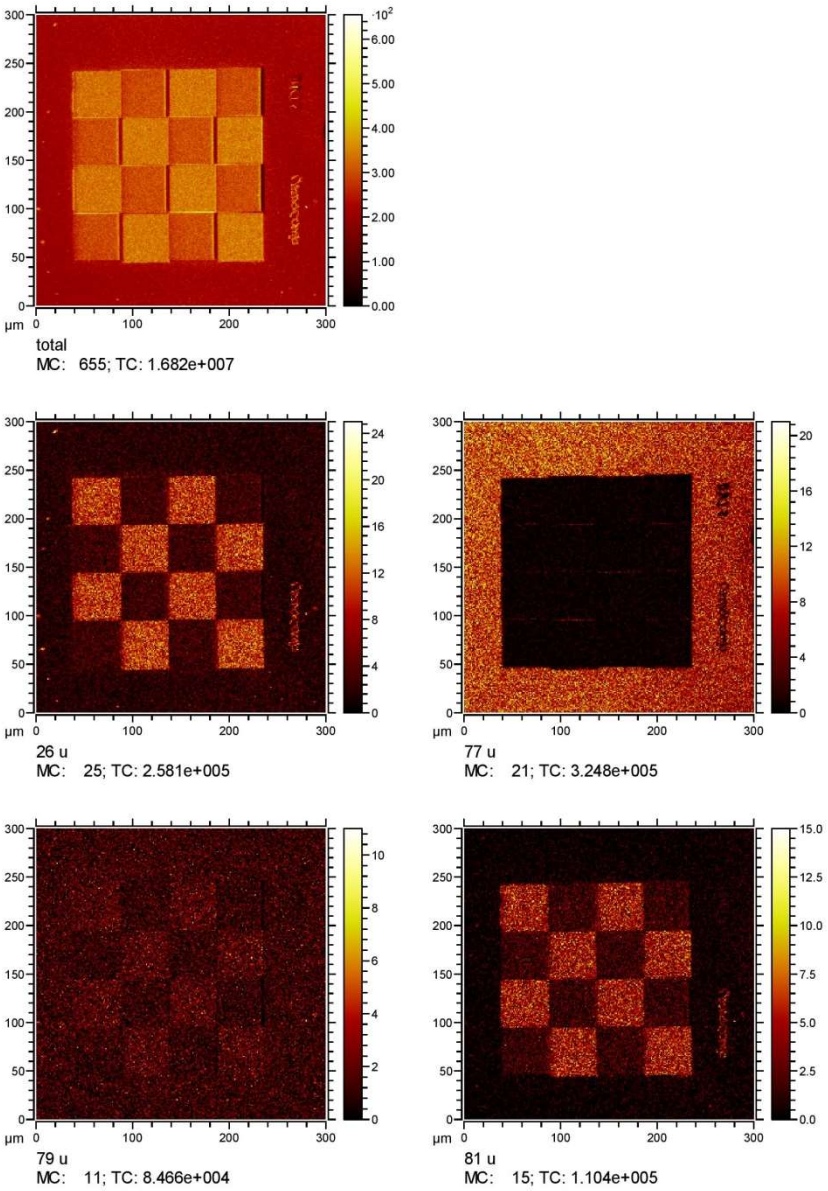

Figure 84: Lateral distributions of total secondary ions, negative polarity, (top); CN^- at 26 m/z, and SiO_3H^- at 77 m/z (middle) and sum of all fragments at 79 m/z and 81 m/z (below), obtained in high lateral resolution "burst alignment" mode.

"Delayed extraction" — a new imaging mode for ToF-SIMS:

If, as shown in **Figure 82** and **Figure 83**, high mass resolution and high lateral resolution are simultaneously required, neither one of the above mentioned modes are applicable. An additional mode, termed "delayed extraction", combines high lateral resolution based on a well-focused long pulse primary beam, with a high spectral resolution. This is achieved by delaying the onset of the extraction pulse with respect to the primary ion impact. Therefore, no longer the duration of the primary ion pulse but the fast rising of the secondary ion extraction field defines the starting timing of the time-of-flight separation. In practice, two consequences arise from this:

1. Due to the delay between impact and emission some of the light and fast secondary ions have already drifted out of the extraction zone between the surface and the extraction lens. Therefore species below m/z = 20 cannot be detected in this mode.
2. An additional effect of the delay between the primary ion impact and the extraction is that the secondary ions see only a fraction of the extraction field depending on their position between the sample and the extraction lens when the field is switched on. This leads to a large energy distribution of the extracted secondary ions. The reflectron type ToF analyzer of the used instrument can compensate this energy spread to a certain extend. Nevertheless, this energy spread limits the maximum achievable mass resolution in the mode to around 5000 m/Δm.

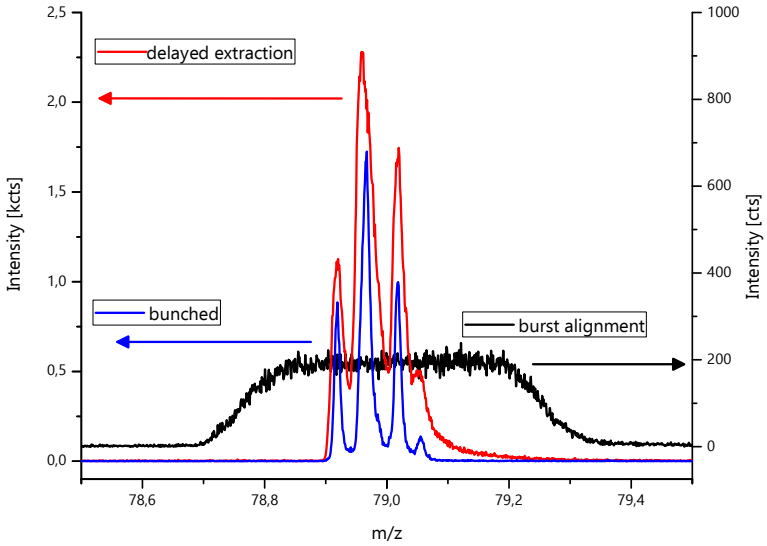

Figure 85: Peak shapes at 79 m/z for "bunched" mode (blue), "delayed extraction" (red), and "burst alignment" (black, right Y scale).

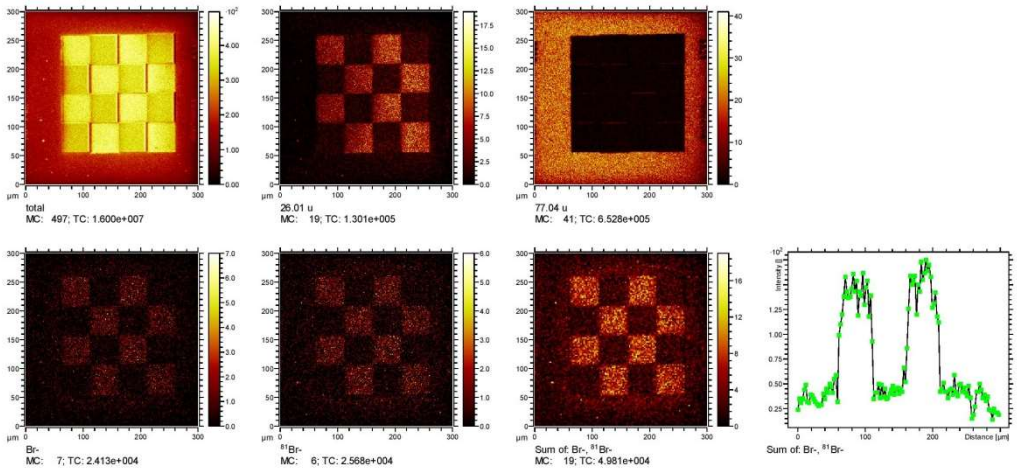

Figure 86: Imaging of total secondary ions, CN^-, SiO_3H^- and both Br isotopes with "delayed extraction" mode (top). Image of sum ^{79}Br + ^{81}Br with 4 point binning (below). Lower right: Horizontal intensity profile of ^{79}Br + ^{81}Br across first and third row of the chess board pattern.

As shown in **Figure 85**, the "burst alignment" spectrum has only nominal mass resolution, whereas the "bunched" spectrum, optimized for high mass resolution, provided 7500 < m/Δm < 8000; and the "delayed extraction" spectrum performed rather good with 4000 < m/Δm < 5000.
Comparing Figure 83 and **Figure 86** reveals that the new "delayed extraction" mode provides high lateral resolution images with full chemical information. More images of 2D and 3D objects are given in Section 3.2.

3D Microscaffold fabrication:
For the fabrication of the 3D structures, a commercially available DLW system (Photonic Professional, Nanoscribe GmbH) equipped with a 100×, NA (numerical aperture) = 1.4 oil-immersion objective was used. The laser is a mode-locked and frequency-doubled Er-doped fiber oscillator emitting femtosecond pulses at 780 nm. Typical average laser powers in the DLW process were 10–20 mW (in front of the microscope lens) and the typical piezoscanning velocity was between 50 and 200 μm s^{-1}, leading to a typical total writing time of ca. 10 min for the pillars and the lower beams of the scaffold shown in **Figure 9**. For the 10 μm thick checkerboard scaffolds utilized in Section 3.4, the writing time increased accordingly to several hours.
To enhance the adhesion of the microscaffolds to the glass substrate surface, plasma-cleaned coverslips were treated with 3-(trimethoxysilyl)propyl methacrylate (1 mmol L^{-1} in toluene) for 1 h, rinsed in water, and dried with a stream of nitrogen. TPE-TA photoresist (containing 3 wt% photoinitiator Irgacure® 369) was drop-cast onto the coverslip and the 3D microscaffolds, including marker structures (for accurate realignment between the writing steps), were fabricated. After exposure, the scaffolds were rinsed in isopropyl alcohol and dried with nitrogen gas. Then, beams between the pillars and hexagons on the glass surface were written applying a second resist (e.g. photoenol resist). To remove the non-polymerized resist, the sample was rinsed in isopropyl alcohol and dried with nitrogen gas. After applying a third resist (e.g. phenacyl sulfide resist) the missing beams between the pillars and circles on the glass surface were polymerized. The three-component microstructures were developed in a 1:1 mixture of 4-methyl-2-pentanone and isopropyl alcohol, rinsed in isopropyl alcohol, and dried with nitrogen gas.

Irradiations were carried out employing a UVAHAND 250 H1 lamp (Dr. Höhnle AG UV Technology, λ_{max} = 365 nm).

7.2.3 Special Methods and Instrumentation from Chapter 4

All light sensitive reactions were carried out in a yellow light environment. This was achieved by adding wavelength filters to normal neon lamps (Asmetec, T8-ASR-G10, gold, 520 nm).

Irradiations were carried out employing either a custom built LED setup consisting of three 3 W LEDs (Avonec Online Handel, λ_{max} = 410 nm) at a distance of 30 mm or a custom built photoreactor equipped with a compact low pressure fluorescent lamp (Cleo PL-L, Philips Deutschland GmbH, λ_{max} = 355 nm) at a distance of 50 mm.

The emission spectra of the irradiation setups were recorded with a UV sensor (Opsytec Dr. Gröbel GmbH; Ettlingen, Germany).

7.2.4 Special Methods and Instrumentation from Chapter 5

Size exclusion Chromatography (SEC) measurements were performed on an Agilent 390 LC MDS instrument fitted with an autosampler, two PLgel 5 mm mixed C columns (300 x 7.5 mm), one PLgel 5 µm guard column and a differential refractive index detector using THF (with 2% TEA and 0.01% BHT as additives) as the eluent at 30 °C with a flow rate of 1 mL min^{-1}. The system was calibrated employing narrow linear poly(methyl methacrylate) and poly(styrene) standards (Agilent EasyVials) with molar masss ranging from 200 to 1.0 $x10^6$. The resulting molar mass distributions were determined using Mark-Houwink parameters for poly(methyl methacrylate) (K = $12.8 \cdot 10^{-5}$ dL g^{-1}, α = 0.69) Experimental molar mass (M_n) and dispersity ($Đ$) values were analyzed using Agilent SEC/SEC software (version 1.2).

Irradiations described in chapter 5 were either carried out employing an OmniCure® S2000 spot UV curing lamp system (200 W) with a suitable wavelength filter (λ = 320-390 nm) or a custom built photoreactor equipped with a compact low pressure fluorescent lamp (Cleo PL-L, Philips Deutschland GmbH, λ_{max} = 355 nm for PS-SCNP experiments or Arimed B_6, Cosmedico, λ_{max} = 320 nm for PE-SCNP experiments) at a distance of 50 mm.

7.3 Synthetic procedures

All manipulations of air- or moisture-sensitive substances or materials were conducted under rigorous exclusion of moisture and oxygen in Schlenk-type glassware on a dual manifold Schlenk line, connected to a high vacuum line (10^{-3} torr). As inert gas, either argon (5.0) or nitrogen (5.0) were employed.

7.3.1 Syntheses from Chapter 3

Phenacyl sulfide methacrylate (PS-MA) 7

Phenacyl sulfide acid **3** was synthesized according to a literature procedure.[222]

In a flame-dried 100 mL Schlenk flask phenacyl sulfide acid **3** (0.50 g, 2.38 mmol, 1.00 eq), DCC (0.49 g, 2.38 mmol, 1 eq) and DMAP (58.9 mg, 0.48 mmol, 0.20 eq) were dissolved in dry DCM (50 mL). The solution was cooled in an ice bath and HEMA (1.55 g, 11.9 mmol, 5.00 eq) were added. Afterwards the mixture was allowed to reach ambient temperature and stirred overnight under an argon atmosphere. After the reaction the precipitated urea was filtered off and the solution was washed three times with deionized H_2O (50 mL). Hydroquinone was added to the organic phase, which was dried over Na_2SO_4. The solvent was then removed under reduced pressure. The crude product was purified by column chromatography (silica gel, eluent: cyclohexane/ethyl acetate 1:1(v/v), R_f= 0.35). The product **7** was obtained as slightly yellow oil (393 mg, 1.21 mmol, 51 %). Hydroquinone was again added for stabilization.

^{1}H-NMR (DMSO-d_6, 400 MHz) δ / ppm = 8.61 (s, 2 H), 8.02—7.88 (m, 2 H), 7.70—7.62 (m, 1 H), 7.58—7.50 (m, 2 H), 6.56 (s, 4 H), 6.04—6.00 (m, 1 H), 5.68—5.64 (m, 1 H), 4.35—4.26 (m, 4 H), 4.20 (s, 2 H), 3.43 (s, 2 H), 1.87—1.83 (m, 3 H).

^{13}C-NMR (DMSO-d_6, 101 MHz) δ / ppm = 194.5, 169.5, 166.3, 149.7, 135.5, 135.2, 133.5, 128.7, 128.4, 126.1, 115.6, 62.6, 62.3, 40.2, 37.9, 32.8, 17.9.

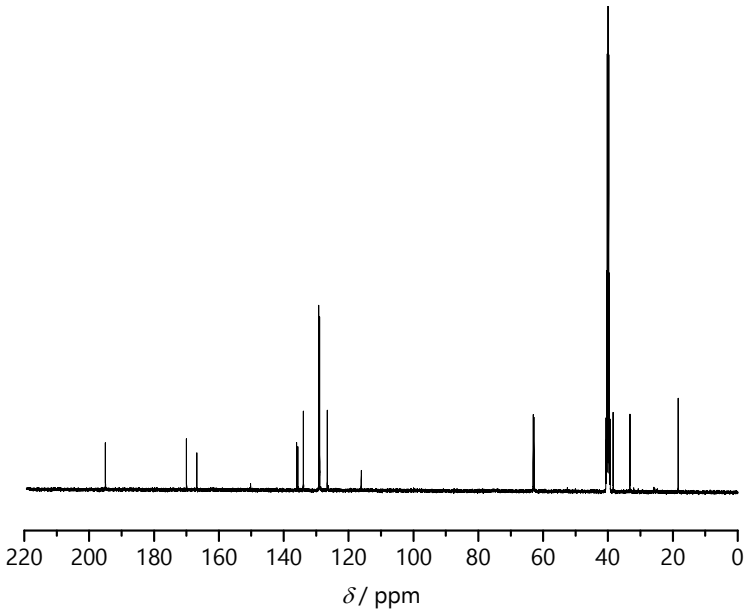

Figure 87: ^{13}C-NMR spectrum (101 MHz, DMSO-d_6, ambient temperature) of PS-MA (**7**), stabilized with hydroquinone to prevent polymerization upon storage.

Photoenol methacrylate (PS-MA) 8

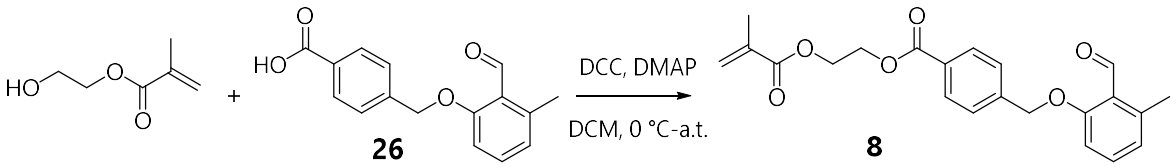

Photoenol acid **26** was synthesized according to a literature procedure.[88]

Photoenol acid **26** (1.00 g, 3.50 mmol, 1.00 eq) and DMAP (170 mg, 1.40 mmol, 0.40 eq) were added into a Schlenk-flask under argon-atmosphere. HEMA (2.275 g, 17.5 mmol, 5.00 eq) and dry DMF/DCM v/v 1:1 (20 mL) were added. The mixture was cooled to 0 °C and a solution of DCC (1.01 g, 4.95 mmol, 1.41 eq) in DMF/DCM v/v 1:1 (5.00 mL) was added. The mixture was stirred over night at ambient temperature. The precipitate was filtered off and the filtrate was washed three times with 0.5 M HCl (30 mL), water (50 mL) and brine (50 mL). The organic layer was dried over Na_2SO_4 and the solvent was removed under reduced pressure. The raw product was purified by column chromatography (cyclohexane/ethyl acetate 5:1, v/v, R_f = 0.2). The product **8** was obtained as a yellow solid (470 mg, 1.23 mmol, 47 %).

^{1}H NMR (DMSO-d_6, 400 MHz): δ / ppm = 10.65 (s, 1 H), 8.01 (d, J = 8.3 Hz, 2 H), 7.66 (d, J = 8.2 Hz, 2 H), 7.48 (t, J = 8.0 Hz, 1 H), 7.13 (d, J = 8.5 Hz, 1 H), 6.89 (d, J = 7.6 Hz, 1 H), 6.07 (s, 1 H), 5.69 (s, 1 H), 5.35 (s, 2 H), 4.61—4.54 (m, 2 H), 4.51—4.45 (m, 2H), 1.89 (s, 3 H), 1.39 (s, 3 H).

^{13}C NMR (DMSO-d_6, 101 MHz): δ / ppm =191.54, 166.40, 165.31, 161.41, 149.71, 142.26, 140.69, 135.60, 134.77, 129.43, 128.93, 127.43, 126.09, 124.20, 123.08, 115.62, 111.34, 69.28, 62.66, 62.37, 20.84, 17.92.

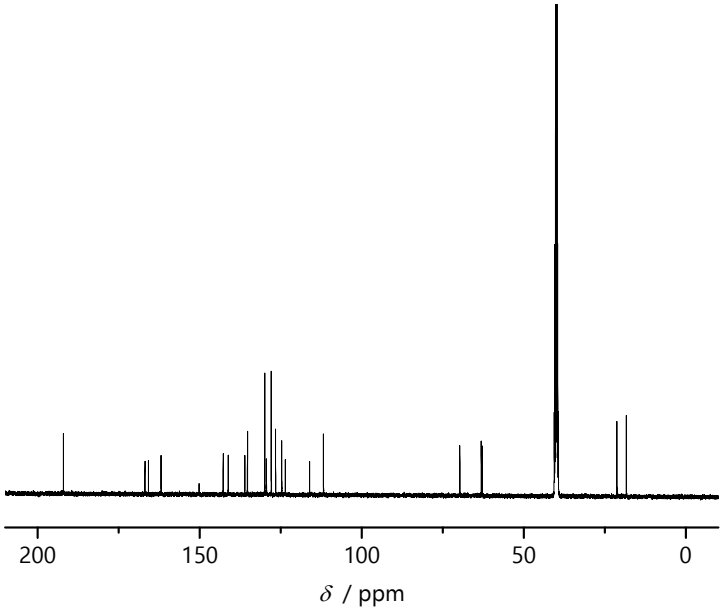

Figure 88: ^{13}C-NMR spectrum (101 MHz, DMSO-*d6*, ambient temperature) of PE-MA (**8**).

Diene-Cl 11

11

In a flame-dried 100 mL Schlenk flask, chloroacetic acid (1.18 g, 12.5 mmol, 2.50 eq), DMAP (125.7 mg, 1.25 mmol, 0.25 eq) and EDC*HCl (2.39 g, 12.5 mmol, 2.50 eq) were dissolved in dry DCM (40 mL). A solution of sorbic alcohol (490.7 mg, 5.00 mmol, 1.00 eq) in dry DCM (10 mL) was added at ambient temperature under an argon-atmosphere and the resulting mixture was stirred overnight. After the reaction the mixture was washed with brine (20 mL), saturated $NaHCO_3$ (20 mL) and deionized H_2O (3 x 20 mL). The organic phase was dried over Na_2SO_4 and the solvent was removed under reduced pressure. The crude product was purified by column chromatography (silica gel, eluent: cyclohexane/ethyl acetate 3:1, v/v, R_f= 0.62). The product **11** was obtained as colorless oil (214.8 mg, 1.23 mmol, 24 %)

^{1}H-NMR (DMSO-d_6, 400 MHz): δ / ppm = 6.36—6.26 (m, 1 H), 6.21—5.99 (m, 1 H), 5.86—5.72 (m, 1 H), 5.70—5.58 (m, 1 H), 4.80—4.54 (m, 2 H), 4.40 (s, 2 H), 1.93—1.51 (m, 3 H).

^{13}C NMR (DMSO-d_6, 101 MHz): δ / ppm = 167.10, 134.82, 131.17, 130.40, 123.46, 65.73, 41.08, 17.90.

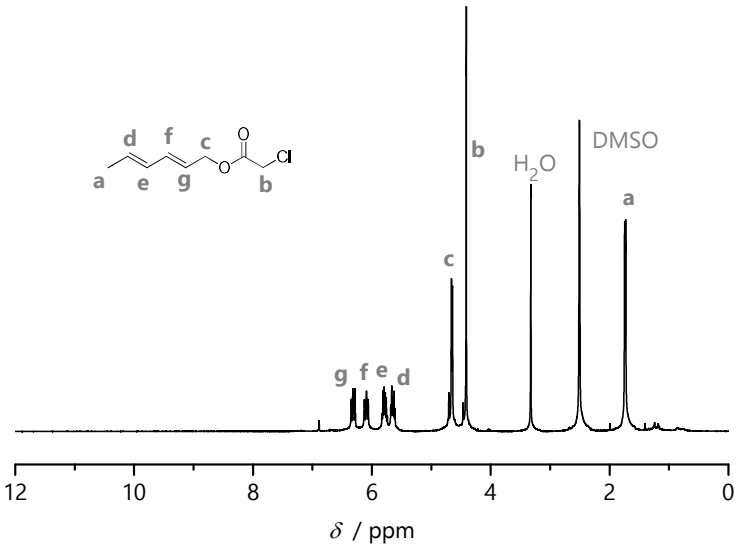

Figure 89: [1]H NMR spectrum (400 MHz, DMSO-d_6, ambient temperature) of Diene-Cl **11**.

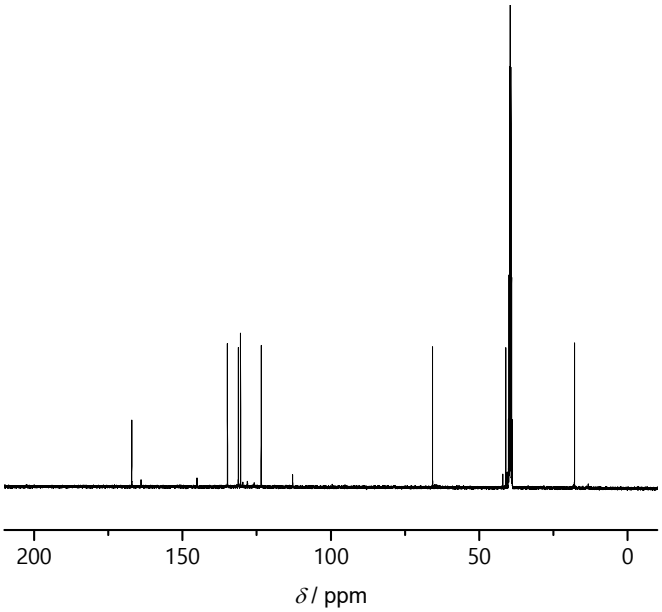

Figure 90: [13]C-NMR spectrum (101 MHz, DMSO-*d6*, ambient temperature) of Diene-Cl **11**.

Covalent simultaneous surface functionalization of polymer microscaffolds

Functionalizations employed in Sections 3.2 and 3.3:

Covalent surface functionalization was obtained by flood irradiation. A solution of the desired ligation partner (either Mal-Br (**10**)/Mal-Rhod (**13**) (Scheme 33/ Scheme 35) and Diene-Cl (**11**)/Amine-Br (**12**)/Biotin-SH (**14**) (**Fehler! Verweisquelle konnte nicht gefunden werden.** / Scheme 35)) (1 mg/mL in DMAc, 0.1 mg/ mL for Mal-Rhod (**13**)) was drop-cast onto the coverslip and irradiated for 30 min with UV light (Hönle UVAHAND 250) to create the mono-functionalized samples (Figure 7 and Figure 10). A ring made of PDMS was used to prevent the solution from flowing and thus evaporating. The coverslips were

rinsed in acetone, washed in DMF for at least 30 min, rinsed in isopropyl alcohol, and dried with a stream of nitrogen.

For the sample shown in Figure 8 and Figure 11 a 1:1 mixture of the Mal-Br solution and the Diene-Cl solution was drop-cast on the coverslip, irradiated with UV light for 30 min and washed as stated above. For the dual patterned fluorescence images (Figure 15) a 1:1 mixture of a solution of Mal-Rhod **13** (0.1 mg mL^{-1} in DMAc) and biotin-PEG-SH **14** (1 mg mL^{-1} in DMAc) was drop-cast onto the coverslip with the microstructures and irradiated for 30 min. For the streptavidin-mediated staining of the biotinylated PS-resist (pink fluorescence), the samples were washed three times for 10 min in phosphate buffer saline (PBS), and incubated for 30 min at ambient temperature with SAv-647 (0.01 mg mL^{-1} in PBS). The samples were then washed three times for 10 min in PBS. The coverslips were finally immersed in Mowiol (Hoechst) containing 1% N-propyl gallate for fluorescence confocal microscopy.

For the control sample of the fluorescence image and to prove the passivating features of the photoresists, samples were prepared as described above, with the exception of the irradiation step left out.

Functionalizations employed in Sections 3.4:

Covalent surface functionalization was obtained by flood irradiation. A solution of the respective polymer (10 mg mL^{-1} in DMAc, either **Mal-p(DEAAm)** or **Diene-p(azidostyrene)**, see Scheme 37) was drop-cast onto the coverslip containing the thick photoreactive checkerboard structures and irradiated for 30 min with UV light (Hönle UVAHAND 250). A ring made of PDMS was used to prevent the solution from flowing and thus evaporating. The coverslips were rinsed in acetone, washed in DMF for at least 30 min, rinsed in isopropyl alcohol, and dried with a stream of nitrogen.

7.3.2 Syntheses from Chapter 4

(Anthracen-9-ylethynyl)trimethylsilane (16)

In a 50 mL flame-dried Schlenk tube equipped with a stirring bar, 9-bromoanthracene (9-BA, 500 mg, 1.95 mmol, 1.00 eq), CuI (43.4 mg, 0.23 mmol, 0.11 eq), $Pd(PPh_3)_2Cl_2$ (140 mg, 0.20 mmol, 0.10 eq), and ethynyltrimethylsilane (750 µL, 517 mg, 5.27 mmol, 2.70 eq) were dissolved in piperidine (1.5 mL) and dry TEA (15 mL). The reaction mixture was stirred at 110 °C overnight and subsequently extracted with 50 mL sat. NH_4Cl solution. The aqueous phase was extracted with 30 mL cyclohexane three times. The combined organic layers were dried over Na_2SO_4 and concentrated under vacuum. The raw product was purified by column chromatography (silica gel, cyclohexane + 0.5 vol% toluene, R_f = 0.5) to yield (anthracen-9-ylethynyl)trimethylsilane as orange solid (**16**) (531 mg, 1.93 mmol, 99 %).

^{1}H NMR ($CDCl_3$, 400 MHz) δ / ppm = 8.56 (dq, J = 8.8, 1.1 Hz, 2 H), 8.42 (s, 1 H), 8.04–7.96 (m, 2 H), 7.59 (ddd, J = 8.8, 6.6, 1.3 Hz, 2 H), 7.50 (ddd, J = 8.0, 6.6, 1.2 Hz, 2 H), 0.43 (s, 9 H).

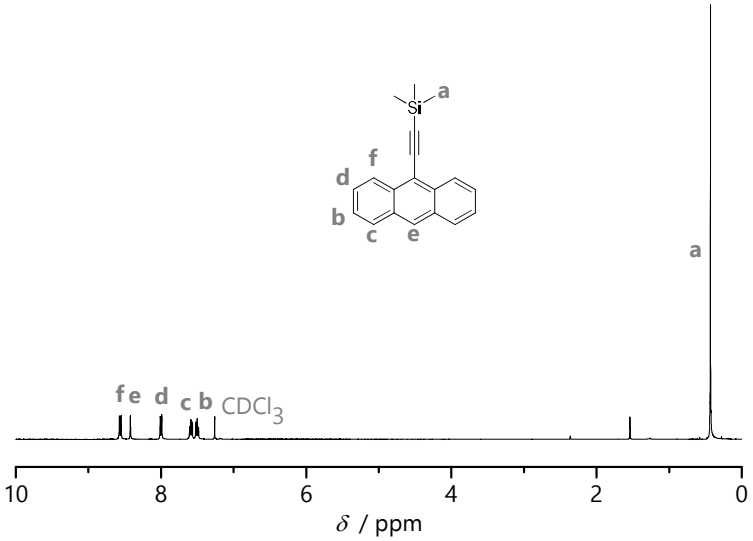

Figure 91: ^{1}H NMR spectrum (400 MHz, $CDCl_3$, ambient temperature) of (anthracen-9-ylethynyl)trimethylsilane (**16**).

9-Ethynylanthracene (17)

(Anthracen-9-ylethynyl)trimethylsilane (**16**) (400 mg, 1.46 mmol, 1.00 eq) and K_2CO_3 (1.41 g, 10.2 mmol, 7.00 eq) were dissolved in a mixture of 40 mL MeOH/THF (1/1 v/v) and stirred overnight at ambient temperature. The reaction solution was poured into a mixture of 40 mL dist. H_2O/Et_2O. The organic phase was washed with 30 mL dist. H_2O three times, dried with Na_2SO_4, and concentrated under vacuum. The raw product was filtered through a short column of silica gel (cyclohexane + 0.5 vol% toluene) to yield 9-ethynylanthracene (**17**) (270 mg, 1.33 mmol, 91 %), which was directly used in the next synthesis due to solubility issues after drying.

^{1}H NMR (CDCl3, 400 MHz) δ / ppm = 8.59 (m, 2 H), 8.46 (s, 1 H), 8.02 (d, J = 8.3 Hz, 2 H), 7.60 (ddd, J = 8.7, 6.6, 1.3 Hz, 2 H), 7.51 (ddd, J = 8.0, 6.6, 1.3 Hz, 2 H), 3.99 (s, 1 H).

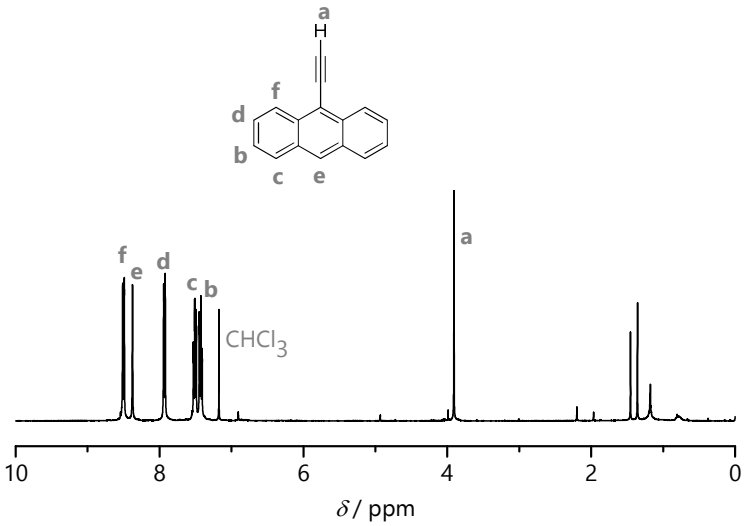

Figure 92: ^{1}H NMR spectrum (400 MHz, $CDCl_3$, ambient temperature) of 9-ethynylanthracene (**17**).

4-Azidobenzoic acid (18)

4-Aminobenzoic acid (1.37 g, 10.0 mmol, 1.00 eq) was suspended in 22 mL dist. H_2O/conc. HCl (1/1 v/v) and cooled in an ice bath at 0 °C. Sodium nitrite ($NaNO_2$, 0.79 g, 11.5 mmol, 1.15 eq) was dissolved in dist. H_2O (8 mL), the solution was cooled to 0 °C and subsequently added dropwise to the 4-amidobenzoic acid. Subsequently, the mixture was stirred for 20 min in an ice bath. Sodium azide (NaN_3, 0.72 g, 11 mmol, 1.10 eq) was dissolved in dist. H_2O (8 mL) and also cooled to 0 °C. The solution was added dropwise to the cooled reaction mixture, which was then stirred for another hour. The white precipitate was filtered off, subsequently washed with ice cooled dist. H_2O, and dried under vacuum to yield 4-azidobenzoic acid (**18**) (1.40 g, 8.60 mmol, 86 %)

^{1}H NMR (400 MHz, DMSO-d_6) δ / ppm = 7.98–7.93 (m, 2 H), 7.24–7.19 (m, 2 H).

^{13}C NMR (101 MHz, DMSO-d_6) δ / ppm = 166.6, 143.9, 131.2, 127.3, 119.2.

ESI-MS: *m/z* calculated for $C_7H_5O_2N_3$ $[M-H]^-$ 162.0309, found 162.0299.

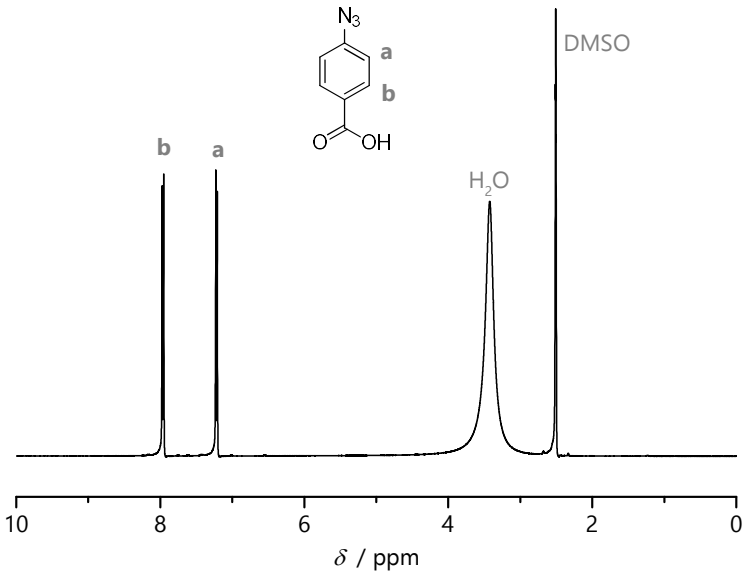

Figure 93: ^{1}H NMR spectrum (400 MHz, DMSO-d_6, ambient temperature) of 4-azidobenzoic acid (**18**).

4-(4-(Anthracen-9-yl)-1*H*-1,2,3-triazol-1-yl)benzoic acid (19)

In a 25 mL flame-dried Schlenk tube 4-azido benzoic acid (**18**, 228 mg, 1.40 mmol, 1 eq), 9-ethynylanthracene (**17**, 283 mg, 1.40 mmol, 1 eq), and PMDETA (453 µL, 376 mg, 2.17 mmol, 1.55 eq) were mixed in dry toluene/DMF (1/1 v/v, 8 mL) and the solution was purged with argon for 30 min. Cu(I)Br (301 mg, 2.10 mmol, 1.50 eq) were added under an argon atmosphere and the mixture was stirred at ambient temperature overnight. The reaction mixture was diluted with 20 mL DCM and subsequently extracted three times with 30 mL sat. NH_4Cl solution. The organic layer was dried with Na_2SO_4 and concentrated under vacuum to yield 4-(4-(anthracen-9-yl)-1*H*-1,2,3-triazol-1-yl)benzoic acid (**19**, 351 mg, 0.93 mmol, 67 %).

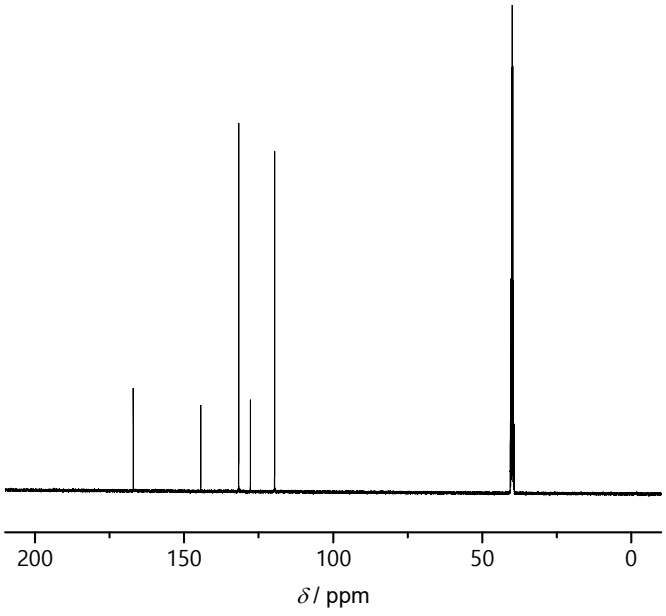

Figure 94: ^{13}C-NMR spectrum (101 MHz, DMSO-d_6, ambient temperature) of 4-azidobenzoic acid (18).

^{1}H NMR (400 MHz, DMSO-d_6) δ / ppm = 13.29 (s, 1 H), 9.37 (s, 1 H), 8.80 (s, 1H), 8.23 (m, 6 H), 7.95 (s, 2 H), 7.55 (m, 4 H).

^{13}C NMR (101 MHz, DMSO-d_6) δ / ppm = 166.5, 162.3, 143.7, 139.7, 131.1, 130.8, 130.6, 128.5, 128.3, 126.5, 125.8, 125.5, 124.4, 124.1, 119.9.

ESI-MS: *m/z* calculated for $C_{23}H_{15}O_2N_3$ $[M-H]^-$ 364.1092, found 364.1097.

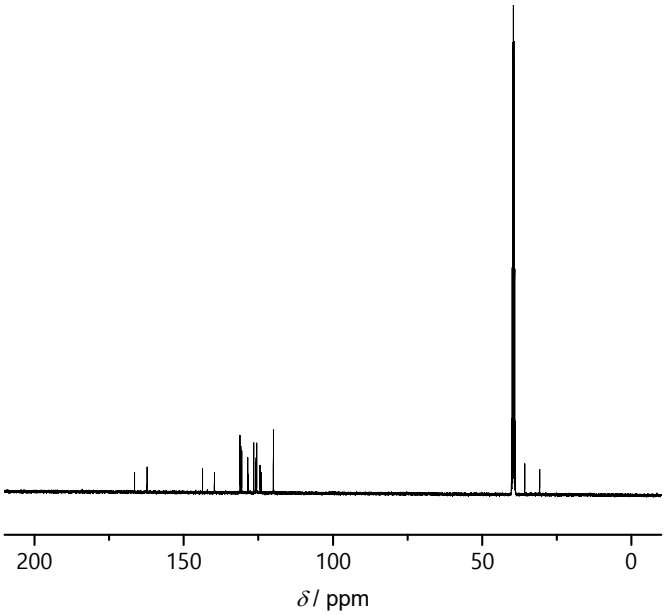

Figure 95: ^{13}C-NMR spectrum (101 MHz, DMSO-d_6, ambient temperature) of 4-(4-(anthracen-9-yl)-1H-1,2,3-triazol-1-yl)benzoic acid (**19**).

4-(4-(Anthracen-9-yl)-1*H*-1,2,3-triazol-1-yl)-*N*-(3-(triethoxysilyl)propyl) benzamide (20)

In a flame-dried 25 mL Schlenk tube, 4-(4-(anthracen-9-yl)-1*H*-1,2,3-triazol-1-yl)benzoic acid (**19**) (180 mg, 0.47 mmol, 1.00 eq) and CDI (76.9 mg, 0.47 mmol, 1.00 eq) were dissolved in dry THF (5 mL) and stirred at ambient temperature for 3 h. Subsequently, APTES (110 µL, 105 mg, 0.47 mmol, 1.00 eq) was added and the reaction mixture was stirred at ambient temperature overnight. The crude reaction mixture was concentrated under vacuum and purified by column chromatography (silica gel, cyclohexane/ ethyl acetate 3:4, R_f = 0.58) to yield 4-(4-(anthracen-9-yl)-1*H*-1,2,3-triazol-1-yl)-*N*-(3-(triethoxysilyl)propyl)benzamide as orange solid (202 mg, 0.36 mmol, 76 %).

^{1}H NMR (400 MHz, DMSO-d_6) δ / ppm = 9.34 (s, 1 H), 8.80 (s, 1 H), 8.67 (t, J = 5.6 Hz, 1 H), 8.24–8.18 (m, 4 H), 8.16–8.11 (m, 2 H), 7.87 (m, 2 H), 7.61–7.49 (m, 4 H), 3.77 (q, J = 7.0 Hz, 6 H), 3.31–3.26 (m, 2 H), 1.68–1.58 (m, 2 H), 1.16 (t, J = 7.0 Hz, 9 H), 0.67–0.60 (m, 2 H).

^{13}C NMR (101 MHz, DMSO-d_6) δ / ppm = 164.9, 143.6, 138.4, 134.5, 130.83, 130.6, 128.9, 128.5, 128.3, 126.5, 125.8, 125.5, 124.3, 124.2, 119.7, 57.7, 42.2, 22.7, 18.2, 7.5. ESI-MS *m/z* calculated for $C_{32}H_{36}O_4N_4Si$ $[M+Cl]^-$ 603.2200, found 603.2204.

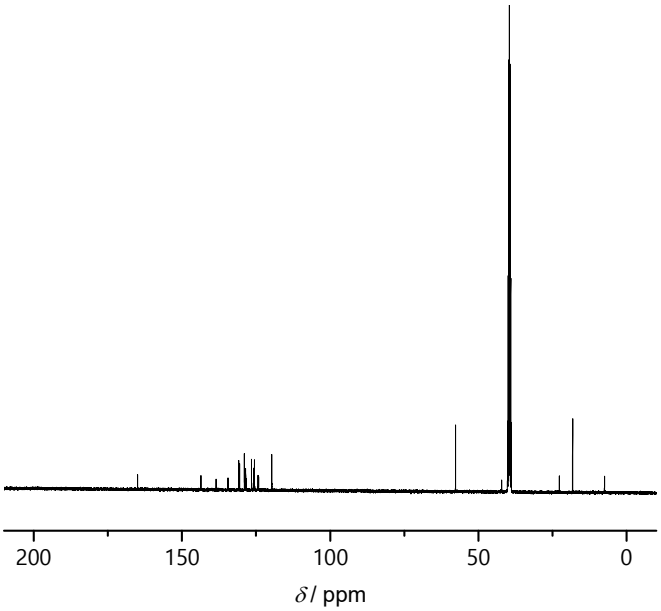

Figure 96: ^{13}C-NMR spectrum (101 MHz, DMSO-d_6, ambient temperature) of 4-(4-(anthracen-9-yl)-1H-1,2,3-triazol-1-yl)-N-(3-(triethoxysilyl)propyl)benzamide (**20**).

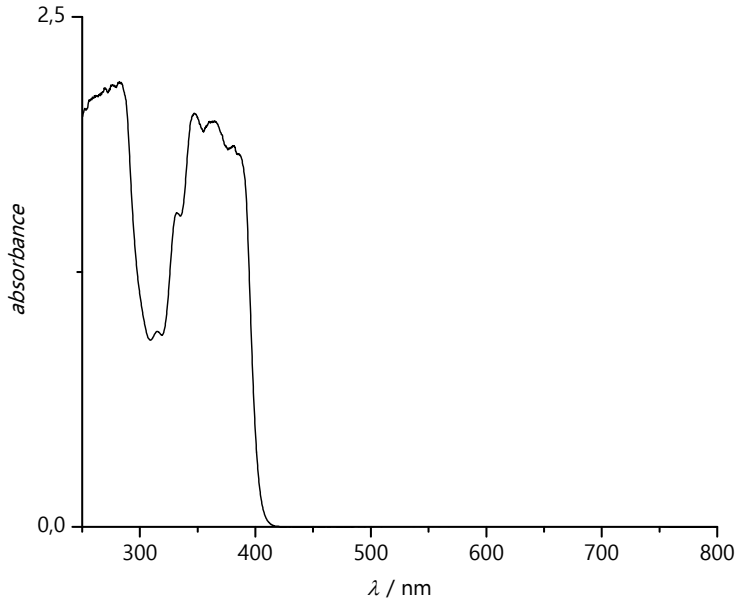

Figure 97: UV-vis absorption spectrum of triazolyl anthracene silane (**20**) (0.5 mg mL^{-1} in acetonitrile, l = 0.5 cm, a.t.).

Synthesis of anthracen-9-ylmethyl benzodithioate (27)[223]

Benzoic acid (1.22 g, 10.0 mmol, 1.00 eq), 9-anthracene methanol (2.08 g, 10.0 mmol, 1.00 eq) and P_4S_{10} (2.22 g, 5.00 mmol, 0.50 eq) were dissolved in toluene (40 mL) in a 100 mL three neck round bottom flask. The solution was stirred at ambient temperature under an argon atmosphere for 1 h and subsequently heated to 110 °C under reflux for 24 h. After cooling, the reaction mixture was filtered and the filtrate was washed with dist. H_2O. The organic layer was dried with Na_2SO_4. The solvent was then removed by evaporation and the crude product was purified by column chromatography (silica gel, petroleum ether/toluene

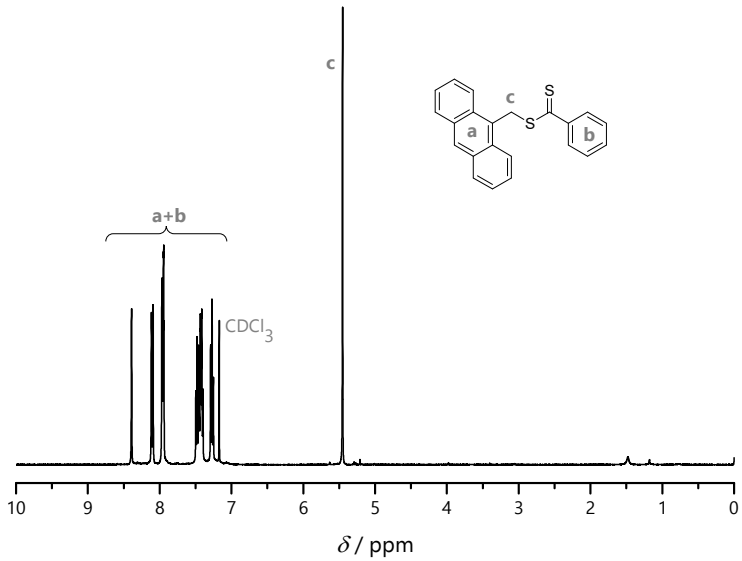

Figure 98: ^{1}H NMR spectrum (400 MHz, $CDCl_3$, ambient temperature) of anthracen-9-ylmethyl benzodithioate (**27**).

10:1, R_f = 0.39) to yield anthracen-9-ylmethyl benzodithioate (**27**, 2.86 g, 8.30 mmol, 83 %) as red crystals.

^{1}H NMR (400 MHz, $CDCl_3$) δ / ppm = 7.2–8.4 (m, 14 H), 4.47 (s, 2 H).

Synthesis of 9-anthrylmethyl 2-bromo-2-methyl propanoate (28)[224]

9-Anthracene methanol (1 g, 4.8 mmol, 1 eq) and triethylamine (0.98 mL, 0.72 g, 7 mmol, 1.45 eq) were dissolved in 20 mL dry THF. The solution was cooled in an ice bath and a solution of 0.87 mL 2-bromoisobutyryl bromide (1.62 g, 7 mmol, 1.45 eq) in 10 mL of dry THF was added dropwise under nitrogen atmosphere. The ice bath was removed and the reaction was stirred at room temperature overnight. The precipitate was filtered off and the solvent was evaporated. The raw product was dissolved in dichloromethane, subsequently washed with aqueous $NaHCO_3$ solution, and dried over Na_2SO_4. The solvent was removed under reduced pressure and the yellow oil was recrystallized from hexane to yield 9-anthrylmethyl 2-bromo-2-methyl propanoate (**28**, 1.49 g, 4.18 mmol, 87 %) as light yellow crystals.

^{1}H NMR (400 mHz, $CDCl_3$) δ / ppm = 7.4–8.4 (m, 9 H), 6.20 (s, 2 H), 1.80 (s, 6 H).

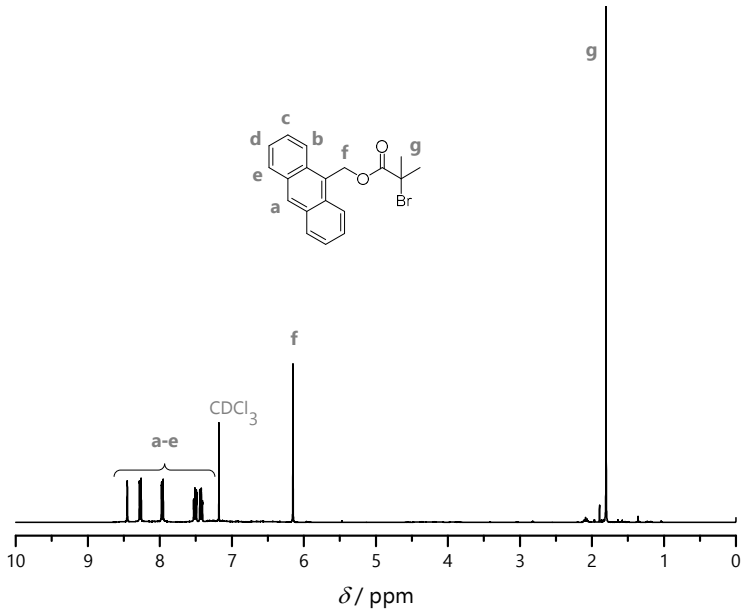

Figure 99: ^{1}H NMR spectrum (400 MHz, $CDCl_3$, ambient temperature) of 9-anthrylmethyl 2-bromo-2-methyl propanoate (**28**).

Synthesis of anthracene functionalized polystyrene (P1)

In a Schlenk tube, anthracen-9-ylmethyl benzodithioate (**27**) (40 mg, 0.116 mmol) and AIBN (3.8 mg, 0.023 mmol) were dissolved in styrene (5.3 mL, 4.82 g, 46.3 mmol). The solution was deoxygenated by percolating with nitrogen for 10 min. The polymerization reaction was performed at 60 °C under nitrogen atmosphere. After 24 h, the reaction was quenched by cooling in an ice bath and the solution was precipitated in methanol. The polymer was obtained by filtration and dried under vacuum. Conversion of styrene was determined gravimetrically and the molar mass was determined by SEC (PS calibration).

$M_{n,SEC}$ = 8400 g mol^{-1}, $Đ$ = 1.03, Conversion 12%

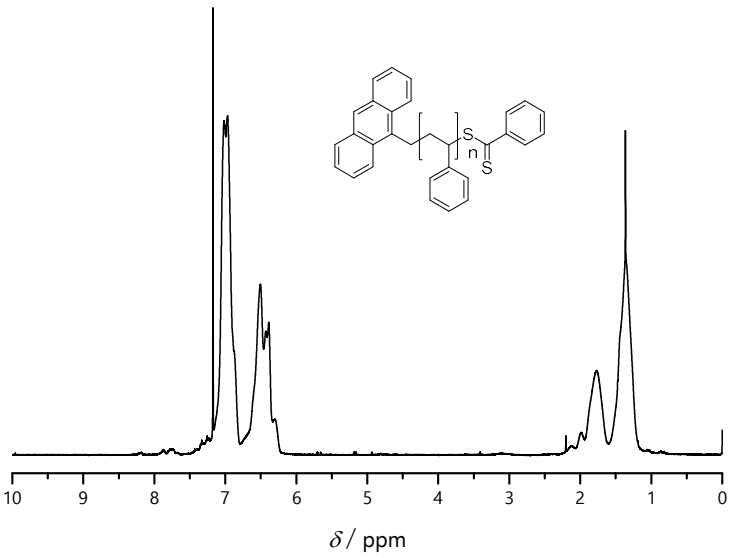

Figure 100: ^{1}H NMR spectrum (400 MHz, $CDCl_3$, ambient temperature) of anthracene functionalized polystyrene (**P1**)

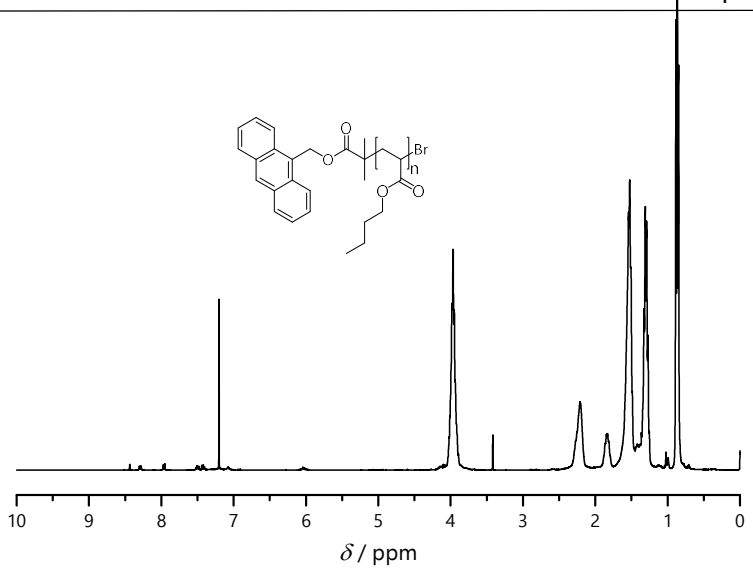

Figure 102: ^{1}H NMR spectrum (400 MHz, $CDCl_3$, ambient temperature) of anthracene functionalized poly(*n*-butyl acrylate) (**P2**).

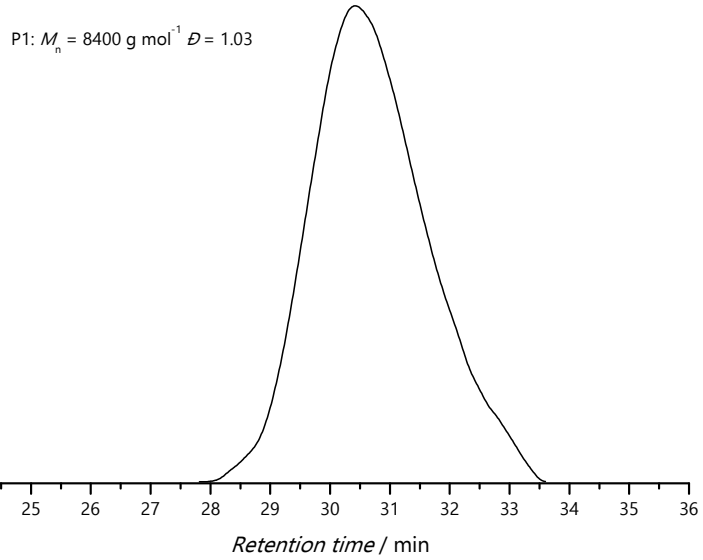

Figure 101: SEC chromatogram (THF, 35 °C) of anthracene functionalized polystyrene (**P1**).

Synthesis of anthracene functionalized poly(*n*-butyl acrylate) (P2)

In a Schlenk tube, 9-anthrylmethyl-2-bromo-2-methyl-propanoate (**28**, 78 mg, 0.219 mmol), PMDETA (46 µL, 38.2 mg, 0.291 mmol) and Cu(I)Br (31.3 mg, 0.219 mmol) were dissolved in *n*-butyl acrylate (6.27 mL, 5.61 g, 43.7 mmol) and deoxygenated by three freeze-pump-thaw cycles. The polymerization reaction was performed at 110 °C under nitrogen atmosphere. After 30 min the reaction was quenched by cooling in an ice bath and the product was precipitated by adding the reaction mixture to a methanol/water mixture. The polymer was then dissolved in THF and purified by passing through a short alumina column. The polymer was dried under vacuum. Conversion of *n*-butyl acrylate was determined by ^{1}H NMR and the molar mass was determined by SEC (PMMA calibration).

$M_{n,SEC}$ = 8200 g mol^{-1}, $Đ$ = 1.26, Conversion 17%

Synthesis of triazolyl anthracene end-capped poly(ethylene glycol) (An-PEG)

A PEG-azide was synthesized according to a literature procedure.[225] In a flame dried 50 mL Schlenk tube, Cu(I)Br (21.5 mg, 0.15 mmol, 0.50 eq) and PMDETA (31.3 µL, 29.9 mg, 0.15 mmol, 0.50 eq) were dissolved in 5 mL dry DMF. The solution was percolated with nitrogen for 20 min and PEG-azide was added (1.00 g, 0.30 mmol, 1 eq). 9-ethynylanthracene (**17**) (182 mg, 0.90 mmol, 3.00 eq) was dissolved in 5 mL dry toluene and percolated with nitrogen for 20 min. The solution of **17** was added to the copper containing mixture and the resulting solution was stirred at ambient temperature overnight. The mixture was concentrated under vacuum and passed over a short column of neutral aluminum oxide. The polymer was precipitated from the solution in ice cold Et_2O to obtain triazolyl anthracene end-capped poly(ethylene glycol) (**An-PEG**) (734 mg, 0.245 mmol, 82 %)

^{1}H NMR (400 MHz, $CDCl_3$) δ / ppm = 8.47 (s, 1 H), 8.01 (s, 1 H), 7.97 (dd, J = 8.4, 1.3 Hz, 2 H), 7.83 – 7.76 (m, 2 H), 7.40 (ddd, J = 8.2, 6.5, 1.2 Hz, 2 H), 7.34 (ddd, J = 8.0, 6.5, 1.4 Hz, 2 H), 4.72 (t, J = 5.0 Hz, 2 H), 3.99 (t, J = 5.0 Hz, 2 H), 3.78 – 3.27 (m, 185 H).

^{13}C NMR (101 MHz, $CDCl_3$) δ / ppm =131.4, 128.5, 128.3, 126.2, 125.3, 124.9, 72.0, 70.5, 69.7, 59.1, 50.6.

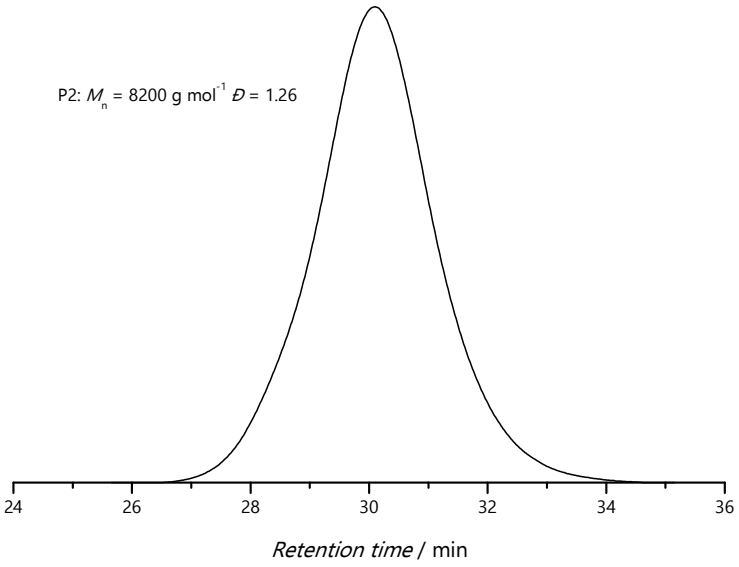

Figure 103: SEC chromatogram (THF, 35 °C) of anthracene functionalized poly(*n*-butyl acrylate) (**P2**).

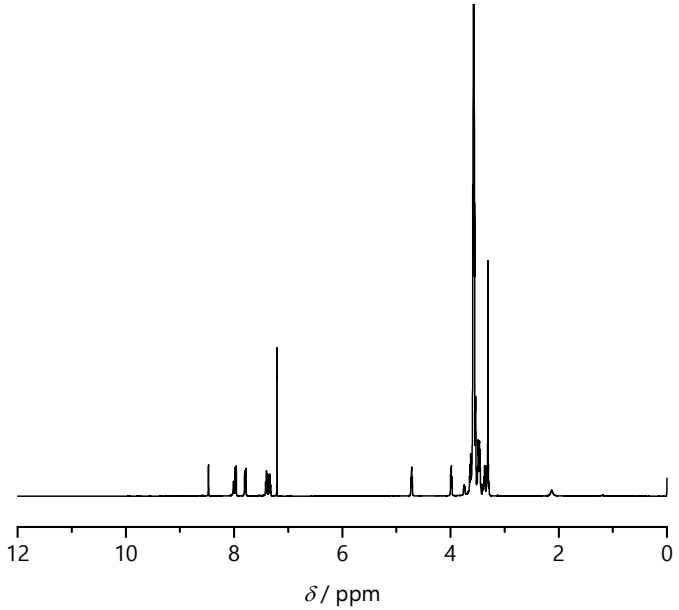

Figure 104: ^{1}H NMR spectrum (400 MHz, $CDCl_3$, ambient temperature) of triazolyl anthracene end-capped poly(ethylene glycol) (An-PEG).

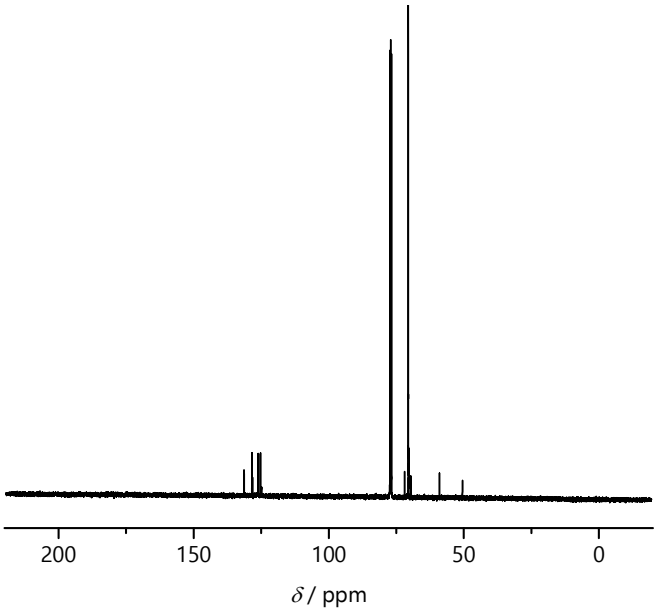

Figure 105: ^{13}C NMR spectrum (101 MHz, $CDCl_3$, ambient temperature) of triazolyl anthracene end-capped poly(ethylene glycol) (An-PEG).

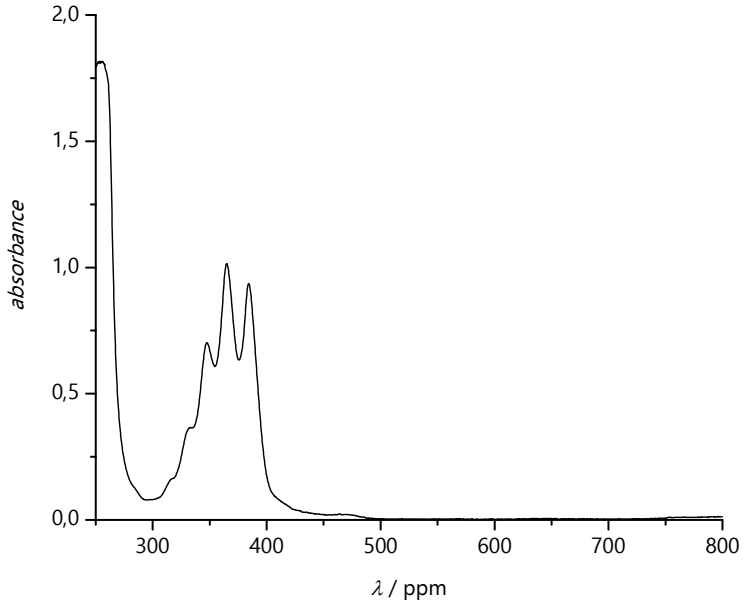

Figure 106: UV-vis absorption spectrum of triazolyl anthracene end-capped poly(ethylene glycol) (An-PEG) (0.5 mg mL^{-1} in acetonitrile, l = 0.5 cm, a.t.).

Silanization Protocol

Silicon wafers were separately placed in 5 mL vials, 3 mL Piranha solution (H_2O_2/H_2SO_4 1/2, v/v) were added and the vials were heated at 80 °C for approx. 1 h. The wafers were rinsed with an excess of water, acetone and DCM and dried under a stream of argon. The activated/cleaned wafers were placed into headspace vials (Pyrex, diameter 20 mm), which were crimped airtight using styrene/butadiene rubber seals with PTFE inner liner. Triazolyl anthracene silane (**20**) was dissolved in extra-dry toluene (2 mg mL^{-1}) and percolated with argon for 5 min. To each substrate, 2 mL of the silane solution were added. The samples were heated in an oven at 50 °C overnight and were subsequently rinsed with an excess of toluene, DCM, acetone, MilliQ water, acetone and DCM and dried under an argon stream.

Surface patterning (Writing step)

For light induced surface patterning, the silanized silicon wafers were placed in a custom made sample holder and covered with a dotted shadow mask (Figure 26a)). The sample holder was placed in a headspace vial (Pyrex, diameter 20 mm) and a solution of the respective anthracene functionalized molecule or polymer in dry MeCN or DCM (1 mg per mL for small molecules, 2 mg per mL for polymers) was added. The vial was crimped airtight using styrene/butadiene rubber seals with PTFE inner liner. The solution war percolated with argon for 5 min and subsequently irradiated at 410 nm with a custom made LED setup (Figure 26 b, refer to Figure 27 for the emission spectrum) for 4 h. Subsequently, the silicon wafer was removed from the sample holder and successively rinsed with MeCN, acetone, toluene and DCM and dried under an argon stream.

Surface erasing (removal of the pattern)

For light-induced erasing, the patterned silicon wafer was placed in a headspace vial (Pyrex, diameter 20 mm) and 5 mL of pure, dry MeCN or DCM was added. The vial was crimped airtight using styrene/butadiene rubber seals with PTFE inner liner and the solvent was percolated with argon for 5 min. Subsequently, the sample was irradiated in a custom built photoreactor (Figure 29) employing a Philips PL-L lamp (emission spectrum see Figure 29) for 24 h. After 24 h irradiation time, the MeCN was exchanged for fresh solvent and the sample was irradiated for another 24 h to complete the erasing process.

7.3.3 Syntheses from Chapter 5

RAFT copolymerization of PE-MA (8) and MMA (PE-MA-*co*-MMA)

The polymerization was carried out in a suitable headspace vial equipped with a rubber septum. MMA (219 µL, 203 mg, 2.03 mmol, 100 mol%) and PE-MA (**8**) (86.4 mg, 0.230 mmol, 10 mol%) were dissolved in 1,4-dioxane (534 µL) to obtain a monomer concentration of 3 mol L^{-1}. CPAETC (5.9 mg, 0.023 mmol) and V-601 (1.04 mg, 0.005 mmol) were added ([CTA] / [I] = 5). The solution was percolated with nitrogen for 5 min and subsequently placed in an oil bath at 60 °C. The polymerization was quenched after 16 h by exposure to air and cooling with an ice bath. The mixture was diluted with THF and the resulting polymer (PE-MA-*co*-MMA) was precipitated in ice cold Et_2O and dried under vacuum.

For the kinetic study illustrated in Section 5.1.1, the same protocol was followed and samples for ^{1}H NMR and SEC analysis were directly withdrawn from the reaction mixture employing a degassed syringe after 30 min, 45 min, 1 h, 2 h, 3 h. 4 h, 6 h, 8 h, 10 h, 13 h and 16 h. The conversion depicted in Figure 51 was calculated from ^{1}H NMR spectra.

RAFT copolymerization of PS-MA (7) and MMA (PS-MA-*co*-MMA)

The polymerization was carried out in a suitable headspace vial equipped with a rubber septum. MMA (639 µL, 601 mg, 6.01 mmol, 100 mol%) and PS-MA (**7**) (193.4 mg, 0.600 mmol, 10 mol%) were dissolved in 1,4-dioxane (1361 µL) to obtain a monomer concentration of 3 mol L^{-1}. CPAETC (15.8 mg, 0.060 mmol) and V-601 (2.76 mg, 0.012 mmol) were added ([CTA]/[I] = 5). The solution was percolated with nitrogen for 10 min and subsequently placed in an oil bath at 60 °C. The polymerization was quenched after 8 h by exposure to air and cooling in an ice bath. The mixture was diluted with THF and the resulting polymer (PS-MA-*co*-MMA) was precipitated in ice cold Et_2O and dried under vacuum.

For the kinetic study illustrated in Section 5.1.1, the same protocol was followed and samples for ^{1}H NMR and SEC analysis were directly withdrawn from the reaction mixture employing a degassed syringe after 30 min, 1 h, 2 h, 3 h. 4 h, 6 h, 8 h, 10 h, 13 h and 16 h. The conversion depicted in Figure 46 was calculated from ^{1}H NMR spectra.

RAFT block copolymerization for (PE-MA-*co*-MMA)$_{100}$-*b*-MMA$_{20}$-*b*-(PS-MA-*co*-MMA)$_{100}$

The three step RAFT copolymerization was carried out in a suitable headspace vial equipped with a rubber septum.

For the first block, (PE-MA-*co*-MMA)$_{100}$, MMA (144 µL, 135 mg, 1.40 mmol, 100 mol%), PE-MA (**8**) (57.8 mg, 0.14 mmol, 10 mol%) and CPAETC (3.9 mg, 0.015 mmol) were dissolved in 1,4-dioxane (307 µL). A stock solution of V601 in 1,4-dioxane was prepared (10 mg mL^{-1}) and 49.2 µL were added to the monomer mixture. An initial monomer concentration of 3 mol L^{-1} and a CTA/I molar ratio of 5 were obtained. The reaction mixture was percolated with nitrogen for 5 min and subsequently placed in an oil bath at 60 °C. After 16 h, the headspace vial was cooled in an ice bath and the reagents for the second block (MMA$_{20}$) were added: MMA (32 µL, 30 mg, 0.3 mmol), initiator stock solution (11.6 µL) and dioxane (10 µL). The solution was again percolated with nitrogen for 5 min and placed in an oil bath at 60 °C. The polymerization was conducted for 4 h. Subsequently, the headspace vial was placed in an ice bath and the reagents for the third block (PS-MA-*co*-MMA)$_{100}$ were added: MMA (144 µL, 135 mg, 1.4 mmol, 100 mol%), PS-MA (**7**) (48 mg, 0.14 mmol, 10 mol%), initiator stock solution (16.4 µL) and dioxane (50 µL) The polymerization mixture was percolated with nitrogen for 5 min placed in an oil bath at 60 °C and the polymerization was conducted for 8 h. Afterwards, the mixture was cooled with an ice bath, diluted with 1,4-dioxane and the polymer was precipitated in ice cold Et_2O. The obtained triblock copolymer was dried under vacuum and characterized by ^{1}H NMR and SEC analysis (results see Figure 55 and Figure 54, respectively, Section 5.1.3).

Light induced SCNP folding procedure of a PS-MA-co-MMA (PS-SCNP(18)/(20))

A PS-MA-co-MMA (DP_n 100 or 200) (10 mg, 0.001 mmol) was dissolved in THF (1 L) and stirred for 30 min in the dark. 3,6 dioxa-1,8-octanedithiol (crosslinker **25**) (0.6 mg, 0.003 mmol, 0.3 eq per PS-unit) was added and the solution was irradiated with a compact low pressure fluorescent lamp (Cleo PL-L, Philips Deutschland GmbH, λ_{max} = 355 nm) for 2 h for DP_n = 100 or 3 h for DP_n = 200, respectively. Subsequently, DPS (3.2 mg, 0.015 mmol) was added and the mixture was stirred for 15 min in the dark. The solvent was removed under reduced pressure and the remaining solid was characterized by SEC and DLS in comparison to the precursor polymer (see Figure 64 and Figure 65, for SEC and Figure 66 for DLS, respectively).

Light induced SCNP folding procedure of a PE-MA-*co*-MMA$_{100}$ (PE-SCP(15))

PE-MA-*co*-MMA$_{100}$ (10 mg, 0.001 mmol) were dissolved in DCM (1 L) and stirred for 30 min in the dark. Di(ethylene glycol) diacrylate **24** (0.3 mg, 0.0015 mmol, 0.15 eq per PE-unit) was added as crosslinker. The reaction mixture was irradiated employing a compact low pressure fluorescent lamp (Arimed B$_6$, Cosmedico, λ_{max} = 320 nm) for 30 min. Subsequently, butyl acrylate (0.2 mL, 0.18 mg) was added and the reaction mixture was irradiated for another 30

min. After the irradiation, DPS was added (0.5 mg, 0.03 mmol) and the mixture was stirred for 15 min in the dark. The solvent was removed under reduced pressure and the obtained solid was characterized by SEC and DLS in comparison to the precursor polymer (see Figure 73 and Figure 74, respectively).

Acetal protection procedure of (PE-MA-*co*-MMA)$_{100}$-*b*-MMA$_{20}$-*b*-(PS-MA-*co*-MMA)$_{100}$

In a flame dried 10 mL Schlenk tube containing dry molecular sieves (4 Å) and a stirring bar, the triblock copolymer (10 mg, 0.0005 mmol, containing 0.0082 mmol PE-units) was dissolved in a mixture of dry MeCN (2.5 mL) and dry MeOH (0.5 mL). Subsequently, trimethyl orthoformate (18.0 µL, 17.4 mg, 0.164 mmol, 20 eq) and tosylic acid (0.22 mg, 0.0013 mmol, 0.16 eq) were added and the reaction mixture was stirred under argon atmosphere at 40 °C overnight. 2,6-Lutidine (5 mg, 0.045 mmol, 5.5 eq) was added at ambient temperature and the solvent was removed under reduced pressure. The obtained solid was analyzed by ^{1}H NMR and SEC (see Figure 78). For the triblock copolymer photocompaction the procedure was repeated and the obtained polymer was directly employed for the light induced folding experiment.

Stepwise photocompaction procedure of protected (PE-MA-*co*-MMA)$_{100}$-*b*-MMA$_{20}$-*b*-(PS-MA-*co*-MMA)$_{100}$

For the light induced dual compaction, the protected triblock copolymer was directly employed after the protection reaction. The PS block was folded first by applying the following procedure. The solid was dissolved in THF (1 L) containing TEA (0.3 mL) and stirred for 30 min in the dark. 3,6-dioxa-1,8-octanedithiol **25** (0.6 mg, 0.003 mmol, 0.3 eq per PS unit) was added and the solution was irradiated with a compact low pressure fluorescent lamp (Cleo PL-L, Philips Deutschland GmbH, λ_{max} = 355 nm) for 2 h. Subsequently, DPS (3.2 mg, 0.015 mmol) was added and the mixture was stirred for 15 min in the dark. The solvent was removed under reduced pressure and the remaining solid was characterized by SEC and DLS in comparison to the precursor polymer (see Figure 79 and Figure 81, respectively).

Half of the material obtained after the first photocompaction was dissolved in DCM (500 mL). Wet molecular sieves (4 Å) were added and the mixture was stirred for 30 min in the dark to ensure complete dissolution of the polymer and remove the protection group in situ. Di(ethylene glycol) diacrylate **24** (0.3 mg, 0.0015 mmol) was added as crosslinker. The reaction mixture was irradiated employing a compact low pressure fluorescent lamp (Arimed B$_6$, Cosmedico, λ_{max} = 320 nm) for 30 min. Subsequently, butyl acrylate (0.2 mL, 0.18 mg) was added and the reaction mixture was irradiated for another 30 min. After the irradiation, DPS was added (0.5 mg, 0.03 mmol) and the mixture was stirred for additional 15 min in the dark. The solvent was removed under reduced pressure and the obtained solid was characterized by SEC and DLS in comparison to the precursor polymers (see Figure 79 and Figure 81, respectively).

BIBLIOGRAPHY

[1] J. Priestley, *Philosophical Transactions* **1772**, *62*, 147.

[2] J. Ingenhousz, *Experiments upon vegetables: discovering their great power of purifying the common air in the sun-shine, and of injuring it in the shade and at night.*, P. Elmsly, H. Payne, London, **1779**.

[3] H. Trommsdorf, *Annaler der Pharmacie* **1834**, *11*, 190.

[4] H. D. Roth, *Angew. Chem.* **1989**, *101*, 1220.

[5] M. Planck, *Annalen der Physik* **1901**, *309*, 553.

[6] A. Einstein, *Annalen der Physik* **1905**, *17*, 132.

[7] T. H. Maiman, *Nature* **1960**, *187*, 493.

[8] N. Hoffmann, *Chem. Rev.* **2008**, 1052.

[9] M. A. Tasdelen, Y. Yagci, *Angew. Chem. Int. Ed. Engl.* **2013**, *52*, 5930.

[10] S. Chatani, C. J. Kloxin, C. N. Bowman, *Polym. Chem.* **2014**, *5*, 2187.

[11] G. Delaittre, A. S. Goldmann, J. O. Mueller, C. Barner-Kowollik, *Angew. Chem. Int. Ed. Engl.* **2015**, *54*, 11388.

[12] W. R. Browne, B. L. Feringa, *Annu. Rev. Phys. Chem.* **2009**, *60*, 407.

[13] M. J. Hansen, W. A. Velema, M. M. Lerch, W. Szymanski, B. L. Feringa, *Chem. Soc. Rev.* **2015**, *44*, 3358.

[14] N. Corrigan, S. Shanmugam, J. Xu, C. Boyer, *Chem. Soc. Rev.* **2016**, *45*, 6165.

[15] G. Dormán, G. D. Prestwich, *Trends in Biotech.* **2000**, *18*, 64.

[16] G. C. Ellis-Davies, *Nat. Methods.* **2007**, *4*, 619.

[17] B. Richter, T. Pauloehrl, J. Kaschke, D. Fichtner, J. Fischer, A. M. Greiner, D. Wedlich, M. Wegener, G. Delaittre, C. Barner-Kowollik, M. Bastmeyer, *Adv. Mater.* **2013**, *25*, 6117.

[18] A. S. Quick, A. de los Santos Pereira, M. Bruns, T. Bückmann, C. Rodriguez-Emmenegger, M. Wegener, C. Barner-Kowollik, *Adv. Funct. Mater.* **2015**, *25*, 3735.

[19] M. P. Lutolf, J. A. Hubbell, *Nat. Biotechnol.* **2005**, *23*, 47.

[20] F. Klein, B. Richter, T. Striebel, C. M. Franz, G. von Freymann, M. Wegener, M. Bastmeyer, *Adv. Mater.* **2011**, *23*, 1341.

[21] T. P. Yoon, M. A. Ischay, J. Du, *Nat. Chem.* **2010**, *2*, 527.

[22] J. Xuan, W. J. Xiao, *Angew. Chem. Int. Ed. Engl.* **2012**, *51*, 6828.

[23] J. O. Mueller, F. G. Schmidt, J. P. Blinco, C. Barner-Kowollik, *Angew. Chem. Int. Ed. Engl.* **2015**, *54*, 10284.

[24] P. Lederhose, K. N. Wust, C. Barner-Kowollik, J. P. Blinco, *Chem. Commun.* **2016**, *52*, 5928.

[25] T. P. Huynh, P. Sonar, H. Haick, *Adv. Mater.* **2017**.

[26] H. D. Becker, *Chem. Rev.* **1933**, *93*, 145.

[27] M. Gonzalez-Burgos, A. Latorre-Sanchez, J. A. Pomposo, *Chem. Soc. Rev.* **2015**, *44*, 6122.
[28] J. Willenbacher, K. N. R. Wuest, J. O. Mueller, M. Kaupp, H.-A. Wagenknecht, C. Barner-Kowollik, *ACS Macro Letters* **2014**, *3*, 574.
[29] A. Sanchez-Sanchez, I. Perez-Baena, J. A. Pomposo, *Molecules* **2013**, *18*, 3339.
[30] Y. Ivarsson, C. Travaglini-Allocatelli, M. Brunori, S. Gianni, *Eur. Biophys. J.* **2008**, *37*, 721.
[31] R. K. Roy, J. F. Lutz, *J. Am. Chem. Soc.* **2014**, *136*, 12888.
[32] J. Zhang, G. Gody, M. Hartlieb, S. Catrouillet, J. Moffat, S. Perrier, *Macromolecules* **2016**, *49*, 8933.
[33] P. Nesvadba, *Radical Polymerization in Industry*, John Wiley and Sons, **2012**.
[34] G. Odian, in *Principles of Polymerization*, John Wiley & Sons, Inc., **2004**, pp. 198.
[35] B. Yamada, P. B. Zetterlund, in *Handbook of Radical Polymerization*, John Wiley & Sons, Inc., **2003**, pp. 117.
[36] C. Barner-Kowollik, P. Vana, T. P. Davis, in *Handbook of Radical Polymerization*, John Wiley & Sons, Inc., **2003**, pp. 187.
[37] D. Hensley, S. Goodrich, *Macromolecules* **1995**, *28*, 1586.
[38] T. Junkers, S. P. S. Koo, T. P. Davis, M. H. Stenzel, C. Barner-Kowollik, *Macromolecules* **2007**, *40*, 8906.
[39] A. G. Anderson, A. Gridnev, G. Moad, E. Rizzardo, S. H. Thang, *E. I. D. P. d. N. Co.*, USA, **1998**.
[40] J.-S. Wang, K. Matyjaszewski, *Macromolecules* **1995**, *28*, 7901.
[41] J. Chiefari, Y. K. Chong, F. Ercole, J. Krstina, J. Jeffery, T. P. T. Le, R. T. A. Mayadunne, G. F. Meijs, C. L. Moad, G. Moad, E. Rizzardo, S. H. Thang, *Macromolecules* **1998**, *31*, 5559.
[42] K. Matyjaszewski, in *Handbook of Radical Polymerization*, John Wiley & Sons, Inc., **2003**, pp. 361.
[43] M. Szwarc, *Nature* **1956**, 1168.
[44] M. H. Stenzel, C. Barner-Kowollik, *Mater. Horiz.* **2016**, *3*, 471.
[45] S. Z. Zard, in *Handbook of RAFT Polymerization*, Wiley-VCH Verlag GmbH & Co. KGaA, **2008**, pp. 151.
[46] G. Moad, C. Barner-Kowollik, in *Handbook of RAFT Polymerization*, Wiley-VCH Verlag GmbH & Co. KGaA, **2008**, pp. 51.
[47] D. J. Keddie, G. Moad, E. Rizzardo, S. H. Thang, *Macromolecules* **2012**, *45*, 5321.
[48] A. J. Inglis, M. H. Stenzel, C. Barner-Kowollik, *Macromol. Rapid Commun.* **2009**, *30*, 1792.
[49] C. J. Dürr, P. Lederhose, L. Hlalele, D. Abt, A. Kaiser, S. Brandau, C. Barner-Kowollik, *Macromolecules* **2013**, *46*, 5915.
[50] B. V. K. J. Schmidt, M. Hetzer, H. Ritter, C. Barner-Kowollik, *Macromolecules* **2011**, *44*, 7220.
[51] Y. K. Chong, Tam P. T. Le, Graeme Moad, Ezio Rizzardo, S. H. Thang, *Macromolecules* **1999**, *32*, 2071.

[52] G. Gody, R. Barbey, M. Danial, S. Perrier, *Polym. Chem.* **2015**, *6*, 1502.
[53] G. Gody, T. Maschmeyer, P. B. Zetterlund, S. Perrier, *Macromolecules* **2014**, *47*, 3451.
[54] J. Vandenbergh, T. de Moraes Ogawa, T. Junkers, *J. Polym. Sci. Part A: Polym. Chem.* **2013**, *51*, 2366.
[55] D. J. Keddie, *Chem. Soc. Rev.* **2014**, *43*, 496.
[56] G. Gody, T. Maschmeyer, P. B. Zetterlund, S. Perrier, *Macromolecules* **2014**, *47*, 639.
[57] M. R. Hill, R. N. Carmean, B. S. Sumerlin, *Macromolecules* **2015**, *48*, 5459.
[58] G. Gody, T. Maschmeyer, P. B. Zetterlund, S. Perrier, *Nat. Commun.* **2013**, *4*, 2505.
[59] T.-N. d. Saussure, *Chemische Untersuchungen über die Vegetation*, C. H. Reclam, Leipzig, **1805**.
[60] P. S. G. Ciamician, *Ber. Dtsch. Chem. Ges.* **1901**, *34*, 2040.
[61] P. S. G. Ciamician, *Ber. Dtsch. Chem. Ges.* **1907**, *39*, 4343.
[62] P. W. Atkins, J. d. Paula, *Physikalische Chemie, Vol. 5*, Wiley-VCH, Weinheim, **2013**.
[63] A. Jablonski, *Nature* **1933**, *131*, 839.
[64] H. G. O. Becker, *Einführung in die Photochemie, Vol. 3*, Dt. Verl. d. Wiss., Berlin, **1991**.
[65] M. Klessinger, *Chemie in unserer Zeit* **1978**, *12*, 1.
[66] E. Frick, C. Schweigert, B. B. Noble, H. A. Ernst, A. Lauer, Y. Liang, D. Voll, M. L. Coote, A.-N. Unterreiner, C. Barner-Kowollik, *Macromolecules* **2016**, *49*, 80.
[67] A. Padwa, J. Smolanott, *J. Am. Chem. Soc.* **1971**, *93*, 548.
[68] G. Bertrand, C. Wentrup, *Angew. Chem. Int. Ed. Engl.* **1994**, *106*, 549.
[69] T. K. Claus, S. Telitel, A. Welle, M. Bastmeyer, A. P. Vogt, G. Delaittre, C. Barner-Kowollik, *Chem. Commun.* **2017**, *53*, 1599.
[70] I. Flemming, *Molecular Orbitals and Organic Chemical Reactions: Reference Edition*, Wiley-VCH, Weinheim, **2010**.
[71] E. Vedejs, T. H. Eberlein, D. L. Varie, *J. Am. Chem. Soc.* **1982**, *104*, 1445.
[72] M. Yamaji, S. Wakabayashi, S. Tobita, *Res. Chem. Intermed.* **2006**, *32*, 749.
[73] M. C. Caserio, W. Lauer, T. Novinson, *J. Am. Chem. Soc.* **1970**, *92*, 6082.
[74] P. J. Wagner, M. J. Lindstrom, *J. Am. Chem. Soc.* **1987**, *109*, 3062.
[75] T. Pauloehrl, A. Welle, K. K. Oehlenschlaeger, C. Barner-Kowollik, *Chem. Sci.* **2013**, *4*, 3503.
[76] E. Vedejs, D. A. Perry, K. N. Houk, N. G. Rondan, *J. Am. Chem. Soc.* **1983**, *105*, 6999.
[77] M. Glassner, K. K. Oehlenschlaeger, A. Welle, M. Bruns, C. Barner-Kowollik, *Chem. Commun.* **2013**, *49*, 633.
[78] C. Lang, S. Bestgen, A. Welle, R. Muller, P. W. Roesky, C. Barner-Kowollik, *Chemistry* **2015**, *21*, 14728.
[79] T. Tischer, T. K. Claus, K. K. Oehlenschlaeger, V. Trouillet, M. Bruns, A. Welle, K. Linkert, A. S. Goldmann, H. G. Borner, C. Barner-Kowollik, *Macromol. Rapid Commun.* **2014**, *35*, 1121.

[80] M. Kaupp, A. S. Quick, C. Rodriguez-Emmenegger, A. Welle, V. Trouillet, O. Pop-Georgievski, M. Wegener, C. Barner-Kowollik, *Adv. Funct. Mater.* **2014**, *24*, 5649.
[81] T. K. Claus, B. Richter, V. Hahn, A. Welle, S. Kayser, M. Wegener, M. Bastmeyer, G. Delaittre, C. Barner-Kowollik, *Angew. Chem. Int. Ed. Engl.* **2016**, *55*, 3817.
[82] B. Richter, V. Hahn, S. Bertels, T. K. Claus, M. Wegener, G. Delaittre, C. Barner-Kowollik, M. Bastmeyer, *Adv. Mater.* **2017**, *29*, 1604342.
[83] T. K. Claus, J. Zhang, L. Martin, M. Hartlieb, H. Mutlu, G. Delaittre, S. Perrier, C. Barner-Kowollik, *Macromol. Rapid Commun.* **2017**, *1700264*. https://doi.org/10.1002/marc.201700264.
[84] P. G. Sammes, *Tetrahedron* **1976**, *32*, 405.
[85] N. C. Yang, C. Rivas, *J. Am. Chem. Soc.* **1961**, *83*, 2213.
[86] G. Porter, M. F. Tchir, *Journal of the Chemical Society D: Chemical Communications* **1970**, 1372.
[87] G. Porter, M. F. Tchir, *Journal of the Chemical Society A: Inorganic, Physical, Theoretical* **1971**, 3772.
[88] T. Pauloehrl, G. Delaittre, V. Winkler, A. Welle, M. Bruns, H. G. Borner, A. M. Greiner, M. Bastmeyer, C. Barner-Kowollik, *Angew. Chem. Int. Ed. Engl.* **2012**, *51*, 1071.
[89] M. Langer, J. O. Mueller, A. S. Goldmann, F. H. Schacher, C. Barner-Kowollik, *ACS Macro Letters* **2016**, *5*, 597.
[90] K. K. Oehlenschlaeger, J. O. Mueller, N. B. Heine, M. Glassner, N. K. Guimard, G. Delaittre, F. G. Schmidt, C. Barner-Kowollik, *Angew. Chem. Int. Ed. Engl.* **2013**, *52*, 762.
[91] T. Tischer, T. K. Claus, M. Bruns, V. Trouillet, K. Linkert, C. Rodriguez-Emmenegger, A. S. Goldmann, S. Perrier, H. G. Borner, C. Barner-Kowollik, *Biomacromolecules* **2013**, *14*, 4340.
[92] H. Bouas-Laurent, J.-P. Desvergne, A. Castellan, R. Lapouyade, *Chem. Soc. Rev.* **2001**, *30*, 248.
[93] J. Fritzsche, *J. prakt. Chem.* **1867**, *101*, 333.
[94] F. D. Greene, S. L. Misrock, J. R. Wolfe, *J. Am. Chem. Soc.* **1955**, *77*, 3852.
[95] H. Bouas-Laurent, A. Castellan, J.-P. Desvergne, R. Lapouyade, *Chem. Soc. Rev.* **2000**, *29*, 43.
[96] R. B. Woodward, R. Hoffmann, *Angew. Chem. Int. Ed. Engl.* **1969**, *8*, 781.
[97] N. Toshima, T. Sugano, H. Hira, *Can. J. Chem.* **1984**, *62*, 2047.
[98] E. Bowen, *Discuss. Faraday Soc.* **1953**, *14*, 143.
[99] J. Van Damme, L. Vlaminck, G. Van Assche, B. Van Mele, O. van den Berg, F. Du Prez, *Tetrahedron* **2016**, *72*, 4303.
[100] J. Ferguson, *Chem. Rev.*, *86*, 957.
[101] G. W. Breton, X. Vang, *J. Chem. Ed.* **1998**, *75*, 81.
[102] F. Fages, J. P. Desvergne, I. Frisch, H. Bousas-Laurent, *J. Chem. Soc.* **1988**, 1413.
[103] T. Zdobinsky, P. S. Maiti, R. Klajn, *J. Am. Chem. Soc.* **2014**, *136*, 2711.
[104] B. Fabre, D. M. Bassani, C.-K. Liang, S. Lhenry, P. Hapiot, *J. Phys. Chem. C* **2013**, *117*, 12725.

[105] K. Rameshbabu, Y. Kim, T. Kwon, J. Yoo, E. Kim, *Tetrahedron Letters* **2007**, *48*, 4755.
[106] P. Payamyar, M. Servalli, T. Hungerland, A. P. Schutz, Z. Zheng, A. Borgschulte, A. D. Schluter, *Macromol. Rapid Commun.* **2015**, *36*, 151.
[107] P. G. Frank, B. T. Tuten, A. Prasher, D. Chao, E. B. Berda, *Macromol. Rapid Commun.* **2014**, *35*, 249.
[108] H. Yamada, E. Kawamura, S. Sakamoto, Y. Yamashita, T. Okujima, H. Uno, N. Ono, *Tetrahedron Letters* **2006**, *47*, 7501.
[109] A. R. Smith, D. F. Watson, *Chemistry of Materials* **2010**, *22*, 294.
[110] Y. Tsuchiya, S. Haraguchi, M. Ogawa, T. Shiraki, H. Kakimoto, O. Gotou, T. Yamada, K. Okumoto, S. Nakatani, K. Sakanoue, S. Shinkai, *Adv. Mater.* **2012**, *24*, 968.
[111] H. Durmaz, B. Colakoglu, U. Tunca, G. Hizal, *J. Polym. Sci. Pol. Chem.* **2006**, *44*, 1667.
[112] C. Cardenas-Daw, A. Kroeger, W. Schaertl, P. Froimowicz, K. Landfester, *Macromol. Chem. Phys.* **2012**, *213*, 144.
[113] R. W. Boyd, in *Nonlinear Optics (Third Edition)*, Academic Press, Burlington, **2008**.
[114] M. Goeppert-Mayer, *Ann. Phys.* **1931**, *401*, 273.
[115] W. Kaiser, C. G. B. Garrett, *Phys. Rev. Lett.* **1961**, *7*, 229.
[116] M. Pawlicki, H. A. Collins, R. G. Denning, H. L. Anderson, *Angew. Chem. Int. Ed. Engl.* **2009**, *48*, 3244.
[117] W. R. Zipfel, R. M. Williams, W. W. Webb, *Nat. Biotechnol.* **2003**, *21*, 1369.
[118] C. N. LaFratta, J. T. Fourkas, T. Baldacchini, R. A. Farrer, *Angew. Chem. Int. Ed. Engl.* **2007**, *46*, 6238.
[119] A. Selimis, V. Mironov, M. Farsari, *Microelectronic Engineering* **2015**, *132*, 83.
[120] S. Maruo, J. T. Fourkas, *Laser & Photonics Review* **2008**, *2*, 100.
[121] T. Buckmann, M. Thiel, M. Kadic, R. Schittny, M. Wegener, *Nat. Commun.* **2014**, *5*, 4130.
[122] M. Farsari, B. N. Chichkov, *Nature Photonics* **2009**, *3*, 450.
[123] M. Malinauskas, M. Farsari, A. Piskarskas, S. Juodkazis, *Phys. Rep.* **2013**, *533*, 1.
[124] S. p. Klein, A. Barsella, H. Leblond, H. Bulou, A. Fort, C. Andraud, G. Lemercier, J. C. Mulatier, K. Dorkenoo, *Applied Physics Letters* **2005**, *86*, 211118.
[125] W. Gao, N. Singh, L. Song, Z. Liu, A. L. Reddy, L. Ci, R. Vajtai, Q. Zhang, B. Wei, P. M. Ajayan, *Nat. Nanotechnol.* **2011**, *6*, 496.
[126] M. Deubel, G. von Freymann, M. Wegener, S. Pereira, K. Busch, C. M. Soukoulis, *Nat. Mater.* **2004**, *3*, 444.
[127] B. B. Xu, Y. L. Zhang, H. Xia, W. F. Dong, H. Ding, H. B. Sun, *Lab Chip* **2013**, *13*, 1677.
[128] A. M. Greiner, B. Richter, M. Bastmeyer, *Macromol Biosci* **2012**, *12*, 1301.
[129] A. S. Quick, J. Fischer, B. Richter, T. Pauloehrl, V. Trouillet, M. Wegener, C. Barner-Kowollik, *Macromol Rapid Commun* **2013**, *34*, 335.

[130] A. S. Quick, H. Rothfuss, A. Welle, B. Richter, J. Fischer, M. Wegener, C. Barner-Kowollik, *Adv. Funct. Mater.* **2014**, *24*, 3571.
[131] E. Ruiz-Hitzky, *Chem. Rec.* **2003**, *3*, 88.
[132] J. H. Schulman, *Journal of Colloid and Interface Science* **1967**, *25*, 1.
[133] H. Kaji, G. Camci-Unal, R. Langer, A. Khademhosseini, *Biochimica et Biophysica Acta (BBA) - General Subjects* **2011**, *1810*, 239.
[134] A. Pimpin, W. Srituravanich, *Engeneering Journal* **2012**, *16*, 37.
[135] A. F. Hirschbiel, S. Geyer, B. Yameen, A. Welle, P. Nikolov, S. Giselbrecht, S. Scholpp, G. Delaittre, C. Barner-Kowollik, *Adv. Mater.* **2015**, *27*, 2621.
[136] S. Flink, F. C. J. M. van Veggel, D. N. Reinhoudt, *Sensors Update* **2000**, *8*, 3.
[137] M.-I. Baraton, *Encyclopedia of Nanoscience and Nanotechnology* **2004**, *10*, 267.
[138] D. J. Dyer, *Adv. Funct. Mater.* **2003**, *13*, 667.
[139] Y. Luo, J. Huang, *Science China Chemistry* **2014**, *57*, 1672.
[140] R. T. Chen, S. Marchesan, R. A. Evans, K. E. Styan, G. K. Such, A. Postma, K. M. McLean, B. W. Muir, F. Caruso, *Biomacromolecules* **2012**, *13*, 889.
[141] Y. Hu, J. S. Li, W. T. Yang, F. J. Xu, *Thin Solid Films* **2013**, *534*, 325.
[142] J. M. Buriak, *Chemistry of Materials* **2014**, *26*, 763.
[143] H. Lee, S. M. Dellatore, W. M. Miller, P. B. Messersmith, *Science* **2007**, *318*, 426.
[144] T. Desmet, R. Morent, N. De Geyter, C. Leys, E. Schacht, P. Dubruel, *Biomacromolecules* **2009**, *10*, 2351.
[145] N. K. Chaki, K. Vijayamohanan, *Biosensors & Bioelectronics* **2002**, *17*, 1.
[146] T. Dey, D. Naughton, *Journal of Sol-Gel Science and Technology* **2015**, *77*, 1.
[147] C. Haensch, S. Hoeppener, U. S. Schubert, *Chem. Soc. Rev.* **2010**, *39*, 2323.
[148] S. Alom Ruiz, C. S. Chen, *Soft Matter* **2007**, *3*, 168.
[149] B. Derby, *Annu. Rev. Mater. Res.* **2010**, *40*, 395.
[150] A. Benninghoven, *Phys. Status Solidi. B* **1969**, *169*, 169.
[151] A. Benninghoven, *Angew. Chem.* **1994**, *106*, 1075.
[152] A. Benninghoven, *Surface Science* **1971**, *28*, 541.
[153] R. Behrisch, W. Eckstein, *Sputtering by Particle Bombardment: Experiments and Computer Calculations from Threshold to MeV Energies*, Springer-Verlag, Berlin, **2007**.
[154] T. Wirtz, P. Philipp, J. N. Audinot, D. Dowsett, S. Eswara, *Nanotechnology* **2015**, *26*, 434001.
[155] ION-TOF GmbH, https://www.iontof.com/tof-sims-secondary-ion-mass-spectrometry.html, Münster, **2017-02-26**.
[156] A. Benninghoven, E. Niehuis, D. Greifendorf, D. L. v. Leyen, W. Lange, *Springer Ser. Chem. Phys.* **1986**, *44*, 497.
[157] M. Guilhaus, *J. Mass Spectrom.* **1995**, *30*, 1519.
[158] R. N. Sodhi, *Analyst* **2004**, *129*, 483.
[159] D. L. Wetzel, S. M. LeVine, *Science* **1999**, *285*, 1224.
[160] R. M. Badger, R. Newman, *Rev. Sci. Instrum.* **1951**, *22*, 935.
[161] R. Barer, A. R. H. Cole, H. W. Thompson, *Nature* **1949**, *163*, 198.

[162] G. Ellis, C. Marco, M. Gomez, *Infrared Phys. Tech.* **2004**, *45*, 349.
[163] E. Abbe, *Arch. Mikrosk. Anat.* **1873**, *9*, 413.
[164] J. H. Rice, *Nanoscale* **2010**, *2*, 660.
[165] Bruker GmbH, *https://www.bruker.com/fileadmin/user_upload/8-PDF-Docs/OpticalSpectrospcopy/FT-IR/Hyperion/Brochures/HYPERION_Brochure_EN.pdf*, Ettlingen, **2017-02-27**.
[166] V. W. Kuhn, H. Majer, *Die Makromolekulare Chemie* **1956**, *18*, 239.
[167] B. V. Schmidt, N. Fechler, J. Falkenhagen, J. F. Lutz, *Nat. Chem.* **2011**, *3*, 234.
[168] S. Mavila, O. Eivgi, I. Berkovich, N. G. Lemcoff, *Chem. Rev.* **2016**, *116*, 878.
[169] O. Altintas, C. Barner-Kowollik, *Macromol. Rapid Commun.* **2015**.
[170] J. A. Pomposo, *Polymer International* **2014**, *63*, 589.
[171] A. M. Hanlon, C. K. Lyon, E. B. Berda, *Macromolecules* **2016**, *49*, 2.
[172] M. K. Aiertza, I. Odriozola, G. Cabanero, H. J. Grande, I. Loinaz, *Cell Mol. Life Sci.* **2012**, *69*, 337.
[173] E. Harth, B. van Horn, V. Y. Lee, D. S. Germack, C. P. Gonzales, R. D. Miller, C. J. Hawker, *J. Am. Chem. Soc.* **2002**, *124*, 8653.
[174] M. Seo, B. J. Beck, J. M. J. Paulusse, C. J. Hawker, S. Y. Kim, *Macromolecules* **2008**, *41*, 6413.
[175] E. B. Berda, E. J. Foster, E. W. Meijer, *Macromolecules* **2010**, *43*, 1430.
[176] A. R. de Luzuriaga, N. Ormategui, H. J. Grande, I. Odriozola, J. A. Pomposo, I. Loinaz, *Macromol. Rapid Commun.* **2008**, *29*, 1156.
[177] J. Willenbacher, B. V. Schmidt, D. Schulze-Suenninghausen, O. Altintas, B. Luy, G. Delaittre, C. Barner-Kowollik, *Chem. Commun.* **2014**, *50*, 7056.
[178] O. Altintas, E. Lejeune, P. Gerstel, C. Barner-Kowollik, *Polym. Chem.* **2012**, *3*, 640.
[179] J. B. Beck, K. L. Killops, T. Kang, K. Sivanandan, A. Bayles, M. E. Mackay, K. L. Wooley, C. J. Hawker, *Macromolecules* **2009**, *42*, 5629.
[180] J. Willenbacher, O. Altintas, V. Trouillet, N. Knöfel, M. J. Monteiro, P. W. Roesky, C. Barner-Kowollik, *Polym. Chem.* **2015**, *6*, 4358.
[181] I. Perez-Baena, I. Loinaz, D. Padro, I. García, H. J. Grande, I. Odriozola, *J. Mater. Chem.* **2010**, *20*, 6916.
[182] Y. Bai, X. Feng, H. Xing, Y. Xu, B. K. Kim, N. Baig, T. Zhou, A. A. Gewirth, Y. Lu, E. Oldfield, S. C. Zimmerman, *J. Am. Chem. Soc.* **2016**, *138*, 11077.
[183] C. Heiler, J. T. Offenloch, E. Blasco, C. Barner-Kowollik, *ACS Macro Lett.* **2017**, *6*, 56.
[184] J. Liu, G. Feng, R. Liu, N. Tomczak, L. Ma, G. G. Gurzadyan, B. Liu, *Small* **2014**, *10*, 3110.
[185] C.-C. Cheng, D.-J. Lee, Z.-S. Liao, J.-J. Huang, *Polym. Chem.* **2016**, *7*, 6164.
[186] P. Huang, J. Liu, W. Wang, C. Li, J. Zhou, X. Wang, L. Deng, D. Kong, J. Liu, A. Dong, *ACS Appl. Mater. Interfaces* **2014**, *6*, 14631.
[187] T. S. Fischer, D. Schulze-Sunninghausen, B. Luy, O. Altintas, C. Barner-Kowollik, *Angew. Chem. Int. Ed. Engl.* **2016**, *55*, 11276.
[188] M. D. Lechner, E. H. Nordmeier, K. Gehrke, *Makromolekulare Chemie, Vol. 4th Ed.*, Birkhäuser, Basel, **2010**.

[189] H. G. Barth, B. E. Boyes, C. Jackson, *Anal. Chem.* **1996**, *68*, 445R.
[190] K. F. Arndt, G. Müller, *Polymercharakterisierung*, Hanser, **1996**.
[191] C. Wu, *Handbook of size exclusion chromatography and related techniques, Vol. 2nd Ed*, CRC Press, New York, **2003**.
[192] J. A. Pomposo, I. Perez-Baena, L. Buruaga, A. Alegría, A. J. Moreno, J. Colmenero, *Macromolecules* **2011**, *44*, 8644.
[193] P. A. Hassan, S. Rana, G. Verma, *Langmuir* **2015**, *31*, 3.
[194] R. Pecora, *Journal of Nanoparticle Research* **2000**, *2*, 123.
[195] R. Pecora, *Makromol. Chem.* **1979**, *2*, 73.
[196] D. E. A. Koppel, *J. Chem. Phys.* **1972**, *57*, 4814–4820.
[197] M. Bertero, E. R. E. Pike, *Inverse Probl.* **1991**, *7*, 21.
[198] I. D. Morrison, E. F. Grabowski, C. A. I. Herb, *Langmuir* **1985**, *1*, 496–501.
[199] S. W. A. Provencher, *Comput. Phys. Commun.* **1982**, *27*, 213–227.
[200] M. M. Stanton, J. Samitier, S. Sanchez, *Lab Chip* **2015**, *15*, 3111.
[201] D. Singh, D. Singh, S. Han, *Polymers* **2016**, *8*, 19.
[202] G. Delaittre, A. M. Greiner, T. Pauloehrl, M. Bastmeyer, C. Barner-Kowollik, *Soft Matter* **2012**, *8*, 7323.
[203] C. Ballestrem, B. Hinz, B. A. Imhof, B. Wehrle-Haller, *J. Cell Biol.* **2001**, *155*, 1319.
[204] S. Hansson, T. Tischer, A. S. Goldmann, A. Carlmark, C. Barner-Kowollik, E. Malmström, *Polym. Chem.* **2012**, *3*, 307.
[205] M. Klimek, *Neoplasma* **1965**, *12*, 559.
[206] W. T. Bovie, *Science* **1913**, *37*, 24.
[207] D. Berthelot, *Compt. rend.* **1911**, *151*, 1349.
[208] J. P. Collman, N. K. Devaraj, T. P. A. Eberspacher, C. E. D.Chidsey, *Langmuir* **2006**, *22*, 2457
[209] R. L. Baldwin, *Annu. Rev. Biochem.* **1975**, *44*, 453.
[210] J. E. Rothman, R. Schekman, *Cell* **2011**, *146*, 851.
[211] B. T. Tuten, D. Chao, C. K. Lyon, E. B. Berda, *Polym. Chem.* **2012**, *3*, 3068.
[212] B. S. Murray, D. A. Fulton, *Macromolecules* **2011**, *44*, 7242.
[213] K. Hiltebrandt, K. Elies, R. D'Hooge D, J. P. Blinco, C. Barner-Kowollik, *J. Am. Chem. Soc.* **2016**, *138*, 7048.
[214] N. Zydziak, W. Konrad, F. Feist, S. Afonin, S. Weidner, C. Barner-Kowollik, *Nat. Commun.* **2016**, *7*, 13672.
[215] G. Galilei, *Dialogo di Galileo Galilei sopra i due Massimi Sistemi del Mondo Tolemaico e Copernicano* Florenz, **1632**.
[216] A. Albini, M. Fagnoni, *Green Chem.* **2004**, *6*, 1.
[217] T. R. Barlow, J. C. Brendel, S. Perrier, *Macromolecules* **2016**, *49*, 6203.
[218] G. Mantovani, F. Lecolley, L. Tao, D. M. Haddleton, J. Clerx, J. Cornelissen, K. Velonia, *J. Am. Chem. Soc.* **2005**, *127*, 2966.
[219] A. F. Hirschbiel, W. Konrad, D. Schulze-Sünninghausen, S. Wiedmann, B. Luy, B. V. K. J. Schmidt, C. Barner-Kowollik, *ACS Macro Letters* **2015**, *4*, 1062.
[220] C. Lang, C. Kiefer, E. Lejeune, A. S. Goldmann, F. Breher, P. W. Roesky, C. Barner-Kowollik, *Polym. Chem.* **2012**, *3*, 2413.

[221] A. J. Inglis, S. Sinnwell, T. P. Davis, C. Barner-Kowollik, M. H. Stenzel, *Macromolecules* **2008**, *41*, 4120.
[222] M. Glassner, K. K. Oehlenschlaeger, A. Welle, M. Bruns, C. Barner-Kowollik, *Chem. Commun.* **2013**, *49*, 633.
[223] N. Zhou, L. Lu, X. Zhu, X. Yang, X. Wang, J. Zhu, D. Zhou, *Polymer Bulletin* **2006**, *57*, 491.
[224] H. Zhang, B.Klumperman, R. v. d. Linde, *Macromolecules* **2002**, *35*, 2261.
[225] J. A. Opsteen, J. C. van Hest, *Chem. Commun.* **2005**, 57.

APPENDIX

List of Schemes

The initiation, propagation and termination resemble their FRP analogs (see **Scheme 6**), whereby the propagation step occurs during both equilibria.[46] In the preequilibrium, a propagating chain (Pn) is trapped by a chain transfer agent (CTA). The radical adds to the thiocarbonyl group of the RAFT agent, forming an intermediate radical (kadd). This intermediate radical can now either fragment back to the propagating chain (Pn) and the CTA (k-add), or decay into a protected chain

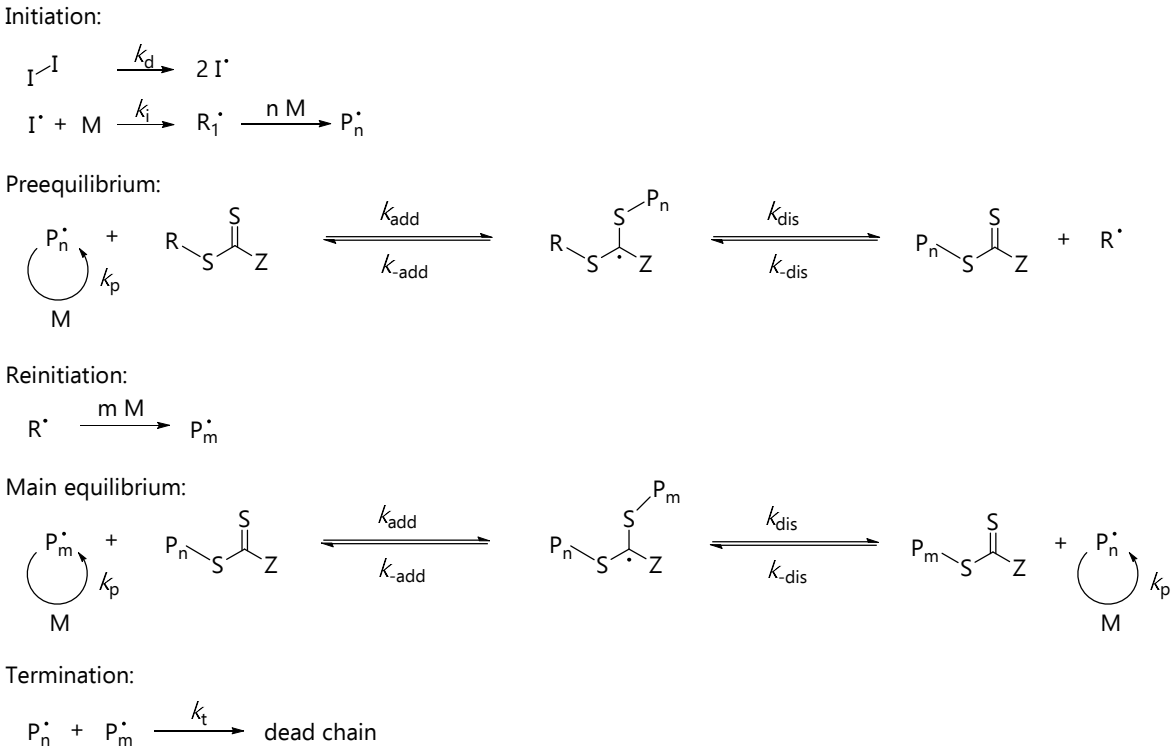

Scheme 6: General overview of the RAFT mechanism. The six reaction steps are depicted (initiation, preequilibrium (with propagation), reinitiation, main equilibrium (again with propagation) and termination.[46] 9

Scheme 7: Schematic overview of R- and Z-group substitutions and their ability to obtain good (—) or limited (---) control when employed in RAFT polymerizations of various monomer groups: methyl methacrylate (MMA), N-(2-hydroxypropyl)methacrylamide (HPMAM), vinyl acetate (VAc), N-vinylpyrrolidone (NVP), styrene (St), methyl acrylate (MA), acrylamide (Am) and acrylonitrile (An). The Scheme was redrawn from Ref. [47], Copyright (2012) ACS publishing.[47] 10

Scheme 8: Jablonski-diagram illustrating the possible photochemical processes in a molecule upon irradiation. Radiationless transitions such as vibrational relaxations, internal conversions (IC) and inter system crossing (ISC) are represented by wavy arrows, Absorption, fluorescence and phosphorescence, aka processes where light is involved, are depicted with straight arrows.[63] 14

Scheme 9: Summary of processes that can occur from an excited molecule, with A, B, C and D illustrating arbitrary molecules.[62] 14

Scheme 10: Overview of the absorption wavelength ranges of the electronic transitions described above. (The scheme was adapted from Ref.[64]) 15

Scheme 11: Comparison between the structures of UV light vs visible light reactive azirine and tetrazole species. The enlargement of the π system from a single benzene ring to a pyrene substituent shifts the wavelength necessary for a photocycloaddition from the UV to the visible range of the light spectrum. 17

Scheme 12: Possible reaction pathways after a photoexcitation of a phenacyl sulfide derivative.[74] 18

List of Figures

List of Abbreviations

1PA	one photon absorption
2D	two dimensions/dimensional
2PA	two photon absorption
3D	three dimensions/dimensional
AFM	atomic force microscopy
Am	acrylamide
An	acrylonitrile
AOM	acoustooptic modulator
APTES	3-aminopropyl)triethoxysilane
ATR-FT-IRM	attenuated total reflectance Fourier transform infrared microscopy
ATRP	atom transfer radical polymerization
CAD	Computer Aided Design
CAM	Computer Aided Manufacturing
$CDCl_3$	deuterated chloroform
CDI	1,1'-carbonyldiimidazole
CFM	confocal fluorescent microscopy
CPAETC	4-cyano-4-(((ethylthio)carbonothioyl)thio)pentanoic acid
CT	charge transfer
CTA	chain transfer agent
CuAAC	copper catalyzed azide alkyne cycloaddition
DA	Diels–Alder
DAPI	4',6-diamidino-2-phenylindole
DCC	N,N'-dicyclohexylcarbodiimide
DCM	dichloromethane
DEAAm	diethyl acrylamide
DLS	dynamic light scattering
DLW	direct laser writing
DMAc	dimethylacetamide
DMAP	dimethylamino pyridine

DMF	dimethylformamide
DMSO	dimethylsulfoxide
DMSO-d_6	deuterated dimethylsulfoxide
DOSY	diffusion ordered spectroscopy
DP_n	degree of polymerization
DPS	2,2′-dipyridyl disulfide
ECM	extracellular matrix
EDC	1-Ethyl-3-(3-dimethylaminopropyl)carbodiimide
eq	equivalent(s)
Et_2O	diethylether
FN	fibronectin
FPA	focal plane array
FRP	free radical polymerization
HAE	heavy atom effect
HDA	hetero Diels–Alder
HEA	2-hydroxethyl acrylate
HEMA	2-hydroxyethylmethacrylate
HOMO	highest occupied molecular orbital
HPMAM	N-(2-hydroxypropyl)methacrylamide
IC	internal conversion
IR	infrared
ISC	inter system crossing
ITX	isopropyl thioxanthone
LDPE	low density polyethylene
LED	light emmiting diode
LN	laminin
LUMO	lowest unoccupied molecular orbital
MA	methyl acrylate
Mal	maleimide
MeCN	acetonitrile
MeOH	methanol
MMA	methyl methacrylate
MMD	molar mass distribution
NA	numerical aperture
NITEC	nitrile-imine mediated tetrazole-ene cycloaddition
NMP	nitroxide mediated polymerization
NMR	nuclear magnetic resonance
NNLS	non-negatively constrained least-squares

NOESY	nuclear Overhauser enhancement spectroscopy
NRD	non radiative transition
NVP	N-vinylpyrrolidone
PBS	phosphate buffered saline
PDMS	poly(dimethyl siloxane)
PE	photoenol
PEG	poly(ethylene glycol)
PE-MA	Photoenol methacrylate
PETA	pentaerytrithol triacrylate
PMDETA	N,N,N′,N″,N″-pentamethyldiethylenetriamine
PS	phenacyl sulfide
PS-MA	Phenacyl sulfide methacrylate
PSt	polystrene
PTFE	poly(tetrafluoroethylene)
PVC	polyvinylchloride
RAFT	reversible addition fragmentation chain transfer
RDRP	Reversible Deactivation Radical Polymerization
SA	sorbic acid
SANS	small angle neutron scattering
SAXS	small angle X-ray scattering
SCNP	single chain nanoparticle
SEC	size exclusion chromatography
SEM	scanning electron microscopy
St	styrene
TEA	triethylamine
TEM	transmission electron microscopy
THF	tetrahydrofuran
TMOF	triethyl orthoformate
TMS	trimethyl silane
ToF-SIMS	Time-of-Flight Secondary-Ion Mass Spectrometry
TosOH	tosylic acid
TPE-TA	trimethylolpropane ethoxylate triacrylate
TPTA	trimethylolypropane triacrylate
U-DPy	uracil-diamidopyridine
UV	ultraviolet
UVA	near ultraviolet
VAc	vinyl acetate
vis	visible

VN	vitronectin
XPS	X-ray photoelectron spectroscopy

LIST OF ALL PUBLICATIONS

Publications arising from the present thesis:

[3] **T. K. Claus**, J. Zhang, L. Martin, M. Hartlieb, H. Mutlu, G. Delaittre, S. Perrier, C. Barner-Kowollik, Macromol. Rapid Commun. **2017**, *1700264*. https://doi.org/10.1002/marc.201700264.

[2] **T. K. Claus**, S. Telitel, A. Welle, M. Bastmeyer, A. P. Vogt, G. Delaittre, C. Barner-Kowollik, *Chem. Commun.*, **2017**, *53*, 1599.

[1b] **T. K. Claus**, B. Richter, V. Hahn, A. Welle, S. Kayser, M. Wegener, M. Bastmeyer, G. Delaittre, C. Barner-Kowollik, *Angew. Chem.*, **2016**, *128*, 3882.

[1a] **T. K. Claus**, B. Richter, V. Hahn, A. Welle, S. Kayser, M. Wegener, M. Bastmeyer, G. Delaittre, C. Barner-Kowollik, *Angew. Chem. Int. Ed. Engl.*, **2016**, *55*, 3817.

Additional publications:

[3] B. Richter, V. Hahn, S. Bertels, **T. K. Claus**, M. Wegener, G. Delaittre, C. Barner-Kowollik, M. Bastmeyer, *Adv. Mater.*, **2017**, *29*, 1604342.

[2] T. Tischer, **T. K. Claus**, K. K. Oehlenschlaeger, V. Trouillet, M. Bruns, A. Welle, K. Linkert, A. S. Goldmann, H. G. Borner, C. Barner-Kowollik, *Macromol. Rapid Commun.*, **2014**, *35*, 1121.

[1] T. Tischer, **T. K. Claus**, M. Bruns, V. Trouillet, K. Linkert, C. Rodriguez-Emmenegger, A. S. Goldmann, S. Perrier, H. G. Borner, C. Barner-Kowollik, *Biomacromolecules*, **2013**, *14*, 4340.

Conference contributions

[2] **T. K. Claus**, B. Richter, V. Hahn, A. Welle, S. Kayser, M. Wegener, M. Bastmeyer, G. Delaittre, C. Barner-Kowollik „*Simultaneous dual encoding of 3D microscaffolds via light-induced modular ligation*", **Warwick Polymer Conference 2016**, Warwick, Großbritannien, 07/2016.

[1] **T. K. Claus**, B. Richter, V. Hahn, A. Welle, S. Kayser, M. Wegener, M. Bastmeyer, G. Delaittre, C. Barner-Kowollik „*Simultaneous dual encoding of 3D microscaffolds via light-induced modular ligation*", **MacroBeGe 2016, 3rd Belgian-German Macromolecular Meeting**, Houffalize, Belgien, 02/2016.

DANKSAGUNG

Die auf den vorhergehenden Seiten dargelegte Arbeit bestand über die Jahre hinweg nicht nur aus Höhen. Während dieser herausfordernden Zeit haben viele Menschen auf unterschiedlichste Weise unterstützt, begleitet oder gefördert. In diesem Abschnitt möchte ich daher meinen tiefen Dank allen aussprechen, die zum Gelingen beigetragen haben.

Der erste Dank an dieser Stelle gebührt Prof. Dr. Christopher Barner-Kowollik, für eine interessante Aufgabenstellung, andauernde Unterstützung bei Problemen und die Freiheit eigenen Ideen nachzugehen. Danke für die herzliche Aufnahme in deinen Arbeitskreis und für dein unermüdliches Bestreben immer das Beste für uns zu erreichen. An gleicher Stelle möchte ich Dr. Guillaume Delaittre für seine engagierte Co-Betreuung danken. Vielen Dank für deine zahlreichen Trips in den Westen, deine guten Ratschläge, viele aufbauende Gespräche und nicht zuletzt das Korrekturlesen meiner kompletten Arbeit.

Die Bearbeitung einer Vielzahl der Projekte wäre ohne die Hilfe von anderen nicht möglich gewesen. Daher gebührt mein aufrichtiger Dank allen Kooperationspartnern, für eine gute und fruchtvolle Zusammenarbeit: dem Biologen-Team um Prof. Dr. Martin Bastmeyer, insbesondere Sarah Bertels für die Zelltests; dem Physiker-Team um Prof. Dr. Martin Wegener, insbesondere Dr. Benjamin Richter und Vincent Hahn für das Schreiben, Funktionalisieren und Untersuchen von unzähligen DLW Strukturen, sowie vielen interessanten Diskussionen mit euch im Grenzbereich zwischen Chemie, Biologie und Physik; Dr. Alexander Welle für zahlreiche, teils sehr fordernde ToF-SIMS Messungen, die du mit unglaublicher Kompetenz und Geschwindigkeit für mich gemacht hast; Dr. Vanessa Troulliet für alle XPS Messungen. One special thanks goes to Prof. Dr. Sébastien Perrier for hosting me as a guest in his group at the University of Warwick, it was an awesome experience. Dr. Matthias Hartlieb and Junliang Zhang and Liam Martin are due to teaching me everything about RAFT block copolymerizations. In diesem Zusammenhang danke ich dem Karlsruher House of Young Scientists (KHYS) für die finanzielle Unterstützung meines Auslandsaufenthaltes in England. Assistance came not only from outside the group, but also from inside. In this context I would like to thank Andrew P. Vogt, Siham Telitel and Hatice Mutlu for your commitment and help in our shared publications.

Außerdem gebührt ein großer Dank Dr. Maria Schneider, Dr. Anja Goldmann, Evelyn Stühring, Vincent Schüler und Katharina Elies, die durch ihr tägliches Bemühen „den Laden am Laufen“ halten.

Ein besonderer Dank geht auch an Christian Schmitt und Tanja Rieder, die ihre Bachelor-/Vertieferarbeit unter meiner Betreuung angefertigt haben. Die Zusammenarbeit mit euch hat großen Spaß gemacht, ich wünsche euch viel Erfolg für eure Zukunft.

As I would surely forget someone when starting to list all people, therefore, I will simply thank all former and current members of the Westies and whole macroarc-team, who I came across on my time here. I had plenty of beneficial discussions and an amazing time during all lunch breaks, coffee breaks, barbecues, Doko sessions, Doctorwagon building, climbing activities, football- or girls' evenings…. We have a great, amicable and productive atmosphere in the group, I hope you can keep these traditions despite the partial move to Australia. At the same point I would like to give many thanks to all Perrier group members and others I have met during my time in Warwick. You made my stay truly memorable.

Alten, sowie neuen Freunden und Kollegen, die zu Freunden wurden, möchte ich für die vielen schönen und unterhaltsamen Stunden abseits der Arbeit danken.

Abschließend möchte ich meine Hochachtung und Dankbarkeit denen aussprechen, ohne die ich nicht die wäre, die ich heute bin: meiner großen, liebevoll verrückten Familie; allen voran natürlich euch: Mama, Papa und meiner (großen) kleinen Schwester Meike. Egal bei was, oder zu welcher Tages- und Nachtzeit, ich kann immer auf eure Hilfe, Unterstützung und Liebe vertrauen.
Der größte Dank jedoch gilt einzig und allein dir, Peter. Einen Menschen wie dich an meiner Seite zu wissen, ist unbeschreiblich wertvoll. Ich freue mich auf unsere gemeinsame Zukunft!